

POLITECNICO DI TORINO

Master Degree in Electrical Engineering

Master Degree Thesis

**Position Sensorless Control of  
Multiphase PMSMs**



**Supervisor:**

Prof. Andrea Cavagnino

**Candidate:**

Ornella Stiscia

**External Supervisor:**

Prof. Emil Levi

April 15, 2019



The external supervisors are Prof. Emil Levi and MSc.ee Marko Slunjski from the Department of Electronics and Electrical Engineering, of the John Moores University (Liverpool).

# Contents

<b>List of Tables</b>	V
<b>List of Figures</b>	VII
<b>1 Introduction</b>	1
1.1 Preliminary Considerations and Thesis Goal . . . . .	1
1.2 Organisation of the Thesis . . . . .	3
<b>2 Model of Sinusoidal Multiphase Surface Permanent Magnet Synchronous Machine</b>	5
2.1 Introduction . . . . .	6
2.2 Multiphase Sinusoidal Surface Permanent Synchronous Machine Modelling . . . . .	10
2.2.1 Mathematical Model of a Multiphase Synchronous Machine in Phase Variable Domain . . . . .	10
2.2.2 Decoupling Transformation . . . . .	21
2.2.3 Synchronous Reference Frame Multiphase surface PMSM modelling . . . . .	26
2.3 Nine-phase Surface PMSM Modeling . . . . .	36
<b>3 Field-Oriented Control and Model Testing Results for Sinusoidal PMSM</b>	43
3.1 Introduction . . . . .	44
3.2 <i>FOC</i> of Multiphase Surface <i>PMSM</i> . . . . .	46
3.3 Speed and Current Control . . . . .	50
3.4 Simulation Results . . . . .	57
<b>4 Modelling and Control of the Surface PMSM with Non-Sinusoidal Back-EMF</b>	65
4.1 Introduction . . . . .	66
4.2 Non-Sinusoidal Machine Model . . . . .	69

4.2.1	Back- <i>EMF</i> and <i>PM</i> harmonic distribution . . . . .	69
4.2.2	Harmonic Model in <i>VSD</i> Variables . . . . .	71
4.2.3	Harmonic Model in Phase Variable Domain . . . . .	77
4.3	Current Harmonic Mapping . . . . .	89
4.3.1	Low Order Harmonics Elimination . . . . .	89
<b>5</b>	<b>Sensorless Control of a Nine-Phase Surface <i>PMSM</i> with Non-Sinusoidal Back-<i>EMF</i></b>	<b>99</b>
5.1	Introduction . . . . .	100
5.2	Back- <i>EMF</i> -Based Method . . . . .	103
5.2.1	Position Estimation using Phase-Locked Loop . . . . .	107
5.2.2	Position Estimation using Harmonic Phase-Locked Loop . . . . .	117
5.3	An <i>I-Hz</i> Starting Method . . . . .	120
5.4	Smooth and Fast Transition to Sensorless <i>FOC</i> . . . . .	127
5.5	The Hybrid Sensorless Control: Simulation Results . . . . .	133
<b>6</b>	<b>Experimental Validation</b>	<b>147</b>
6.1	Test rig . . . . .	148
6.2	Characterization of the Machine Parameters . . . . .	152
6.2.1	Zero-Sequence Test . . . . .	152
6.2.2	Single Phase Test . . . . .	157
6.2.3	Short Circuit Test and Design approach . . . . .	159
6.2.4	Test rig characterization . . . . .	163
6.3	Experimental results . . . . .	168
<b>7</b>	<b>Conclusion</b>	<b>189</b>
7.1	Conclusions . . . . .	189
7.2	Future Work . . . . .	192
	<b>Bibliography</b>	<b>193</b>

# List of Tables

3.1	Electrical and mechanical parameters of surface <i>PMSM</i> machine . . .	57
3.2	Control parameters of current and speed loop. . . . .	58
4.1	Harmonics of the permanent magnets flux surface <i>PMSM</i> machine. .	70
5.1	Phase-Locked Loop parameters. . . . .	111
6.1	Zero-sequence test: leakage inductance. . . . .	157
6.2	Single phase test: isotropic inductance. . . . .	159
6.3	<i>FFT</i> analysis: back-EMF and current in <i>VSD</i> variables. . . . .	163
6.4	Main data of nine-phase <i>PMSM</i> machine. . . . .	164
6.5	Magnetizing inductance related to <i>h</i> harmonic. . . . .	164
6.6	Test rig characterization: mechanical parameters. . . . .	165
6.7	Values of the control parameters. . . . .	171



# List of Figures

2.1	Schematic of main elements of a multiphase electric drive. . . . .	6
2.2	Synchronous machine structures. . . . .	7
2.3	Classification of permanent magnet electric machines. . . . .	8
2.4	Cross-section of surface and interior permanent magnet rotor. . . . .	9
2.5	Multiphase machine winding distribution around stator circumference. . . . .	11
2.6	Multiphase machine equivalent circuit in phase variable domain. . . . .	12
2.7	Angle distribution for mutual inductance definition. . . . .	14
2.8	Scheme for the computation of the magnetomotive force. . . . .	14
2.9	Scheme for the computation of the magnetic flux in the magnetic $i$ -axis due to the current in $j$ -axis. . . . .	15
2.10	Single-phase $PM$ flux linkage computation scheme. . . . .	18
2.11	Dynamic electromagnetic model of the machine. . . . .	20
2.12	Equivalent circuit of sinusoidal machine: (a) - $(\alpha, \beta)$ ; (b) - $(x, y)$ i (i = 1, 2, 3) subplanes; (c) - zero-sequence component. . . . .	27
2.13	A schematic representation of complete $[T] = [D] \cdot [C]$ transformation. . . . .	28
2.14	Generic waveforms in different references frame. . . . .	29
2.15	Equivalent circuit of machine in synchronous reference frame. . . . .	31
2.16	Electromagnetic torque (green blocks), mechanical equilibrium on ro- tor shaft (peach blocks) and electrical speed and position (blue blocks). . . . .	34
2.17	Nine-phase $PMSM$ winding distribution around stator circumference. . . . .	36
2.18	Winding arrangement of slots in nine-phase surface $PMSM$ . . . . .	37
2.19	Equivalent circuit of nine-phase surface $PMSM$ in phase variables. . . . .	39
3.1	Schematic of current, speed and position loops. . . . .	44
3.2	Vector control of a nine-phase surface $PMSM$ : drive control (orange blocks); machine control (blue blocks); $RF$ s transformation (green blocks). . . . .	46
3.3	$FOC$ of sinusoidal nine-phase surface $PMSM$ . . . . .	47
3.4	Proportional-integral control with Anti-windup algorithm. . . . .	49
3.5	Anti-windup algorithm. . . . .	49
3.6	Schematic block of the current regulation loop. . . . .	50

3.7	Asymptotic Bode plot of the open-loop transfer function magnitude for current regulation loop. . . . .	52
3.8	Schematic block of the speed regulation loop. . . . .	54
3.9	Asymptotic Bode plot of the open-loop transfer function magnitude for speed regulation loop. . . . .	55
3.10	Speed reference and measured response under <i>FOC</i> . . . . .	59
3.11	Torque reference and measured response under <i>FOC</i> . . . . .	59
3.12	Flux linkage vector caused by only the <i>PM</i> presence. . . . .	60
3.13	Back-electromotive forces for sinusoidal nine-phase <i>PMSM</i> . . . . .	60
3.14	Phase voltages for sinusoidal nine-phase <i>PMSM</i> . . . . .	62
3.15	Phase currents for sinusoidal nine-phase <i>PMSM</i> . . . . .	62
3.16	Current in $(\alpha, \beta)$ subplane after <i>VSD</i> transformation. . . . .	63
3.17	Current in $(x, y)$ subplanes after <i>VSD</i> transformation. . . . .	63
3.18	Flux producing current after the rotational transformation. . . . .	64
3.19	Torque producing current after the rotational transformation. . . . .	64
4.1	Magnet span of surface <i>PMSM</i> : 180° magnet span on rotor (left) and 45° magnet span on rotor (right). . . . .	66
4.2	Back- <i>EMF</i> waveforms of real machine: experimental results at 1465 <i>rpm</i> . . . . .	67
4.3	Back- <i>EMF</i> ( $e_{a1}, e_{a2}, e_{a3}$ ) in steady-state at 1465 <i>rpm</i> : CH.1 - CH.3: 40 <i>V/div</i> . . . . .	68
4.4	Fourier analysis of non-sinusoidal back- <i>EMF</i> on recorded data at 1465 <i>rpm</i> . . . . .	68
4.5	The back- <i>EMF</i> in $(\alpha, \beta)$ subplane and zero-sequence component. . . . .	72
4.6	The back- <i>EMF</i> in $(x, y)1$ subplane. . . . .	73
4.7	The back- <i>EMF</i> in $(x, y)2$ subplane. . . . .	73
4.8	The back- <i>EMF</i> in $(x, y)3$ subplane. . . . .	74
4.9	Equivalent circuit of non-sinusoidal machine: (a) - $(\alpha, \beta)$ ; (b) - $(x, y)i$ ( $i = 1, 2, 3$ ) subplanes; (c) - zero-sequence component. . . . .	76
4.10	Schematic of harmonic mapping analysis. . . . .	89
4.11	Schematic of the <i>VPI</i> transfer function. . . . .	90
4.12	Schematic block of the harmonic current regulation loop. . . . .	90
4.13	Asymptotic Bode plot of the open-loop transfer function magnitude for harmonic current regulation loop with <i>VPI</i> . . . . .	92
4.14	Block diagram of <i>VPI</i> resonant controller. . . . .	93
4.15	<i>VPIs</i> resonant controllers: parallel connection. . . . .	93
4.16	Asymptotic Bode plot of the closed-loop transfer function magnitude for harmonic current regulation loop with <i>VPI</i> . . . . .	94
4.17	Phase currents without <i>VPI</i> controllers for non-sinusoidal machine. . . . .	95
4.18	Phase currents with <i>VPI</i> controllers for non-sinusoidal machine. . . . .	95

4.19	Phase current spectrum harmonic without <i>VPI</i> controllers. . . . .	96
4.20	Phase current spectrum harmonic with <i>VPI</i> controllers. . . . .	96
4.21	<i>FOC</i> with low order harmonic elimination for non-sinusoidal nine-phase surface <i>PMSM</i> . . . . .	97
4.22	Block diagram of <i>PRES</i> . . . . .	97
4.23	Asymptotic Bode plot of the open-loop and closed-loop transfer function magnitude for harmonic current regulation loop with <i>PRES</i> . . . . .	98
5.1	A classification of position and speed estimation methods (blue blocks) and schemes (white blocks). . . . .	101
5.2	Sensorless control system of surface <i>PMSM</i> . . . . .	103
5.3	A schematic view of a closed-loop observer. . . . .	104
5.4	Observer current in third subplane. . . . .	106
5.5	Block diagram of rotor position and speed estimations based on <i>PLL</i> . . . . .	108
5.6	Block diagram of <i>PLL</i> using trigonometric functions. . . . .	108
5.7	Block diagram of angle demodulation. . . . .	108
5.8	Asymptotic Bode plot of the <i>PLL</i> open-loop transfer function magnitude. . . . .	109
5.9	<i>PLL</i> effectiveness: speed response. . . . .	112
5.10	<i>PLL</i> effectiveness: speed filtered and no filtered responses. . . . .	112
5.11	<i>PLL</i> effectiveness: trigonometric functions at low speed. From top to bottom: sine; cosine. . . . .	113
5.12	<i>PLL</i> effectiveness: trigonometric functions at high speed. From top to bottom: sine; cosine. . . . .	114
5.13	<i>PLL</i> effectiveness: rotor position at low speed. From top to bottom: <i>PLL</i> output; demodulation output. . . . .	115
5.14	<i>PLL</i> effectiveness: rotor position at high speed. From top to bottom: <i>PLL</i> output; demodulation output. . . . .	116
5.15	Block diagram of harmonic <i>PLL</i> . . . . .	117
5.16	Harmonic <i>PLL</i> effectiveness: trigonometric functions at high speed. From top to bottom: sine; cosine. . . . .	118
5.17	Harmonic <i>PLL</i> effectiveness: estimated rotor position. . . . .	119
5.18	Relationship among stationary, rotor and arbitrary <i>RFs</i> . . . . .	120
5.19	Block diagram of <i>I-Hz</i> starting method. . . . .	121
5.20	Open-loop <i>I-Hz</i> : speed response. . . . .	122
5.21	Open-loop <i>I-Hz</i> : torque response. . . . .	123
5.22	Measured current along <i>d</i> -axis in estimated rotor and arbitrary <i>RFs</i> . . . . .	124
5.23	Measured current along <i>q</i> -axis in estimated rotor and arbitrary <i>RFs</i> . . . . .	124
5.24	Reference, measured and estimated angle in <i>I-Hz</i> control at low speed. From top to bottom: <i>PLL</i> output; demodulated. . . . .	125

5.25	Reference, measured and estimated angle in $I$ -Hz control at high speed. From top to bottom: $PLL$ output; demodulated. . . . .	126
5.26	Switch conditions from $I$ -Hz control to sensorless $FOC$ . . . . .	127
5.27	Measured current along estimated $d$ -axis in transition to sensorless $FOC$ . From top to bottom: the time trend; corresponding zoom. . . .	129
5.28	Measured current along estimated $q$ -axis in transition to sensorless $FOC$ . From top to bottom: the time trend; corresponding zoom. . . .	130
5.29	Transition to sensorless $FOC$ : phase currents. . . . .	131
5.30	Transition to sensorless $FOC$ : speed response. . . . .	132
5.31	Block diagram of hybrid sensorless $FOC$ for nine-phase surface $PMSM$ . . . . .	133
5.32	Hybrid control under no-load conditions. From top to bottom: speed response; torque response. . . . .	135
5.33	Hybrid control under no-load conditions. From top to bottom: angle error; zoom area of the angle. . . . .	137
5.34	Hybrid control under no-load conditions. From top to bottom: vector $\underline{e}_{xy3}$ magnitude; phase error. . . . .	138
5.35	Measured currents in estimated rotor $RF$ . From top to bottom: $d$ -axis; $q$ -axis. . . . .	140
5.36	Hybrid control under no-load conditions. From top to bottom: phase current responses; corresponding zoom area. . . . .	141
5.37	Hybrid control under no-load conditions. From top to bottom: phase voltage references; corresponding zoom area. . . . .	142
5.38	Hybrid control under load conditions. From top to bottom: speed response; torque response. . . . .	144
5.39	Measured currents in estimated rotor $RF$ . From top to bottom: $d$ -axis; $q$ -axis. . . . .	145
6.1	Block diagram of experimental setup. . . . .	148
6.2	The machine under test (left) and the driving machine (right). . . . .	149
6.3	dc voltage source <i>Sorensen SGI 600/25</i> . . . . .	149
6.4	Modular power converter. . . . .	149
6.5	<i>Tektronix</i> oscilloscope. . . . .	150
6.6	Example of the graphic user interface developed in <i>Control Desk</i> . . . . .	151
6.7	Equivalent circuit of the zero-sequence test. . . . .	155
6.8	Equivalent circuit of the single phase test. . . . .	158
6.9	Short circuit test: back- $EMF$ and current in $(\alpha, \beta)$ subplane. . . . .	160
6.10	Short circuit test: back- $EMF$ and current in $(x, y)1$ subplane. . . . .	161
6.11	Short circuit test: back- $EMF$ and current in $(x, y)2$ subplane. . . . .	161
6.12	Short circuit test: back- $EMF$ and current in $(x, y)3$ subplane. . . . .	162
6.13	Test rig characterization: iterative methodology. From top to bottom: acceleration; deceleration. . . . .	167

6.14	The digital control implemented in laboratory. . . . .	169
6.15	Hybrid control for experimental validation. . . . .	170
6.16	No-load conditions in experimental validation. From top to bottom: speed response; torque response. . . . .	173
6.17	Measured current along estimated and arbitrary $d$ -axes. From top to bottom: the time trend; corresponding zoom. . . . .	174
6.18	Measured current along estimated and arbitrary $q$ -axes. From top to bottom: the time trend; corresponding zoom. . . . .	175
6.19	No-load conditions in experimental validation. From top to bottom: vector $\underline{e}_{xy3}$ magnitude; phase error. . . . .	176
6.20	No-load conditions in experimental validation. From top to bottom: angle error; zoom area of the angle. . . . .	177
6.21	No-load conditions in experimental validation. From top to bottom: phase current responses; corresponding zoom area. . . . .	178
6.22	No-load conditions in experimental validation. From top to bottom: phase voltage references; corresponding zoom area. . . . .	179
6.23	No-load conditions: speed response. 250 <i>rpm/div</i> . . . . .	180
6.24	No-load conditions: currents response. 2 <i>A/div</i> . . . . .	180
6.25	No-load conditions: currents and speed response during the transition. CH.1 - CH.3: 2 <i>A/div</i> ; CH.4: 250 <i>rpm/div</i> . . . . .	181
6.26	No-load conditions: currents and speed responses in steady-state at 1500 <i>rpm</i> . CH.1 - CH.3: 2 <i>A/div</i> ; CH.4: 250 <i>rpm/div</i> . . . . .	181
6.27	Load conditions in experimental validation. From top to bottom: speed response; torque response. . . . .	183
6.28	Measured currents along estimated and arbitrary RFs. From bottom to top: $d$ -axes; $q$ -axes. . . . .	184
6.29	Load conditions in experimental validation. From top to bottom: angle error; zoom area of the angle. . . . .	185
6.30	Load conditions in experimental validation. From top to bottom: phase currents; phase voltage references. . . . .	186
6.31	Load conditions: speed response. 250 <i>rpm/div</i> . . . . .	187
6.32	Load conditions: currents response. 2 <i>A/div</i> . . . . .	187
6.33	Load conditions: currents and speed responses in steady-state at 1500 <i>rpm</i> . CH.1 - CH.3: 2 <i>A/div</i> ; CH.4: 250 <i>rpm/div</i> . . . . .	188

# List of Notation and Acronyms

Symbol(s)	Meaning
<i>ac</i>	Alternating Current
<i>back – EMF</i>	back-electromotive force [V]
<i>BLDCM</i>	Brushless <i>dc</i> electric motor
<i>CVC</i>	Current vector controller
<i>dc</i>	Direct Current
<i>DCA</i>	Drive control algorithm
<i>DSP</i>	Digital Signal Processing
<i>FFT</i>	Fast Fourier transform
<i>f<sub>s</sub></i>	Sampling frequency
<i>f<sub>sw</sub></i>	Switching frequency
<i>FOC</i>	Field-Oriented Control
<i>IPM</i>	Interior Permanent Magnet
<i>MMF</i>	magnetomotive force [A]
<i>MS</i>	Multi-Stator
<i>n</i>	Phase number
<i>P</i>	Pole pairs
<i>PEC</i>	Power electronic converters

<i>PM</i>	Permanent Magnet
<i>PMAC</i>	Permanent Magnet Alternating Current
<i>PMDC</i>	Permanent Magnet Direct Current
<i>PMSM</i>	Permanent Magnet Synchronous Machine
<i>PWM</i>	Pulse width modulation
<i>PRES</i>	Proportional resonant controller
<i>RF</i>	Reference frame
<i>VPI</i>	Vector proportional integral
<i>VSD</i>	Vector Space Decomposition
<i>VSI</i>	Voltage Source Inverter

# Chapter 1

## Introduction

### 1.1 Preliminary Considerations and Thesis Goal

Multiphase electric drives, termed multiphase when the stator number of phases ( $n$ ) is higher than 3 ( $n > 3$ ), have also remarkably increased as a potential solution for various industrial applications: safety critical system where fault tolerance is a main concern e.g., aircraft [1] applications where the continuous operation means economic benefit, e.g. offshore wind and energy systems [2]. The increased complexity of multiphase machine with respect to their three-phase counterparts, is drowned by the phase redundancy. Some advantages in multiphase machines are: fault tolerance, lower torque ripple, lower phase stator current for the same voltage and power rating, capability to benefit from exclusive modes of operation and many others [3]. Despite these advantages, three-phase machines are today the most commonly used for industrial applications.

The multiphase permanent magnet synchronous machines have the advantages of high efficiency, high power density and excellent control performance [4]. The development of permanent magnet materials and power electronic devices have contributed significantly to multiphase *PMSM*. The essential requirement in multiphase *PMSM* control is to achieve the high-performance of electric drive. The accurate knowledge of rotor position and/or speed information is traditionally measured with mechanical sensors, mounted on the motor shaft. These sensors are not desirable in the control system for many reasons. The position sensors not only increase the mounting and maintenance cost, but also reduce the reliability of the whole system, as they are prone to environment disturbances. Consequently, in certain applications the position sensors cannot be used because the mentioned drawbacks are not acceptable. Hence, sensorless control techniques have been widely researched and applied in industry. The sensorless techniques can be categorized in two main groups: back-*EMF* methods and saliency-based methods.

The aim of this work is to remove the mechanical sensors under field-oriented control for multiphase *PMSM*. Compared to the three-phase counterparts, the harmonic model and sensorless control for multiphase machine are not very well-known and off-the-shelf solutions are not available.

Sensorless *FOC* is implemented in rotor reference frame. When the machine model is defined in *VSD* variables, it is decoupled into several subplanes [7]: the fundamental subplane, called  $(\alpha, \beta)$ , and other subplanes, called  $(x, y)$ . Electro-mechanical energy conversion does not take place only in first subplane  $(\alpha, \beta)$  in case of non-sinusoidal back-*EMF* harmonic and winding distribution. The harmonic current in  $(x, y)$  subplanes can be eliminated with current control. The resonant controller, presented in [8], [9], [10] can be used of the current control for harmonic components [11]. An important advantage of the *VSD* approach is a unique harmonic mapping.

On the basis of harmonic model in *VSD* variables, the back-*EMF* harmonics can be researched for sensorless field-oriented control. The resonant controllers in stationary reference frame are employed to eliminate the induced current harmonics. The consequence is evident: if the current harmonics are eliminated, the *VSD* reference phase voltages in output to the control are almost equal to harmonic back-*EMF*. It is well known that the instantaneous magnitude of the back-*EMF*, induced by the rotor movement in the armature windings, depends on the position of permanent magnets with respect to the windings positions. However, the rotor position is extracted from the reference phase voltages when the machine is operating.

## 1.2 Organisation of the Thesis

This thesis is divided into 7 chapters as follows:

- Chapter 1 provides a general introduction about the multiphase electric drives and sensorless control. A brief discussion about advantages of multiphase drives and sensorless control is presented together with a brief literature survey concerning the current state-of-the-art. This chapter is completed with organisation of the thesis.
- Chapter 2 deals with model of sinusoidal *PM* multiphase machines in phase variable domain, in stationary and in synchronous reference frames. The chapter is completed with the model of nine-phase surface *PMSM* with sinusoidal back-electromotive force.
- Chapter 3 deals the field-oriented control theory of sinusoidal nine-phase surface *PMSM*. The control is composed by cascaded *PI* controllers and the anti-windup technique is added. The analysis and design of *PI* gains in speed and current loops regulation is given. This chapter is completed with simulation results in *Matlab/Simulink* environment to evaluate the control performance.
- Chapter 4 deals the machine prototype. The back-*EMF* and *PM* harmonic distribution are the starting point to obtain the harmonic model in *VSD* variables and in phase variable domain. The chapter is completed with vector proportional integral and resonant controller theories for the analysis and design of current loop regulation.
- Chapter 5 deals the sensorless field-oriented control. A brief literature survey of current state-of-the-art in sensorless control is provided: estimation methods are presented. Most importantly, this chapter provides how the novelty of the conducted work comes from the use of back-*EMF* harmonic to estimate the rotor position and/or speed informations. The angle estimation is based on back-*EMF*. Through the use of third harmonic of back-*EMF* and the employed resonant controller, the rotor position is obtained. This method fails at low speed and for this reason the starting method *I-Hz* is necessary. This chapter is completed with simulation results in *Matlab/Simulink* environment under hybrid control.
- Chapter 6 deals the experimental validation. The employed test rig and digital controller is given. To follow, the machine tests to obtain the electrical and mechanical parameters are presented. In particular, the following tests have been conducted: zero sequence test, single phase test, short circuit test and test rig characterization. Most importantly, this chapter is completed with

experimental validation of the proposed hybrid control on machine highly non-sinusoidal back-*EMF*. The mechanical rotor position has been measured with an encoder in order to compare the measured value with its estimate. The experimental results are obtained under sensorless control.

- Chapter 7 provides conclusions. In addition, possibilities for future work are discussed in this chapter as well.

## Chapter 2

# Model of Sinusoidal Multiphase Surface Permanent Magnet Synchronous Machine

In this chapter the preliminary remarks and multiphase machine modelling are described to obtain a mathematical model of Surface Permanent Machine Magnet Synchronous.

Chapter is organised as follows:

- In Section 2.1 general considerations about multiphase machine, different types of synchronous machine and the assumptions used in the sections to follow are presented.
- In Section 2.2 the mathematical model of surface *PMSM* is developed, i.e., the general model with arbitrary phase number on the stator is analysed. Machine model in phase variable domain, vector space decomposition variables and, finally, synchronous reference frame are reported.
- In Section 2.3 model of nine-phase surface *PMSM* is developed using phase variables modelling equations and synchronous reference frame derived in the previous section.

## 2.1 Introduction

An electric machine is called multiphase machine when the stator phase number is higher than three ( $n > 3$ ). This machine is supplied from multiphase converter in order to perform the electromechanical energy conversion. The conversion is reversible: from electrical power to mechanical power (motor  $M$ ) or from mechanical power to electrical power (generator  $G$ ). The main elements of a multiphase electric drive are shown in Fig. 2.1.

The principle of rotating field is the same as in three-phase machine: a symmetric rotating magnetic field can be produced with as few as two polar wound coils driven at  $90^\circ$  phasing. However, three sets of coils are nearly always used because it is compatible with a symmetric three-phase alternating current system (power supply). All rotating fields in multiphase synchronous machines, caused by the fundamental harmonic of the supply, rotate at synchronous speed, governed with the stator winding frequency. In the case of synchronous machine, the rotor speed rotates at the same speed as does stator field.

The advantages of multiphase machines over three-phase machines are summarised in the following [12]:

- Fault tolerance against machine and converter faults that allows a smooth postfault operation with no additional hardware than their three-phase counterparts. If one phase of a three-phase machine becomes open-circuited the machine becomes single-phase. It may continue to run but requires some external means for starting, and must be massively de-rated. If one phase of a  $n$ -phase machine becomes open circuited, it will still self-start and will run with only minimal de-rating [13].
- Power density improvement with current harmonic injection: torque production can be enhanced by injection of higher stator current harmonics [14].

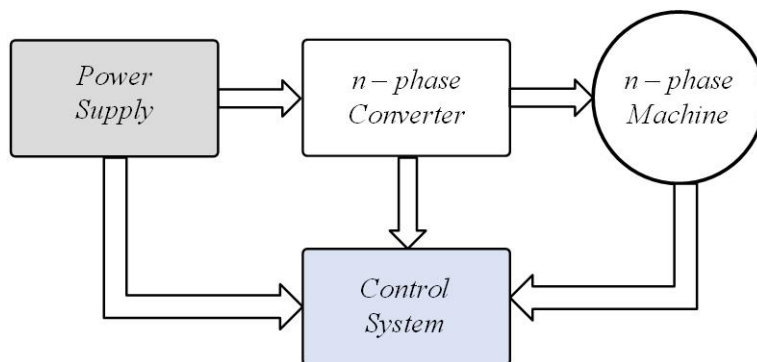


Figure 2.1: Schematic of main elements of a multiphase electric drive.

Torque enhancement in this manner is possible only if the stator winding magnetomotive force distribution contains corresponding time-spatial harmonics, so that the machine is in this case designed with concentrated rather than distributed stator winding (only for synchronous machines) [15].

- Multiphase machines are less susceptible than their three-phase counterparts to time-harmonic components in the excitation waveform. Such excitation components produce pulsating torques at even multiples of the fundamental excitation frequency.
- Lower current per phase without increase the phase voltage. This advantages feature may be useful for electric vehicles and similar applications where lower, upper limit of voltage and current is desirable.

Most of synchronous machines have excitation on rotor, which can be provided either by permanent magnets or direct current supplied excitation (or field) winding. If the rotor is not equipped with magnets or the excitation winding, the machine is called synchronous reluctance type.

Two principal geometries of the rotor are illustrated in Fig. 2.2. Only one phase ( $1s$ ) of the stator multiphase winding is shown and it is illustrated schematically with its magnetic axis. The rotor is shown as having an excitation winding, which is supplied from a  $dc$  source and which produces rotor field. This field is stationary with respect to rotor and acts along the  $d$ -axis ( $N$ -pole of the magnets). But, since rotor rotates at synchronous speed, the rotor field rotates at synchronous speed in the air-gap as well.

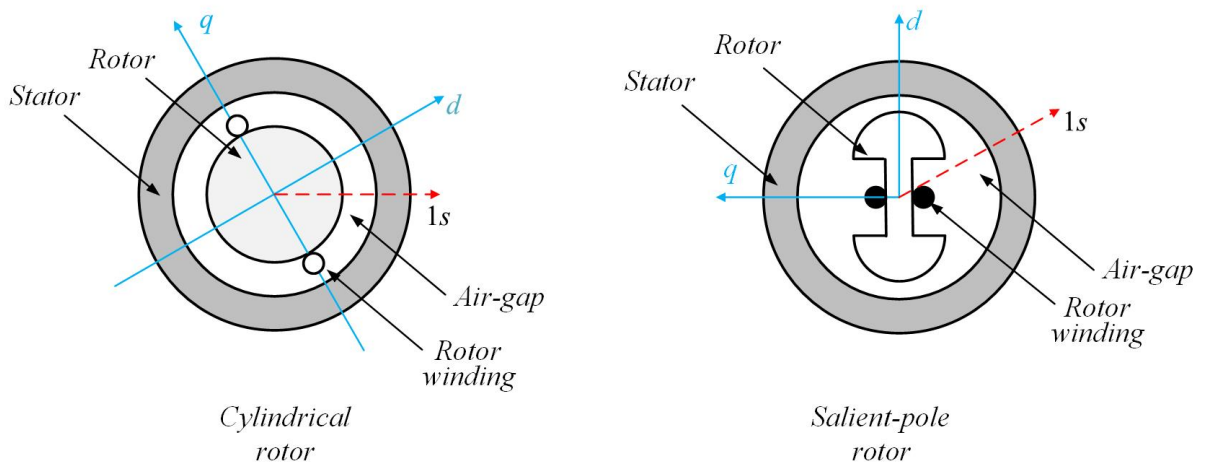


Figure 2.2: Synchronous machine structures.

Permanent magnets are installed when machine rotor is without excitation windings. The permanent magnet electric machines can be classified as shown in Fig. 2.3. In red is highlighted the electric machine of interest in this thesis. A brief classification of permanent magnet machines is presented [4].

In *PM* electric machines the field is generated by permanent magnets, eliminating the requirement of field windings and external electrical source for it. In contrast to the conventional doubly excited electric machines, which have two sources of excitation (armature and field), the copper loss due to field windings does not exist, increasing the efficiency of the machine. The synchronous machine with permanent magnet allows reducing the size and the weight than the conventional doubly excited electric machines. The first classification of permanent magnet machines is based on the excitation: permanent magnet *dc* and permanent magnet *ac*. The *PMDC* is very similar to separately excited *dc* machine because *PM* in the place of field windings are used. The *PMAC* are synchronous machines: the field is created by permanent magnets on the rotor. The *PMAC* machines can be classified into trapezoidal and sinusoidal types. The distinction is based on waveform of back-electromotive force: in trapezoidal machines the induced back-*EMF* is trapezoidal instead it is sinusoidal in sinusoidal machines. The sinusoidal machines are favorite in application where the high control performance is required. The sinusoidal *PMAC* are also called permanent magnet synchronous machines. Different rotor configurations of *PMSM*s exist based on how the magnets are placed in the rotor. The two common types are shown in Fig. 2.4: the permanent magnets may be either fixed along the circumference of a cylindrical rotor (Surface Permanent Magnets) or they are inside the rotor (Interior Permanent Magnets). The structure of *SPM* and *IPM* machine is shown in the left and in the right of Fig. 2.4, respectively.

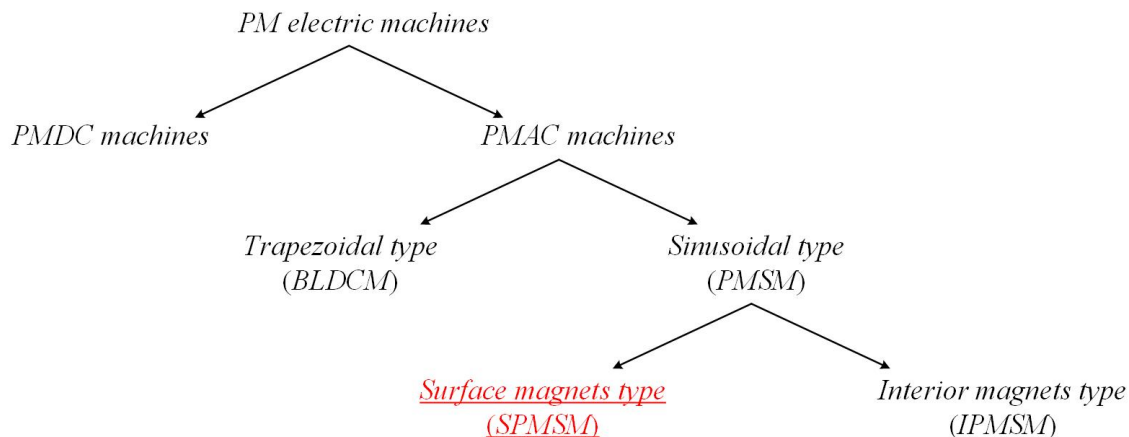


Figure 2.3: Classification of permanent magnet electric machines.

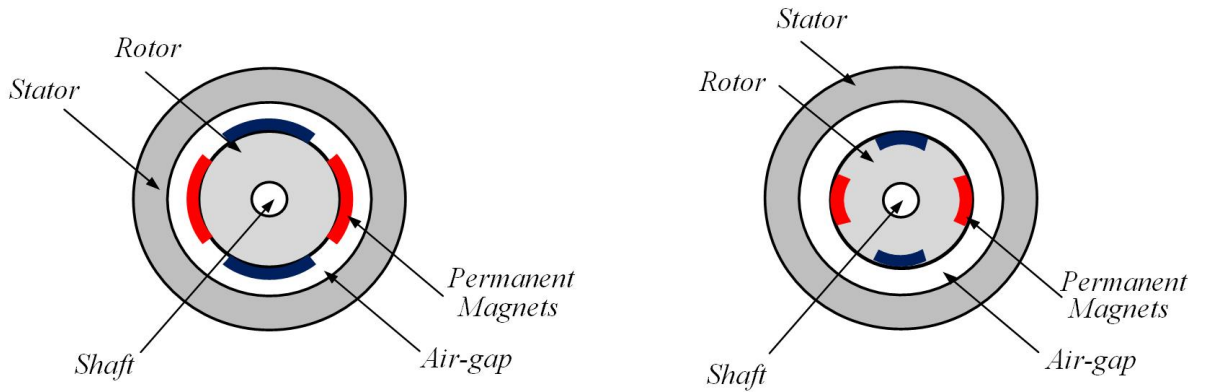


Figure 2.4: Cross-section of surface and interior permanent magnet rotor.

The *SPM* machine is a sinusoidal isotropic brushless, without reluctance torque contribution. The torque is product by the interaction between permanent magnets on rotor and stator currents. Therefore the torque control is directly proportional to the current along  $q$ -axis ( $T_{em} \propto i_q$ ). It is recalled that, this motor type is analysed in this work.

Reluctance torque contribution in *IPM* machine is obtained with the combination of the currents in  $(d, q)$  axes due to the anisotropic (motor structure property) torque contribution.

## 2.2 Multiphase Sinusoidal Surface Permanent Synchronous Machine Modelling

In this thesis a symmetrical surface *PMSM* is considered. The stator winding is formed by  $n$  windings. The stator frame is redesigned:  $n$  independent windings and  $2n$  terminals are obtained. Modeling of multiphase *ac* machines usually takes into account number of simplifying assumption. They are:

- Every phase is identical to other phases in the machine.
- Stator resistance of windings are assumed to be constant because the variation due to the temperature and skin-effect are neglected.
- The winding is distributed across the circumference of the stator and is designed in such a way that the magnetomotive force is sinusoidal. The flux distribution around the air-gap has the same trend and the air-gap is considered uniform (isotropic machine).
- Machine with one pole-pair and a typical rotor of a generic three-phase *SPM* machine is considered.  $d$ -axis is coincident with the  $N$ -pole of the magnets.
- The ferromagnetic material is considered ideal: the nonlinearity is neglected and the losses due to ferromagnetic material (hysteresis and eddy currents) are neglected.
- The impact of the stator slots is neglected.
- Full decoupling between the leakage fluxes.

From the operational point of view, the most relevant feature of the winding arrangement is the existence or absence of higher order spatial harmonics in the air gap magnetomotive force. With an appropriate stator winding design, these higher order harmonics can be mostly neglected in distributed winding machines and the *MMF* can be regarded as sinusoidal.

### 2.2.1 Mathematical Model of a Multiphase Synchronous Machine in Phase Variable Domain

Based on the initial assumptions, the mathematical model in phase variable domain of a multiphase machine is formulated. The mathematical model can be described in phase domain using the general theory of electric machines with standard assumption [5].

Any  $n$ -phase machines is described by the  $n$ -electric and  $n$ -magnetic equations. The electric equations put in relation the voltages and flux linkages of the electric machine, while the magnetic equations put in relation the currents and flux linkages. Both equations are combined to obtain the input voltages and output currents of the machine. The phase variable domain is preferable to analyse the developed dynamic behaviours in the machine. Instead other reference frames are most appropriate to implement the control algorithm, as shown below.

The number of phases on stator  $n$  can be represented as:

$$n = k_{ws} \cdot a \tag{2.1}$$

where:

- $k_{ws}$  is number of winding sets and it is any integer higher or equal to 1 and
- $a$  is the number of the phases per each winding set and it is a prime number which is equal or larger than 3 ( $a=3, 5, 7, \dots$ ).

Another difference for multiphase machines is based on the distribution of the phases around stator's circumference, as shown in Fig. 2.5: (i) the machine is symmetrical if the spatial displacement between magnetic axes of any two consecutive phases is equal to  $\alpha = 2\pi/n$  electrical degrees, (ii) if the spatial shift leads to asymmetrical positioning of the stator phase magnetic axes in the cross section of the machine, the machine is termed asymmetrical machine and spatial shift between the first phases belonging to two consecutive winding sets is governed by  $\alpha = \pi/n$ . The distinction between symmetrical and asymmetrical machine is synthesized as:

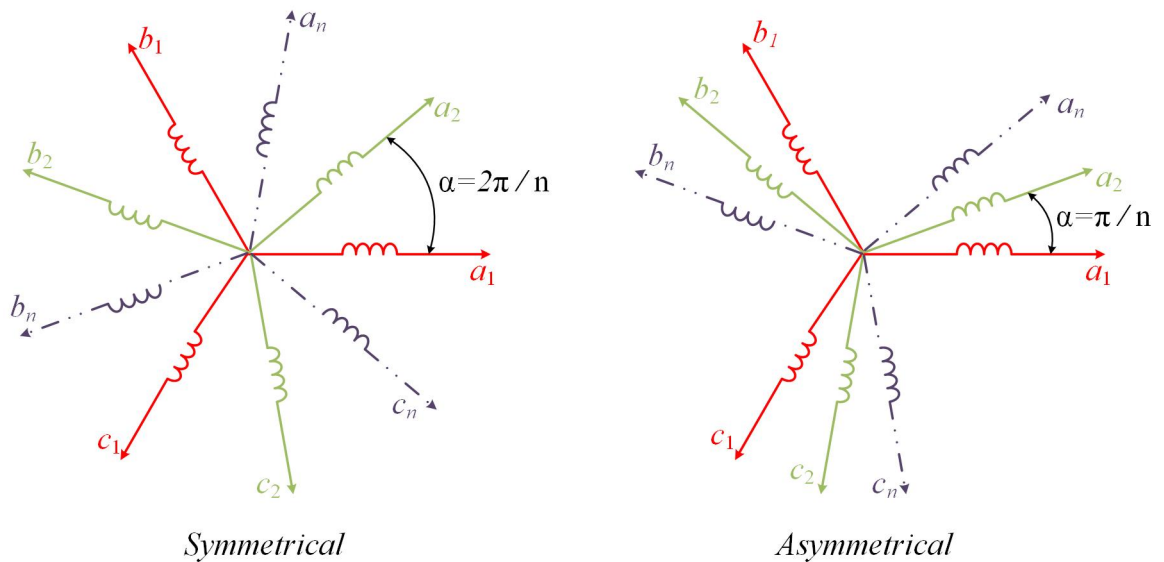


Figure 2.5: Multiphase machine winding distribution around stator circumference.

$$\alpha = \begin{cases} \frac{2\pi}{n}, & \text{symmetrical} \\ \frac{\pi}{n}, & \text{asymmetrical} \end{cases} \quad (2.2)$$

In Fig. 2.6 the equivalent circuit of  $n$ -phase surface *PMSM* machine is presented with the following characteristics:

- The phases of stator are denoted with subscripts  $a1$  to  $n$ , according to the spatial distribution of the windings, as shown in Fig. 2.5.
- Single isolated neutral point is assumed.

The Kirchhoff's law is possible applicable at any stator winding. The nature of winding is resistive-inductive and therefore voltage equilibrium equation of any phase of stator presents the same principal form defined as:

$$v = R \cdot i + \frac{d\lambda}{dt} \quad (2.3)$$

where:

- $v$  stands for instantaneous voltage,
- $i$  stands for instantaneous current,
- $\lambda$  stands for instantaneous flux and
- $R$  stands for stator resistance.

On the basis of Kirchhoff's law and consider the equivalent circuit, shown in Fig. 2.6, the knowledge of both magnetic and electrical equations are necessary.

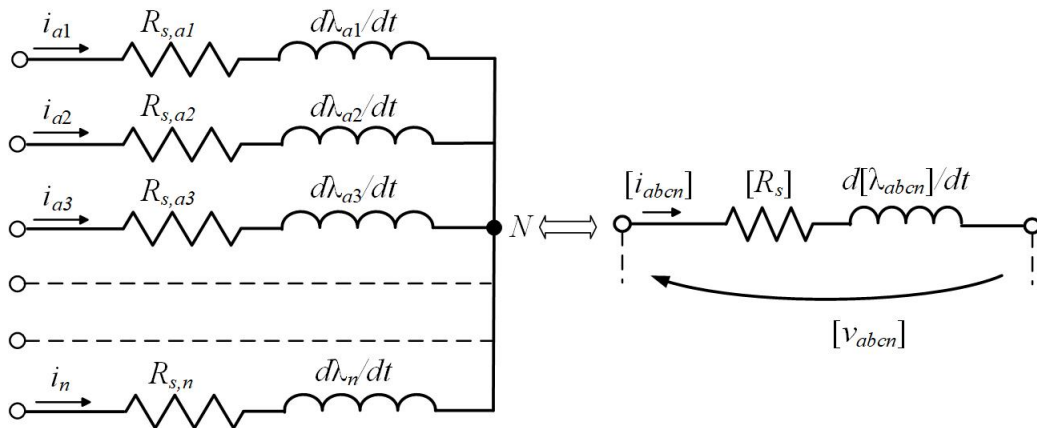


Figure 2.6: Multiphase machine equivalent circuit in phase variable domain.

The electric and magnetic equations for the machine, using passive sign convention, is written as:

$$\begin{cases} [v_{abcn}] = [R_s] \cdot [i_{abcn}] + \frac{d[\lambda_{abcn}]}{dt} \\ [\lambda_{abcn}] = [\lambda_{PM,abcn}] + [L_{ls}] \cdot [i_{abcn}] + [M_{ss}] \cdot [i_{abcn}] \end{cases} \quad (2.4)$$

where:

- $[v_{abcn}]$  stands for vector of the stator voltages,
- $[i_{abcn}]$  stands for vector of the stator currents,
- $[\lambda_{abcn}]$  stands for vector of the total stator flux linkages in phase sets,
- $[\lambda_{PM,abcn}]$  stands for vector of the flux produced by permanent magnets,
- $[R_s]$  stands for matrix of stator phase winding resistance,
- $[L_{ls}]$  stands for matrix of the leakage inductance and
- $[M_{ss}]$  stands for matrix of the mutual magnetizing inductance.

The phase voltage, current, total flux and permanent magnets column vector are defined in Eqs. (2.5) - (2.8).

$$[v_{abcn}] = [v_{a1} \quad v_{a2} \quad v_{a3} \quad \dots \quad v_n]^T \quad (2.5)$$

$$[i_{abcn}] = [i_{a1} \quad i_{a2} \quad i_{a3} \quad \dots \quad i_n]^T \quad (2.6)$$

$$[\lambda_{abcn}] = [\lambda_{a1} \quad \lambda_{a2} \quad \lambda_{a3} \quad \dots \quad \lambda_n]^T \quad (2.7)$$

$$[\lambda_{PM,abcn}] = [\lambda_{PM,a1} \quad \lambda_{PM,a2} \quad \lambda_{PM,a3} \quad \dots \quad \lambda_{PM,n}]^T \quad (2.8)$$

About the magnetic equation, the mutual magnetizing inductance computation between two generic phase-windings of the machine and the computation of the phase flux linkage caused by the  $PM$  are inputs necessary. In electrical equation the focus is the stator resistance.

Starting with the magnetic model, consider Fig. 2.7 where:

- $\theta_d$  stands for arbitrary position of the rotor in space ( $N$ -pole) and
- $\theta_i$  and  $\theta_j$  are angle positions for two arbitrary chosen stator phases.

Usually it is taken that phase angle  $\theta_{a1} = 0^\circ$  and the mutual magnetizing inductances are calculated for every single phase in relation to this angle datum value. The mutual magnetizing inductance between all phases in machine is represented by the  $[M_{ss}]$  matrix. The matrix element between two generic phase winding  $i$  and  $j$  is computed as:

$$M_{ij} = \left. \frac{\lambda_{ij}}{i_j} \right|_{i_i=0} \quad (2.9)$$

$$M_{ji} = \left. \frac{\lambda_{ji}}{i_i} \right|_{i_j=0} \quad (2.10)$$

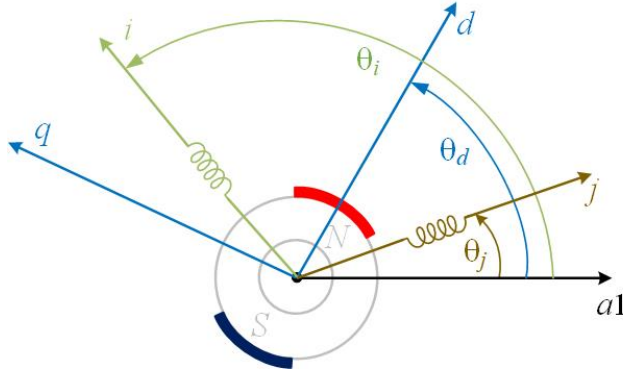


Figure 2.7: Angle distribution for mutual inductance definition.

The presented equations mean that the mutual inductance  $M_{ij}$  is related to the flux linkage of the winding  $i$   $\lambda_{ij}$ , produced by the current in the winding  $j$  while the current in the winding  $i$  is equal to zero. The same consideration can be extended to the mutual inductance  $M_{ji}$  (the flux  $\lambda_{ji}$  is caused by the current in the winding  $i$ ). Finally, from the electromagnetic theory:

$$M_{ij} = M_{ji} \quad (2.11)$$

The current injection in the winding  $j$  causes the magnetomotive force vector, which is aligned with the magnetic  $j$ -axis, as shown in Fig. 2.8. The amplitude of the magnetomotive force is computed as product between the turns number of the winding  $j$  and the current in the same winding. With the assumption that all windings are composed by the  $N_s$  turns, the magnetomotive force vector is modelled as:

$$F_j = N_s \cdot i_j \quad (2.12)$$

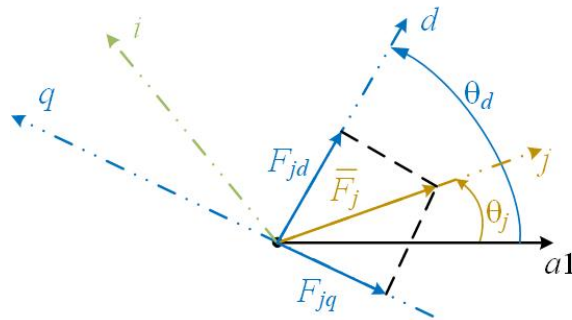


Figure 2.8: Scheme for the computation of the magnetomotive force.

The projections of the magnetomotive force vector are:

$$\begin{cases} F_{jd} = F_j \cdot \cos(\theta_d - \theta_j) \\ F_{jq} = -F_j \cdot \sin(\theta_d - \theta_j) \end{cases} \quad (2.13)$$

By replacing Eq. (2.12) in Eq. (2.13), the projections are computed as:

$$\begin{cases} F_{jd} = N_s \cdot i_j \cdot \cos(\theta_d - \theta_j) \\ F_{jq} = -N_s \cdot i_j \cdot \sin(\theta_d - \theta_j) \end{cases} \quad (2.14)$$

On the basis of the magnetomotive force projections, the fluxes along the magnetic ( $d, q$ ) are computed as:

$$\begin{cases} \phi_{jd} = \frac{F_{j,d}}{\mathfrak{R}_d} = \frac{N_s \cdot i_j}{\mathfrak{R}_d} \cdot \cos(\theta_d - \theta_j) \\ \phi_{jq} = \frac{F_{j,q}}{\mathfrak{R}_q} = -\frac{N_s \cdot i_j}{\mathfrak{R}_q} \cdot \sin(\theta_d - \theta_j) \end{cases} \quad (2.15)$$

where  $\mathfrak{R}_d$  and  $\mathfrak{R}_q$  are the equivalent magnetic reluctances along  $d$ -axis and  $q$ -axis, respectively. However, the flux caused by the current in the winding  $j$  produces the effect on the  $i$  winding, through the magnetomotive force projections. In Fig. 2.9 the projections of the flux  $\phi_j$  in the magnetic  $i$ -axis are shown and they are computed as:

$$\begin{cases} \phi_{ij,d} = \phi_{j,d} \cdot \cos(\theta_i - \theta_d) \\ \phi_{ij,q} = \phi_{j,q} \cdot \cos(\theta_i - \theta_d) \end{cases} \quad (2.16)$$

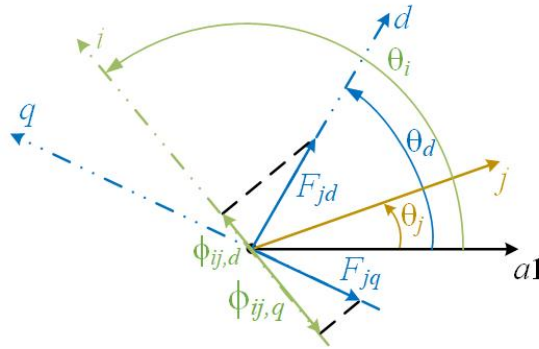


Figure 2.9: Scheme for the computation of the magnetic flux in the magnetic  $i$ -axis due to the current in  $j$ -axis.

By replacing Eq. (2.15) in Eq. (2.16) the projections in the magnetic  $i$ -axis are expressed as:

$$\begin{cases} \Phi_{ij,d} = \frac{N_s \cdot i_j}{\mathfrak{R}_d} \cdot \cos(\theta_d - \theta_j) \cdot \cos(\theta_i - \theta_d) \\ \Phi_{ij,q} = -\frac{N_s \cdot i_j}{\mathfrak{R}_q} \cdot \cos(\theta_d - \theta_j) \cdot \cos(\theta_i - \theta_d) \end{cases} \quad (2.17)$$

In conclusion, the magnetic flux axis are computed as:

$$\Phi_{ij} = \frac{N_s \cdot i_j}{2} \cdot \left( \frac{1}{\mathfrak{R}_d} + \frac{1}{\mathfrak{R}_q} \right) \cdot \cos(\theta_i - \theta_j) + \frac{N_s \cdot i_j}{2} \cdot \left( \frac{1}{\mathfrak{R}_d} - \frac{1}{\mathfrak{R}_q} \right) \cdot \cos(2 \cdot \theta_d - \theta_i - \theta_j) \quad (2.18)$$

The flux linkage of the winding  $i$  caused by the current in winding  $j$  is:

$$\lambda_{ij} = N_i \cdot \Phi_{ij} = N_s \cdot \Phi_{ij} \quad (2.19)$$

By replacing Eq. (2.18) in Eq. (2.19), the linkage flux is:

$$\lambda_{ij} = \frac{N_s^2 \cdot i_j}{2} \cdot \left( \frac{1}{\mathfrak{R}_d} + \frac{1}{\mathfrak{R}_q} \right) \cdot (\theta_i - \theta_j) + \frac{N_s^2 \cdot i_j}{2} \cdot \left( \frac{1}{\mathfrak{R}_d} - \frac{1}{\mathfrak{R}_q} \right) \cdot (2 \cdot \theta_d - \theta_i - \theta_j) \quad (2.20)$$

Referring to the Eqs. (2.9) and (2.10), the following equation is obtained:

$$M_{ij} = \left. \frac{\lambda_{ij}}{i_j} \right|_{i_i=0} = \frac{N_s^2}{2} \cdot \left( \frac{1}{\mathfrak{R}_d} + \frac{1}{\mathfrak{R}_q} \right) \cdot \cos(\theta_i - \theta_j) + \frac{N_s^2}{2} \cdot \left( \frac{1}{\mathfrak{R}_d} - \frac{1}{\mathfrak{R}_q} \right) \cdot \cos(2 \cdot \theta_d - \theta_i - \theta_j) \quad (2.21)$$

In order to write the Eq. (2.21) in a compact form, the new inductances are defined as:

$$L_{m,d} = \frac{N_s^2}{\mathfrak{R}_d}, \quad L_{m,q} = \frac{N_s^2}{\mathfrak{R}_q} \quad (2.22)$$

A new fictitious isotropic mutual inductance factor  $M_I$  and anisotropic mutual inductance factor  $M_A$  are introduced:

$$M_I = \frac{L_{m,d} + L_{m,q}}{2}, \quad M_A = \frac{L_{m,d} - L_{m,q}}{2}, \quad (2.23)$$

By replacing Eqs. (2.22) and (2.23) in Eq. (2.21), the mutual inductance  $M_{ij}$  ( $i_i=0$ ) is:

$$\begin{aligned} M_{ij} &= \left( \frac{L_{m,d} + L_{m,q}}{2} \right) \cdot \cos(\theta_i - \theta_j) + \left( \frac{L_{m,d} - L_{m,q}}{2} \right) \cdot \cos(2 \cdot \theta_d - \theta_i - \theta_j) = \\ &= M_I \cdot \cos(\theta_i - \theta_j) + M_A \cdot \cos(2 \cdot \theta_d - \theta_i - \theta_j) = \\ &= M_I \cdot \cos(\theta_j - \theta_i) + M_A \cdot \cos(2 \cdot \theta_d - \theta_j - \theta_i) = M_{ji} \end{aligned} \quad (2.24)$$

The employed machine in this thesis is isotropic and for this reason the anisotropic inductance is zero:

$$M_A = 0 \Rightarrow L_{m,d} = L_{m,q} = L_m \Rightarrow M_I = L_m \quad (2.25)$$

In conclusion, the mutual inductance is computed as:

$$M_{ij} = M_I \cdot \cos(\theta_i - \theta_j) \quad (2.26)$$

The final matrix for  $n$  windings is defined as:

$$[M_{ss}] = \begin{bmatrix} M_{a1,a1} & M_{a1,a2} & M_{a1,a3} & M_{a1,b1} & \dots & M_{a1,n} \\ M_{a2,a1} & M_{a2,a2} & M_{a2,a3} & M_{a2,b1} & \dots & M_{a2,n} \\ M_{a3,a1} & M_{a3,a2} & M_{a3,a3} & M_{a3,b1} & \dots & M_{a3,n} \\ M_{b1,a1} & M_{b1,a2} & M_{b1,a3} & M_{b1,b1} & \dots & M_{b1,n} \\ \dots & \dots & \dots & \dots & \dots & \dots \\ M_{n,a1} & M_{n,a2} & M_{n,a3} & M_{n,b1} & \dots & M_{n,n} \end{bmatrix} \quad (2.27)$$

The leakage inductances matrix is expressed as:

$$[L_{ls}] = \begin{bmatrix} L_{ls,a1} & 0 & 0 & 0 & \dots & 0 \\ 0 & L_{ls,a2} & 0 & 0 & \dots & 0 \\ 0 & 0 & L_{ls,a3} & 0 & \dots & 0 \\ 0 & 0 & 0 & L_{ls,b1} & \dots & 0 \\ \dots & \dots & \dots & \dots & \dots & \dots \\ 0 & 0 & 0 & 0 & \dots & L_{ls,n} \end{bmatrix} \quad (2.28)$$

As it is assumed that all individual phase winding are identical from each other, then:

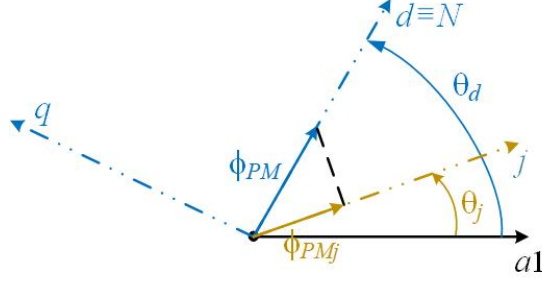
$$L_{ls,a1} = L_{ls,n} = L_{ls} \quad (2.29)$$

As shown in system Eq. (2.4), the magnetic model takes into account the flux linkage of the windings caused by the permanent magnet with assumption of the magnetic linearity. The  $PM$  is modeled as an ideal magnetomotive force generator  $F_{PM}$ . The effect of the flux produced by  $PM$  is represented by a vector, alligned with the physical  $d$ -axis ( $N$ -pole) and its amplitude is equal to  $\Phi_{PM}$ , as shown in Fig. 2.10. This is computed as:

$$\Phi_{PM} = \frac{F_{PM}}{\mathfrak{R}_d} \quad (2.30)$$

The effect of the magnetic flux vector on the generic winding  $j$  is computed as:

$$\Phi_{PM,j} = \frac{F_{PM}}{\mathfrak{R}_d} \cdot \cos(\theta_d - \theta_j) \quad (2.31)$$


 Figure 2.10: Single-phase  $PM$  flux linkage computation scheme.

The flux linkage for the considered winding  $j$  is:

$$\begin{aligned}\lambda_{PM,j} &= N_s \cdot \phi_{PM,j} = \frac{N_s \cdot F_{PM}}{\mathfrak{R}_d} \cdot \cos(\theta_d - \theta_j) = \\ &= \lambda_{PM} \cdot \cos(\theta_d - \theta_j) = \lambda_{PM} \cdot \cos(\theta - \theta_j)\end{aligned}\quad (2.32)$$

where the amplitude of the  $PM$  flux is defined as:

$$\lambda_{PM} = \frac{N_s \cdot F_{PM}}{\mathfrak{R}_d} \quad (2.33)$$

while from now on the  $d$ -axis position  $\theta_d$  will be replaced with  $\theta$ .

For a generic winding  $n$ , Eq. (2.32) in phase variable domain is written considering a generic angle  $\theta_n$ , which depends on spatial phase distribution around the circumference:

$$\lambda_{PM,n} = \lambda_{PM} \cdot \cos(\theta - \theta_n), \quad \theta_n \in [0, \dots, (n-1) \cdot \alpha]_{n \times 1} \quad (2.34)$$

The Eq. (2.34) is valid in machine modelling only if sinusoidal back-electromotive force is assumed. In multiphase machines, this equation can be extended in its complete vector form as:

$$[\lambda_{PM,abcn}] = \lambda_{PM} \cdot \begin{bmatrix} \cos(\theta - 0 \cdot \alpha) \\ \cos(\theta - 1 \cdot \alpha) \\ \cos(\theta - 2 \cdot \alpha) \\ \cos(\theta - 3 \cdot \alpha) \\ \dots \\ \cos(-(n-1) \cdot \alpha) \end{bmatrix} \quad (2.35)$$

The total back-electromotive force ( $EMF_{total}$ ) and the back-electromotive force produced by the permanent magnets ( $EMF_{PM}$ ) are obtained by the time derivative of produced flux, as it is shown in Eq. (2.36) and (2.37), respectively.

$$[back - EMF_{total}] = \frac{d[\lambda_{abcn}]}{dt} \quad (2.36)$$

$$[back - EMF_{PM}] = \frac{d[\lambda_{PM,abcn}]}{dt} \quad (2.37)$$

Now, it is necessary to define the machine electric model. The stator resistance matrix is expressed as:

$$[R_s] = \begin{bmatrix} R_{s,a1} & 0 & 0 & 0 & \dots & 0 \\ 0 & R_{s,a2} & 0 & 0 & \dots & 0 \\ 0 & 0 & R_{s,a3} & 0 & \dots & 0 \\ 0 & 0 & 0 & R_{s,b1} & \dots & 0 \\ \dots & \dots & \dots & \dots & \dots & \dots \\ 0 & 0 & 0 & 0 & \dots & R_{s,n} \end{bmatrix} \quad (2.38)$$

As it is assumed that all individual phase winding are identical from each other, then:

$$R_{s,a1} = R_{s,n} = R_s \quad (2.39)$$

Finally, consider an arbitrary number of stator phases  $n$ , on the basis of the Eq. (2.4), the presented matrices, the flux linkage caused by the  $PM$ , the dynamic model of the machine is written as:

$$\left\{ \begin{array}{l} \begin{bmatrix} v_{a1} \\ v_{a2} \\ v_{a3} \\ v_{b1} \\ \dots \\ v_n \end{bmatrix} = \begin{bmatrix} R_s & 0 & 0 & 0 & \dots & 0 \\ 0 & R_s & 0 & 0 & \dots & 0 \\ 0 & 0 & R_s & 0 & \dots & 0 \\ 0 & 0 & 0 & R_s & \dots & 0 \\ \dots & \dots & \dots & \dots & \dots & \dots \\ 0 & 0 & 0 & 0 & \dots & R_s \end{bmatrix} \cdot \begin{bmatrix} i_{a1} \\ i_{a2} \\ i_{a3} \\ i_{b1} \\ \dots \\ i_{s,n} \end{bmatrix} + \frac{d}{dt} \begin{bmatrix} \lambda_{a1} \\ \lambda_{a2} \\ \lambda_{a3} \\ \lambda_{b1} \\ \dots \\ \lambda_n \end{bmatrix} \\ \\ \begin{bmatrix} \lambda_{a1} \\ \lambda_{a2} \\ \lambda_{a3} \\ \lambda_{b1} \\ \dots \\ \lambda_{s,n} \end{bmatrix} = \begin{bmatrix} \lambda_{PM,a1} \\ \lambda_{PM,a2} \\ \lambda_{PM,a3} \\ \lambda_{PM,b1} \\ \dots \\ \lambda_{PM,n} \end{bmatrix} + \begin{bmatrix} L_{ls} & 0 & 0 & 0 & \dots & 0 \\ 0 & L_{ls} & 0 & 0 & \dots & 0 \\ 0 & 0 & L_{ls} & 0 & \dots & 0 \\ 0 & 0 & 0 & L_{ls} & \dots & 0 \\ \dots & \dots & \dots & \dots & \dots & \dots \\ 0 & 0 & 0 & 0 & \dots & L_{ls} \end{bmatrix} \cdot \begin{bmatrix} i_{a1} \\ i_{a2} \\ i_{a3} \\ i_{b1} \\ \dots \\ i_n \end{bmatrix} + \\ + \begin{bmatrix} M_{a1,a1} & M_{a1,a2} & M_{a1,a3} & M_{a1,b1} & \dots & M_{a1,n} \\ M_{a2,a1} & M_{a2,a2} & M_{a2,a3} & M_{a2,b1} & \dots & M_{a2,n} \\ M_{a3,a1} & M_{a3,a2} & M_{a3,a3} & M_{a3,b1} & \dots & M_{a3,n} \\ M_{b1,a1} & M_{b1,a2} & M_{b1,a3} & M_{b1,b1} & \dots & M_{b1,n} \\ \dots & \dots & \dots & \dots & \dots & \dots \\ M_{n,a1} & M_{n,a2} & M_{n,a3} & M_{n,b1} & \dots & M_{n,n} \end{bmatrix} \cdot \begin{bmatrix} i_{a1} \\ i_{a2} \\ i_{a3} \\ i_{b1} \\ \dots \\ i_n \end{bmatrix} \end{array} \right. \quad (2.40)$$

The magnetic equation can be written as:

$$\begin{bmatrix} \lambda_{a1} \\ \lambda_{a2} \\ \lambda_{a3} \\ \lambda_{b1} \\ \dots \\ \lambda_n \end{bmatrix} = \begin{bmatrix} \lambda_{PM,a1} \\ \lambda_{PM,a2} \\ \lambda_{PM,a3} \\ \lambda_{PM,b1} \\ \dots \\ \lambda_{PM,n} \end{bmatrix} + \begin{bmatrix} L_{a1,a1} & L_{a1,a2} & L_{a1,a3} & L_{a1,b1} & \dots & 0 \\ L_{a2,a1} & L_{a2,a2} & L_{a2,a3} & L_{a2,b1} & \dots & 0 \\ L_{a3,a1} & L_{a3,a2} & L_{a3,a3} & L_{a3,b1} & \dots & 0 \\ L_{b1,a1} & L_{b1,a2} & L_{b1,a3} & L_{b1,b1} & \dots & 0 \\ \dots & \dots & \dots & \dots & \dots & \dots \\ L_{n,a1} & L_{n,a2} & L_{n,a3} & L_{n,b1} & \dots & L_{n,n} \end{bmatrix} \cdot \begin{bmatrix} i_{a1} \\ i_{a2} \\ i_{a3} \\ i_{b1} \\ \dots \\ i_n \end{bmatrix} \quad (2.41)$$

where the overall inductance matrix is indicated as:

$$[L_{ss}] = [L_{ls}] + [M_{ss}] \quad (2.42)$$

The final equation in phase variable domain, obtained with the combination of electrical and magnetic equation in compact matrix form, is:

$$[i_{abcn}] = [L_{ss}]^{-1} \left( \int \left( [v_{abcn}] - [R_s] \cdot [i_{abcn}] \right) dt - [\lambda_{PM,abcn}] \right) \quad (2.43)$$

In Fig. 2.11 the schematic representation of mentioned equation is shown, where peach and blue blocks represent the magnetic and electrical equations, respectively.

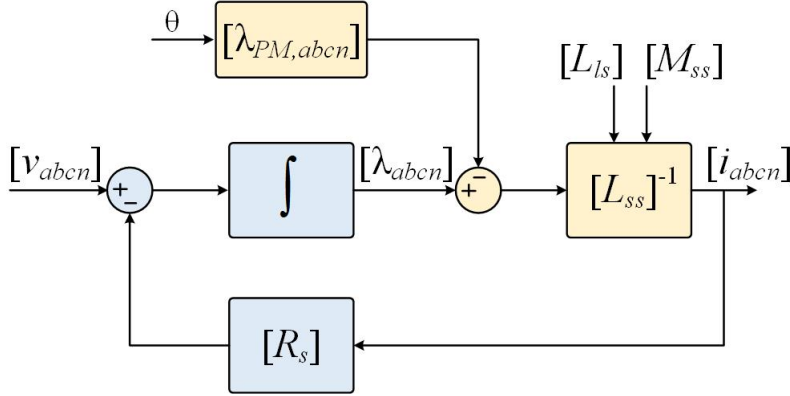


Figure 2.11: Dynamic electromagnetic model of the machine.

### 2.2.2 Decoupling Transformation

The machine model in stationary reference frame can be obtained with two methods. The first one consists to apply the reference transformations set by set, following the standard procedure of the *MS*-approach [16]. The second one consists into defining a single reference transformation, which is applied to the complete set of machine's equations, called *VSD* approach [17]. However, when a multiphase machine has multiple winding sets, it is advantageous to have independent control over each individual winding set. For example, in generation systems this can be used to switch off any winding set in the case of fault. By doing so, the machine is divided into multiple flux/torque producing subplanes and well-known control techniques developed for three-phase machines can be implemented in each subplane. The advantage of this modelling approach is the possibility for individual and independent control of all winding sets. However, multiple pairs of *PI* controllers are required for simple flux/torque control. With *VSD* modelling approach independent control over each individual winding set is not possible, but a clear harmonic mapping is obtained. For this reason, in this thesis the *VSD* approach is used.

The machine model in the phase variable domain is transformed using decoupling transformation matrix (*VSD* matrix). The reason of this transformation are (i) the description of electric machine behaviour in phase variable domain with time-varying coefficients does not provide a good insight into the physical phenomena and (ii) the model in phase variable domain is not suitable for control purposes. The consequence is to describe the machine using the *VSD* approach. Applying the *VSD*, the model is decomposed into orthogonal subplanes by applying Clarke's transformation [18]. Its aim is to replace the original sets of  $n$  variables with the new sets of  $n$  variables. After this transformation, the machine is represented with  $n/2$  two-dimensional subplanes if the phase number  $n$  is even. If the number of phase  $n$  is odd, the original plane is transformed in  $(n-1)/2$  planes plus one single-dimensional quantity. The new planes after the Clarke's transformation are orthogonal from each other. The consequence is no coupling between them. Further, in each two-dimensional subplane, there is a pair of quantities, positioned along two mutually perpendicular axes. This leads to significant simplification of the model, compared to original phase variable domain.

A generic relationship between original phase variable domain and new set of variables is defined in Eq. (2.44). In what follows, the variables in stationary reference frame, obtained after decoupling matrix application, are denoted with *vsd* subscript.

$$[f_{vsd}] = [VSD] \cdot [f_{abcn}] \quad (2.44)$$

where:

- $[f_{vsd}]$  stands for voltage, current, flux linkage of the stator windings or for the vector of the *PM* stator fluxes linkages after the transformation,

-[ $VSD$ ] stands for Clarke matrix i.e. for the decoupling transformation matrix and

-[ $f_{abcn}$ ] stands for the corresponding vector listed above in terms of the phase variable domain.

For an arbitrary phase number  $n$ , the  $VSD$  matrix is shown in Eq. (2.47).

The coefficient in front of the matrix is associated with the power per phase of the original and new machine. If the power is kept invariant, the transformation is usually termed power invariant transformation and the coefficient in front of the matrix is equal to  $\sqrt{(2/n)}$ ; if the coefficient in front of  $VSD$  matrix is equal to  $n/2$ , the power is not kept invariant, but the amplitude is invariant. In this work the amplitude invariant transformation is used, hence in front of the matrix there is  $2/n$ . The relationship between the inverse  $VSD$  and its transpose is defined as:

$$[VSD]^{-1} = \frac{n}{2} \cdot [VSD]^T \quad (2.45)$$

By replacing Eq. (2.45) in Eq. (2.44), the relation between  $vsd$  variables and phase variable domain is written as:

$$\begin{aligned} [f_{abcn}] &= [VSD]^{-1} \cdot [f_{vsd}] = \\ &= \frac{n}{2} \cdot [VSD]^T \cdot [f_{vsd}] \end{aligned} \quad (2.46)$$

The first two rows in Eq. (2.47) define variables that will lead to fundamental flux and torque production: the first subplane is a flux/torque producing one, meaning that all electromechanical energy conversion is happening here, assuming the sinusoidal winding distribution. Other subplane variables can be used as additional degrees of freedom for some multiphase machine specific purpose, i.e. fault tolerance: these subplanes are not flux/torque production [19]. To conclude, the structure of  $VSD$  matrix depends on the number of considered  $n$  phases.

- If  $n$  is even, the last two rows define the zero-sequence components and in between there are  $(n-4)/2$  pairs of rows that define pairs of variables, termed further on  $xy$  components. The  $xy$  components don't participate in electromechanical energy conversion and in fact the torque is produced only by the  $\alpha\beta$  components (sinusoidal winding). The  $(\alpha, \beta)$ ,  $(x, y)_1$ ,  $(x, y)_2, \dots$ ,  $(x, y)_{(n-4)/2}$  planes are orthogonal from each other.
- If  $n$  is odd, the last row of the transformation matrix is omitted and in between there are  $(n-3)/2$  pairs of rows that define pairs of variables, termed further on  $xy$  components.

$$\left[ \text{VSD} \right] = \frac{2}{n} \begin{bmatrix}
 1 & \cos(\alpha) & \cos(2\alpha) & \cos(3\alpha) & \dots & \cos(3\alpha) & \dots & \cos(3\alpha) & \dots & \cos(\alpha) \\
 0 & \sin(\alpha) & \sin(2\alpha) & \sin(3\alpha) & \dots & \sin(3\alpha) & \dots & -\sin(3\alpha) & \dots & -\sin(\alpha) \\
 1 & \cos(2\alpha) & \cos(4\alpha) & \cos(6\alpha) & \dots & \cos(6\alpha) & \dots & \cos(6\alpha) & \dots & \cos(\alpha) \\
 0 & \sin(2\alpha) & \sin(4\alpha) & \sin(6\alpha) & \dots & \sin(6\alpha) & \dots & -\sin(6\alpha) & \dots & -\sin(2\alpha) \\
 1 & \cos(3\alpha) & \cos(6\alpha) & \cos(9\alpha) & \dots & \cos(9\alpha) & \dots & \cos(9\alpha) & \dots & \cos(3\alpha) \\
 0 & \sin(3\alpha) & \sin(6\alpha) & \sin(9\alpha) & \dots & \sin(9\alpha) & \dots & -\sin(9\alpha) & \dots & -\sin(3\alpha) \\
 \dots & \dots \\
 1 & \cos\left(\frac{n-2}{2} \cdot \alpha\right) & \cos\left(2 \cdot \frac{n-2}{2} \cdot \alpha\right) & \cos\left(3 \cdot \frac{n-2}{2} \cdot \alpha\right) & \dots & \cos\left(3 \cdot \frac{n-2}{2} \cdot \alpha\right) & \dots & \cos\left(2 \cdot \frac{n-2}{2} \cdot \alpha\right) & \dots & \cos\left(\frac{n-2}{2} \cdot \alpha\right) \\
 0 & \sin\left(\frac{n-2}{2} \cdot \alpha\right) & \sin\left(2 \cdot \frac{n-2}{2} \cdot \alpha\right) & \sin\left(3 \cdot \frac{n-2}{2} \cdot \alpha\right) & \dots & \sin\left(3 \cdot \frac{n-2}{2} \cdot \alpha\right) & \dots & -\sin\left(2 \cdot \frac{n-2}{2} \cdot \alpha\right) & \dots & -\sin\left(\frac{n-2}{2} \cdot \alpha\right) \\
 \frac{1}{\sqrt{2}} & \frac{1}{\sqrt{2}} & \frac{1}{\sqrt{2}} & \frac{1}{\sqrt{2}} & \dots & \frac{1}{\sqrt{2}} & \dots & \frac{1}{\sqrt{2}} & \dots & \frac{1}{\sqrt{2}} \\
 \frac{1}{\sqrt{2}} & -\frac{1}{\sqrt{2}} & \frac{1}{\sqrt{2}} & -\frac{1}{\sqrt{2}} & \dots & -\frac{1}{\sqrt{2}} & \dots & -\frac{1}{\sqrt{2}} & \dots & -\frac{1}{\sqrt{2}}
 \end{bmatrix} \quad (2.47)$$

The new perpendicular planes can be considered as a complex and define one axis component as a real part and the other axis component as an imaginary part of a complex number, as shown in Eq. (2.48). The complex numbers are known as space vectors. In what follows, space vectors are denoted with underline symbols.

$$\underline{a} = a + jb = e^{j\alpha} = \cos(\alpha) + j\sin(\alpha) \quad (2.48)$$

where  $\alpha = 2\pi/n$  (symmetrical machine). It is natural to introduce the complex number because each pair of rows contains sine and cosine functions of the same angles. However, each pair of rows in Eq. (2.47) then defines one space vector, with odd rows determining the real parts and the even rows imaginary parts of the corresponding complex numbers. Let  $f$  stand once more for voltage, current, or flux linkage of the stator. Space vectors are then governed by Eqs. (2.49) - (2.52). In these equations it is assumed that the phase number is odd and there is a single isolated neutral point (the zero-sequence can not be excited). The number in front the equations is in agreement with the power-variant convention (amplitude invariant) assumed in *VSD* matrix.

$$\underline{f}_{\alpha\beta} = f_\alpha + jf_\beta = \frac{2}{n}(f_1 + \underline{a} \cdot f_2 + \underline{a}^2 \cdot f_3 + \dots \underline{a}^{n-1} \cdot f_n) \quad (2.49)$$

$$\underline{f}_{xy_1} = f_{x_1} + jf_{y_1} = \frac{2}{n}(f_1 + \underline{a}^2 \cdot f_2 + \underline{a}^4 \cdot f_3 + \dots \underline{a}^{2(n-1)} \cdot f_n) \quad (2.50)$$

$$\underline{f}_{xy_2} = f_{x_2} + jf_{y_2} = \frac{2}{n}(f_1 + \underline{a}^3 \cdot f_2 + \underline{a}^6 \cdot f_3 + \dots \underline{a}^{3(n-1)} \cdot f_n) \quad (2.51)$$

$$\underline{f}_{xy_{(n-3)/2}} = f_{x_{(n-3)/2}} + jf_{y_{(n-3)/2}} = \frac{2}{n}(f_1 + \underline{a}^{(n-1)/2} \cdot f_2 + \underline{a}^{2[(n-1)/2]} \cdot f_3 + \dots \underline{a}^{(n-1)^2/2} \cdot f_n) \quad (2.52)$$

To conclude the presented theory in *VSD* variables is a complex form because each variable can be expressed as a complex vector, as explained above. In the following, the matrix form in the same reference frame is introduced for a multiphase surface *PMSM* with  $n$  stator windings.

The magnetic and electrical machine equations in phase variable domain are considered. For convenience, both are below reported:

$$\begin{cases} [v_{abcn}] = [R_s] \cdot [i_{abcn}] + \frac{d[\lambda_{abcn}]}{dt} \\ [\lambda_{abcn}] = [\lambda_{PM,abcn}] + [L_{ls}] \cdot [i_{abcn}] + [M_{ss}] \cdot [i_{abcn}] \end{cases} \quad (2.53)$$

By applying the  $VSD$  matrix to the electrical and magnetic equations, the model in stationary reference frame is:

$$\begin{cases} [VSD] \cdot [v_{abcn}] = [VSD] \cdot [R_s] \cdot [VSD]^{-1} \cdot [i_{vsd}] + [VSD] \cdot \frac{d}{dt} ([VSD]^{-1} \cdot [\lambda_{vsd}]) \\ [VSD] \cdot [\lambda_{abcn}] = [VSD] \cdot [L_{ls}] \cdot [VSD]^{-1} \cdot [i_{vsd}] + [VSD] \cdot [M_{ss}] \cdot [VSD]^{-1} \cdot [i_{vsd}] + \\ \quad + [VSD] \cdot [\lambda_{PM,abcn}] \end{cases} \quad (2.54)$$

By replacing the relationship shown in Eq. (2.44), the machine model is written as:

$$\begin{cases} [v_{vsd}] = [R_s] \cdot [i_{vsd}] + \frac{d[\lambda_{vsd}]}{dt} \\ [\lambda_{vsd}] = [L_{ls}] \cdot [i_{vsd}] + [M_{ss,vsd}] \cdot [i_{vsd}] + [\lambda_{PM,vsd}] \end{cases} \quad (2.55)$$

where:

- $[v_{vsd}]$  stands for the vector of the stator voltages for  $n$  phase windings,
- $[i_{vsd}]$  stands for the vector of the stator currents for  $n$  phase windings,
- $[\lambda_{vsd}]$  stands for the vector of the stator fluxes linkage for  $n$  phase windings,
- $[\lambda_{PM,vsd}]$  stands for the vector of the  $PM$  stator fluxes linkage,
- $[L_{ls}]$  stands for the matrix related to the stator leakage inductances. This matrix is immune to the transformation  $VSD$ ,
- $[R_s]$  stands for the matrix related to the stator resistances. This matrix is immune to the transformation  $VSD$  and
- $[M_{ss,vsd}]$  stands for the matrix related to the mutual magnetizing inductance. The mutual inductance matrix in stationary  $RF$  is computed as:

$$\begin{aligned} M_{ss,vsd} &= [VSD] \cdot [M_{ss}] \cdot [VSD]^{-1} = \\ &= \frac{n}{2} \cdot \begin{bmatrix} M_I & 0 & 0 & 0 & \dots & 0 \\ 0 & M_I & 0 & 0 & \dots & 0 \\ 0 & 0 & 0 & 0 & \dots & 0 \\ 0 & 0 & 0 & 0 & \dots & 0 \\ \dots & \dots & \dots & \dots & \dots & \dots \\ 0 & 0 & 0 & 0 & \dots & 0 \end{bmatrix} \end{aligned} \quad (2.56)$$

The stator leakage inductance matrix and stator matrix in stationary  $RF$  are computed as:

$$[VSD] \cdot [L_{ls}] \cdot [VSD]^{-1} = [L_{ls}] = L_{ls} \cdot [Id] \quad (2.57)$$

$$[VSD] \cdot [R_s] \cdot [VSD]^{-1} = [R_s] = R_s \cdot [Id] \quad (2.58)$$

where  $[Id]$  stands for identity matrix, which dimension depend on the phase number  $n$ .

About the  $PM$  stator flux linkage vector:

$$[\lambda_{PM,vsd}] = \lambda_{PM} \cdot \begin{bmatrix} \cos(\theta) \\ \sin(\theta) \\ 0 \\ 0 \\ \dots \\ 0 \end{bmatrix} \quad (2.59)$$

Because the sinusoidal machine is analysed, the vector of the  $PM$  stator fluxes linkage is composed only by the fundamental components.

About the zero-sequence component, the electrical and magnetic equations are:

$$\begin{cases} v_0 = R_s \cdot i_0 + \frac{d\lambda_0}{dt} \\ \lambda_0 = L_{ls} \cdot i_0 \end{cases} \quad (2.60)$$

where:

- $v_0$  is the zero-sequence stator voltage,
- $i_0$  is the zero-sequence stator current,
- $\lambda_0$  is the zero-sequence stator flux,

This transformation allows at drawing a new equivalent circuit in  $(\alpha, \beta)$ ,  $(x, y)$  subplanes and zero-sequence component, as shown in Fig. 2.12. In mentioned figure (c), the zero-sequence current cannot flow due to the neutral point connection, this modelled with an open switch.

### 2.2.3 Synchronous Reference Frame Multiphase surface PMSM modelling

After the application of  $VSD$  matrix, by applying the rotational transformation the model in a synchronous reference frame is obtained. However, the choice of the rotating frame depends by the machine control type: *Rotor Control Schemes* or *Stator Control Schemes*. In the first category it is included the well-known field oriented control. At the second one belongs the Direct Torque Control (*DTC*) or the more recent Direct Flux Vector Control (*DFVC*) [20]. In terms of machine modelling the only difference between them is the choice of the rotating frame. In the Rotor Control Schemes for surface *PMSMs* the equations are referred to the physical  $(d, q)$  reference frame. In this thesis this approach is used.

The fictious  $vsd$  components, obtained in the previous section, are still firmly attached to the stationary axes. Now another transformation is performed: rotational transformation. The fictious components are transformed once more to obtain another fictious windings and components. The aim of this transformation is to obtain

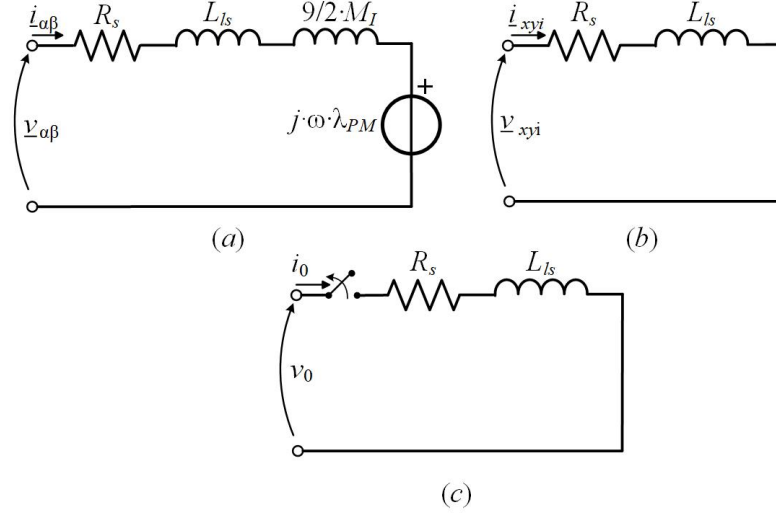


Figure 2.12: Equivalent circuit of sinusoidal machine: (a) -  $(\alpha, \beta)$ ; (b) -  $(x, y)$  ( $i = 1, 2, 3$ ) subplanes; (c) - zero-sequence component.

a new sets of stator variables with the same speed of the rotor, where the input angle in rotational matrix is equal to the electrical rotor position  $\theta$ . The relationship between  $vsd$  and  $dq$  components is:

$$[f_{dq}] = [D] \cdot [f_{vsd}] \quad (2.61)$$

The number of phase is equal to  $n$ , but the rotational transformation is applied only to the first two rows of the  $VSD$  matrix:

$$\begin{bmatrix} f_d \\ f_q \end{bmatrix} = \begin{bmatrix} \cos(\theta) & \sin(\theta) \\ -\sin(\theta) & \cos(\theta) \end{bmatrix} \cdot \begin{bmatrix} f_\alpha \\ f_\beta \end{bmatrix} \quad (2.62)$$

The inverse rotational matrix is computed as:

$$\begin{bmatrix} f_\alpha \\ f_\beta \end{bmatrix} = \begin{bmatrix} \cos(\theta) & -\sin(\theta) \\ \sin(\theta) & \cos(\theta) \end{bmatrix} \cdot \begin{bmatrix} f_d \\ f_q \end{bmatrix} \quad (2.63)$$

Because  $xy$  component equations do not need to be transformed, rotational matrix form for an  $n$ -phase machine is identical as for the three-phase counterpart. The transformation is defined in such a way that the resulting new sets of stator windings, which will replace  $\alpha\beta$  windings, rotate at the same rotor angular speed, so-called speed of the synchronous reference frame. For multiphase machine the

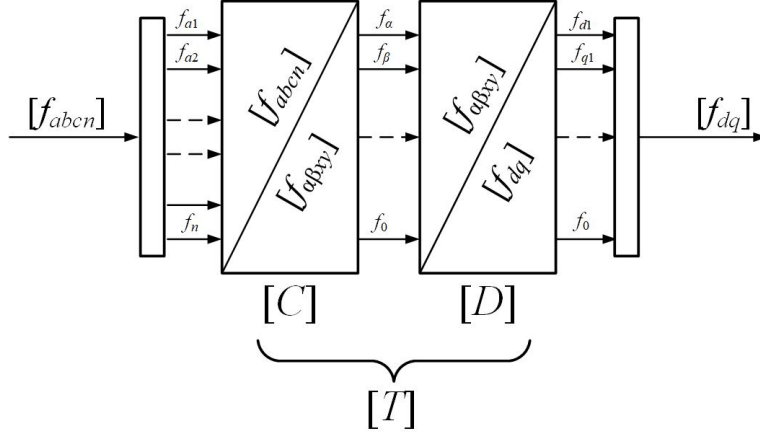


Figure 2.13: A schematic representation of complete  $[T] = [D] \cdot [C]$  transformation.

transformation from  $vsd$  to  $dq$  is obtained with  $[D]$  matrix, defined as:

$$[D] = \begin{bmatrix} \cos(\theta) & \sin(\theta) & 0 & 0 & \dots & 0 \\ -\sin(\theta) & \cos(\theta) & 0 & 0 & \dots & 0 \\ 0 & 0 & 1 & 0 & \dots & 0 \\ 0 & 0 & 0 & 1 & \dots & 0 \\ \dots & \dots & \dots & \dots & \dots & \dots \\ 0 & 0 & 0 & 0 & \dots & 1 \end{bmatrix} \quad (2.64)$$

The first two rows in Eq. (2.64) are again responsible for the flux and torque production, while the other subplanes don't participate in electromechanical energy conversion (assuming the sinusoidal winding distribution).

Finally, a single matrix, called Park's matrix, to obtain the machine modelling in synchronous  $RF$  from phase variable domain is defined as:

$$\begin{aligned} [f_{dq}] &= [D] \cdot [C] \cdot [f_{abcn}] = \\ &= [T] \cdot [f_{abcn}] \end{aligned} \quad (2.65)$$

In Fig. 2.13 and 2.14 the complete transformation and waveforms of variable transformation between different references frame can be seen, respectively. It is possible to observe in Fig. 2.14 the difference in frequency due to the transformations.

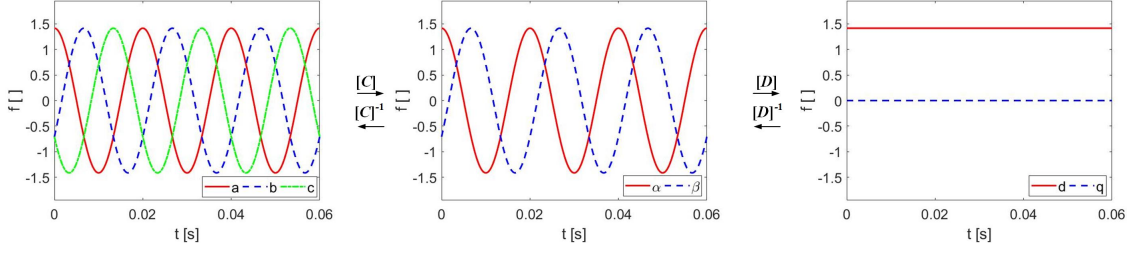


Figure 2.14: Generic waveforms in different references frame.

The machine model in synchronous reference frame for a generic multiphase surface *PMSM* with the same hypothesis is now computed. In this case the magnetic and electrical equations in *vsd* variables are considered. By applying the matrix presented in Eq. (2.64) the machine model in rotor reference frame (*d,q*) is obtained:

$$\left\{ \begin{array}{l} [D] \cdot [v_{vsd}] = [D] \cdot [R_s] \cdot [D]^{-1} \cdot [i_{dq}] + [D] \cdot \frac{d}{dt} ([D]^{-1} \cdot [\lambda_{dq}]) \\ [D] \cdot [\lambda_{vsd}] = [D] \cdot [L_{ls}] \cdot [D]^{-1} \cdot [i_{dq}] + [D] \cdot [M_{s,vsd}] \cdot [D]^{-1} \cdot [i_{dq}] + \\ \quad + [D] \cdot [\lambda_{PM,vsd}] \end{array} \right. \Rightarrow (2.66)$$

$$\Rightarrow \left\{ \begin{array}{l} [v_{dq}] = [R_s] \cdot [i_{dq}] + \frac{d[\lambda_{dq}]}{dt} + j \cdot \omega \cdot [\lambda_{dq}] \\ [\lambda_{vsd}] = [L_{ls}] \cdot [i_{dq}] + [M_{ss,dq}] \cdot [i_{dq}] + [\lambda_{PM,dq}] = \\ \quad = [L_{s,dq}] \cdot [i_{dq}] + [\lambda_{PM,dq}] \end{array} \right.$$

where:

- $[v_{dq}]$  is the stator voltage vector in rotor *RF*,
- $[i_{dq}]$  is the stator current vector,
- $[\lambda_{dq}]$  stands for the vector of the stator fluxes linkage for *n* phase windings,
- $[\lambda_{PM,dq}]$  stands for the vector of the *PM* stator fluxes linkage. This vector is immune to the rotational transformation than vector in *VSD* variables,
- $[M_{ss,dq}]$  stands for mutual magnetizing inductances matrix. It is immune to the rotational transformation,
- $[L_{ls}]$  stands for stator leakage inductances matrix. It is immune to the rotational transformation,
- $[R_s]$  stands for stator resistances matrix. This matrix is immune to the rotational transformation and
- $\omega$  stands for the electrical rotor position.

The matrices in rotor reference frame related to the stator leakage inductances and the mutual inductances is:

$$[L_{s,dq}] = [L_{ls}] + [M_{ss,dq}] \quad (2.67)$$

where the mutual magnetizing inductance matrix is defined as:

$$[M_{ss,dq}] = \begin{bmatrix} M_{ss,d} & 0 & 0 & 0 & \dots & 0 \\ 0 & M_{ss,q} & 0 & 0 & \dots & 0 \\ 0 & 0 & 0 & 0 & \dots & 0 \\ \dots & \dots & \dots & \dots & \dots & \dots \\ 0 & 0 & 0 & 0 & \dots & 0 \end{bmatrix} \quad (2.68)$$

where:

$$M_{ss,d} = M_{ss,q} = \frac{n}{2} \cdot M_I \quad \Rightarrow \quad L_{s,d} = L_{s,q} = L_s \quad (2.69)$$

Since the rotational transformation is applied to the two components  $\alpha\beta$ , explained the system Eq. (2.66), the electrical and magnetic equations become:

$$\begin{cases} v_d = R_s \cdot i_d + L_s \cdot \frac{di_d}{dt} - \omega \cdot \lambda_q \\ v_q = R_s \cdot i_q + L_s \cdot \frac{di_q}{dt} + \omega \cdot \lambda_d \\ \lambda_d = L_s \cdot i_d + \lambda_{PM,dq} = L_s \cdot i_d + \lambda_{PM} \\ \lambda_q = L_s \cdot i_q \end{cases} \quad (2.70)$$

In Fig. 2.15 the equivalent circuit for  $dq$  component of surface *PMSM* in synchronous *RF* is shown.

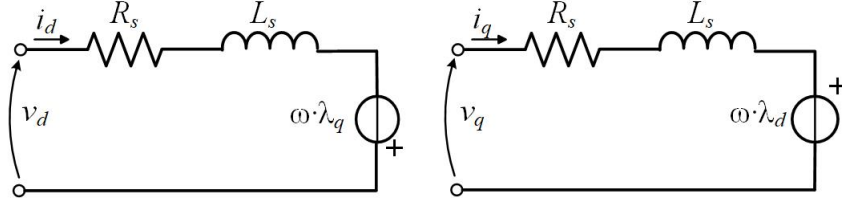


Figure 2.15: Equivalent circuit of machine in synchronous reference frame.

After the rotational transformation, the equations and the parameters values in  $(x, y)$  subplanes do not change. The reason is evident: the submatrix related to  $xy$  components in rotational matrix is diagonal. The electrical and magnetic equations in mentioned subplanes for a multiphase machine ( $n$  odd) are shown below:

$$\begin{cases} v_{xi} = R_s \cdot i_{xi} + \frac{d\lambda_{xi}}{dt}, & i = (n-3)/2 \\ v_{yi} = R_s \cdot i_{yi} + \frac{d\lambda_{yi}}{dt}, & i = (n-3)/2 \\ \lambda_{xi} = L_{ls} \cdot i_{xi}, & i = (n-3)/2 \\ \lambda_{yi} = L_{ls} \cdot i_{yi}, & i = (n-3)/2 \end{cases} \quad (2.71)$$

About the zero-sequence component, the electrical and magnetic equations are not changed. For convenience, both are reported below:

$$\begin{cases} v_0 = R_s \cdot i_0 + \frac{d\lambda_0}{dt} \\ \lambda_0 = L_{ls} \cdot i_0 \end{cases} \quad (2.72)$$

To complete the machine modelling, mechanical equation must also be taken into account. The electromagnetic torque can be carried out by performing the electrical power balance of the machine [21]. The electromagnetic torque equation depend on the transformations that are applied to the machine model. Until now, the *VSD* and rotational transformation are applied with the power variant property. The electrical power in multiphase machine is computed as:

$$P_{abcn} = [i_{abcn}]^T \cdot [v_{abcn}] \quad (2.73)$$

By applying the *VSD* matrix to the electrical powers in stationary reference frame, the power balance becomes:

$$\begin{cases} P_{abcn} = [[VSD]^{-1} \cdot [i_{vsd}]]^T \cdot [VSD]^{-1} \cdot [v_{vsd}] = \\ = [i_{vsd}]^T \cdot [[VSD]^{-1}]^T \cdot [VSD]^{-1} \cdot [v_{vsd}] \end{cases} \quad (2.74)$$

The product between the inverse decoupling matrix and its transpose in power equations carried out the following result:

$$[[VSD]^{-1}]^T \cdot [VSD]^{-1} = \begin{bmatrix} n/2 & 0 & 0 & 0 & \dots & 0 \\ 0 & n/2 & 0 & 0 & \dots & 0 \\ 0 & 0 & n/2 & 0 & \dots & 0 \\ 0 & 0 & 0 & n/2 & \dots & 0 \\ \dots & \dots & \dots & \dots & \dots & \dots \\ 0 & 0 & 0 & 0 & \dots & n/2 \end{bmatrix} \quad (2.75)$$

The zero-sequence component are not relevant because they do not contribute to the electromechanical conversion. Therefore, the electrical power in stationary reference frame is:

$$P_{vsd} = \frac{n}{2} \cdot [i_{vsd}]^T \cdot [v_{vsd}] \quad (2.76)$$

Applying the rotational transformation, presented in Eq. (2.64), the following equation is obtained:

$$\begin{cases} P_{vsd} &= [[D]^{-1} \cdot [i_{dq}]^T] \cdot [D]^{-1} \cdot [v_{dq}] = \\ &= [i_{dq}]^T \cdot [[D]^{-1}]^T \cdot [D]^{-1} \cdot [v_{dq}] \end{cases} \quad (2.77)$$

In this case the product between the inverse rotational matrix and its transpose in power equations carried out the following result:

$$[[D]^{-1}]^T \cdot [D]^{-1} = [Id]_{n \times n} \quad (2.78)$$

Therefore, the electrical power for the multiphase machine in the physical ( $d, q$ ) reference frame is computed as:

$$P_{dq} = \frac{n}{2} \cdot [i_{dq}]^T \cdot [v_{dq}] = P_J + P_M + P_m \quad (2.79)$$

From now on, only the power in the main subplane is considered. The Joule power dissipated by the stator resistance is:

$$P_J = \frac{n}{2} \cdot R_s \cdot (i_d^2 + i_q^2) \quad (2.80)$$

The magnetizing power, which is zero in steady-state condition because it appears only in dynamic conditions to generate the machine magnetic field, is:

$$P_M = \frac{n}{2} \cdot \left( \frac{d\lambda_d}{dt} \cdot i_d + \frac{d\lambda_q}{dt} \cdot i_q \right) \quad (2.81)$$

Introducing the inner product between the stator flux and the currents, the produced mechanical power is:

$$P_m = \frac{n}{2} \cdot \omega \cdot \langle [\lambda_{dq}] \cdot [i_{dq}] \rangle \quad (2.82)$$

The Eq. (2.82) can be related with mechanical speed  $\omega_m$ , introducing pole pairs number  $P$ , using the following relationship:

$$\omega = P \cdot \omega_m \quad (2.83)$$

By applying the Eq. (2.83) to Eq. (2.82):

$$P_m = \frac{n}{2} \cdot P \cdot \omega_m \cdot \langle [\lambda_{dq}] \cdot [i_{dq}] \rangle \quad (2.84)$$

On the basis of the Eq. (2.84), the electromagnetic torque is computed as:

$$T_{em} = \frac{n}{2} \cdot P \cdot \langle [\lambda_{dq}] \cdot [i_{dq}] \rangle \quad (2.85)$$

By extending Eq. (2.85), in synchronous reference frame modeling the formulation of the torque with amplitude invariant transformation is expressed as:

$$T_{em} = \frac{n}{2} \cdot P \cdot [\lambda_{PM} \cdot i_q + (L_{s,d} - L_{s,q}) \cdot i_d \cdot i_q] \quad (2.86)$$

Because analysis concerns surface *PMSM*, the second part of the Eq. (2.86) is zero. The torque equation (green blocks in Fig. 2.16) is written as:

$$T_{em} = \frac{n}{2} \cdot P \cdot \lambda_{PM} \cdot i_q \quad (2.87)$$

Indices  $d$  and  $q$  in any variable stand for the component along permanent magnet flux axis ( $d$ ) and the torque current axis ( $q$ ). The index  $s$  is omitted because only the stator winding is present in surface *PMSM* and all variables are related to it. In front of the Eq. (2.87) it is possible to note the constant  $n/2$  in accordance with the power-variant transformation and it is possible to observe that the torque is produced only by current along  $q$ -axis. In fact  $q$ -axis is responsible of the torque production, while  $d$  is the axis characterized by the presence of permanent magnets.

Taking into consideration the load torque, the mechanical equilibrium on rotor shaft (Fig. 2.16) is:

$$\begin{aligned} T_{em} - T_L &= J \cdot \frac{d\omega_m}{dt} + T_B = \\ &= \frac{J}{P} \cdot \frac{d\omega}{dt} + T_B \end{aligned} \quad (2.88)$$

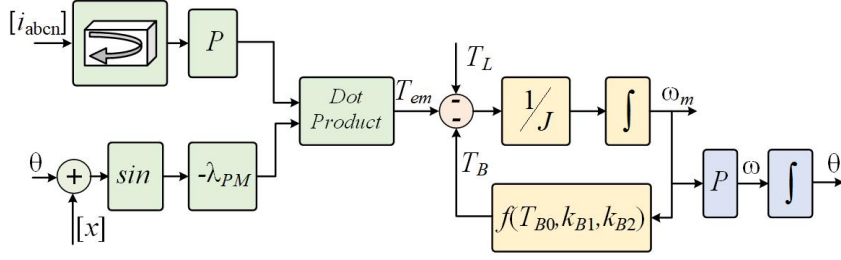


Figure 2.16: Electromagnetic torque (green blocks), mechanical equilibrium on rotor shaft (peach blocks) and electrical speed and position (blue blocks).

where:

$-T_L$  is load torque,

$-J$  is inertia of rotating masses,

$-T_B$  is the friction torque, shown in Eq. (2.89), which depends on the rotor speed (i.e. static, linear and parabolic contributions can be considered).

$$T_B = T_{B0} + T_{B1} + T_{B2} + \dots = T_{B0} + k_{B1} \cdot \omega_m + k_{B2} \cdot \omega_m^2 + \dots \quad (2.89)$$

The electromagnetic torque computation is shown through the green blocks in Fig. 2.16, while the mechanical equilibrium on the rotor shaft is highlighted with peach blocks and, finally, in blue blocks the relationship between the mechanical and electrical speed and its time integration ( $\theta = \int \omega dt$ ) are shown.

The Eq. (2.88) links the electromagnetic subsystem with the mechanical subsystem and it is responsible for the electromechanical energy conversion.

Another approach to compute the electromagnetic torque is now shown. In general, from the concept of co-energy  $W_{co}$

$$T_{em} = \frac{\partial W_{co}}{\partial \theta} \quad (2.90)$$

By applying Eq. (2.90) at machine model, the torque equation for surface sinusoidal *PMSM* machine is computed as:

$$T_{em} = P \cdot \left( [i_{abcn}]^T \cdot \frac{d[L_{ss}]}{d\theta} \cdot [i_{abcn}] + [i_{abcn}]^T \cdot \frac{d[\lambda_{PM,abcn}]}{d\theta} \right) \quad (2.91)$$

where the *PM* presence is considered and modeled as an ideal magnetomotive force generator, as explain above.

By observing the  $[L_{ss}]$  defined in Eq. (2.42), it is possible to conclude that matrix doesn't depend on the electrical position  $\theta$  and for this reason the first part of the Eq. (2.91) can be neglected. The Eq. (2.91) is overwritten as:

$$T_{em} = P \cdot [i_{abcn}]^T \cdot \frac{d[\lambda_{PM,abcn}]}{d\theta} \quad (2.92)$$

By considering the *PM* model:

$$[\lambda_{PM,abcn}] = \lambda_{PM} \cdot [\cos(\theta - x \cdot \alpha)] \quad (2.93)$$

the Eq. (2.92) becomes:

$$T_{em} = -P \cdot \lambda_{PM} \cdot [i_{abcn}]^T \cdot [\sin(\theta - x \cdot \alpha)] \quad (2.94)$$

where  $x \in [0, \dots, (n - 1)]$ .

By observing the torque equation (green block in Fig. 2.16), it can be seen that the electromagnetic torque is entirely produced by the interaction of the stator winding and permanent magnets on rotor surface.

In conclusion, the energy conversion model of  $n$ -phase machine is composed by a total  $2n+2$  equations:

- $n$ -electrical voltage equilibrium equations ( $v = R \cdot i + d\lambda/dt$ ),
- $n$ -magnetic equation ( $\lambda = \lambda_{PM} + M_{ss} \cdot \hat{i}$ ) and
- 2 mechanical equilibrium equations: mechanical equilibrium on rotor shaft and the time integral on rotor speed to compute the angular position.

## 2.3 Nine-phase Surface PMSM Modeling

The previous model can be easily adapted to nine-phase machine. The nine-phase machine is characterized by 3 winding sets ( $k_{ws}=3$ ) and number of phases is equal to 3 per each winding set ( $a=3$ ). The stator windings are arranged as three-phase sets and labelled as  $a_1, b_1, c_1$ , - *Set1*,  $a_2, b_2, c_2$ , - *Set2*, and  $a_3, b_3, c_3$ , - *Set3*. The angles of the symmetrical and asymmetrical configuration for nine-phase machine, shown in Fig. 2.17, are:

$$\alpha = \frac{2\pi}{9} = 40^\circ, \quad \alpha = \frac{\pi}{9} = 20^\circ \quad (2.95)$$

From now on, the symmetrical configuration will be considered. The symmetrical winding distribution of nine-phase machine with  $k_{ws}=3$  and  $a=3$  is represented in the left of Fig. 2.17. The stator active sides of nine-phase symmetrical surface PMSM is shown in Fig. 2.18 and the conventional sign is assigned to it. The conventional sign is opposite between two active sides of the same phase located one polar step far. In particular, in those conductors the same value of current flows, but with opposite sign. There are  $120^\circ$  electrical between  $a_1$  and  $b_1$  phase. The number of slot per pole per phase  $q$  and polar step  $\tau$  are calculated in Eqs. (2.96) and (2.97). Regular winding is designed and mounted on stator and the rotor is formed by two magnet poles (one north and one south).

$$q = \frac{N_{slots}}{2 \cdot P \cdot n} = \frac{36}{18} = 2 \quad (2.96)$$

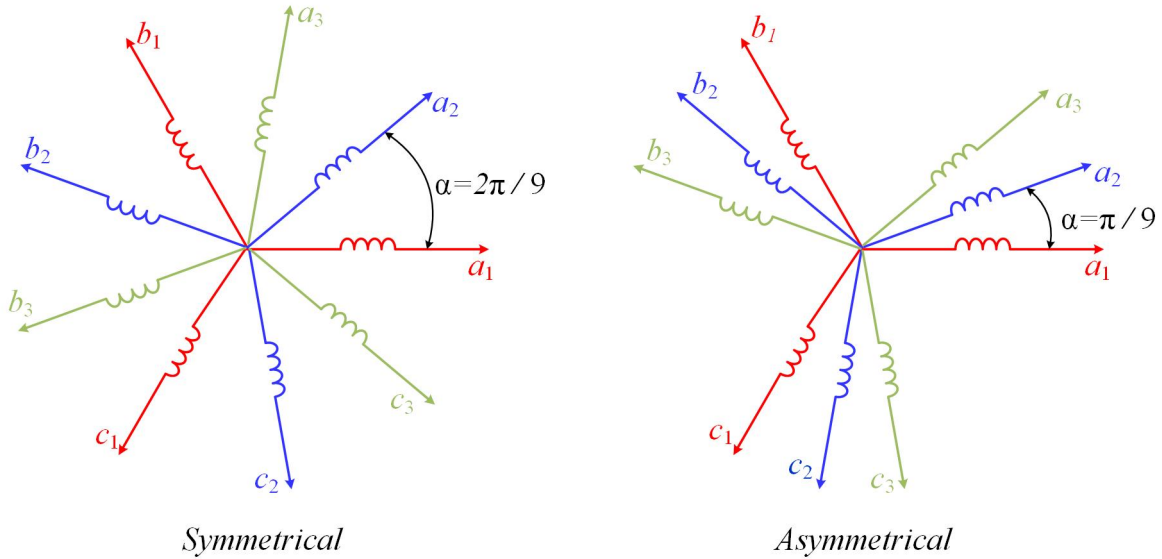
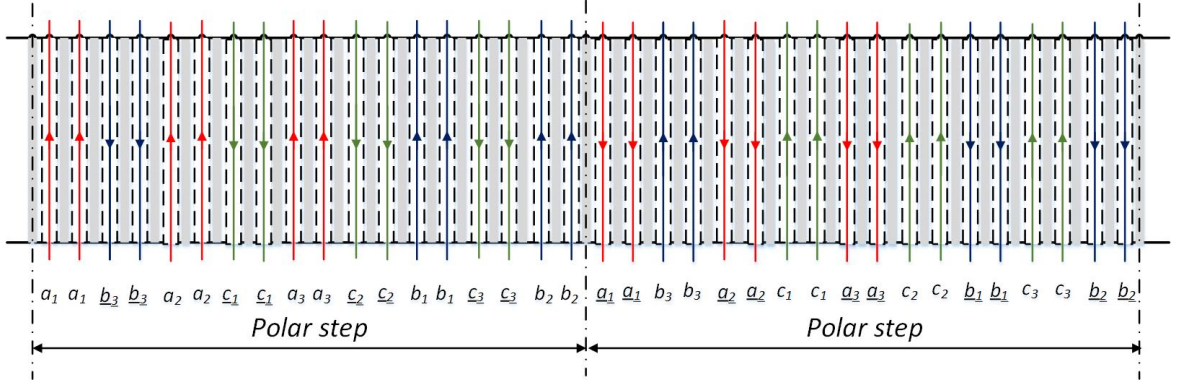


Figure 2.17: Nine-phase PMSM winding distribution around stator circumference.


 Figure 2.18: Winding arrangement of slots in nine-phase surface *PMSM*.

$$\tau = \frac{N_{slots}}{2 \cdot P} = \frac{36}{2} = 18slots \quad (2.97)$$

The vectors and matrices presented in previous section for a multiphase machine with arbitrary stator phase number can be now written as shown in Eqs. (2.98) - (2.103):

$$[v_{abc9}] = [v_{a1} \ v_{a2} \ v_{a3} \ v_{b1} \ v_{b2} \ v_{b3} \ v_{c1} \ v_{c2} \ v_{c3}]^T \quad (2.98)$$

$$[i_{abc9}] = [i_{a1} \ i_{a2} \ i_{a3} \ i_{b1} \ i_{b2} \ i_{b3} \ i_{c1} \ i_{c2} \ i_{c3}]^T \quad (2.99)$$

$$[\lambda_{abc9}] = [\lambda_{a1} \ \lambda_{a2} \ \lambda_{a3} \ \lambda_{b1} \ \lambda_{b2} \ \lambda_{b3} \ \lambda_{c1} \ \lambda_{c2} \ \lambda_{c3}]^T \quad (2.100)$$

$$[\lambda_{PM,abc9}] = [\lambda_{PM,a1} \ \lambda_{PM,a2} \ \lambda_{PM,a3} \ \lambda_{PM,b1} \ \lambda_{PM,b2} \ \dots \dots \lambda_{PM,b3} \ \lambda_{PM,c1} \ \lambda_{PM,c2} \ \lambda_{PM,c3}]^T \quad (2.101)$$

About the stator resistance matrix and stator leakage inductances for nine-phase machine, the matrices are:

$$[R_s] = \begin{bmatrix} R_s & 0 & 0 & 0 & 0 & 0 & 0 & 0 & 0 \\ 0 & R_s & 0 & 0 & 0 & 0 & 0 & 0 & 0 \\ 0 & 0 & R_s & 0 & 0 & 0 & 0 & 0 & 0 \\ 0 & 0 & 0 & R_s & 0 & 0 & 0 & 0 & 0 \\ 0 & 0 & 0 & 0 & R_s & 0 & 0 & 0 & 0 \\ 0 & 0 & 0 & 0 & 0 & R_s & 0 & 0 & 0 \\ 0 & 0 & 0 & 0 & 0 & 0 & R_s & 0 & 0 \\ 0 & 0 & 0 & 0 & 0 & 0 & 0 & R_s & 0 \\ 0 & 0 & 0 & 0 & 0 & 0 & 0 & 0 & R_s \end{bmatrix} \quad (2.102)$$

$$[L_{ls}] = \begin{bmatrix} L_{ls} & 0 & 0 & 0 & 0 & 0 & 0 & 0 & 0 \\ 0 & L_{ls} & 0 & 0 & 0 & 0 & 0 & 0 & 0 \\ 0 & 0 & L_{ls} & 0 & 0 & 0 & 0 & 0 & 0 \\ 0 & 0 & 0 & L_{ls} & 0 & 0 & 0 & 0 & 0 \\ 0 & 0 & 0 & 0 & L_{ls} & 0 & 0 & 0 & 0 \\ 0 & 0 & 0 & 0 & 0 & L_{ls} & 0 & 0 & 0 \\ 0 & 0 & 0 & 0 & 0 & 0 & L_{ls} & 0 & 0 \\ 0 & 0 & 0 & 0 & 0 & 0 & 0 & L_{ls} & 0 \\ 0 & 0 & 0 & 0 & 0 & 0 & 0 & 0 & L_{ls} \end{bmatrix} \quad (2.103)$$

The matrix  $[L_{ss}]$  presented in Eq. (2.42), can be now written as:

$$[L_{ss}] = \begin{bmatrix} M_{a1,a1} + L_{ls} & M_{a1,a2} & M_{a1,a3} & M_{a1,b1} & \dots & M_{a1,c3} \\ M_{a2,a1} & M_{a2,a2} + L_{ls} & M_{a2,a3} & M_{a2,b1} & \dots & M_{a2,c3} \\ M_{a3,a1} & M_{a3,a2} & M_{a3,a3} + L_{ls} & M_{a3,b1} & \dots & M_{a3,c3} \\ M_{b1,a1} & M_{b1,a2} & M_{b1,a3} & M_{b1,b1} + L_{ls} & \dots & M_{b1,c3} \\ \dots & \dots & \dots & \dots & \dots & \dots \\ M_{c3,a1} & M_{c3,a2} & M_{c3,a3} & M_{c3,b1} & \dots & M_{c3,c3} + L_{ls} \end{bmatrix} \quad (2.104)$$

If the winding distribution is sinusoidal, the flux linkage vector caused by only the *PM* presence is modelled as:

$$[\lambda_{PM,abc9}] = \lambda_{PM} \cdot \cos(\theta - [x] \cdot \alpha), \quad [x] \in [0, \dots, 8] \quad (2.105)$$

The Eq.(2.105) is extended as:

$$[\lambda_{PM,abc9}] = \lambda_{PM} \cdot \begin{bmatrix} \cos(\theta - 0 \cdot 2\pi/9) \\ \cos(\theta - 1 \cdot 2\pi/9) \\ \cos(\theta - 2 \cdot 2\pi/9) \\ \cos(\theta - 3 \cdot 2\pi/9) \\ \cos(\theta - 4 \cdot 2\pi/9) \\ \cos(\theta - 5 \cdot 2\pi/9) \\ \cos(\theta - 6 \cdot 2\pi/9) \\ \cos(\theta - 7 \cdot 2\pi/9) \\ \cos(\theta - 8 \cdot 2\pi/9) \end{bmatrix} \quad (2.106)$$

The dynamic mathematical model for nine-phase in phase variable domain can now be written as shown in Eq. (2.107) and its equivalent circuit is given in Fig. 2.19.

$$\begin{cases} [v_{abc9}] = [R_s] \cdot [i_{abc9}] + \frac{d[\lambda_{abc9}]}{dt} \\ [\lambda_{abc9}] = [\lambda_{PM,abc9}] + [L_{ls}] \cdot [i_{abc9}] + [M_{ss}] \cdot [i_{abc9}] = [\lambda_{PM,abc9}] + [L_{ss}] \cdot [i_{abc9}] \end{cases} \quad (2.107)$$

The machine model in the nine phase variable domain can be transformed using decoupling transformation matrix because the mathematical model in phase variable domain is complex, as explained above. After this transformation, the machine is represented in four two-dimensional subplanes plus one single-dimensional quantity (zero-sequence). The *VSD* matrix for nine-phase symmetrical machine is shown in Eq. (2.108).

$$[VSD] = \frac{2}{9} \begin{bmatrix} \cos(1 \cdot [\theta_{sym}]) & \alpha \\ \sin(1 \cdot [\theta_{sym}]) & \beta \\ \cos(2 \cdot [\theta_{sym}]) & x1 \\ \sin(2 \cdot [\theta_{sym}]) & y1 \\ \cos(4 \cdot [\theta_{sym}]) & x2 \\ \sin(4 \cdot [\theta_{sym}]) & y2 \\ \cos(3 \cdot [\theta_{sym}]) & y3 \\ \cos(3 \cdot [\theta_{sym}]) & x3 \\ 1/\sqrt{2} \cdot \cos(9 \cdot [\theta_{sym}]) & 0 \end{bmatrix} \quad (2.108)$$

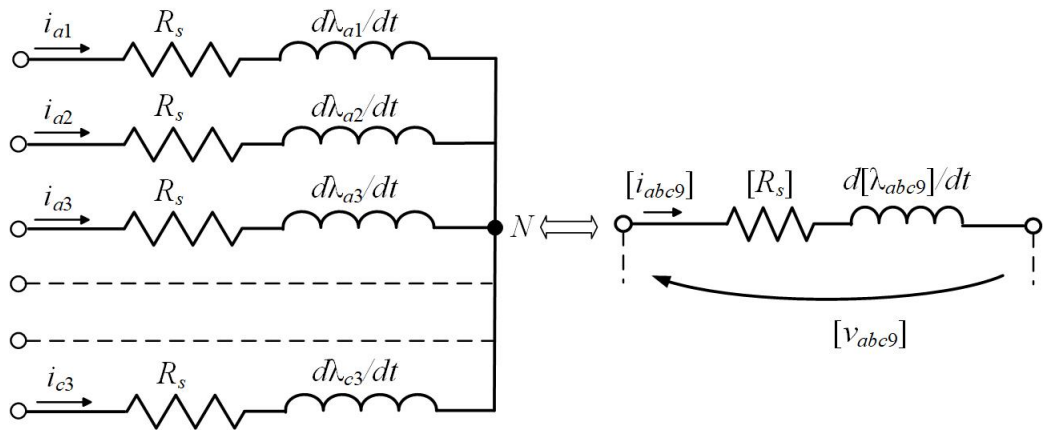


Figure 2.19: Equivalent circuit of nine-phase surface *PMSM* in phase variables.

where the row vector is defined as:

$$[\theta_{sym}] = \frac{2\pi}{9} \cdot [0 \ 1 \ 2 \ 3 \ 4 \ 5 \ 6 \ 7 \ 8] \quad (2.109)$$

The relation between phase variable and stationary  $RF$  is defined in Eq. (2.110):

$$[f_{vsd}] = [VSD]_{9 \times 9} \cdot [f_{abc9}] \quad (2.110)$$

In decoupled  $vsd$  model, stator windings are stationary (rotor windings don't exist in surface  $PMSM$  machine). From the electromechanical energy conversion point of view, it is important to note that the first two rows of the Eq. (2.108) define variables that will lead the fundamental flux and torque productions. The last row is zero-sequence (only 1 zero sequence in this case with  $n=9$  and single neutral point). In between there are three  $xy$  pairs of variables which don't participate in electromechanical energy conversion (sinusoidal winding distribution).

The fictitious  $\alpha\beta xy$  stator windings can be transformed in  $dq$  windings. This means that the fictitious machine's windings, obtained after application of the decoupling transformation, are now transformed once again into another set of fictitious windings. In order to obtain the  $dq$  components, it is possible to apply the matrix  $[D]$ . This matrix for nine-phase surface  $PMSM$  machine is direct consequence of Eq. (2.64) because the rotational transformation is applied only to the first two components. The  $[D]$  for nine-phase machine ( $n=9$ ) is:

$$[D] = \begin{bmatrix} \cos(\theta) & \sin(\theta) & 0 & 0 & 0 & 0 & 0 & 0 & 0 \\ -\sin(\theta) & \cos(\theta) & 0 & 0 & 0 & 0 & 0 & 0 & 0 \\ 0 & 0 & 1 & 0 & 0 & 0 & 0 & 0 & 0 \\ 0 & 0 & 0 & 1 & 0 & 0 & 0 & 0 & 0 \\ 0 & 0 & 0 & 0 & 1 & 0 & 0 & 0 & 0 \\ 0 & 0 & 0 & 0 & 0 & 1 & 0 & 0 & 0 \\ 0 & 0 & 0 & 0 & 0 & 0 & 1 & 0 & 0 \\ 0 & 0 & 0 & 0 & 0 & 0 & 0 & 1 & 0 \\ 0 & 0 & 0 & 0 & 0 & 0 & 0 & 0 & 1 \end{bmatrix} \quad (2.111)$$

By applying  $VSD$  presented in Subsection 2.2.2 and the rotational transformation to the phase variable reference frame for nine-phase surface  $PMSM$ , the obtained

model is given. The electrical equations in synchronous reference frame for nine-phase surface *PMSM* is defined as:

$$\begin{cases} v_d = R_s \cdot i_d + L_s \cdot \frac{di_d}{dt} - \omega \cdot \lambda_q \\ v_q = R_s \cdot i_q + L_s \cdot \frac{di_q}{dt} + \omega \cdot \lambda_d \\ v_{xi} = R_s \cdot i_{xi} + \frac{d\lambda_{xi}}{dt}, & i = 1, 2, 3 \\ v_{yi} = R_s \cdot i_{yi} + \frac{d\lambda_{yi}}{dt}, & i = 1, 2, 3 \\ v_0 = R_s \cdot i_0 + \frac{d\lambda_0}{dt} \end{cases} \quad (2.112)$$

About the magnetic equations in synchronous reference frame for nine-phase surface *PMSM* machine, it is defined as:

$$\begin{cases} \lambda_d = L_s \cdot i_d + \lambda_{PM} \\ \lambda_q = L_s \cdot i_q \\ \lambda_{xi} = L_{ls} \cdot i_{xi}, & i = 1, 2, 3 \\ \lambda_{yi} = L_{ls} \cdot i_{yi}, & i = 1, 2, 3 \\ \lambda_0 = L_{ls} \cdot i_0 \end{cases} \quad (2.113)$$

To conclude, the torque equation for nine-phase surface permanent magnet synchronous machine is:

$$T_{em} = \frac{9}{2} \cdot P \cdot \lambda_{PM} \cdot i_q \quad (2.114)$$



## Chapter 3

# Field-Oriented Control and Model Testing Results for Sinusoidal *PMSM*

In this chapter Field-Oriented Control method and system performance evaluation of nine-phase synchronous machine are presented. The system performance is evaluated using proposed simulation sequence.

Chapter is organised as follows:

- In Section 3.1 theory behind *FOC* and corresponding advantages are given.
- In Section 3.2 field-oriented control of nine-phase surface *PMSM* is analysed. The control is composed by cascaded *PI* controllers. The anti-windup technique is added, otherwise wind-up problems can emerge using integrator with step/speed/current change.
- In Section 3.3 the analysis and design of current and speed loops are shown in Laplace domain.
- In Section 3.4 the simulation results are presented. The results are obtained in *Matlab/Simulink* environment. They are related to speed, torque and currents in phase variable domain and in synchronous reference frame.

### 3.1 Introduction

Variable speed electric drives are nowadays utilized in almost every aspect of life, from most basic devices on one side to the highly sophisticated on the other. In variable speed drives control method usually plays big role. In most cases, the cost of control algorithms is negligible with respect to the one of electrical machine.

The following discussion concerns surface permanent magnet synchronous machine, which has higher power density, higher efficiency and better dynamic performance than induction machine of the same rating. The accurate control of this machine requires rotor position to know the coordinate transformation of the vector control and to obtain speed and position feedback control signals. Significant research efforts have been also conducted to achieve vector control of the surface *PMSM* without encoders or resolvers (sensorless control). These techniques can be divided into model based techniques, where the back-*EMF* of the machine is used for rotor magnet flux detection, and injection techniques, where a test signal, either high-frequency *ac* voltage or voltage pulse, is used to detect the rotor saliency position [22], [23]. More about this is going to be investigated in following chapters.

From a generic point of view, the implemented control scheme must be able to control machine's electromagnetic torque, rotor speed and position. This means that the machine must be able to achieve desired dynamic response of the controlled variable in a minimum time interval. The high-performance drives are obtained with closed-loop control. The machine is supplied from a power electronic converter and current/speed/position measure is necessary in this case.

A generic schematic of the position closed-loop is shown in Fig. 3.1. The control is composed of three cascaded controllers. Typically, the controller is composed of the proportional *P* plus integral *I* components. Three controllers (torque, speed and position) are represented in Fig. 3.1. In this, *PEC* stands for power electronic converter and *DCA* stands for Drive control algorithm.

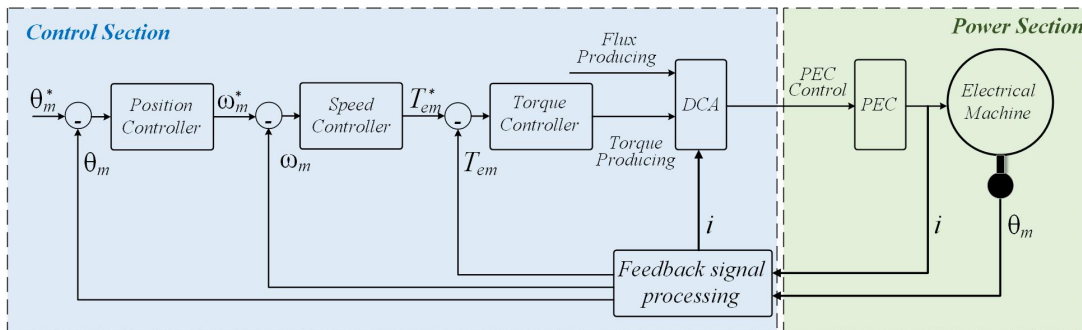


Figure 3.1: Schematic of current, speed and position loops.

The electromagnetic torque of an electrical machine can be expressed as a product between current and flux. The reference electromagnetic torque value  $T_{em}^*$  represents the input in current loop. The reference torque is obtained from the speed loop. Finally, the input of speed loop is received from the position loop. This means that the output of the position controller can be made to be directly the speed producing torque reference and the output of the speed controller can be made to be directly the torque producing current reference. The inputs of controllers are reference quantities and are represented with asterisk, while the same quantities without asterisk represents their real instantaneous value (measured/estimated).

High-performance drives typically involve measurement of the rotor position (speed) and motor supply currents, as indicated in Fig. 3.1. Since the machine's torque is governed by currents rather than voltages, measured currents are used in the block *DCA* to incorporate the close-loop current control algorithm. What this means is that the power electronic converter is current-controlled, so that applied voltages are such as to minimize the errors in the current tracking.

It is important to note that the control principles are valid in the same manner regardless of the number of the phases.

## 3.2 FOC of Multiphase Surface PMSM

Assuming that the machine is operated as a speed-controlled drive, a generic representation of vector control of nine-phase surface PMSM is presented in Fig. 3.2. The scheme is a mathematical model obtained using the reference transformation of the general theory of electrical machines, presented in Chapter 6.24. The machine control consists of a Current vector control implemented in the rotating physical ( $d, q$ ) reference frame, leading to a field-oriented control scheme. Since the 1980s of the last century, FOC has been extensively researched and it has been treated in a number of textbooks at varying levels of the complexity and detail [24]- [25]. In this control the reference current along  $d$ -axis is equal to zero ( $i_d^*=0$ ), as shown in Fig. 3.2. This assumption results in torque equation which is written as:

$$T_{em} = \frac{9}{2} \cdot P \cdot \lambda_{PM} \cdot i_{s,q} \quad (3.1)$$

As already noted, in surface permanent magnet synchronous machine, the current along  $q$ -axis is related to the electromagnetic torque ( $T_{em} \propto i_q$ ). From Eq. (3.1) the value of reference current along  $q$ -axis can be extracted. A linear function between  $i_q^*$  and produced torque is defined as:

$$i_q^* = T_{em}^* \cdot \frac{2}{9} \cdot \frac{1}{P \cdot \lambda_{PM}} \quad (3.2)$$

The Eq. (3.2) shows the relationship between the control current along  $q$ -axis and control torque: it consists of a constant coefficient and it is called  $k_1$ , defined as:

$$k_1 = \frac{2}{9} \cdot \frac{1}{P \cdot \lambda_{PM}} \quad (3.3)$$

The just presented vector control is applicable in the base speed region. If it is required that the machine operates at speeds higher then rated one, it is necessary

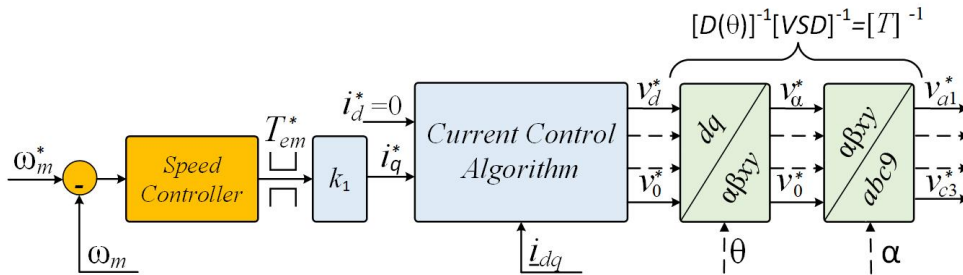


Figure 3.2: Vector control of a nine-phase surface PMSM: drive control (orange blocks); machine control (blue blocks); RFs transformation (green blocks).

to weaken the flux so that the voltage applied to the machine doesn't exceed the rated value. In surface *PMSM* when the speed is higher than rated value, the value of the current along *d*- axis must be reduce. The principle control of surface *PMSM* machine in base speed region and above rated speed value  $\omega_n$  is:

$$\begin{cases} i_d^* = 0, & \omega_m < \omega_n \\ i_d^* < 0, & \omega_m > \omega_n \end{cases} \quad (3.4)$$

In Fig. 3.3 is presented the schematic representation of field-oriented control of surface *PMSM* machine in base region speed. The *FOC* is a detailed schematic of Fig. 3.2. The FOC technique, presented in Fig. 3.3, is able to control the field and torque of the motor separately. The algorithm is executed in two control loops: current loop and speed loop. The speed loop (orange blocks in Fig. 3.3) is external to current loop (blue blocks). The aim of the speed loop is to regulate motor speed. The current command value along *q*-axis is set by the external speed loop. To achieve the goal of the surface *PMSM* control, the algorithm uses feedback signals. The essential feedback signals are the nine-phase stator currents and the electrical rotor position/speed.

The internal control loop executes two independent current control loops:

- The *PI* regulator of the direct axis current ( $i_d$ ) is used to control the rotor magnetizing flux.
- The *PI* regulator of the quadrature axis current ( $i_q$ ) is used to control the motor torque.

To operate properly, the proposed control structure requires speed of the motor shaft. The external control loop executes the speed controller and lower-priority control tasks. The *PI* speed controller sets a reference for the torque producing

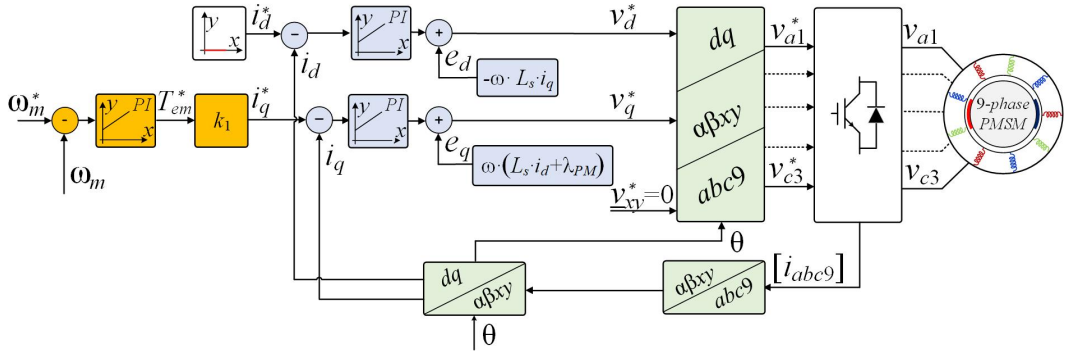


Figure 3.3: FOC of sinusoidal nine-phase surface *PMSM*.

current component ( $i_q$ ). After the reference currents are obtained, the output of  $dq$  current  $PI$  regulators are:

$$\begin{cases} v'_d = R_s \cdot i_d + L_s \cdot \frac{di_d}{dt} \\ v'_q = R_s \cdot i_q + L_s \cdot \frac{di_q}{dt} \end{cases} \quad (3.5)$$

The total stator voltage  $dq$  references are created by summing the outputs of the  $PI$  current controllers with decoupling voltages:

$$\begin{cases} v_d^* = v'_d + e_d \\ v_q^* = v'_q + e_q \end{cases} \quad (3.6)$$

By reintroducing the Eq. (2.70) presented in Chapter 6.24, the voltage equations take the following form:

$$\begin{cases} v_d = R_s \cdot i_d + L_s \cdot \frac{di_d}{dt} - \omega \cdot \lambda_q \\ v_q = R_s \cdot i_q + L_s \cdot \frac{di_q}{dt} + \omega \cdot \lambda_d \end{cases} \quad (3.7)$$

Comparison of Eqs. (3.5) - (3.6) with Eq. (3.7), shows that the decoupling voltages  $e$  are in the general case given as:

$$\begin{cases} e_d = -\omega \cdot L_s \cdot i_q \\ e_q = \omega \cdot (L_s \cdot i_d + \lambda_{PM}) \end{cases} \quad (3.8)$$

In region where the speed is higher than rated value, permanent magnet flux cannot be changed, as mentioned above. The only way to achieve operation at speeds higher than rated value is to keep the term  $e_q$  (Eq. (3.8)) constant and equal to its value at rated speed. This can be achieved using control law for the machine with low resistance, defined as:

$$i_d^* = -\frac{(\omega_m - \omega_n)}{\omega_m} \cdot \frac{\lambda_{PM}}{L_s}, \quad \omega_m > \omega_n \quad (3.9)$$

The implementation of proportional-integrator  $PI$ , presented in Fig. 3.3, can be explored in Fig. 3.4. An anti-windup algorithm is usually implemented together with the  $PI$  controller. Since the  $PI$  speed controller is designed in linear conditions, step speed commands can disturb the performance. The anti-windup algorithm is implemented in order to avoid this disturbance. The output of controller is compared with maximum (saturation limit high,  $LH$ ) and minimum (saturation limit low,  $LL$ ) values. If the output value of  $PI$  is not compatible with one of the allowed limits (the logical  $OR$  operator represented in Fig. 3.5), integral component integrator is restarted by sending zero to its input, as shown in Fig. 3.5.

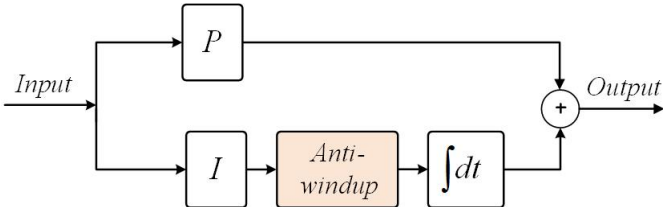


Figure 3.4: Proportional-integral control with Anti-windup algorithm.

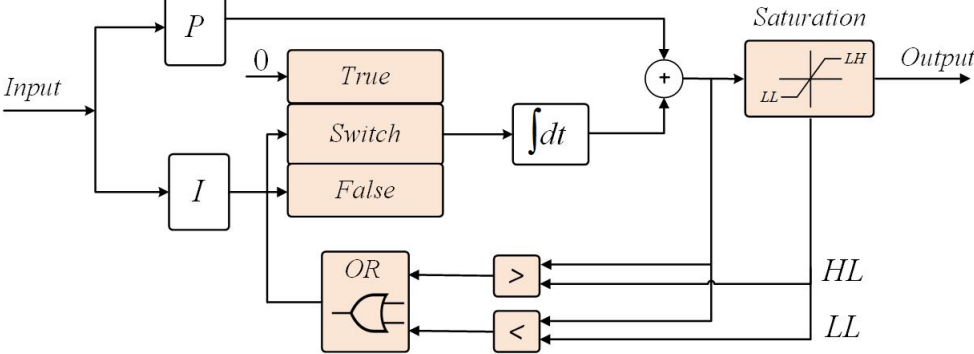


Figure 3.5: Anti-windup algorithm.

### 3.3 Speed and Current Control

As mentioned above, the speed and currents in the machine are controlled with *PI* controllers. The speed controller implements the speed regulation in closed-loop to obtain the reference electromagnetic torque. The closed-loop regulation is based on the feedback of measurement/estimated speed. The internal loop implements the current regulation in closed-loop to obtain the reference voltages and it is based on measurement currents. The analysis and design of both regulation loops are necessary. The following analysis and design are focused on the current regulation first and finally about speed regulation. The mentioned study is performed in Laplace domain, denoted with  $s$  symbol.

#### Current Loop Regulation

In Fig. 3.6 a simplified schematic of the current proportional-integral controller plus a feed-forward compensation, voltage source inverter and motor are shown. The input to the *PI* regulator (green block) is the current error, computed as difference between reference value, obtained by the torque scaling, and its measurement feedback. However, the current measurement process is considered ideal and, for this reason, the sensors function transfer can be approximated with unitary gain. This error is corrected using the mentioned controller. The voltage supply inverter is modelled as a low pass-filter. This means that the *VSI* is modelled as a delay component and its transfer function is:

$$H_{VSI}(s) = \frac{1}{1 + s \cdot \tau_d} \quad (3.10)$$

where the voltage source inverter time constant  $\tau_d$  is due to the application of the power converter commands, which are subjected to the digital controller

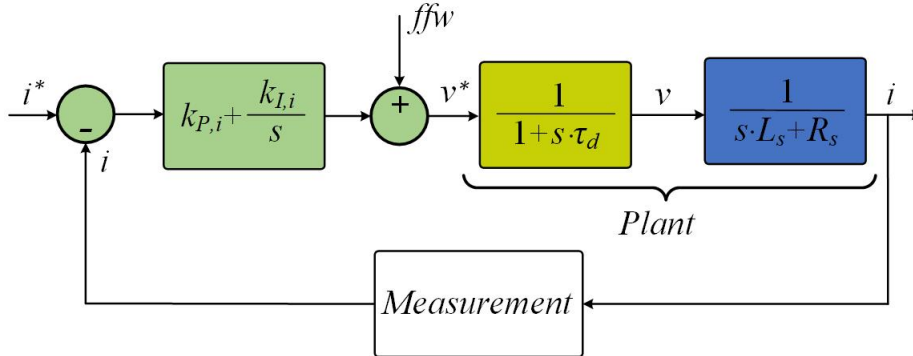


Figure 3.6: Schematic block of the current regulation loop.

execution delay (equal to sampling period  $T_s$ ) and average delay related to the implementation in the switching period following (equal to half sampling period  $T_s/2$ ). The voltage source inverter and the electrical machine represent the plant (yellow and blue blocks) and its transfer function is known while the  $PI$  (green block) must be tuned.

Consider Fig. 3.6, the design of the  $PI$  gains is based on the open-loop transfer function, which is written as:

$$H_{i,OL}(s) = \left( k_{P,i} + \frac{k_{I,i}}{s} \right) \cdot \frac{1}{1 + s \cdot \tau_d} \cdot \frac{1}{s \cdot L_s + R_s} \quad (3.11)$$

The design of the current  $PI$  gains can be performed in various ways. In this work, the pole-zero cancellation method is proposed. In other words, the motor pole is compensated by  $PI$  zero. The reason is evident: the high control dynamic is required and this requires to eliminate the poles positioned very close to the complex plane origin or should be taken away from the mentioned point. In mathematical formulation this is represented by the Eq. (3.12) and, following from stated, one of the degrees of freedom is lost.

$$\frac{k_{I,i}}{k_{P,i}} = \frac{R_s}{L_s} \quad (3.12)$$

By replacing the Eq. (3.12) into Eq. (3.11), the open-loop transfer function is written as:

$$\begin{aligned} H_{i,OL}(s) &= \frac{k_{P,i}}{s} \cdot \left( s + \frac{R_s}{L_s} \right) \cdot \frac{1}{1 + s \cdot \tau_d} \cdot \frac{\frac{1}{L_s}}{s + \frac{R_s}{L_s}} = \\ &= \frac{k_{P,i}}{L_s} \cdot \frac{1}{1 + s \cdot \tau_d} \cdot \frac{1}{s} \end{aligned} \quad (3.13)$$

Now, the magnitude and phase of the open-loop transfer function is computed as:

$$\begin{cases} |H_{i,OL}(\omega)| = \frac{k_{P,i}}{L_s} \cdot \frac{1}{\omega} \cdot \sqrt{\frac{1}{1 + (\omega \cdot \tau_d)^2}} \\ \angle H_{i,OL}(\omega) = -\frac{\pi}{2} - \arctan(\omega \cdot \tau_d) \end{cases} \quad (3.14)$$

In Fig. 3.7 the asymptotic Bode magnitude plot of the current regulator is shown, where the Bode frequency (rad/s) is denoted with the symbol  $\omega$ .

By computing the Eq. (3.14) at the crossover frequency, denoted with the symbol  $\omega_{cr}$ , where the magnitude of the open-loop transfer function is unitary (0dB), it can be now written as:

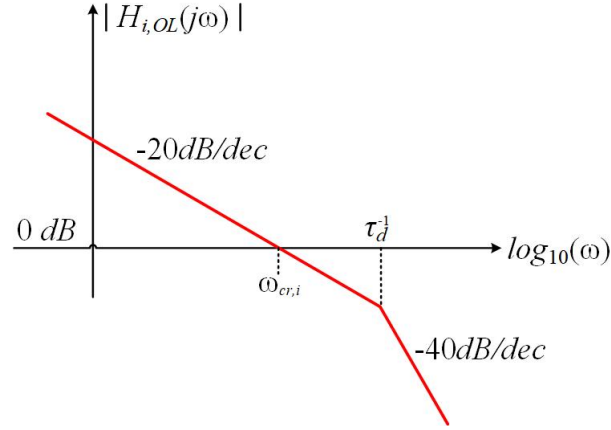


Figure 3.7: Asymptotic Bode plot of the open-loop transfer function magnitude for current regulation loop.

$$\begin{cases} \frac{k_{P,i}}{L_s} \cdot \frac{1}{\omega_{cr,i}} \cdot \sqrt{\frac{1}{1 + (\omega_{cr,i} \cdot \tau_d)^2}} = 1 \\ \Phi_{pm,i} = \left( -\frac{\pi}{2} - \arctan(\omega_{cr,i} \cdot \tau_d) \right) + \pi \end{cases} \quad (3.15)$$

where  $\Phi_{pm,i}$  stands for phase-margin of the current regulation loop. It is an equivalent measure of proximity to stability and is the distance of the phase at crossover frequency in degrees above  $-180^\circ$ .

With simple mathematical manipulations and several reasonable approximations, the first relation in Eq. (3.15), computed at crossover frequency, can be overwritten as:

$$\begin{cases} k_{P,i} \simeq \omega_{cr,i} \cdot L_s \\ \Phi_{pm,i} = \frac{\pi}{2} - \arctan(\omega_{cr,i} \cdot \tau_d) \end{cases} \quad (3.16)$$

As mentioned above, the consequence of pole-zero cancellation method is reduction of degrees of freedom and, for this reason, just one variable of the crossover frequency and phase-margin can be set at the desired value. If the phase-margin is imposed in Eq. (3.16), the crossover frequency is:

$$\omega_{cr,i} = \frac{\tan\left(-\Phi_{pm,i} + \frac{\pi}{2}\right)}{\tau_d} = \frac{1}{\tau_d \cdot \tan(\Phi_{pm,i})} \quad (3.17)$$

By replacing the Eq. (3.17) in Eq. (3.16), the *PI* gains can be written as:

$$\begin{cases} k_{P,i} \simeq \frac{L_s}{\tau_d \cdot \tan(\Phi_{pm,i})} \\ k_{I,i} \simeq \frac{R_s}{\tau_d \cdot \tan(\Phi_{pm,i})} \end{cases} \quad (3.18)$$

If the crossover frequency is chosen as a main variable, the proportional and integral gains are tuned as:

$$\begin{cases} k_{P,i} \simeq \omega_{cr,i} \cdot L_s \\ k_{I,i} \simeq \omega_{cr,i} \cdot R_s \end{cases} \quad (3.19)$$

Note that the crossover frequency represents the dynamic response and the system stability is related to it. The crossover frequency is very close to the bandwidth frequency. The theoretical limit of the crossover frequency is the reciprocal of the voltage source inverter time constant. In mathematical terms this can be written as:

$$\omega_{cr,i} \leq \frac{1}{\tau_d} \Rightarrow \omega_{cr,i} \leq \frac{f_{sw}}{1.5} \quad (3.20)$$

where  $f_{sw}$  is a switching frequency equal to the reciprocal of the switching period. By replacing the Eq. (3.20) in Eq. (3.15), the phase-margin of the current regulation loop must verify the following equations:

$$\frac{\pi}{4} \leq \Phi_{PM,i} < \frac{\pi}{2} \quad (3.21)$$

Finally, the design of the current *PI* controller can be written as:

$$\begin{cases} k_{P,i} \simeq \omega_{cr,i} \cdot L_s \\ k_{I,i} \simeq \omega_{cr,i} \cdot R_s \\ \frac{\pi}{4} \leq \Phi_{PM,i} < \frac{\pi}{2} \end{cases} \quad (3.22)$$

It can be concluded that the bandwidth of current loop is sufficiently high and it is limited by voltage source inverter dynamic. Usually, the current bandwidth is one decade lower than switching frequency. Indeed, the current loop regulation limits the speed bandwidth. If the current loop bandwidth is at least one decade higher than speed loop bandwidth, the current loop can be approximated as a unitary gain in analysis and design of the speed *PI* controller. However, in design of the speed *PI* controller, the current loop is modelled as a delay in order to increase the accuracy.

### Speed Loop Regulation

According with field-oriented control theory and the theory of the current regulation loop, the schematic of the speed loop is shown in Fig. 3.8. The input to the  $PI$  speed (green block) is the speed error, computed as difference between reference value and its measurement/estimated feedback. However, the transfer function of speed sensors can be approximated with unitary gain. The speed error is corrected using the  $PI$  speed controller. The output of the speed  $PI$  regulator is scaled to obtain the reference quadrature axis current (the electromagnetic torque is proportional to quadrature axis current). This latest reference represents the input of the current regulation loop, which is modelled as a delay element (orange block), whose time constant is defined as follow:

$$\tau_i = \frac{1}{\omega_{cr,i}} \quad (3.23)$$

where  $\omega_{cr,i}$  represents the the crossover frequency of the current loop regulation. The current loop delay take in account the current  $PI$  control and the plant ( $VSI$  and motor), shown in Fig. 3.6. The output of the current regulation loop is rescaled. Finally, the combination of the previous block and additive disturbance, related to the load torque, allows to obtain the speed value, considering the equivalent inertia.

To design of the  $PI$  gains is based on the open-loop transfer function of speed loop regulation, computed as:

$$H_{w,OL}(s) = \left( k_{P,w} + \frac{k_{I,w}}{s} \right) \cdot \frac{1}{1 + s \cdot \tau_i} \cdot \frac{1}{s \cdot J_{eq}} \quad (3.24)$$

By performing the computation of both magnitude and phase belonging to the open-loop transfer function, the following results are obtained:

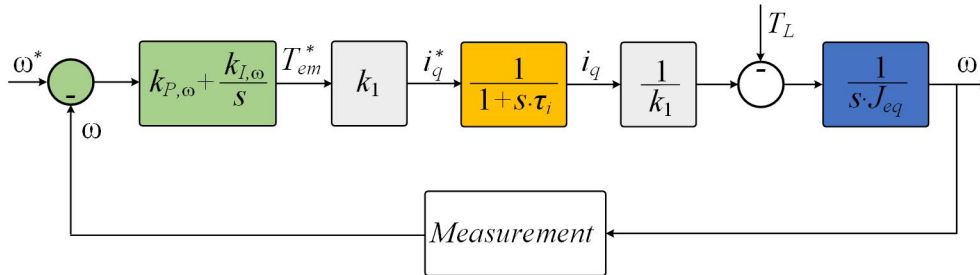


Figure 3.8: Schematic block of the speed regulation loop.

$$\begin{cases} |H_{\omega,OL}(\omega)| = \frac{k_{P,\omega}}{J_{eq} \cdot \omega} \cdot \sqrt{\frac{1 + \left(\frac{k_{I,\omega}}{k_{P,\omega} \cdot \omega}\right)^2}{1 + (\omega \cdot \tau_i)^2}} \\ \angle H_{\omega,OL}(\omega) = -\frac{\pi}{2} - \arctan(\omega \cdot \tau_i) + \arctan\left(\frac{\omega \cdot k_{P,\omega}}{k_{I,\omega}}\right) - \frac{\pi}{2} \end{cases} \quad (3.25)$$

In Fig. 3.9 the asymptotic Bode magnitude plot of the speed regulator is shown.

By computing Eq. (3.25) at the crossover frequency, which corresponds to unitary magnitude of the open-loop transfer function, the mentioned equation can be written as:

$$\begin{cases} \frac{k_{P,\omega}}{J_{eq} \cdot \omega_{cr,\omega}} \cdot \sqrt{\frac{1 + \left(\frac{k_{I,\omega}}{k_{P,\omega} \cdot \omega_{cr,\omega}}\right)^2}{1 + (\omega_{cr,\omega} \cdot \tau_i)^2}} = 1 \\ \phi_{pm,\omega} = \left(-\frac{\pi}{2} - \arctan(\omega_{cr,\omega} \cdot \tau_i) + \arctan\left(\frac{\omega_{cr,\omega} \cdot k_{P,\omega}}{k_{I,\omega}}\right) - \frac{\pi}{2}\right) + \pi \end{cases} \quad (3.26)$$

where  $\phi_{pm,\omega}$  stands for the phase-margin of speed loop regulation. In conclusion, with mathematical manipulations and several reasonable approximations, the Eq. (3.26) is simplified as follows:

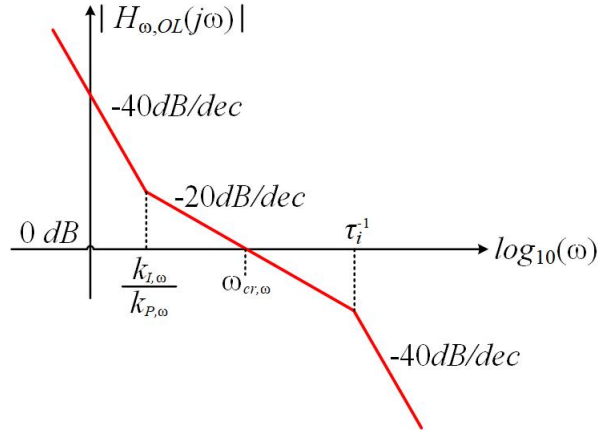


Figure 3.9: Asymptotic Bode plot of the open-loop transfer function magnitude for speed regulation loop.

$$\begin{cases} k_{P,\omega} \simeq \omega_{cr,\omega} \cdot k_{P,\omega} \\ k_{I,\omega} \simeq \frac{\omega_{cr,\omega}^2}{\tan(\phi_{pm,\omega} + \arctan(\omega_{cr,\omega} \cdot \tau_i))} \\ \phi_{pm,\omega} < \frac{\pi}{2} - \arctan(\omega_{cr,\omega} \cdot \tau_i) \end{cases} \quad (3.27)$$

Note that the theoretical limit of the speed bandwidth is equal to the crossover frequency of the current loop, which in mathematical terms can be written as:

$$\omega_{cr,\omega} \leq \tau_i^{-1} \quad (3.28)$$

Finally, the design of *PI* gains is:

$$\begin{cases} k_{P,\omega} \simeq \omega_{cr,\omega} \cdot k_{P,\omega} \\ k_{I,\omega} \simeq \frac{\omega_{cr,\omega}^2}{\tan(\phi_{pm,\omega} + \arctan(\omega_{cr,\omega} \cdot \tau_i))} \\ \phi_{pm,\omega} < \frac{\pi}{2} - \arctan(\omega_{cr,\omega} \cdot \tau_i) \\ \omega_{cr,\omega} \leq \tau_i^{-1} \end{cases} \quad (3.29)$$

Note that, in speed loop regulation the degree of freedom are both crossover frequency (*rad/s*) and phase-margin, conversely to current loop regulation. Following from stated, the design of the speed *PI* controller is performed on the basis of selected crossover frequency and phase-margin.

It is important to note that the real crossover frequency of the speed loop regulation is much lower than theoretical limit. However, the initial assumption that sensor transfer function can be modelled as unitary gain is not exactly verified due to encoder accuracy. In particular, the bandwidth of speed loop regulation is limited by the discretization performed by this instrument.

### 3.4 Simulation Results

The performance of surface permanent magnet synchronous machine model with field-oriented control, presented in Section 3.2, has been evaluated. The implemented machine model in simulation is in phase variable reference frame ( $abcn$ ) and it is controlled under  $FOC$  method. The results are obtained in *Matlab/Simulink* environment.

The input in *Simulink* model is mechanical speed reference  $\omega_m^*$  and the load torque  $T_L$ . The electrical and mechanical parameters used in simulation are given in Table 3.1, while in Table 3.2 the control parameters of external and internal loops are given.

Table 3.1: Electrical and mechanical parameters of surface  $PMSM$  machine

<b>Electrical parameters</b>	
Parameter	Value [Units]
Number of phases, $n$	9 [-]
Number of pole-pairs, $P$	1 [-]
Winding configuration	Symmetrical [-]
Nominal output power, $P_n$	1 [ $kW$ ]
Nominal torque, $T_n$	3 [ $Nm$ ]
Overload capability	150 %
Nominal frequency, $f_n$	50 [ $Hz$ ]
Nominal speed, $n_{rpm}$	3000 [ $rpm$ ]
Stator resistance, $R_s$	31.8 [ $\Omega$ ]
Stator leakage inductance, $L_{ls}$	84.7 [ $mH$ ]
Isotropic coefficient, $M_I$	75.9 [ $mH$ ]
Anisotropic coefficient, $M_A$	0 [ $mH$ ]
( $dq$ ) stator inductance $L_s$	426.4 [ $mH$ ]
Permanent magnets flux, $\lambda_{PM}$	385.8 [ $mWb$ ]
<b>Mechanical parameters</b>	
Rotor inertia, $J_{eq}$	0.0094 [ $kgm^2$ ]
Static torque, $T_{B0}$	0.4500 [ $Nm$ ]
Linear torque, $T_{B1}$	0.0042 [ $Nm/(rad/s)$ ]
Parabolic torque, $T_{B21}$	0.0000 [ $Nm/(rad/s)^2$ ]

Table 3.2: Control parameters of current and speed loop.

Control parameters	
Parameter	Value [Units]
Drive Control - Speed <i>PI</i> controllers	
Proportional gain $k_{P,\omega}$	0.7 [ $Nm/(rad/s)$ ]
Integral gain $k_{I,\omega}$	10 [ $Nm/rad$ ]
Machine Control - Current <i>PI</i> controller	
Proportional gain $k_{P,i}$	650 [ $V/A$ ]
Integral gain $k_{I,i}$	50000 [ $V/(As)$ ]

The testing sequence of the nine-phase surface *PMSM* machine is presented in Figs. 3.10 and 3.11. In Figs. 3.10 and 3.11 the speed and torque sequences are shown, respectively.

- Initially, the speed reference is zero. At 0.1 *s* the speed reference is increased up to 750 *rpm* (1/4 of nominal speed) with step function. The step function is used in order to evaluate the performances of control. At 2 *s* a further speed increase to 1500 *rpm* is implemented.
- Initially the machine is not loaded, i.e. the load torque is zero. After reaching steady-state, at 1 *s* a step load torque of 1.5 *Nm* is added until 4 *s*. The simulation ends without load torque (0 *Nm*).

In Fig. 3.10, when a step speed is applied the fast response of electrical machine in terms of mechanical speed is shown. At 1 *s* the small temporary speed drop due to additional load torque (1.5 *Nm*) is shown. The small speed drop is about 15 *rpm*. When the load torque is removed (at 4 *s*) the speed is increased of the same value. The entire sequence takes 5 *s*.

In Fig. 3.11 is shown the electromagnetic torque: the produced torque depend on the speed transients, friction contributions and load torque (1.5 *Nm* at 1 *s* until 4 *s*). The electromagnetic torque is increased when the control algorithm requires time to adapt and when the machine is loaded. When steady-state is reached, the electromagnetic torque follows the load torque and the friction contribution precisely. It should be noted that the maximum value of the electromagnetic torque is governed by the overload torque limit. The electromagnetic torque reaches the maximum allowed value. The set value in simulation is equal to overload torque ( $T_n = 4.5Nm$ ). The maximum value of electromagnetic torque is about this value.

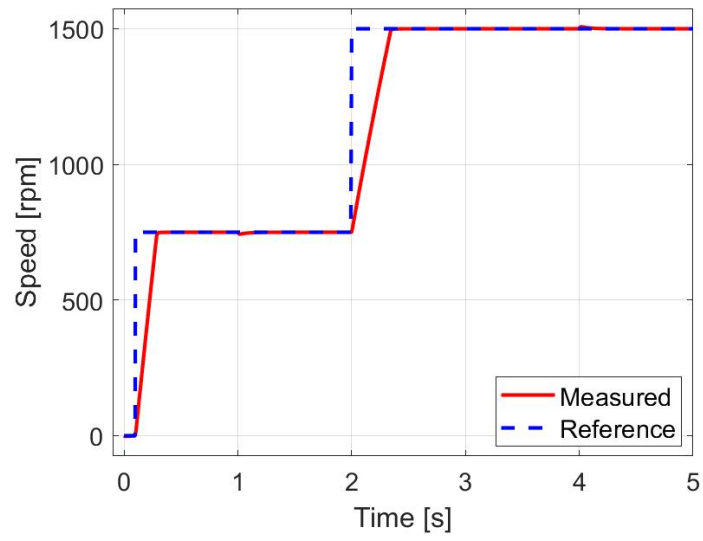


Figure 3.10: Speed reference and measured response under *FOC*.

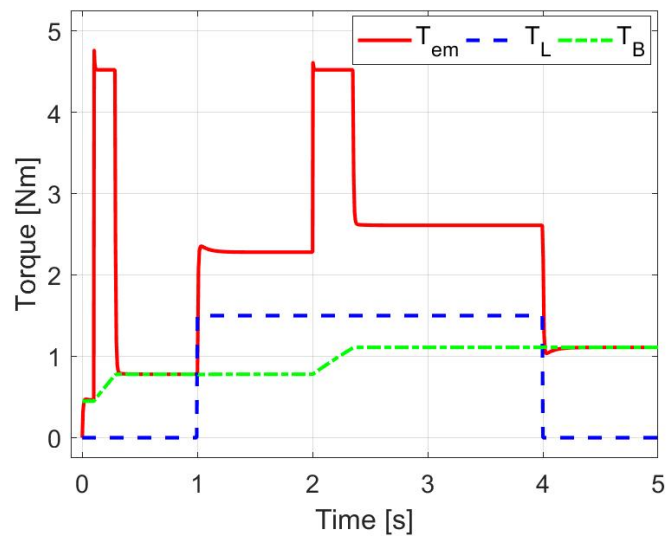


Figure 3.11: Torque reference and measured response under *FOC*.

In Fig. 3.12 the time trends of permanent magnets flux is shown. It is constant and the value is in accordance with Table 3.1. The back-electromotive force obtain after permanent magnets flux derivation is presented in Fig. 3.13. The variation of back- $EMF$  is related to variation of voltage and current values in the machine while its amplitude depends by the speed.

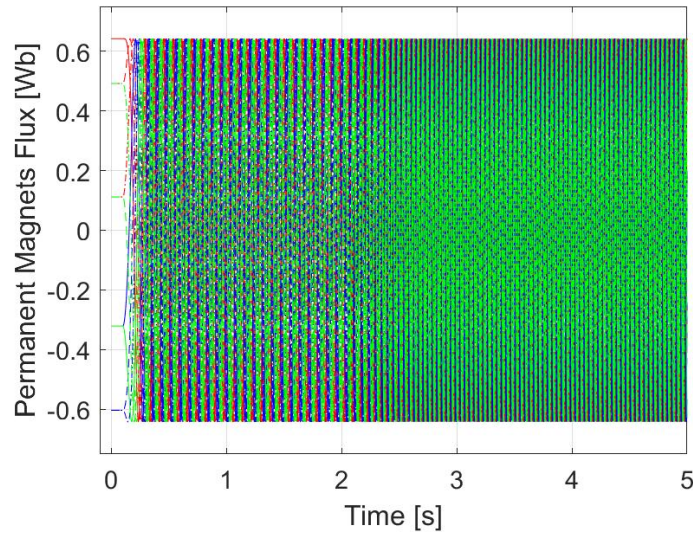


Figure 3.12: Flux linkage vector caused by only the  $PM$  presence.

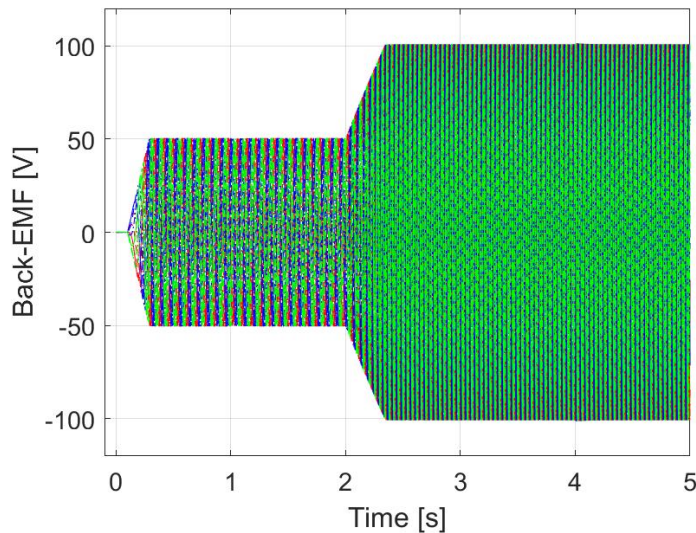


Figure 3.13: Back-electromotive forces for sinusoidal nine-phase  $PMSM$ .

In Figs. 3.14 and 3.15 the phase voltage and phase current are shown. During speed increase to 750 *rpm*, voltage and current increase transients can be seen. When the steady-state is reached, the current value is no zero because there is torque required to spin the machine. The value of phase voltage during steady-state is related to back-electromotive force and voltage drop due to the stator resistance. The value of voltage is increased for set speed and in this way the value of back-electromotive force does not change. Indeed, if the simulation ends without load torque and without friction contribution the consequence would be: the phase currents vanish (the electromagnetic torque would be null) and the phase voltage value would be the same of back-*EMF* (the speed doesn't change).

Following from decoupling *VSD* transformation, presented in Chapter 6.24, Subsection 2.2.2, in Figs. 3.16 and 3.17 the current mapping is shown. The current in  $(\alpha, \beta)$  subplane is shown in Fig. 3.16 and the current in another subplanes  $(x, y)1, (x, y)2, (x, y)3$  and zero-sequence component are shown in Fig. 3.17. The current values in  $(x, y)$  subplanes are equal to zero and these current components do not participate to electromechanical conversion (because the back-*EMF* is sinusoidal). The electromechanical conversion is therefore performed using  $\alpha\beta$  components.

After *VSD* transformation, the rotational transformation is applied on  $\alpha\beta$  components. The flux and torque producing currents are shown in Figs. 3.18 and 3.19, respectively. In these figures the flux producing ( $i_d$ ) is equal to zero, while the torque producing ( $i_q$ ) follows the electromagnetic torque.

To conclude, the implemented control of the machine in *Matlab/Simulink* environment achieves desired dynamic response.

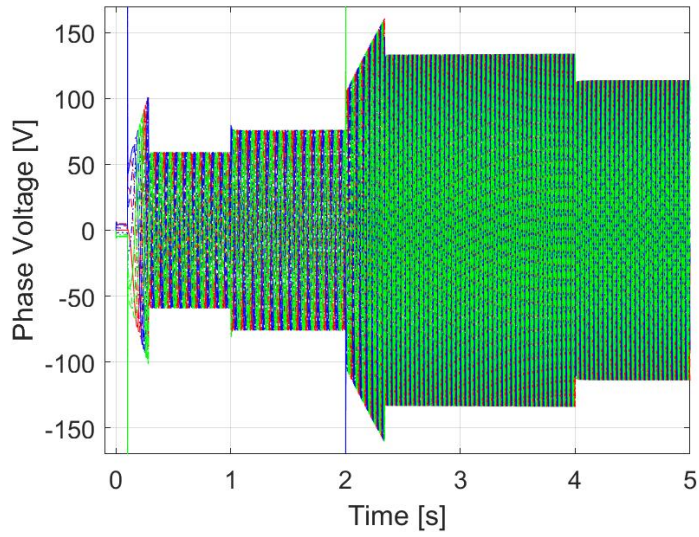


Figure 3.14: Phase voltages for sinusoidal nine-phase *PMSM*.

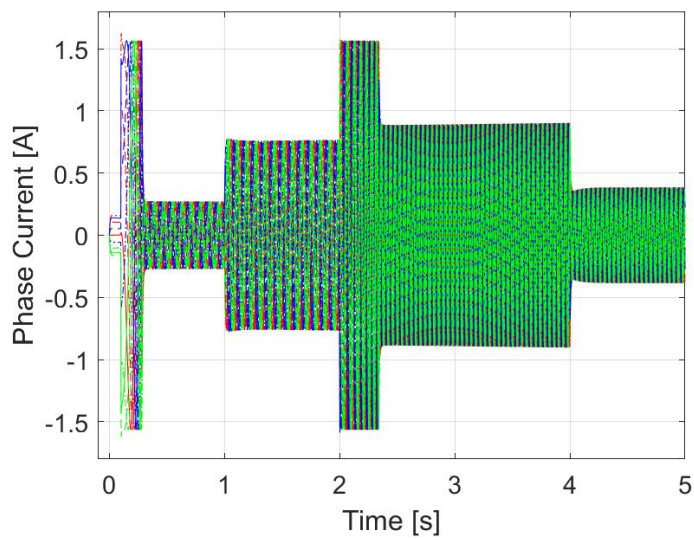
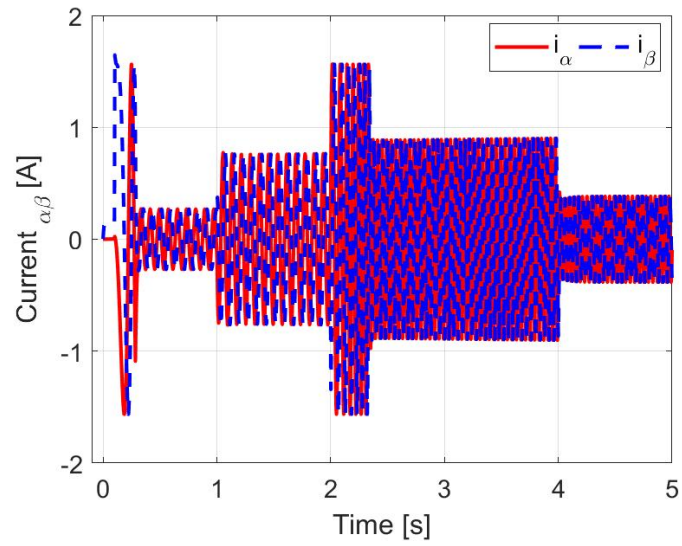
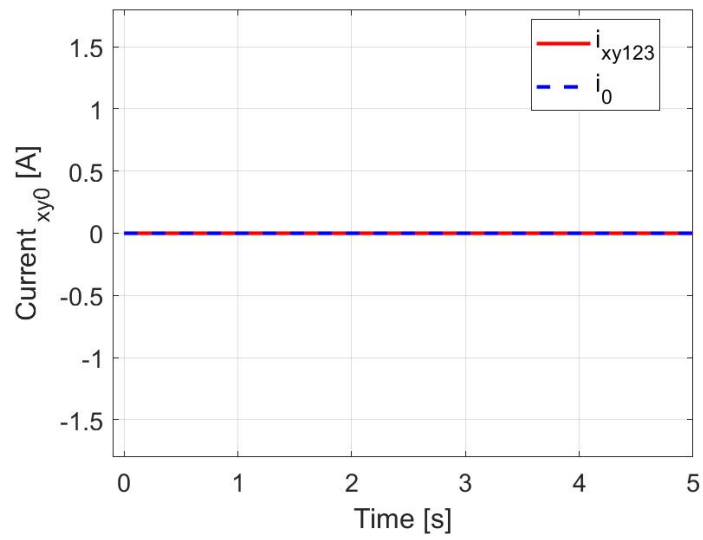


Figure 3.15: Phase currents for sinusoidal nine-phase *PMSM*.

Figure 3.16: Current in  $(\alpha, \beta)$  subplane after *VSD* transformation.Figure 3.17: Current in  $(x, y)$  subplanes after *VSD* transformation.

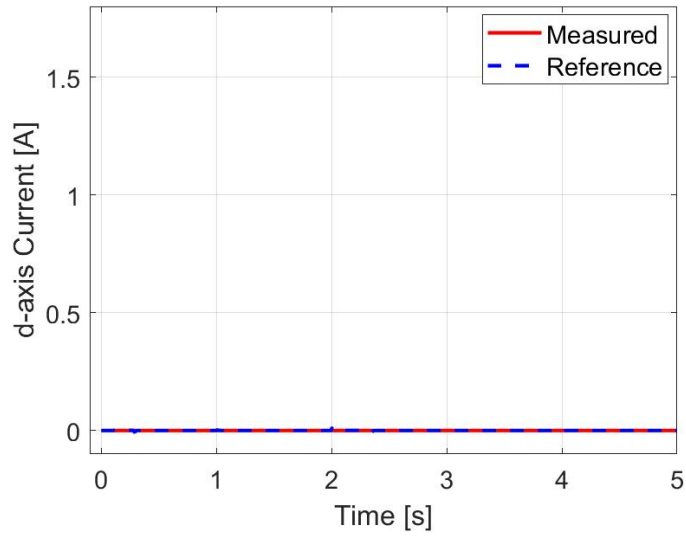


Figure 3.18: Flux producing current after the rotational transformation.

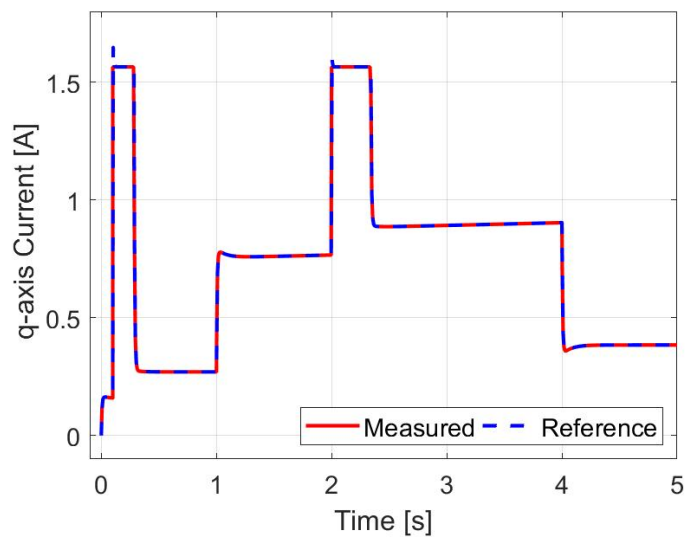


Figure 3.19: Torque producing current after the rotational transformation.

## Chapter 4

# Modelling and Control of the Surface *PMSM* with Non-Sinusoidal Back-*EMF*

In this chapter the symmetrical nine-phase surface *PMSM* with single-layer winding distribution and single isolated neutral point is analysed. The rotor is designed with two poles. Unlike the previous chapters, where the magnet length was  $180^\circ$ , magnet span on rotor are shortened. As it will be shown in this chapter, this causes production of highly non-sinusoidal back-electromotive force [26].

Chapter is organised as follows:

- In Section 4.1 the prototype machine under test is presented. The specific non-sinusoidal back-electromotive force was obtained in experimental test. The back-*EMF* distribution is the result of the removal of the four poles from the original six poles.
- In Section 4.2 the non-sinusoidal back-*EMF* machine modelling is developed: machine model in phase variable domain and in vector space decomposition variables.
- In Section 4.3 the Vector Proportional Integral and Proportional Resonant Controller are studied and implemented to eliminate the current harmonics.

## 4.1 Introduction

The machine prototype is characterized by highly non-sinusoidal back- electromotive force. The back- $EMF$  distribution is the consequence of the poles removal. Indeed, to reduce the cost and design time, the machine has been obtained by rewinding a three-phase machine prototype having 6 poles and 36 slots. Nevertheless, to obtain a symmetrical configuration of the winding, only two poles are present from the original six ones. These are spanning  $45^\circ$  each, as shown in the right of Fig. 4.1. The previous analysed structure in Chapters 6.24 and 6.25 is recalled in the left of Fig. 4.1. For this reason, the machine model presented in Chapter 6.24 is modified: the back- $EMF$  is modelled using the real harmonic spectrum from experimental test.

If winding distribution is suitable, non-sinusoidal back- $EMF$  means a specific harmonic content: low order harmonics are present in  $FFT$  spectrum. If not eliminated, these harmonics can induce the current harmonics in stator windings, producing losses and torque ripple. A specific current harmonic is generated only if its order is present in both  $PM$  distribution and winding distribution (the harmonic distribution factor ( $k_d^h$ ) is not zero).

However, the current harmonics can be used for additional purposes (f.e. harmonic injection in order to increase the electromagnetic torque) or eliminated. In this thesis, the current harmonics will be eliminated with adequate controllers, as shown below. This means that the field-oriented control, presented in Chapter 6.25, is modified to reach this goal.

The back- $EMF$  harmonics will be used to estimate the rotor angular position. Techniques based on back- $EMF$  estimation are consolidated in the area of sensorless control of permanent magnet synchronous machine as methods ensuring good performance at medium/high speed, with a little computational surplus and the same

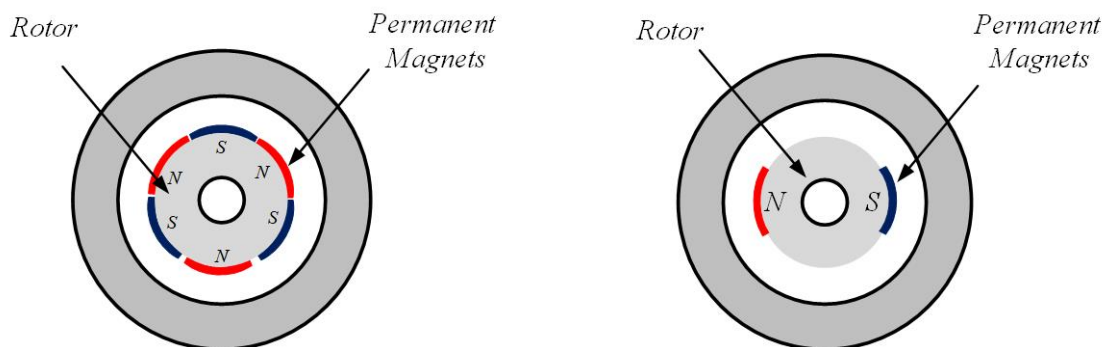


Figure 4.1: Magnet span of surface  $PMSM$ :  $180^\circ$  magnet span on rotor (left) and  $45^\circ$  magnet span on rotor (right).

hardware requirement of standard field-oriented control drives [27]. In field-oriented control the knowledge of the rotor angular position is needed. The exact knowledge of the position can be obtained with sensor (encoder or resolver) in real time or can be estimated. In this thesis the back- $EMF$  in  $VSD$  variables is the starting point to estimate the rotor position, as shown below.

The back- $EMF$  distribution highly non-sinusoidal is confirmed by experimental test and  $FFT$  analysis. The recorded data are shown in Figs. 4.2 and 4.3. The values are recorded at 1465  $rpm$  which corresponds to the frequency of 24.42  $Hz$  ( $P=1$ ). The recorded back-electromotive force of real machine is obtained in no-load condition and open-winding configuration and then, the  $FFT$  analysis is performed in *Matlab* environment. The presented analysis is developed in steady-state because it depends on the angular speed. As is known from the theory, the back- $EMF$  distribution is related only to one specific rotor speed of the machine. In Fig. 4.4 the magnitudes and angles of the recorded back- $EMF$  in winding  $a1$  are shown. In magnitude spectrum the significant values can be noted from the fundamental component to thirteenth harmonic. For this reason in real machine model only the first 13 harmonics will be modelled. From  $FFT$  analysis the third harmonic magnitude is relevant and it plays a key role in rotor angular position estimation.

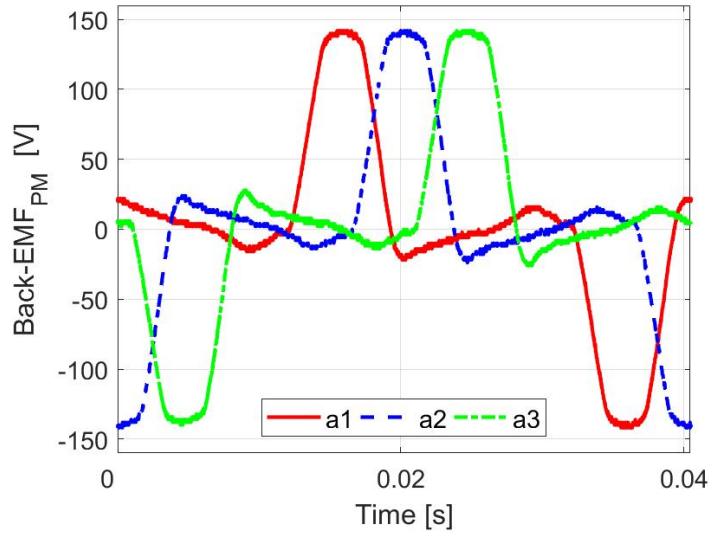


Figure 4.2: Back- $EMF$  waveforms of real machine: experimental results at 1465  $rpm$ .

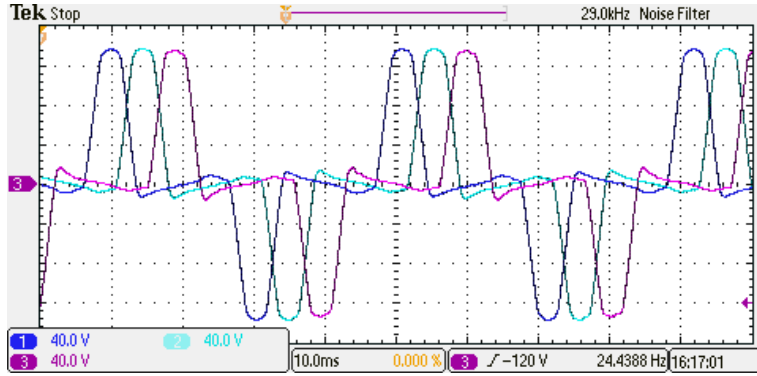


Figure 4.3: Back-EMF ( $e_{a1}, e_{a2}, e_{a3}$ ) in steady-state at 1465 rpm: CH.1 - CH.3: 40 V/div.

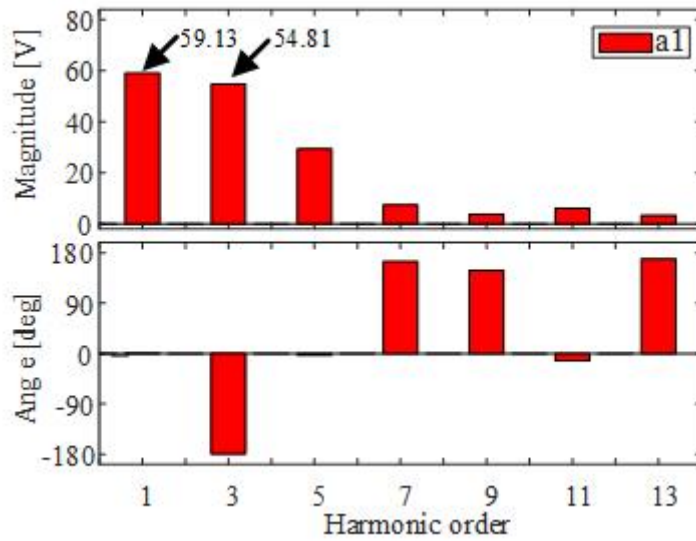


Figure 4.4: Fourier analysis of non-sinusoidal back-EMF on recorded data at 1465 rpm.

## 4.2 Non-Sinusoidal Machine Model

### 4.2.1 Back-*EMF* and *PM* harmonic distribution

The model of nine-phase surface *PMSM* in phase variable reference frame was presented in Chapter 6.24, Subsection 2.2.1. One of the assumptions was related to magnetomotive force and back-electromotive force distributions. They were assumed to be sinusoidal, i.e. the flux linkage vector caused by only the *PM* presence was modelled as:

$$[\lambda_{PM,abc9}] = \lambda_{PM} \cdot \cos(\theta - [\theta_n]), \quad [\theta_n] \in [0, \dots, 8\alpha], \quad \alpha = \frac{2\pi}{9} \quad (4.1)$$

The electrical machine in laboratory and analysed in this work is characterised by highly non-sinusoidal back-*EMF*. Therefore, the Eq. (4.1) is not correct, hence must be opportunely modified. The modelling of real machine in phase variable domain presents the same form of the machine with sinusoidal back-electromotive force, but the flux produced by permanent magnet must be modified. For convenience, both electrical and magnetic equations in phase variable domain for nine-phase surface *PMSM* are below reported:

$$\begin{cases} [v_{abc9}] = [R_s] \cdot [i_{abc9}] + \frac{d[\lambda_{abc9}]}{dt} \\ [\lambda_{abc9}] = [\lambda_{PM,abc9}] + [L_{ss}] \cdot [i_{abc9}] \end{cases} \quad (4.2)$$

where all symbols are consistent with the ones defined in previous chapters. Nevertheless, both  $[\lambda_{PM,abc9}]$  and  $[L_{ss}]$  are composed of all harmonic contributions [28].

The flux linkage vector caused by only the *PM* presence is modelled as:

$$\begin{aligned} [\lambda_{PM,abc9}] = & \lambda_{PM1} \cdot \cos(1 \cdot (\theta - [\theta_n]) + \theta_{sh1}) + \lambda_{PM3} \cdot \cos(3 \cdot (\theta - [\theta_n]) + \theta_{sh3}) + \\ & + \lambda_{PM5} \cdot \cos(5 \cdot (\theta - [\theta_n]) + \theta_{sh5}) + \dots + \lambda_{PMh} \cdot \cos(h \cdot (\theta - [\theta_n]) + \theta_{shh}) \end{aligned} \quad (4.3)$$

where:

$-\lambda_{PM1}, \lambda_{PM3}, \dots, \lambda_{PMh}$  stand for harmonic magnitudes related to the  $h^{th}$  harmonic and

$-\theta_{sh1}, \theta_{sh3}, \dots, \theta_{shh}$  stand for harmonic phase shifts.

The form of current equation in phase variable domain, obtained with the combination of electrical and magnetic equations, is the same as in sinusoidal machine, but the flux linkage and the mutual magnetizing matrix must be replaced. The new machine model is used to obtain the future simulation results. For convenience, the final machine model for real machine is below reported:

$$[i_{abc9}] = [L_{ss}]^{-1} \left( \int \left( [v_{abc9}] - [R_s] \cdot [i_{abc9}] \right) dt - [\lambda_{PM,abc9}] \right) \quad (4.4)$$

It is also important to observe that the non-sinusoidal back-*EMF* is modelled using the Eq. (4.3) which is related to permanent magnets flux. The reason is: the magnitude of back-*EMF* is related to the specific speed, used in experimental test to record the data. The problem is solved using in machine model the Eq. (4.3) because the magnitudes of flux linkage are constant and these values are correctly non-sensitive to speed. The flux linkage magnitude of the generic harmonic  $h^{th}$  is related to back-*EMF* magnitude of  $h^{th}$  harmonic as shown below:

$$\lambda_{PM,h} = \frac{\text{back-EMF}_h}{h \cdot \omega} \quad (4.5)$$

The back-*EMF* magnitude and phase shift values are obtained experimentally and shown in Table 4.1. Usually the fundamental angle  $\theta_{sh1} = 0^\circ$  is taken as reference and the phases shift are calculated for every harmonics in relation to this angle datum value.

Table 4.1: Harmonics of the permanent magnets flux surface *PMSM* machine.

<b>Harmonics flux linkage</b>			
$h^{th}$	back-EMF [V]	$\lambda_{PM}[mWb]$	Angle
1 <sup>st</sup>	59.13	385.8	0°
3 <sup>rd</sup>	54.81	119.2	-179°
5 <sup>th</sup>	29.37	38.33	3.1°
7 <sup>th</sup>	7.54	7.03	164.5°
9 <sup>th</sup>	3.72	2.70	148°
11 <sup>th</sup>	6.09	3.62	-12.9°
13 <sup>th</sup>	3.42	1.72	168.9°

### 4.2.2 Harmonic Model in *VSD* Variables

Since the rotor position is estimated using the non-sinusoidal back-*EMF* in vector space decomposition variables, *VSD* modelling is studied in detail.

In Chapter 6.24, Subsection 2.2.2, *VSD* matrix for nine-phase symmetrical machine with sinusoidal winding was introduced. The machine model in *VSD* variables is obtained when the *VSD* matrix is applied to each winding of the nine-phase surface as:

$$\begin{aligned} [f_{vsd}] &= [f_\alpha, f_\beta, f_{x1}, f_{y1}, f_{x2}, f_{y2}, f_{x3}, f_{y3}, f_0]^T = \\ &= [VSD] \cdot [f_{a1}, f_{a2}, f_{a3}, f_{b2}, f_{b3}, f_{c1}, f_{c2}, f_{c3}]^T \end{aligned} \quad (4.6)$$

For convenience, the equations in *VSD* variables are below shown, where the obtained matrices in this domain for the machine with non-sinusoidal winding are different then the matrices presented in Chapter 6.24.

$$\begin{cases} [v_{vsd}] = [R_s] \cdot [i_{vsd}] + \frac{d[\lambda_{vsd}]}{dt} \\ [\lambda_{vsd}] = [L_{ls}] \cdot [i_{vsd}] + [M_{ss,vsd}] \cdot [i_{vsd}] + [\lambda_{PM,vsd}] \end{cases} \quad (4.7)$$

The index *vsd* denotes *VSD* variables. All other symbols are consistent with the ones defined in previous chapters.

In matrix form, with the same approach presented in Chapter 6.24, the inductance matrix is defined as:

$$[L_{ss,vsd}] = \begin{bmatrix} L_{\alpha\beta} & 0 & 0 & 0 & 0 & 0 & 0 & 0 & 0 \\ 0 & L_{\alpha\beta} & 0 & 0 & 0 & 0 & 0 & 0 & 0 \\ 0 & 0 & L_1 + L_{1'} & 0 & 0 & 0 & 0 & 0 & 0 \\ 0 & 0 & 0 & L_1 - L_{1'} & 0 & 0 & 0 & 0 & 0 \\ 0 & 0 & 0 & 0 & L_2 + L_{2'} & 0 & 0 & 0 & 0 \\ 0 & 0 & 0 & 0 & 0 & L_2 - L_{2'} & 0 & 0 & 0 \\ 0 & 0 & 0 & 0 & 0 & 0 & L_3 & 0 & 0 \\ 0 & 0 & 0 & 0 & 0 & 0 & 0 & L_3 & 0 \\ 0 & 0 & 0 & 0 & 0 & 0 & 0 & 0 & L_9 \end{bmatrix} \begin{matrix} \alpha \\ \beta \\ x_1 \\ y_1 \\ x_2 \\ y_2 \\ x_3 \\ y_3 \\ 0 \end{matrix} \quad (4.8)$$

where in each subplane a fictitious inductance is defined as:

$$\begin{cases} \alpha\beta : & L_{\alpha\beta} = L_{ls} + L_m^{(1)} \\ xy1 : & L_1 = L_{ls} + L_m^{(11)}; & L_{1'} = L_m^{(7)} \\ xy2 : & L_2 = L_{ls} + L_m^{(13)}; & L_{2'} = L_m^{(5)} \\ xy3 : & L_3 = L_{ls} + L_m^{(3)} \\ 0 : & L_9 = L_{ls} + L_m^{(9)} \end{cases} \quad (4.9)$$

where  $L_{ls}$  stands for stator leakage inductance and  $L_m^{(h)}$  stands for mutual inductance due to  $h$ -th spatial harmonic.

About the back-*EMF* in the machine with non-sinusoidal winding, which is the time derivative of the flux produced by permanent magnets, is defined as:

$$[e_{PM,vsd}] = \begin{bmatrix} -\lambda_{PM1} \cdot \omega \cdot \sin(\theta) \\ \lambda_{PM1} \cdot \omega \cdot \cos(\theta) \\ \omega \cdot (7 \cdot \lambda_{PM7} \cdot \sin(7 \cdot \theta) - 11 \cdot \lambda_{PM11} \cdot \sin(11 \cdot \theta)) \\ \omega \cdot (7 \cdot \lambda_{PM7} \cdot \cos(7 \cdot \theta) + 11 \cdot \lambda_{PM11} \cdot \cos(11 \cdot \theta)) \\ \omega \cdot (-5 \cdot \lambda_{PM5} \cdot \sin(5 \cdot \theta) + 13 \cdot \lambda_{PM13} \cdot \sin(13 \cdot \theta)) \\ \omega \cdot (-5 \cdot \lambda_{PM5} \cdot \cos(5 \cdot \theta) - 13 \cdot \lambda_{PM13} \cdot \cos(13 \cdot \theta)) \\ 3 \cdot \omega \cdot \lambda_{PM3} \cdot \sin(3 \cdot \theta) \\ -3 \cdot \omega \cdot \lambda_{PM3} \cdot \cos(3 \cdot \theta) \\ 9 \cdot \omega \cdot \lambda_{PM9} \cdot \sin(9 \cdot \theta) \end{bmatrix} \begin{matrix} \alpha \\ \beta \\ x_1 \\ y_1 \\ x_2 \\ y_2 \\ x_3 \\ y_3 \\ 0 \end{matrix} \quad (4.10)$$

The waveforms of modelled back-electromotive force in vector space decomposition are shown in Figs. 4.5 - 4.8 obtained in *Simulink* environment at 1500 *rpm*. The simulation results confirm the model presented in Eq. (4.10): in Fig. 4.5 only the fundamental harmonic is present; in Fig. 4.6 the 7<sup>th</sup> and 11<sup>th</sup> harmonics are present; in Fig. 4.7 the 5<sup>th</sup> and 13<sup>th</sup> harmonics are present; finally Fig. 4.8 only the 3<sup>th</sup> harmonic is present.

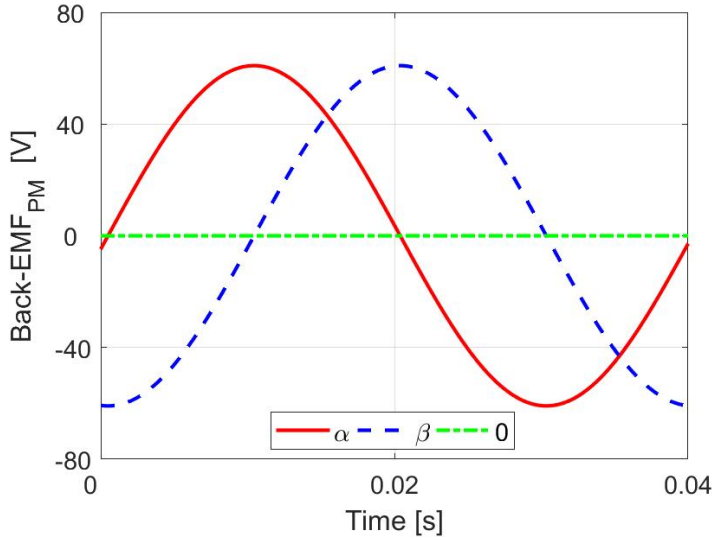
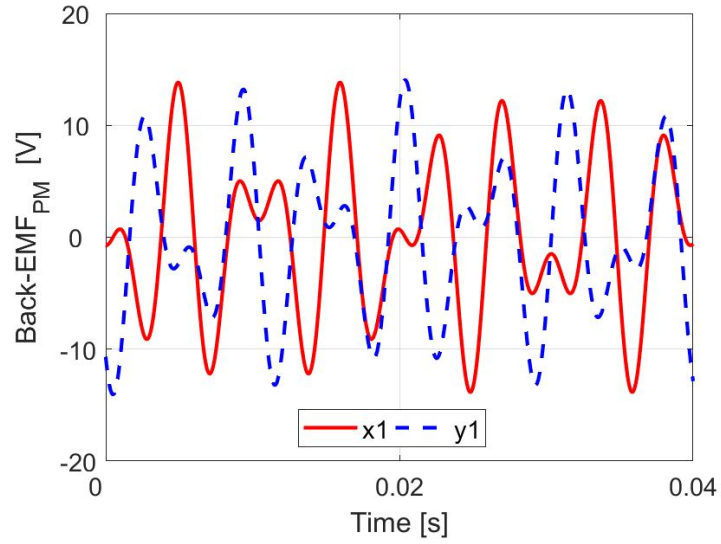
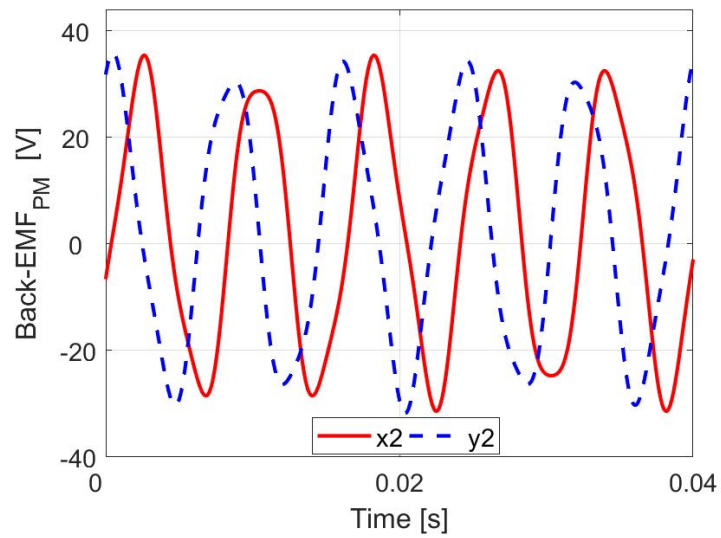
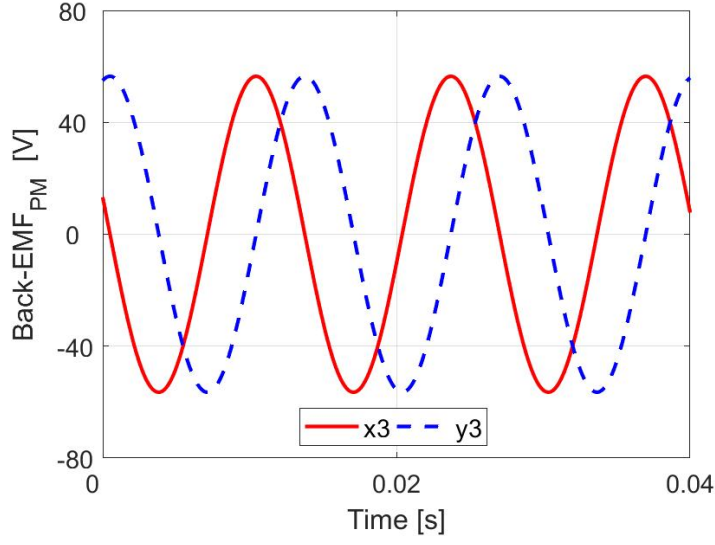


Figure 4.5: The back-*EMF* in  $(\alpha, \beta)$  subplane and zero-sequence component.

Figure 4.6: The back- $EMF$  in  $(x, y)1$  subplane.Figure 4.7: The back- $EMF$  in  $(x, y)2$  subplane.


 Figure 4.8: The back-EMF in  $(x, y)_3$  subplane.

Finally, the machine model in matrix form can be written as:

$$\left\{ \begin{array}{l} [v_{\alpha\beta}] = R_s \cdot [i_{\alpha\beta}] + L_{\alpha\beta} \cdot \frac{d[i_{\alpha\beta}]}{dt} + [e_{PM,\alpha\beta}] \\ [v_{xy_1}] = R_s \cdot [i_{xy_1}] + [L_{11'}] \cdot \frac{d[i_{xy_1}]}{dt} + [e_{PM,xy_1}] \\ [v_{xy_2}] = R_s \cdot [i_{xy_2}] + [L_{22'}] \cdot \frac{d[i_{xy_2}]}{dt} + [e_{PM,xy_2}] \\ [v_{xy_3}] = R_s \cdot [i_{xy_3}] + L_3 \cdot \frac{d[i_{xy_3}]}{dt} + [e_{PM,xy_3}] \\ v_0 = R_s \cdot i_0 + L_9 \cdot \frac{di_0}{dt} + e_{PM,0} \end{array} \right. \quad (4.11)$$

where the matrix inductance  $L_{11'}$  and  $L_{22'}$  are defined as:

$$L_{11'} = \begin{bmatrix} L_1 + L_{1'} & 0 \\ 0 & L_1 - L_{1'} \end{bmatrix} \quad (4.12)$$

$$L_{22'} = \begin{bmatrix} L_2 + L_{2'} & 0 \\ 0 & L_2 - L_{2'} \end{bmatrix} \quad (4.13)$$

Since *VSD* transformation produces multiple complex subplanes, instead of representation in matrix form, it is possible to express model in complex form. The relationship between the matrix form and complex form is:

$$\left\{ \begin{array}{l} \underline{f}_{\alpha\beta} = [1 \quad j] \cdot \begin{bmatrix} f_{\alpha} \\ f_{\beta} \end{bmatrix} \\ \underline{f}_{xyi} = [1 \quad j] \cdot \begin{bmatrix} f_{xi} \\ f_{yi} \end{bmatrix}, \quad i = 1, 2, 3 \end{array} \right. \quad (4.14)$$

where  $\underline{f}$  stands for a generic variable vector.

By replacing Eq. (4.14) in Eq. (4.11) the following model is carried out:

$$\left\{ \begin{array}{l} \underline{v}_{\alpha\beta} = R_s \cdot \underline{i}_{\alpha\beta} + L_{\alpha\beta} \cdot \frac{d\underline{i}_{\alpha\beta}}{dt} + j \cdot \omega \cdot \lambda_{PM1} \cdot e^{j \cdot \theta} \\ \underline{v}_{xy1} = R_s \cdot \underline{i}_{xy1} + L_1 \cdot \frac{d\underline{i}_{xy1}}{dt} + L_{1'} \cdot \frac{d\bar{\underline{i}}_{xy1}}{dt} + j \cdot 7 \cdot \omega \cdot \lambda_{PM7} \cdot e^{-j \cdot 7 \cdot \theta} + \\ \quad + j \cdot 11 \cdot \omega \cdot \lambda_{PM11} \cdot e^{j \cdot 11 \cdot \theta} \\ \underline{v}_{xy2} = R_s \cdot \underline{i}_{xy2} + L_2 \cdot \frac{d\underline{i}_{xy2}}{dt} + L_{2'} \cdot \frac{d\bar{\underline{i}}_{xy2}}{dt} - j \cdot 5 \omega \cdot \lambda_{PM5} \cdot e^{-j \cdot 5 \cdot \theta} + \\ \quad - j \cdot 13 \cdot \omega \cdot \lambda_{PM13} \cdot e^{j \cdot 13 \cdot \theta} \\ \underline{v}_{xy3} = R_s \cdot \underline{i}_{xy3} + L_3 \cdot \frac{d\underline{i}_{xy3}}{dt} - j \cdot 3 \cdot \omega \cdot \lambda_{PM3} \cdot e^{j \cdot 3 \cdot \theta} \\ \underline{v}_0 = R_s \cdot i_0 + L_{ls} \cdot \frac{di_0}{dt} + 9 \cdot \omega \cdot \lambda_{PM9} \cdot \sin(9 \cdot \theta) \end{array} \right. \quad (4.15)$$

Equivalent circuit for  $(\alpha, \beta)$ ,  $(x, y)_i$  subplanes and zero-sequence are shown in Fig. 4.9. If the subplane  $i$  ( $i=1, 2, 3$ ), shown in Fig. 4.9 (b), is containing more than one harmonic, the equivalent mutual inductance  $L_{eq}^{(h)}$  stands for the sum of individual magnetizing harmonic. About the voltage generator (representative of back-*EMF*) stands for the sum of individual back-*EMF* contribution. Finally, in Fig. 4.9 (c) the zero-sequence circuit is shown, where the open circuit stands to highlight that the zero-sequence current cannot to flow in stator windings due to the neutral connection.

By analysing the final equations and produced equivalent circuits, it is noted that electromechanical energy conversion is not taking place only in the  $(\alpha, \beta)$  subplane due to the specific back-*EMF* distribution. Following from stated, the  $(x, y)$

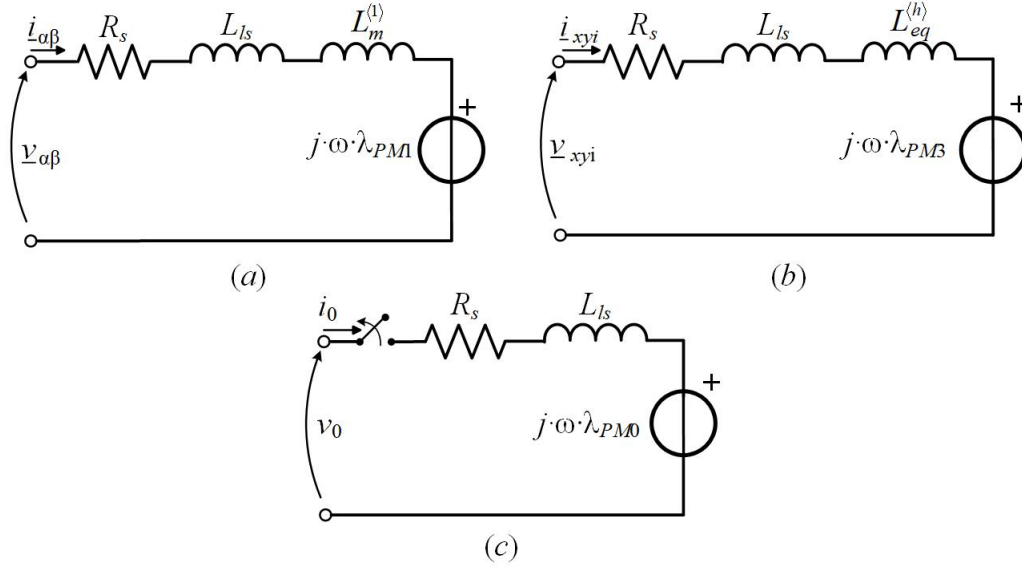


Figure 4.9: Equivalent circuit of non-sinusoidal machine: (a) -  $(\alpha, \beta)$ ; (b) -  $(x, y)i$  ( $i = 1, 2, 3$ ) subplanes; (c) - zero-sequence component.

subplanes can be used to achieve the torque enhancement or for additional purposes. However, additional controllers in  $(x, y)$  subplane can be employed to utilise additional degree of freedom for multiphase machine specific applications, such as fault tolerance, power sharing or low order harmonic elimination. In fundamental subplane the machine can be controlled in the same well-know way as the 3-phase machine. Instead each  $(x, y)$  subplane can be independently controlled without disturbing the other subplanes.

To complete the machine model, the electromagnetic torque equation in  $VSD$  variables must be computed. Starting from the equation in phase variable domain and for convenience below is reported:

$$T_{em} = P \cdot [i_{abc9}]^T \cdot \frac{d[\lambda_{PM,abc9}]}{d\theta} \quad (4.16)$$

By expressing the phase domain variables as function of  $VSD$  ones, the following is obtained:

$$\begin{aligned} T_{em} &= P \cdot \left[ [VSD]^{-1} \cdot [i_{vsd}] \right]^T \cdot \frac{d}{d\theta} \left( [VSD]^{-1} [\lambda_{PM,vsd}] \right) = \\ &= P \cdot [i_{vsd}]^T \cdot \left( [VSD]^{-1} \right)^T \cdot [VSD]^{-1} \cdot \frac{d[\lambda_{PM,vsd}]}{d\theta} \end{aligned} \quad (4.17)$$

where:

$$\left([VSD]^{-1}\right)^T \cdot [VSD]^{-1} = \frac{9}{2} \cdot [Id] \quad (4.18)$$

By replacing the Eq. (4.18) into Eq. (4.17) the carried out equation is:

$$\begin{aligned} T_{em} &= \frac{9}{2} \cdot P \cdot [i_{vsd}]^T \cdot \frac{d[\lambda_{PM,vsd}]}{d\theta} = \\ &= \frac{9}{2} \cdot P \cdot \left( t^{(1)} + t^{(3)} + t^{(5)} + t^{(7)} + t^{(9)} + t^{(11)} + t^{(13)} \right) \end{aligned} \quad (4.19)$$

where the single harmonic contributions are computed as follows:

$$t^{(1)} = \lambda_{PM1} \cdot (-i_\alpha \cdot \sin(\theta) + i_\beta \cdot \cos(\theta)) \quad (4.20)$$

$$t^{(3)} = 3 \cdot \lambda_{PM3} \cdot (i_{x3} \cdot \sin(3 \cdot \theta) - i_{y3} \cdot \cos(3 \cdot \theta)) \quad (4.21)$$

$$t^{(5)} = -5 \cdot \lambda_{PM5} \cdot (i_{x2} \cdot \sin(5 \cdot \theta) + i_{y2} \cdot \cos(5 \cdot \theta)) \quad (4.22)$$

$$t^{(7)} = 7 \cdot \lambda_{PM7} \cdot (i_{x1} \cdot \sin(7 \cdot \theta) + i_{y1} \cdot \cos(7 \cdot \theta)) \quad (4.23)$$

$$t^{(9)} = 9 \cdot \lambda_{PM9} \cdot i_0 \cdot \sin(9 \cdot \theta) \quad (4.24)$$

$$t^{(11)} = 11 \cdot \lambda_{PM11} \cdot (-i_{x1} \cdot \sin(11 \cdot \theta) + i_{y1} \cdot \cos(11 \cdot \theta)) \quad (4.25)$$

$$t^{(13)} = 13 \cdot \lambda_{PM13} \cdot (i_{x2} \cdot \sin(13 \cdot \theta) - i_{y2} \cdot \cos(13 \cdot \theta)) \quad (4.26)$$

### 4.2.3 Harmonic Model in Phase Variable Domain

The fictitious harmonic model in  $VSD$  variables can be evaluated in phase variable domain. Compared to the model presented in Chapter 6.24, the inductance matrix in phase variable domain is computed starting from the one defined in Eq. (4.8). The inductance matrix can be written as the sum of all harmonic contributions. To explain the idea, consider Eq. (4.27):

$$[L_{ss,vsd}] = [L_{ls}] + [L_m^{(1)}] + [L_m^{(3)}] + [L_m^{(5)}] + [L_m^{(7)}] + [L_m^{(9)}] + [L_m^{(11)}] + [L_m^{(13)}] \quad (4.27)$$

where matrix for each harmonic is defined as (Eqs. (4.28) - (4.35)):

$$[L_{ls}] = \begin{bmatrix} L_{ls} & 0 & 0 & 0 & 0 & 0 & 0 & 0 & 0 \\ 0 & L_{ls} & 0 & 0 & 0 & 0 & 0 & 0 & 0 \\ 0 & 0 & L_{ls} & 0 & 0 & 0 & 0 & 0 & 0 \\ 0 & 0 & 0 & L_{ls} & 0 & 0 & 0 & 0 & 0 \\ 0 & 0 & 0 & 0 & L_{ls} & 0 & 0 & 0 & 0 \\ 0 & 0 & 0 & 0 & 0 & L_{ls} & 0 & 0 & 0 \\ 0 & 0 & 0 & 0 & 0 & 0 & L_{ls} & 0 & 0 \\ 0 & 0 & 0 & 0 & 0 & 0 & 0 & L_{ls} & 0 \\ 0 & 0 & 0 & 0 & 0 & 0 & 0 & 0 & L_{ls} \end{bmatrix} \quad (4.28)$$

$$[L_m^{(1)}] = \begin{bmatrix} L_m^{(1)} & 0 & 0 & 0 & 0 & 0 & 0 & 0 & 0 \\ 0 & L_m^{(1)} & 0 & 0 & 0 & 0 & 0 & 0 & 0 \\ 0 & 0 & 0 & 0 & 0 & 0 & 0 & 0 & 0 \\ 0 & 0 & 0 & 0 & 0 & 0 & 0 & 0 & 0 \\ 0 & 0 & 0 & 0 & 0 & 0 & 0 & 0 & 0 \\ 0 & 0 & 0 & 0 & 0 & 0 & 0 & 0 & 0 \\ 0 & 0 & 0 & 0 & 0 & 0 & 0 & 0 & 0 \\ 0 & 0 & 0 & 0 & 0 & 0 & 0 & 0 & 0 \\ 0 & 0 & 0 & 0 & 0 & 0 & 0 & 0 & 0 \end{bmatrix} \quad (4.29)$$

$$[L_m^{(3)}] = \begin{bmatrix} 0 & 0 & 0 & 0 & 0 & 0 & 0 & 0 & 0 \\ 0 & 0 & 0 & 0 & 0 & 0 & 0 & 0 & 0 \\ 0 & 0 & 0 & 0 & 0 & 0 & 0 & 0 & 0 \\ 0 & 0 & 0 & 0 & 0 & 0 & 0 & 0 & 0 \\ 0 & 0 & 0 & 0 & 0 & 0 & 0 & 0 & 0 \\ 0 & 0 & 0 & 0 & 0 & 0 & 0 & 0 & 0 \\ 0 & 0 & 0 & 0 & 0 & 0 & L_m^{(3)} & 0 & 0 \\ 0 & 0 & 0 & 0 & 0 & 0 & 0 & L_m^{(3)} & 0 \\ 0 & 0 & 0 & 0 & 0 & 0 & 0 & 0 & 0 \end{bmatrix} \quad (4.30)$$

$$[L_m^{(5)}] = \begin{bmatrix} 0 & 0 & 0 & 0 & 0 & 0 & 0 & 0 & 0 \\ 0 & 0 & 0 & 0 & 0 & 0 & 0 & 0 & 0 \\ 0 & 0 & 0 & 0 & 0 & 0 & 0 & 0 & 0 \\ 0 & 0 & 0 & 0 & 0 & 0 & 0 & 0 & 0 \\ 0 & 0 & 0 & 0 & L_m^{(5)} & 0 & 0 & 0 & 0 \\ 0 & 0 & 0 & 0 & 0 & -L_m^{(5)} & 0 & 0 & 0 \\ 0 & 0 & 0 & 0 & 0 & 0 & 0 & 0 & 0 \\ 0 & 0 & 0 & 0 & 0 & 0 & 0 & 0 & 0 \\ 0 & 0 & 0 & 0 & 0 & 0 & 0 & 0 & 0 \end{bmatrix} \quad (4.31)$$

$$[L_m^{(7)}] = \begin{bmatrix} 0 & 0 & 0 & 0 & 0 & 0 & 0 & 0 & 0 \\ 0 & 0 & 0 & 0 & 0 & 0 & 0 & 0 & 0 \\ 0 & 0 & L_m^{(7)} & 0 & 0 & 0 & 0 & 0 & 0 \\ 0 & 0 & 0 & -L_m^{(7)} & 0 & 0 & 0 & 0 & 0 \\ 0 & 0 & 0 & 0 & 0 & 0 & 0 & 0 & 0 \\ 0 & 0 & 0 & 0 & 0 & 0 & 0 & 0 & 0 \\ 0 & 0 & 0 & 0 & 0 & 0 & 0 & 0 & 0 \\ 0 & 0 & 0 & 0 & 0 & 0 & 0 & 0 & 0 \\ 0 & 0 & 0 & 0 & 0 & 0 & 0 & 0 & 0 \end{bmatrix} \quad (4.32)$$

$$[L_m^{(9)}] = \begin{bmatrix} 0 & 0 & 0 & 0 & 0 & 0 & 0 & 0 & 0 \\ 0 & 0 & 0 & 0 & 0 & 0 & 0 & 0 & 0 \\ 0 & 0 & 0 & 0 & 0 & 0 & 0 & 0 & 0 \\ 0 & 0 & 0 & 0 & 0 & 0 & 0 & 0 & 0 \\ 0 & 0 & 0 & 0 & 0 & 0 & 0 & 0 & 0 \\ 0 & 0 & 0 & 0 & 0 & 0 & 0 & 0 & 0 \\ 0 & 0 & 0 & 0 & 0 & 0 & 0 & 0 & 0 \\ 0 & 0 & 0 & 0 & 0 & 0 & 0 & 0 & 0 \\ 0 & 0 & 0 & 0 & 0 & 0 & 0 & 0 & L_m^{(9)} \end{bmatrix} \quad (4.33)$$

$$[L_m^{(11)}] = \begin{bmatrix} 0 & 0 & 0 & 0 & 0 & 0 & 0 & 0 & 0 \\ 0 & 0 & 0 & 0 & 0 & 0 & 0 & 0 & 0 \\ 0 & 0 & L_m^{(11)} & 0 & 0 & 0 & 0 & 0 & 0 \\ 0 & 0 & 0 & L_m^{(11)} & 0 & 0 & 0 & 0 & 0 \\ 0 & 0 & 0 & 0 & 0 & 0 & 0 & 0 & 0 \\ 0 & 0 & 0 & 0 & 0 & 0 & 0 & 0 & 0 \\ 0 & 0 & 0 & 0 & 0 & 0 & 0 & 0 & 0 \\ 0 & 0 & 0 & 0 & 0 & 0 & 0 & 0 & 0 \\ 0 & 0 & 0 & 0 & 0 & 0 & 0 & 0 & 0 \end{bmatrix} \quad (4.34)$$

$$[L_m^{(13)}] = \begin{bmatrix} 0 & 0 & 0 & 0 & 0 & 0 & 0 & 0 & 0 \\ 0 & 0 & 0 & 0 & 0 & 0 & 0 & 0 & 0 \\ 0 & 0 & 0 & 0 & 0 & 0 & 0 & 0 & 0 \\ 0 & 0 & 0 & 0 & 0 & 0 & 0 & 0 & 0 \\ 0 & 0 & 0 & 0 & L_m^{(13)} & 0 & 0 & 0 & 0 \\ 0 & 0 & 0 & 0 & 0 & L_m^{(13)} & 0 & 0 & 0 \\ 0 & 0 & 0 & 0 & 0 & 0 & 0 & 0 & 0 \\ 0 & 0 & 0 & 0 & 0 & 0 & 0 & 0 & 0 \\ 0 & 0 & 0 & 0 & 0 & 0 & 0 & 0 & 0 \end{bmatrix} \quad (4.35)$$

Now, the matrix in phase variable domain related to stator leakage inductance is computed as:

$$\begin{aligned} [L_{ls}] &= [VSD]^{-1} \cdot [L_{ls}] \cdot [VSD] = \\ &= L_{ls} \cdot [VSD]^{-1} \cdot [VSD] = L_{ls} \cdot [Id]_{9 \times 9} \end{aligned} \quad (4.36)$$

About the matrix in phase variable domain related to  $h^{th}$  spatial harmonic, this is computed as:

$$[L_{abs9}^{(h)}] = [VSD]^{-1} \cdot [L_m^{(h)}] \cdot [VSD], \quad h = 1, \dots, 13, h \neq 2i, i \in \mathbb{N} \quad (4.37)$$

The application of  $VSD$  matrix and its inverse leads to the following rows of the matrices, where the operators  $c$  and  $s$  stand for cosine and sine, respectively.

About the magnetizing inductance related to 1<sup>st</sup> harmonic:

$$[L_m^{(1)}] = \frac{2}{9} L_m^{(1)} \dots$$

$$\dots \quad 1: \begin{bmatrix} 1 \\ c(\alpha) \\ s\left(\frac{\alpha}{4}\right) \\ -\frac{1}{2} \\ -c\left(\frac{\alpha}{2}\right) \\ -c\left(\frac{\alpha}{2}\right) \\ -\frac{1}{2} \\ s\left(\frac{\alpha}{4}\right) \\ c(\alpha) \end{bmatrix}^T, \quad 2: \begin{bmatrix} c(\alpha) \\ 1 \\ c(\alpha) \\ -\frac{1}{2}(-c(\alpha) + \sqrt{3}s(\alpha)) \\ -\frac{1}{2} \\ -c\left(\frac{\alpha}{2}\right) \\ -\frac{1}{2}(c(\alpha) + \sqrt{3}s(\alpha)) \\ -\frac{1}{2} \\ s\left(\frac{\alpha}{4}\right) \end{bmatrix}^T, \quad 3: \begin{bmatrix} s\left(\frac{\alpha}{4}\right) \\ c(\alpha) \\ 1 \\ \frac{1}{2}\left(\sqrt{3}c\left(\frac{\alpha}{4}\right) - s\left(\frac{\alpha}{4}\right)\right) \\ s\left(\frac{\alpha}{4}\right) \\ -\frac{1}{2} \\ -\frac{1}{2}\left(\sqrt{3}c\left(\frac{\alpha}{4}\right) + s\left(\frac{\alpha}{4}\right)\right) \\ c\left(\frac{\alpha}{2}\right) \\ -\frac{1}{2} \end{bmatrix}^T \quad (4.38)$$

$$4: \begin{bmatrix} -\frac{1}{2} \\ -\frac{1}{2}(-c(\alpha) + \sqrt{3}s(\alpha)) \\ -\frac{1}{2}\left(\sqrt{3}c\left(\frac{\alpha}{4}\right) - s\left(\frac{\alpha}{4}\right)\right) \\ -1 \\ -\frac{1}{2}\left(c\left(\frac{\alpha}{2}\right) + \sqrt{3}s\left(\frac{\alpha}{2}\right)\right) \\ -\frac{1}{2}\left(c\left(\frac{\alpha}{2}\right) - \sqrt{3}s\left(\frac{\alpha}{2}\right)\right) \\ -\frac{1}{2} \\ -\frac{1}{2}\left(\sqrt{3}c\left(\frac{\alpha}{4}\right) + s\left(\frac{\alpha}{4}\right)\right) \\ -\frac{1}{2}(c(\alpha) + s(\alpha)) \end{bmatrix}^T, \quad 5: \begin{bmatrix} c(\alpha) \\ -\frac{1}{2} \\ s\left(\frac{\alpha}{4}\right) \\ -\frac{1}{2}\left(c\left(\frac{\alpha}{2}\right) + \sqrt{3}s\left(\frac{\alpha}{2}\right)\right) \\ 1 \\ c(\alpha) \\ \frac{1}{2}\left(c\left(\frac{\alpha}{2}\right) - \sqrt{3}s\left(\frac{\alpha}{2}\right)\right) \\ -\frac{1}{2} \\ c\left(\frac{\alpha}{2}\right) \end{bmatrix}^T, \quad 6: \begin{bmatrix} -c\left(\frac{\alpha}{2}\right) \\ -c\left(\frac{\alpha}{2}\right) \\ -\frac{1}{2} \\ -\frac{1}{2}\left(c\left(\frac{\alpha}{2}\right) - \sqrt{3}s\left(\frac{\alpha}{2}\right)\right) \\ c(\alpha) \\ 1 \\ -\frac{1}{2}\left(c\left(\frac{\alpha}{2}\right) + \sqrt{3}s\left(\frac{\alpha}{2}\right)\right) \\ -\frac{1}{2}\left(c\left(\frac{\alpha}{2}\right) - \sqrt{3}s\left(\frac{\alpha}{2}\right)\right) \\ -\frac{1}{2} \end{bmatrix}^T \quad (4.39)$$

$$\begin{aligned}
 7: & \begin{bmatrix} -\frac{1}{2} \\ -\frac{1}{2}(c(\alpha) + \sqrt{3}s(\alpha)) \\ -\frac{1}{2}\left(c\left(\frac{\alpha}{4}\right) + s\left(\frac{\alpha}{4}\right)\right) \\ -\frac{1}{2} \\ \frac{1}{2}\left(c\left(\frac{\alpha}{2}\right) - \sqrt{3}s\left(\frac{\alpha}{2}\right)\right) \\ \frac{1}{2}\left(c\left(\frac{\alpha}{2}\right) + \sqrt{3}s\left(\frac{\alpha}{2}\right)\right) \\ 1 \\ \frac{1}{2}\left(\sqrt{3}c\left(\frac{\alpha}{4}\right) - s\left(\frac{\alpha}{4}\right)\right) \\ \frac{1}{2}(-c(\alpha) + \sqrt{3}s(\alpha)) \end{bmatrix}^T, & \quad 8: \begin{bmatrix} s\left(\frac{\alpha}{4}\right) \\ -\frac{1}{2} \\ c\left(\frac{\alpha}{2}\right) \\ -\frac{1}{2}\left(\sqrt{3}c\left(\frac{\alpha}{4}\right) + s\left(\frac{\alpha}{4}\right)\right) \\ -\frac{1}{2} \\ s\left(\frac{\alpha}{2}\right) \\ -\frac{1}{2}\left(\sqrt{3}c\left(\frac{\alpha}{2}\right) - s\left(\frac{\alpha}{2}\right)\right) \\ 1 \\ c(\alpha) \end{bmatrix}^T, & \quad 9: \begin{bmatrix} c(\alpha) \\ s\left(\frac{\alpha}{2}\right) \\ -\frac{1}{2} \\ -\frac{1}{2}(c(\alpha) + \sqrt{3}s(\alpha)) \\ -c\left(\frac{\alpha}{2}\right) \\ -\frac{1}{2} \\ \frac{1}{2}(-c(\alpha) + \sqrt{3}s(\alpha)) \\ c(\alpha) \\ 1 \end{bmatrix}^T
 \end{aligned} \tag{4.40}$$

About the magnetizing inductance related to 3<sup>th</sup> harmonic:

$$[L_{abs9}^{(3)}] = \frac{2}{9} L_m^{(3)} \cdot \dots$$

$$\begin{aligned}
 \dots & \quad 1: \begin{bmatrix} 1 \\ -\frac{1}{2} \\ -\frac{1}{2} \\ 1 \\ -\frac{1}{2} \\ -\frac{1}{2} \\ 1 \\ -\frac{1}{2} \\ -\frac{1}{2} \end{bmatrix}^T, & \quad 2: \begin{bmatrix} -\frac{1}{2} \\ 1 \\ -\frac{1}{2} \\ -\frac{1}{2} \\ 1 \\ -\frac{1}{2} \\ 1 \\ -\frac{1}{2} \\ -\frac{1}{2} \end{bmatrix}^T, & \quad 3: \begin{bmatrix} -\frac{1}{2} \\ -\frac{1}{2} \\ 1 \\ -\frac{1}{2} \\ -\frac{1}{2} \\ 1 \\ -\frac{1}{2} \\ -\frac{1}{2} \\ 1 \end{bmatrix}^T, & \quad 4: \begin{bmatrix} 1 \\ -\frac{1}{2} \\ -\frac{1}{2} \\ 1 \\ -\frac{1}{2} \\ 1 \\ -\frac{1}{2} \\ -\frac{1}{2} \\ 1 \end{bmatrix}^T, & \quad 5: \begin{bmatrix} -\frac{1}{2} \\ 1 \\ -\frac{1}{2} \\ -\frac{1}{2} \\ 1 \\ -\frac{1}{2} \\ 1 \\ -\frac{1}{2} \\ -\frac{1}{2} \end{bmatrix}^T, & \quad 6: \begin{bmatrix} -\frac{1}{2} \\ -\frac{1}{2} \\ 1 \\ -\frac{1}{2} \\ -\frac{1}{2} \\ 1 \\ -\frac{1}{2} \\ -\frac{1}{2} \\ 1 \end{bmatrix}^T, & \quad 7: \begin{bmatrix} 1 \\ -\frac{1}{2} \\ -\frac{1}{2} \\ 1 \\ -\frac{1}{2} \\ 1 \\ -\frac{1}{2} \\ -\frac{1}{2} \\ 1 \end{bmatrix}^T, & \quad 8: \begin{bmatrix} -\frac{1}{2} \\ 1 \\ -\frac{1}{2} \\ -\frac{1}{2} \\ 1 \\ -\frac{1}{2} \\ 1 \\ -\frac{1}{2} \\ -\frac{1}{2} \end{bmatrix}^T, & \quad 9: \begin{bmatrix} -\frac{1}{2} \\ -\frac{1}{2} \\ 1 \\ -\frac{1}{2} \\ 1 \\ -\frac{1}{2} \\ 1 \\ -\frac{1}{2} \\ 1 \end{bmatrix}^T
 \end{aligned} \tag{4.41}$$

About the magnetizing inductance related to 5<sup>th</sup> harmonic:

$$[L_{abs9}^{(5)}] = \frac{2}{9} L_m^{(5)} \cdot \dots$$

$$\dots \quad 1: \begin{bmatrix} 1 \\ s\left(\frac{\alpha}{4}\right) \\ -c\left(\frac{\alpha}{2}\right) \\ -\frac{1}{2} \\ c(\alpha) \\ c(\alpha) \\ -\frac{1}{2} \\ -c\left(\frac{\alpha}{2}\right) \\ s\left(\frac{\alpha}{4}\right) \end{bmatrix}^T, \quad 2: \begin{bmatrix} s\left(\frac{\alpha}{4}\right) \\ -c\left(\frac{\alpha}{2}\right) \\ -\frac{1}{2} \\ \frac{1}{2}\left(\sqrt{3}c\left(\frac{\alpha}{4}\right) + s\left(\frac{\alpha}{4}\right)\right) \\ c(\alpha) \\ -\frac{1}{2} \\ -\frac{1}{2}\left(\sqrt{3}c\left(\frac{\alpha}{4}\right) + s\left(\frac{\alpha}{4}\right)\right) \\ s\left(\frac{\alpha}{4}\right) \\ 1 \end{bmatrix}^T, \quad 3: \begin{bmatrix} -c(\alpha) \\ -\frac{1}{2} \\ c(\alpha) \\ \frac{1}{2}\left(c\left(\frac{\alpha}{2}\right) - \sqrt{3}s\left(\frac{\alpha}{2}\right)\right) \\ -\frac{1}{2} \\ c\left(\frac{\alpha}{2}\right) \\ -\frac{1}{2}\left(\sqrt{3}c\left(\frac{\alpha}{2}\right) + s\left(\frac{\alpha}{2}\right)\right) \\ 1 \\ s\left(\frac{\alpha}{4}\right) \end{bmatrix}^T \quad (4.42)$$

$$4: \begin{bmatrix} -\frac{1}{2} \\ \frac{1}{2}\left(\sqrt{3}c\left(\frac{\alpha}{4}\right) - s\left(\frac{\alpha}{4}\right)\right) \\ \frac{1}{2}\left(c\left(\frac{\alpha}{2}\right) + \sqrt{3}s\left(\frac{\alpha}{2}\right)\right) \\ -\frac{1}{2} \\ -\frac{1}{2}(c(\alpha) + \sqrt{3}s(\alpha)) \\ \frac{1}{2}(-c(\alpha) + \sqrt{3}s(\alpha)) \\ 1 \\ \frac{1}{2}\left(c\left(\frac{\alpha}{2}\right) - \sqrt{3}s\left(\frac{\alpha}{2}\right)\right) \\ -\frac{1}{2}\left(c\left(\frac{\alpha}{4}\right) + \sqrt{3}s\left(\frac{\alpha}{4}\right)\right) \end{bmatrix}^T, \quad 5: \begin{bmatrix} c(\alpha) \\ c(\alpha) \\ -\frac{1}{2} \\ -\frac{1}{2}(c(\alpha) + \sqrt{3}s(\alpha)) \\ s\left(\frac{\alpha}{4}\right) \\ 1 \\ \frac{1}{2}(-c(\alpha) + \sqrt{3}s(\alpha)) \\ -c\left(\frac{\alpha}{2}\right) \\ -\frac{1}{2} \end{bmatrix}^T, \quad 6: \begin{bmatrix} c(\alpha) \\ -\frac{1}{2} \\ -c\left(\frac{\alpha}{2}\right) \\ \frac{1}{2}(-c(\alpha) + \sqrt{3}s(\alpha)) \\ 1 \\ s\left(\frac{\alpha}{4}\right) \\ -\frac{1}{2}(c(\alpha) + \sqrt{3}s(\alpha)) \\ -\frac{1}{2} \\ c(\alpha) \end{bmatrix}^T \quad (4.43)$$

$$\begin{aligned}
 7: & \begin{bmatrix} -\frac{1}{2} \\ -\frac{1}{2}\left(\sqrt{3}c\left(\frac{\alpha}{4}\right) + s\left(\frac{\alpha}{4}\right)\right) \\ -\frac{1}{2}\left(c\left(\frac{\alpha}{2}\right) - \sqrt{3}s\left(\frac{\alpha}{2}\right)\right) \\ 1 \\ \frac{1}{2}(-c(\alpha) + \sqrt{3}s(\alpha)) \\ -\frac{1}{2}(c(\alpha) + \sqrt{3}s(\alpha)) \\ -\frac{1}{2} \\ \frac{1}{2}\left(c\left(\frac{\alpha}{2}\right) + s\left(\frac{\alpha}{2}\right)\right) \\ \frac{1}{2}\left(\sqrt{3}c\left(\frac{\alpha}{4}\right) + s\left(\frac{\alpha}{4}\right)\right) \end{bmatrix}^T, & 8: \begin{bmatrix} c\left(\frac{\alpha}{2}\right) \\ s\left(\frac{\alpha}{4}\right) \\ 1 \\ \frac{1}{2}\left(c\left(\frac{\alpha}{2}\right) - \sqrt{3}s\left(\frac{\alpha}{2}\right)\right) \\ -c\left(\frac{\alpha}{2}\right) \\ -\frac{1}{2} \\ \frac{1}{2}\left(c\left(\frac{\alpha}{2}\right) + \sqrt{3}s\left(\frac{\alpha}{2}\right)\right) \\ c(\alpha) \\ -\frac{1}{2} \end{bmatrix}^T, & 9: \begin{bmatrix} s\left(\frac{\alpha}{4}\right) \\ 1 \\ s\left(\frac{\alpha}{4}\right) \\ -\frac{1}{2}\left(\sqrt{3}c\left(\frac{\alpha}{4}\right) + s\left(\frac{\alpha}{4}\right)\right) \\ -\frac{1}{2} \\ c(\alpha) \\ \frac{1}{2}\left(\sqrt{3}c\left(\frac{\alpha}{4}\right) - s\left(\frac{\alpha}{4}\right)\right) \\ -\frac{1}{2} \\ -c\left(\frac{\alpha}{2}\right) \end{bmatrix}^T
 \end{aligned} \tag{4.44}$$

About the magnetizing inductance related to 7<sup>th</sup> harmonic:

$$[L_{abs9}^{(7)}] = \frac{2}{9}L_m^{(7)} \cdot \dots$$

$$\begin{aligned}
 \dots & 1: \begin{bmatrix} 1 \\ s\left(\frac{\alpha}{4}\right) \\ -c\left(\frac{\alpha}{2}\right) \\ -\frac{1}{2} \\ c(\alpha) \\ c(\alpha) \\ -\frac{1}{2} \\ -c\left(\frac{\alpha}{2}\right) \\ s\left(\frac{\alpha}{4}\right) \end{bmatrix}^T, & 2: \begin{bmatrix} s\left(\frac{\alpha}{4}\right) \\ -c\left(\frac{\alpha}{2}\right) \\ -\frac{1}{2} \\ \frac{1}{2}\left(\sqrt{3}c\left(\frac{\alpha}{4}\right) - s\left(\frac{\alpha}{4}\right)\right) \\ c(\alpha) \\ -1 \\ -\frac{1}{2}\left(\sqrt{3}c\left(\frac{\alpha}{4}\right) + s\left(\frac{\alpha}{4}\right)\right) \\ s\left(\frac{\alpha}{4}\right) \\ 1 \end{bmatrix}^T, & 3: \begin{bmatrix} -c\left(\frac{\alpha}{2}\right) \\ -\frac{1}{2} \\ c(\alpha) \\ \frac{1}{2}\left(c\left(\frac{\alpha}{2}\right) + \sqrt{3}s\left(\frac{\alpha}{2}\right)\right) \\ -\frac{1}{2} \\ -c\left(\frac{\alpha}{2}\right) \\ \frac{1}{2}\left(c\left(\frac{\alpha}{2}\right) - \sqrt{3}s\left(\frac{\alpha}{2}\right)\right) \\ 1 \\ s\left(\frac{\alpha}{4}\right) \end{bmatrix}^T
 \end{aligned} \tag{4.45}$$

$$4 : \begin{bmatrix} -\frac{1}{2} \\ \frac{1}{2} \left( \sqrt{3}c\left(\frac{\alpha}{4}\right) - s\left(\frac{\alpha}{4}\right) \right) \\ \frac{1}{2} \left( c\left(\frac{\alpha}{2}\right) + \sqrt{3}s\left(\frac{\alpha}{2}\right) \right) \\ -\frac{1}{2} \\ -\frac{1}{2} (c(\alpha) + \sqrt{3}s(\alpha)) \\ \frac{1}{2} (c(\alpha) + \sqrt{3}s(\alpha)) \\ 1 \\ \frac{1}{2} \left( c\left(\frac{\alpha}{2}\right) + s\left(\frac{\alpha}{2}\right) \right) \\ -\frac{1}{2} \left( \sqrt{3}c\left(\frac{\alpha}{4}\right) + s\left(\frac{\alpha}{4}\right) \right) \end{bmatrix}^T, \quad 5 : \begin{bmatrix} c(\alpha) \\ c(\alpha) \\ -\frac{1}{2} \\ -\frac{1}{2} (c(\alpha) + \sqrt{3}s(\alpha)) \\ s\left(\frac{\alpha}{4}\right) \\ 1 \\ \frac{1}{2} (-c(\alpha) + \sqrt{3}s(\alpha)) \\ -c\left(\frac{\alpha}{2}\right) \\ -\frac{1}{2} \end{bmatrix}^T, \quad 6 : \begin{bmatrix} c(\alpha) \\ -\frac{1}{2} \\ -c\left(\frac{\alpha}{2}\right) \\ \frac{1}{2} (c(\alpha) + \sqrt{3}s(\alpha)) \\ 1 \\ s\left(\frac{\alpha}{4}\right) \\ -\frac{1}{2} (c(\alpha) + \sqrt{3}s(\alpha)) \\ -\frac{1}{2} \\ c(\alpha) \end{bmatrix}^T \quad (4.46)$$

$$7 : \begin{bmatrix} -\frac{1}{2} \\ -\frac{1}{2} \left( \sqrt{3}c\left(\frac{\alpha}{4}\right) + s\left(\frac{\alpha}{4}\right) \right) \\ \frac{1}{2} \left( c\left(\frac{\alpha}{2}\right) - \sqrt{3}s\left(\frac{\alpha}{2}\right) \right) \\ 1 \\ \frac{1}{2} (c(\alpha) + \sqrt{3}s(\alpha)) \\ \frac{1}{2} (c(\alpha) + \sqrt{3}s(\alpha)) \\ -\frac{1}{2} \\ \frac{1}{2} \left( c\left(\frac{\alpha}{2}\right) + s\left(\frac{\alpha}{2}\right) \right) \\ \frac{1}{2} \left( \sqrt{3}c\left(\frac{\alpha}{4}\right) + s\left(\frac{\alpha}{4}\right) \right) \end{bmatrix}^T, \quad 8 : \begin{bmatrix} c\left(\frac{\alpha}{2}\right) \\ s\left(\frac{\alpha}{4}\right) \\ 1 \\ \frac{1}{2} \left( c\left(\frac{\alpha}{2}\right) - \sqrt{3}s\left(\frac{\alpha}{2}\right) \right) \\ -c\left(\frac{\alpha}{2}\right) \\ -\frac{1}{2} \\ \frac{1}{2} \left( c\left(\frac{\alpha}{2}\right) + \sqrt{3}s\left(\frac{\alpha}{2}\right) \right) \\ c(\alpha) \\ \frac{1}{2} \end{bmatrix}^T, \quad 9 : \begin{bmatrix} s\left(\frac{\alpha}{4}\right) \\ 1 \\ s\left(\frac{\alpha}{4}\right) \\ -\frac{1}{2} \left( \sqrt{3}c\left(\frac{\alpha}{4}\right) + s\left(\frac{\alpha}{4}\right) \right) \\ -\frac{1}{2} \\ c(\alpha) \\ \frac{1}{2} \left( \sqrt{3}c\left(\frac{\alpha}{4}\right) - s\left(\frac{\alpha}{4}\right) \right) \\ -\frac{1}{2} \\ -c\left(\frac{\alpha}{2}\right) \end{bmatrix}^T \quad (4.47)$$

About the magnetizing inductance related to 9<sup>th</sup> harmonic:

$$[L_{abs9}^{(9)}] = \frac{2}{9} L_m^{(9)} \cdot \dots$$

$$\dots \quad 1: \begin{bmatrix} \frac{1}{2} \\ \frac{1}{2} \end{bmatrix}^T, \quad 2: \begin{bmatrix} \frac{1}{2} \\ \frac{1}{2} \end{bmatrix}^T, \quad 3: \begin{bmatrix} \frac{1}{2} \\ \frac{1}{2} \end{bmatrix}^T, \quad 4: \begin{bmatrix} \frac{1}{2} \\ \frac{1}{2} \end{bmatrix}^T, \quad 5: \begin{bmatrix} \frac{1}{2} \\ \frac{1}{2} \end{bmatrix}^T, \quad 6: \begin{bmatrix} \frac{1}{2} \\ \frac{1}{2} \end{bmatrix}^T, \quad 7: \begin{bmatrix} \frac{1}{2} \\ \frac{1}{2} \end{bmatrix}^T, \quad 8: \begin{bmatrix} \frac{1}{2} \\ \frac{1}{2} \end{bmatrix}^T, \quad 9: \begin{bmatrix} \frac{1}{2} \\ \frac{1}{2} \end{bmatrix}^T \quad (4.48)$$

About the magnetizing inductance related to 11<sup>th</sup> harmonic:

$$[L_{abs9}^{(11)}] = \frac{2}{9} L_m^{(11)} \cdot \dots$$

$$\dots \quad 1: \begin{bmatrix} 1 \\ s\left(\frac{\alpha}{4}\right) \\ -c\left(\frac{\alpha}{2}\right) \\ -\frac{1}{2} \\ c(\alpha) \\ c(\alpha) \\ -\frac{1}{2} \\ -c\left(\frac{\alpha}{2}\right) \\ s\left(\frac{\alpha}{4}\right) \end{bmatrix}^T, \quad 2: \begin{bmatrix} s\left(\frac{\alpha}{4}\right) \\ 1 \\ s\left(\frac{\alpha}{4}\right) \\ -\frac{1}{2}\left(\sqrt{3}c\left(\frac{\alpha}{4}\right) + s\left(\frac{\alpha}{4}\right)\right) \\ -\frac{1}{2} \\ c(\alpha) \\ \frac{1}{2}\left(\sqrt{3}c\left(\frac{\alpha}{4}\right) - s\left(\frac{\alpha}{4}\right)\right) \\ -\frac{1}{2} \\ -c\left(\frac{\alpha}{2}\right) \end{bmatrix}^T, \quad 3: \begin{bmatrix} -c\left(\frac{\alpha}{2}\right) \\ -s\left(\frac{\alpha}{4}\right) \\ 1 \\ \frac{1}{2}\left(c\left(\frac{\alpha}{2}\right) - \sqrt{3}s\left(\frac{\alpha}{2}\right)\right) \\ -c\left(\frac{\alpha}{2}\right) \\ -\frac{1}{2} \\ -\frac{1}{2}\left(c\left(\frac{\alpha}{2}\right) + \sqrt{3}s\left(\frac{\alpha}{2}\right)\right) \\ c(\alpha) \\ -\frac{1}{2} \end{bmatrix}^T \quad (4.49)$$

$$4 : \begin{bmatrix} -\frac{1}{2} \\ -\frac{1}{2} \left( \sqrt{3}c\left(\frac{\alpha}{4}\right) + s\left(\frac{\alpha}{4}\right) \right) \\ \frac{1}{2} \left( c\left(\frac{\alpha}{2}\right) - \sqrt{3}s\left(\frac{\alpha}{2}\right) \right) \\ 1 \\ \frac{1}{2} (-c(\alpha) + \sqrt{3}s(\alpha)) \\ -\frac{1}{2} (c(\alpha) + \sqrt{3}s(\alpha)) \\ -\frac{1}{2} \\ \frac{1}{2} \left( c\left(\frac{\alpha}{2}\right) + \sqrt{3}s\left(\frac{\alpha}{2}\right) \right) \\ \frac{1}{2} \left( \sqrt{3}c\left(\frac{\alpha}{4}\right) - s\left(\frac{\alpha}{4}\right) \right) \end{bmatrix}^T, \quad 5 : \begin{bmatrix} c(\alpha) \\ -\frac{1}{2} \\ -c(\alpha) \\ \frac{1}{2} (-c(\alpha) + \sqrt{3}s(\alpha)) \\ 1 \\ s\left(\frac{\alpha}{4}\right) \\ -\frac{1}{2} (c(\alpha) + \sqrt{3}s(\alpha)) \\ -\frac{1}{2} \\ c(\alpha) \end{bmatrix}^T, \quad 6 : \begin{bmatrix} c(\alpha) \\ c(\alpha) \\ -\frac{1}{2} \\ -\frac{1}{2} (c(\alpha) + \sqrt{3}s(\alpha)) \\ s\left(\frac{\alpha}{4}\right) \\ 1 \\ \frac{1}{2} (-c(\alpha) + \sqrt{3}s(\alpha)) \\ -c(\alpha) \\ -\frac{1}{2} \end{bmatrix}^T \quad (4.50)$$

$$7 : \begin{bmatrix} -\frac{1}{2} \\ \frac{1}{2} \left( \sqrt{3}c\left(\frac{\alpha}{4}\right) - s\left(\frac{\alpha}{4}\right) \right) \\ \frac{1}{2} \left( c\left(\frac{\alpha}{2}\right) - \sqrt{3}s\left(\frac{\alpha}{2}\right) \right) \\ -\frac{1}{2} \\ -\frac{1}{2} (c(\alpha) + \sqrt{3}s(\alpha)) \\ \frac{1}{2} (-c(\alpha) + \sqrt{3}s(\alpha)) \\ 1 \\ \frac{1}{2} \left( c\left(\frac{\alpha}{2}\right) - s\left(\frac{\alpha}{2}\right) \right) \\ -\frac{1}{2} \left( \sqrt{3}c\left(\frac{\alpha}{4}\right) + s\left(\frac{\alpha}{4}\right) \right) \end{bmatrix}^T, \quad 8 : \begin{bmatrix} -c\left(\frac{\alpha}{2}\right) \\ -\frac{1}{2} \\ c(\alpha) \\ \frac{1}{2} \left( c\left(\frac{\alpha}{2}\right) + \sqrt{3}s\left(\frac{\alpha}{2}\right) \right) \\ -\frac{1}{2} \\ -c\left(\frac{\alpha}{2}\right) \\ \frac{1}{2} \left( c\left(\frac{\alpha}{2}\right) - \sqrt{3}s\left(\frac{\alpha}{2}\right) \right) \\ 1 \\ s\left(\frac{\alpha}{4}\right) \end{bmatrix}^T, \quad 9 : \begin{bmatrix} s\left(\frac{\alpha}{4}\right) \\ -c\left(\frac{\alpha}{2}\right) \\ -\frac{1}{2} \\ \frac{1}{2} \left( \sqrt{3}c\left(\frac{\alpha}{4}\right) - s\left(\frac{\alpha}{4}\right) \right) \\ c(\alpha) \\ -\frac{1}{2} \\ -\frac{1}{2} \left( \sqrt{3}c\left(\frac{\alpha}{4}\right) + s\left(\frac{\alpha}{4}\right) \right) \\ s\left(\frac{\alpha}{4}\right) \\ 1 \end{bmatrix}^T \quad (4.51)$$

About the magnetizing inductance related to 13<sup>th</sup> harmonic:

$$[L_{abs9}^{(13)}] = \frac{2}{9} L_m^{(13)} \cdot \dots$$

$$\dots \quad 1: \begin{bmatrix} 1 \\ -c\left(\frac{\alpha}{2}\right) \\ c(\alpha) \\ -\frac{1}{2} \\ s\left(\frac{\alpha}{4}\right) \\ s\left(\frac{\alpha}{4}\right) \\ -\frac{1}{2} \\ c(\alpha) \\ c\left(\frac{\alpha}{2}\right) \end{bmatrix}^T, \quad 2: \begin{bmatrix} -c\left(\frac{\alpha}{2}\right) \\ 1 \\ -c\left(\frac{\alpha}{2}\right) \\ \frac{1}{2}\left(c\left(\frac{\alpha}{2}\right) + \sqrt{3}s\left(\frac{\alpha}{2}\right)\right) \\ -\frac{1}{2} \\ s\left(\frac{\alpha}{4}\right) \\ \frac{1}{2}\left(c\left(\frac{\alpha}{2}\right) - \sqrt{3}s\left(\frac{\alpha}{2}\right)\right) \\ -\frac{1}{2} \\ -c(\alpha) \end{bmatrix}^T, \quad 3: \begin{bmatrix} -c(\alpha) \\ -c(\alpha) \\ 1 \\ -\frac{1}{2}(c(\alpha) + \sqrt{3}s(\alpha)) \\ c(\alpha) \\ -\frac{1}{2} \\ \frac{1}{2}(-c(\alpha) + \sqrt{3}s(\alpha)) \\ s\left(\frac{\alpha}{4}\right) \\ -\frac{1}{2} \end{bmatrix}^T \quad (4.52)$$

$$4: \begin{bmatrix} -\frac{1}{2} \\ \frac{1}{2}\left(c\left(\frac{\alpha}{2}\right) + \sqrt{3}s\left(\frac{\alpha}{2}\right)\right) \\ -\frac{1}{2}(c(\alpha) + \sqrt{3}s(\alpha)) \\ 1 \\ -\frac{1}{2}\left(\sqrt{3}c\left(\frac{\alpha}{4}\right) + s\left(\frac{\alpha}{4}\right)\right) \\ \frac{1}{2}\left(\sqrt{3}c\left(\frac{\alpha}{4}\right) - s\left(\frac{\alpha}{4}\right)\right) \\ -\frac{1}{2} \\ \frac{1}{2}(-c(\alpha) + \sqrt{3}s(\alpha)) \\ \frac{1}{2}\left(\sqrt{3}c\left(\frac{\alpha}{2}\right) - s\left(\frac{\alpha}{2}\right)\right) \end{bmatrix}^T, \quad 5: \begin{bmatrix} s\left(\frac{\alpha}{4}\right) \\ -\frac{1}{2} \\ c(\alpha) \\ -\frac{1}{2}\left(\sqrt{3}c\left(\frac{\alpha}{4}\right) - s\left(\frac{\alpha}{4}\right)\right) \\ 1 \\ -c\left(\frac{\alpha}{2}\right) \\ \frac{1}{2}\left(\sqrt{3}c\left(\frac{\alpha}{4}\right) - s\left(\frac{\alpha}{4}\right)\right) \\ -\frac{1}{2} \\ s\left(\frac{\alpha}{4}\right) \end{bmatrix}^T, \quad 6: \begin{bmatrix} s\left(\frac{\alpha}{4}\right) \\ s\left(\frac{\alpha}{4}\right) \\ -\frac{1}{2} \\ \frac{1}{2}\left(-c\left(\frac{\alpha}{4}\right) + \sqrt{3}s\left(\frac{\alpha}{4}\right)\right) \\ c\left(\frac{\alpha}{2}\right) \\ \frac{1}{2} \\ -\frac{1}{2}\left(\sqrt{3}c\left(\frac{\alpha}{4}\right) + s\left(\frac{\alpha}{4}\right)\right) \\ c(\alpha) \\ -\frac{1}{2} \end{bmatrix}^T \quad (4.53)$$

$$7 : \begin{bmatrix} -\frac{1}{2} \\ \frac{1}{2} \left( c\left(\frac{\alpha}{2}\right) - \sqrt{3}s\left(\frac{\alpha}{2}\right) \right) \\ \frac{1}{2} (-c(\alpha) + \sqrt{3}s(\alpha)) \\ -\frac{1}{2} \\ -\frac{1}{2} \left( \sqrt{3}c\left(\frac{\alpha}{4}\right) - \sqrt{3}s\left(\frac{\alpha}{4}\right) \right) \\ -\frac{1}{2} \left( \sqrt{3}c\left(\frac{\alpha}{4}\right) + \sqrt{3}s\left(\frac{\alpha}{4}\right) \right) \\ 1 \\ \frac{1}{2} (c(\alpha) + \sqrt{3}s(\alpha)) \\ -\frac{1}{2} \left( \sqrt{3}c\left(\frac{\alpha}{2}\right) + s\left(\frac{\alpha}{2}\right) \right) \end{bmatrix}^T, \quad
 8 : \begin{bmatrix} c(\alpha) \\ -\frac{1}{2} \\ s\left(\frac{\alpha}{4}\right) \\ \frac{1}{2} (-c(\alpha) + \sqrt{3}s(\alpha)) \\ -\frac{1}{2} \\ c(\alpha) \\ -\frac{1}{2} (c(\alpha) + \sqrt{3}s(\alpha)) \\ 1 \\ -c\left(\frac{\alpha}{2}\right) \end{bmatrix}^T, \quad
 9 : \begin{bmatrix} c\left(\frac{\alpha}{2}\right) \\ c(\alpha) \\ -\frac{1}{2} \\ \frac{1}{2} \left( c\left(\frac{\alpha}{2}\right) - \sqrt{3}s\left(\frac{\alpha}{2}\right) \right) \\ s\left(\frac{\alpha}{4}\right) \\ -\frac{1}{2} \\ \frac{1}{2} \left( c\left(\frac{\alpha}{2}\right) + \sqrt{3}s\left(\frac{\alpha}{2}\right) \right) \\ -c\left(\frac{\alpha}{2}\right) \\ 1 \end{bmatrix}^T \quad (4.54)$$

The computed model, related to spatial harmonics in *VSD* variables and phase variable domain has been validated on real machine as shown in Chapter 6.32, Section 6.2, Subsection 6.2.3. The magnetizing inductance related to  $h^{th}$  harmonic in stator short-circuit and design approach configuration is evaluated, as explained below.

## 4.3 Current Harmonic Mapping

In this thesis the current harmonics are eliminated because the current components are losses producers losses. In Fig. 4.10, the procedure of harmonic mapping in  $(\alpha, \beta)$ ,  $(x, y)$  subplanes and zero-sequence is shown. Each harmonic is mapped only into a single subplane or zero-sequence and in the same subplane or zero-sequence than back-*EMF* harmonic. Following from stated, the current elimination is simplified by the use of vector proportional integral or proportional resonant controller.

The modelled current harmonics in the real machine are only the first 13 harmonics as the consequence of back-*EMF* harmonic spectrum. The current fundamental is mapped only in  $(\alpha, \beta)$  subplane and it is responsible of torque production due to the low order harmonic elimination in other subplanes.

### 4.3.1 Low Order Harmonics Elimination

#### Vector Proportional Integral

The method with harmonic elimination need to be designed to minimize the harmonic content in the stator currents. By adding the vector proportional integral, the unwanted current harmonics are suppressed, as shown below.

The employed *VPI*, shown in Fig. 4.11 [11], allows to eliminate the induced current harmonics in a generic subplane  $i$  ( $i=1, 2, 3$ ). It is implemented in  $(x, y)$  subplanes. The transfer function of the employed controller is defined as:

$$H_{VPI}(s) = \frac{s^2 \cdot k_{I,VPIh} + s \cdot k_{P,VPIh}}{s^2 + h^2 \cdot \omega_1^2} \quad (4.55)$$

where:

- $k_{P,VPIh}$  is the proportional value related to  $h^{th}$  harmonic,
- $k_{I,VPIh}$  is integral value related to  $h^{th}$  harmonic,
- $\omega_1$  is the fundamental component frequency (*rad/s*), which in steady-state condition is equal to the machine electrical speed and
- $h$  is the number of unwanted harmonic.

In Fig. 4.12 a simplified schematic of the *VPI* controller, voltage supply inverter and electrical machine are shown. The following analysis and design are performed in Laplace domain. The input to the *VPI* (green block) is the current error in

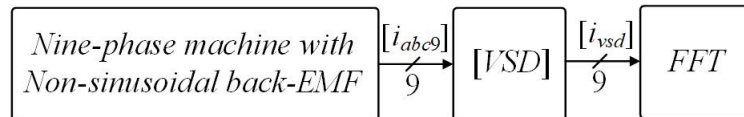


Figure 4.10: Schematic of harmonic mapping analysis.

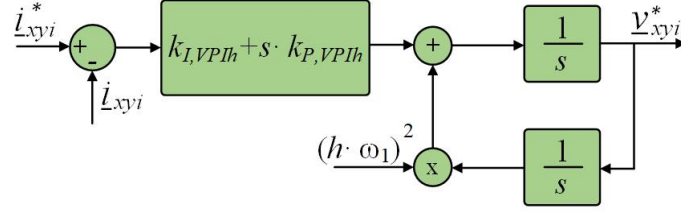


Figure 4.11: Schematic of the VPI transfer function.

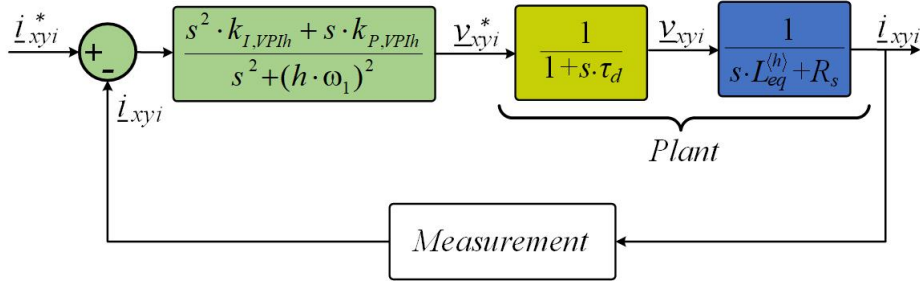


Figure 4.12: Schematic block of the harmonic current regulation loop.

a generic subplane  $(x, y)$ , computed as difference between zero reference value and its measurement feedback in *VSD* variables. However, the current measurement process is considered ideal, and, for this reason, the sensor function transfer can be approximated with unitary gain. As in analysis and design of current loop regulation in fundamental subplane, the *VSI* is modelled as a low pass-filter and its transfer function is reported for convenience:

$$H_{VSI}(s) = \frac{1}{1 + s \cdot \tau_d}, \quad \tau_d = \frac{3}{2} \cdot \frac{1}{f_{sw}} \quad (4.56)$$

where  $\tau_d$  stands for voltage supply inverter time constant and  $f_{sw}$  stands for switching frequency.

Consider Fig. 4.12, the design of the *VPI* gains is based on the open-loop transfer function, which is computed as:

$$H_{VPIh,OL}(s) = \frac{s^2 \cdot k_{I,VPIh} + s \cdot k_{P,VPIh}}{s^2 + h^2 \cdot \omega_1^2} \cdot \frac{1}{1 + s \cdot \tau_d} \cdot \frac{1}{s \cdot L_{eq}^{(h)} + R_s} \quad (4.57)$$

As mentioned above, the *VPI* design is performed with pole-zero cancellation method. In mathematical formulation this is expressed as:

$$\frac{k_{I,VPIh}}{k_{P,VPIh}} = \frac{R_s}{L_{eq}^{(h)}} \quad (4.58)$$

By replacing the Eq. (4.58) in Eq. (4.57), the open-loop transfer function is computed as:

$$\begin{aligned}
 H_{VPIh,OL}(s) &= \frac{s \cdot k_{P,VPIh}}{s^2 + (h \cdot \omega_1)^2} \cdot \left( s + \frac{R_s}{L_{eq}^{(h)}} \right) \cdot \frac{1}{1 + s \cdot \tau_d} \cdot \frac{\frac{1}{L_{eq}^{(h)}}}{s + \frac{R_s}{L_{eq}^{(h)}}} = \\
 &= \frac{k_{P,VPIh}}{L_{eq}^{(h)}} \cdot \frac{s}{s^2 + (h \cdot \omega_1)^2} \cdot \frac{1}{1 + s \cdot \tau_d}
 \end{aligned} \tag{4.59}$$

The magnitude and phase of the open-loop transfer function is computed as:

$$\begin{cases} |H_{VPIh,OL}(\omega)| = \frac{k_{P,VPIh}}{L_{eq}^{(h)}} \cdot \frac{\omega}{|-\omega^2 + (h \cdot \omega_1)^2|} \cdot \sqrt{\frac{1}{1 + (\omega \cdot \tau_d)^2}} \\ \angle H_{VPIh,OL} = \frac{\pi}{2} - \arctan(\omega \cdot \tau_d) - k \cdot \pi \end{cases} \tag{4.60}$$

where  $k$  is defined as follows:

$$k = \begin{cases} 0, & \omega < h \cdot \omega_1 \\ 1, & \omega > h \cdot \omega_1 \end{cases} \tag{4.61}$$

In detail, the magnitude of  $VPI$  controller is approximated as follows:

$$|H_{VPIh,OL}(\omega)| = \begin{cases} \frac{k_{P,VPIh}}{L_{eq}^{(h)}} \cdot \frac{\omega}{(h \cdot \omega_1)^2}, & \omega \ll h \cdot \omega_1 \\ \frac{k_{P,VPIh}}{L_{eq}^{(h)}} \cdot \frac{1}{\omega}, & (\omega \gg h \cdot \omega_1 \quad \& \quad \omega \ll \tau_d^{-1}) \\ \frac{k_{P,VPIh}}{L_{eq}^{(h)}} \cdot \frac{1}{\tau_d} \cdot \frac{1}{\omega^2}, & \omega \gg \tau_d^{-1} \end{cases} \tag{4.62}$$

In Fig. 4.13 the asymptotic Bode magnitude plot of open-loop transfer function is shown. Following from the theory and Bode plot, the crossover frequency must be set close to the system bandwidth. However, to ensure acceptable system performance, the crossover frequency must be chosen in the second frequency range listed in system Eq. (4.62). In conclusion, the magnitude and phase are computed as:

$$\begin{cases} |H_{VPIh,OL}(\omega)| = \frac{k_{P,VPIh}}{L_{eq}^{(h)}} \cdot \frac{1}{\omega} \\ \angle H_{VPIh,OL} = -\frac{\pi}{2} - \arctan(\omega \cdot \tau_d) \end{cases} \tag{4.63}$$

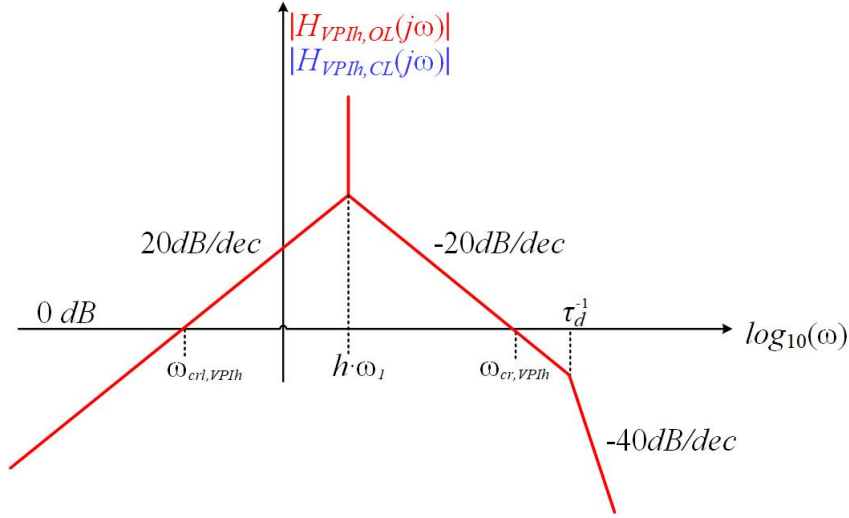


Figure 4.13: Asymptotic Bode plot of the open-loop transfer function magnitude for harmonic current regulation loop with VPI.

By computing The Eq. (4.63) at the crossover frequency  $\omega_{cr,VPI}$ , where the magnitude of the open-loop function is unitary, the following is obtained:

$$\begin{cases} \frac{k_{P,VPIh}}{L_{eq}^{(h)}} \cdot \frac{1}{\omega_{cr,VPIh}} = 1 \\ \Phi_{pm,VPIh} = \left( -\frac{\pi}{2} - \arctan(\omega_{cr,VPIh} \cdot \tau_d) \right) + \pi \end{cases} \quad (4.64)$$

where  $\Phi_{pm,VPIh}$  stand for the phase-margin of the current control, which is always within the range  $[0, \pi/2]$ .

As mentioned above, the consequence of pole-zero cancellation method is reduction of degrees of freedom and, for this reason, just one variable among the crossover frequency and phase-margin can assume the desired value. If the crossover frequency is imposed in Eq. (4.64), the proportional and integral gains are tuned as:

$$\begin{cases} k_{P,VPIh} \simeq \omega_{cr,VPIh} \cdot L_{eq}^{(h)} \\ k_{I,VPIh} \simeq \omega_{cr,VPIh} \cdot R_s \end{cases} \quad (4.65)$$

The tuned VPI block scheme is shown in Fig. 4.14, where  $k_{Bw,h}$  stands for bandwidth related to  $h^{th}$  harmonic. In VPI block scheme  $\omega_1$  stands for electrical rotor speed and the proportional and integral gains are replaced with Eq. (4.65). The bandwidth of the harmonic current regulation is introduced and it is approximated with the crossover frequency.

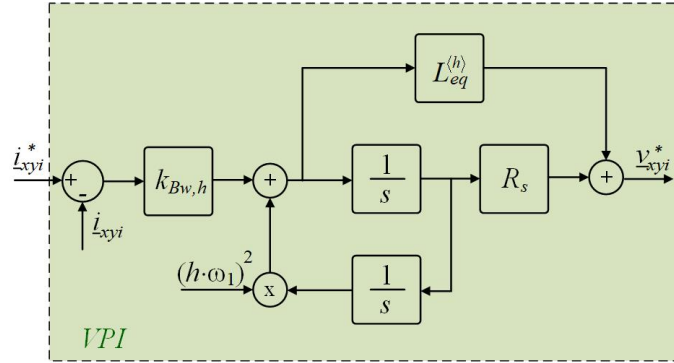


Figure 4.14: Block diagram of *VPI* resonant controller.

More *VPI* current regulators in parallel can be employed when the subplane contains more than one unwanted harmonics. In Fig. 4.15 the block scheme with two *VPI* is given which allows to obtain the reference voltage in  $(x, y)$  subplane from current error. To explain the idea, consider a  $(x, y)$  subplane, in which the  $h_p$  and  $h_k$  harmonics are present. Each employed *VPI* is characterised by the bandwidth  $k_{Bw,h}$  and inductance  $L_{eq}^{(h)}$  related to  $h^{th}$  harmonic.

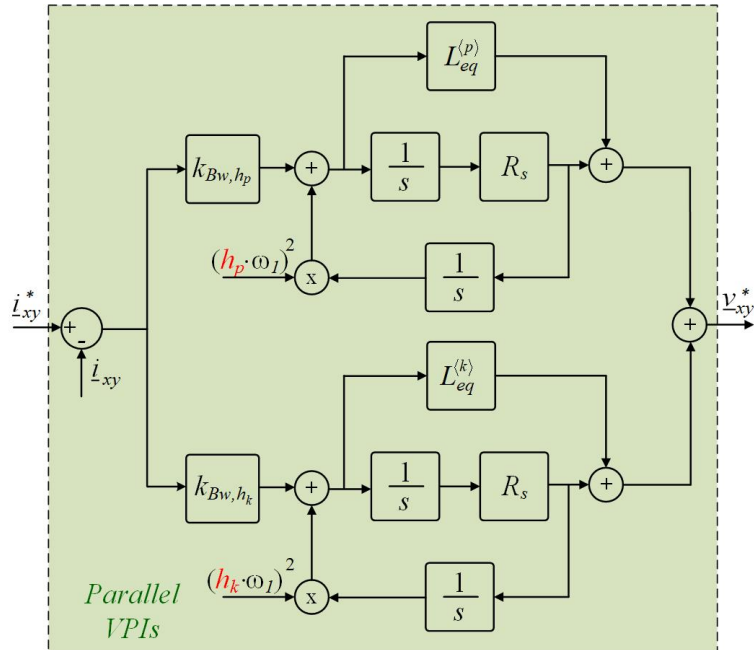


Figure 4.15: *VPIs* resonant controllers: parallel connection.

To conclude the analysis and design of *VPI*, closed-loop transfer function is studied as follows:

$$H_{VPIh,CL}(\omega) = \frac{H_{VPIh,OL}(\omega)}{1 + H_{VPIh,OL}(\omega)} = \begin{cases} \simeq H_{VPIh,OL}(\omega), & |H_{VPIh,OL}(\omega)| \ll 0dB \\ \simeq 1, & |H_{VPIh,OL}(\omega)| \gg 0dB \end{cases} \quad (4.66)$$

By considering the first cases listed in system Eq. (4.62), the lower crossover frequency  $\omega_{crl,VPI}$  is obtained as:

$$\frac{k_{P,VPIh}}{L_{eq}^{(h)}} \cdot \frac{\omega_{crl,VPIh}}{(h \cdot \omega_1)^2} = 1 \Rightarrow \omega_{crl,VPIh} = \frac{L_{eq}^{(h)}}{k_{P,VPIh}} \cdot (h \cdot \omega_1)^2 \quad (4.67)$$

In Fig. 4.16, the asymptotic Bode magnitude plot of closed-loop transfer function is shown.

The effectiveness of the employed *VPI* is shown in Figs. 4.17 and 4.18. These are obtained in simulation performed at 1500 *rpm* under *FOC*. In figure the phase stator currents in *a1*, *a2* and *a3* winding are shown. In detail, in Figs. 4.17 and 4.18 the phase current waveforms without and with *VPIs* are shown, respectively.

Finally, spectrum harmonic of the phase stator current in *a1* winding is performed. In Fig. 4.19 the harmonic spectrum contains all current harmonics, induced by the back-*EMF* harmonics. Conversely, in Fig. 4.20 the harmonic spectrum contains only the fundamental component i.e. the low order harmonics are eliminated from harmonic spectrum with activated harmonic control.

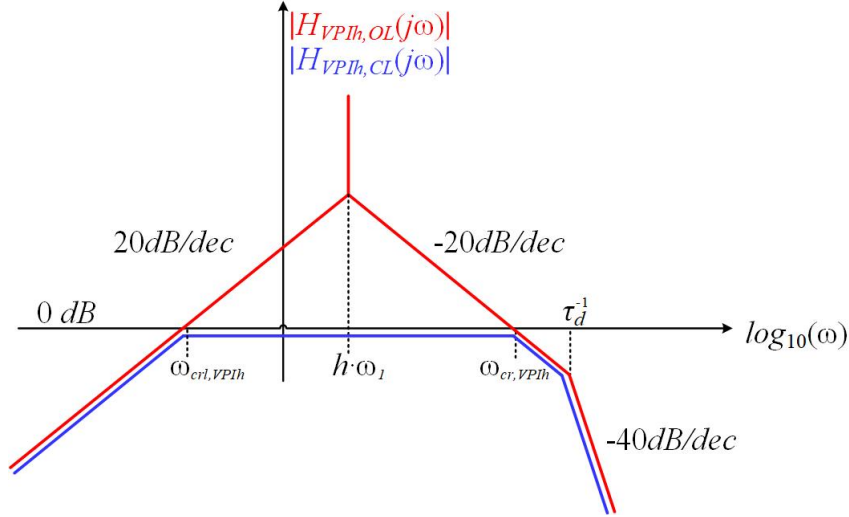


Figure 4.16: Asymptotic Bode plot of the closed-loop transfer function magnitude for harmonic current regulation loop with *VPI*.

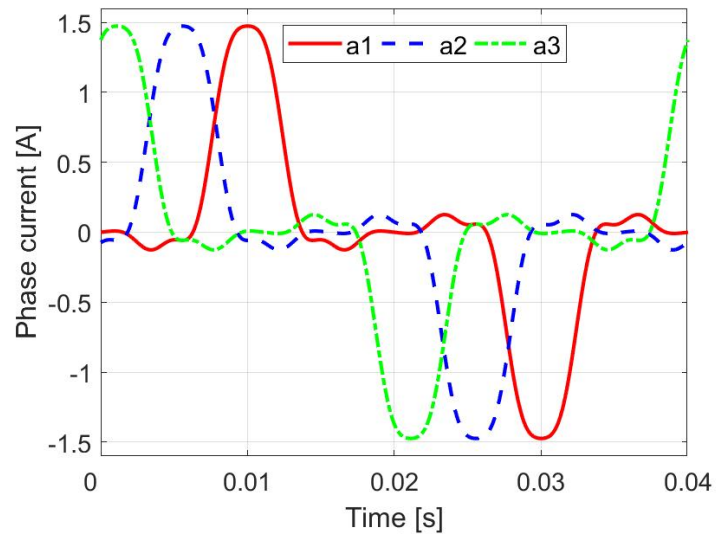


Figure 4.17: Phase currents without *VPI* controllers for non-sinusoidal machine.

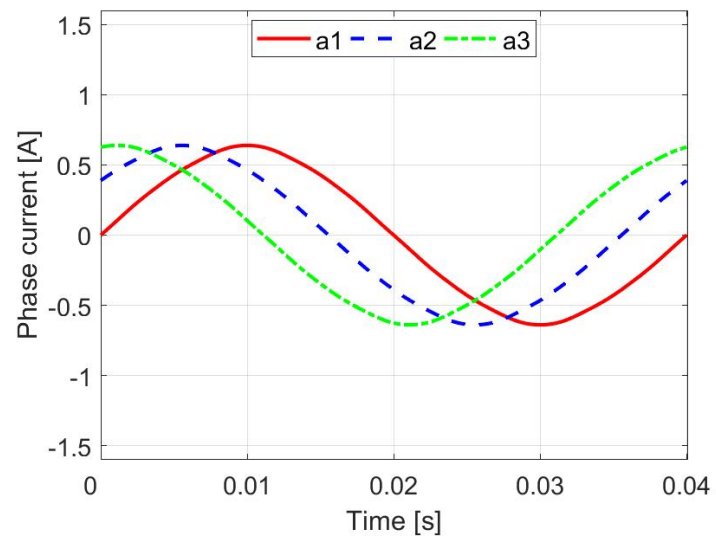
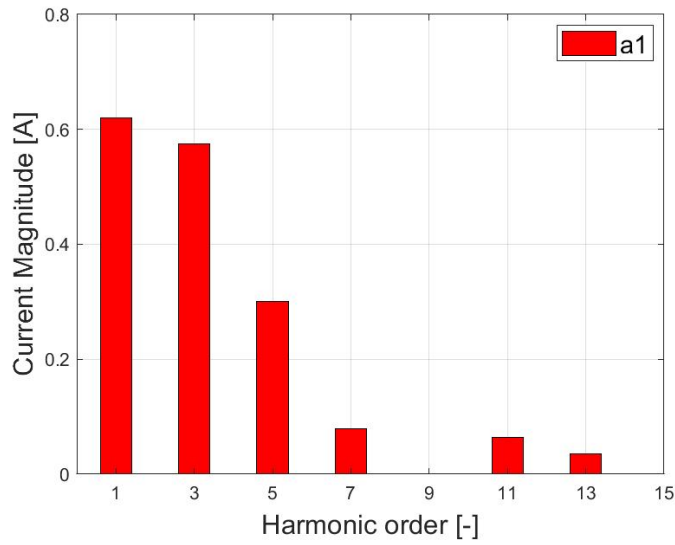
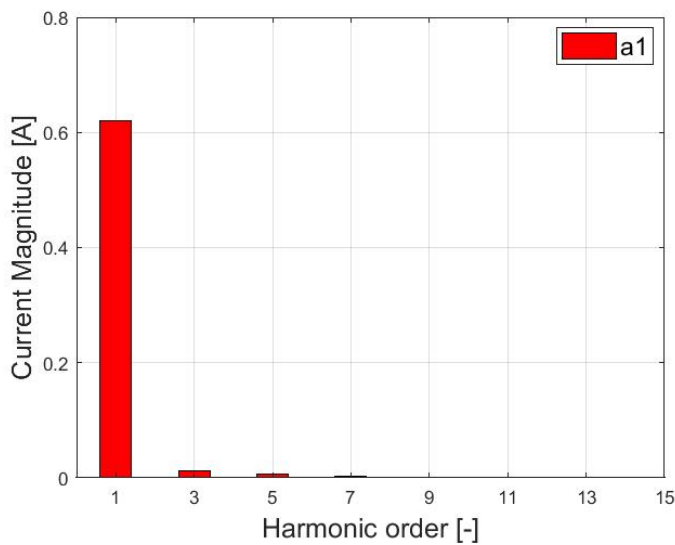


Figure 4.18: Phase currents with *VPI* controllers for non-sinusoidal machine.

Figure 4.19: Phase current spectrum harmonic without *VPI* controllers.Figure 4.20: Phase current spectrum harmonic with *VPI* controllers.

The modified *FOC* scheme is shown in Fig. 4.21. The *VPI* resonant controllers are implemented in *Low order harmonic elimination* block (pink block). In addition, to simplify the schematic the inductance  $L_{\alpha\beta}$  has been replaced with the  $L_s$  symbol.

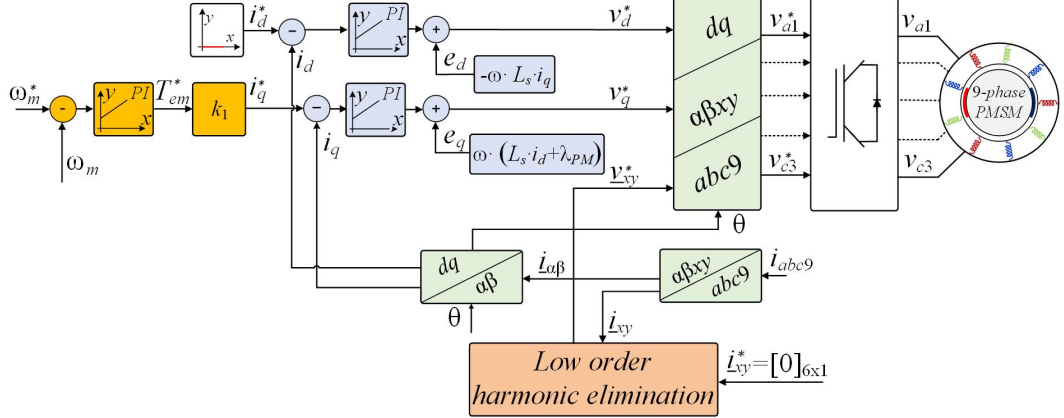


Figure 4.21: FOC with low order harmonic elimination for non-sinusoidal nine-phase surface PMSM.

### Proportional Resonant Controller

An alternative current regulator, called proportional resonant controller [8], to eliminate the harmonics can be employed. In the continuous-time domain, the transfer function of *PRES* is written as:

$$H_{PRES}(s) = \frac{s^2 \cdot k_{P,PRES_h} + k_{I,PRES_h} \cdot s + k_{P,PRES_h} \cdot \omega_0^2}{s^2 + \omega_0^2}, \quad \omega_0 = h \cdot \omega_1 \quad (4.68)$$

where  $k_{P,PRES_h}$  and  $k_{I,PRES_h}$  are the proportional and integral gains, respectively. These gains can be assumed equal to ones of *VPI* and in Fig. 4.22 its block diagram is shown, where the crossover frequency is approximated with the bandwidth and it is tuned in according with *VPI* bandwidth. The schematic block of the harmonic current regulation loop is shown in Fig. 4.12, less than transfer function controller (green block), which must be replaced with the schematic shown in Fig. 4.22.

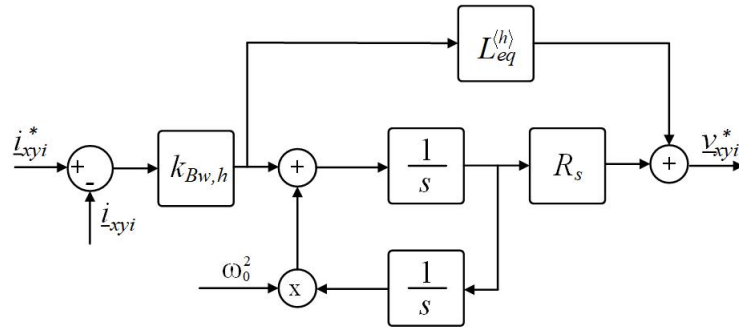


Figure 4.22: Block diagram of *PRES*.

On the basis of the mentioned schematic block, the open-loop transfer function is computed as:

$$H_{PRES,h,OL}(s) = \frac{s^2 \cdot k_{P,VPIh} + s \cdot k_{I,VPIh} + k_{P,VPIh} \cdot \omega_0}{s^2 + \omega_0^2} \cdot \frac{1}{1 + s \cdot \tau_d} \cdot \frac{1}{s \cdot L_{eq}^{(h)} + R_s} \quad (4.69)$$

The magnitude of *PRES* controller is computed as:

$$|H_{PRES,h,OL}(\omega)| = \frac{k_{P,VPIh}}{R_s} \cdot \sqrt{1 + \left( \frac{k_{I,VPIh} \cdot \omega}{k_{P,VPIh} \cdot (\omega_0^2 - \omega^2)} \right)^2} \cdot \frac{1}{\sqrt{1 + (\omega \cdot \tau_d)^2}} \cdot \frac{1}{\sqrt{1 + \left( \frac{L_{eq}^{(h)}}{R_s} \right)^2 \cdot \omega^2}} \quad (4.70)$$

In Fig. 4.23 the asymptotic Bode magnitude plot of open-loop (red line) and closed-loop (blue line) are shown. In mentioned figure the lower crossover frequency does not exist, while the crossover frequency is equal to the one defined for *VPI*.

In experimental validation to eliminate the current harmonics the proportional resonant controllers are employed.

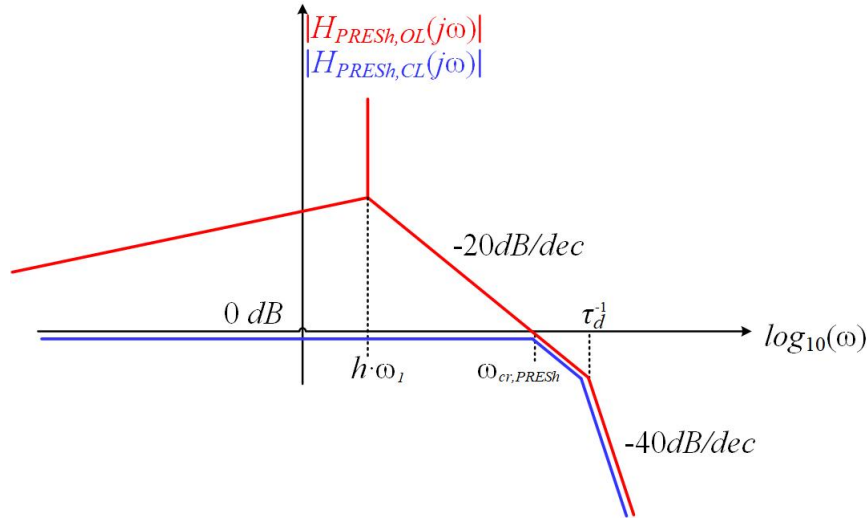


Figure 4.23: Asymptotic Bode plot of the open-loop and closed-loop transfer function magnitude for harmonic current regulation loop with *PRES*.

## Chapter 5

# Sensorless Control of a Nine-Phase Surface *PMSM* with Non-Sinusoidal Back-*EMF*

In this chapter an *I-Hz* starting method for smooth and fast transition from open-loop frequency to sensorless field-oriented control of a nine-phase surface *PMSM* with non-sinusoidal back-*EMF* is reported.

Chapter is organised as follows:

- In Section 5.1 a literature survey related to the position estimation methods is presented. It is followed by the description of the adopted method in this thesis.
- In Section 5.2 the back-*EMF* method is briefly presented in order to highlight the code-saving through the use of back-*EMF* harmonic. In Subsection 5.2.1 the phase-locked loop theory is shown: the rotor position estimation is based on *PLL*. Finally, a harmonic *PLL* is presented.
- In Section 5.3 the starting method to accelerate the motor is presented: the speed is imposed in open loop while the stator currents are controlled in an arbitrary reference frame.
- In Section 5.4 the transition strategy is performed: at switch instant the current references in rotor reference frame are set equal to measured values evaluated in the estimated rotor reference frame.
- In Section 5.5 simulation results obtained in *Matlab/Simulink* environment are presented. The hybrid control is validated: the machine starting is performed in open-loop frequency control, while at medium-high speed the sensorless *FOC* based on estimated back-*EMF* is employed.

## 5.1 Introduction

The motor position and speed control are highly important control loops in motor control applications. The control loops need actual rotor position and/or speed signals. There are several means for sensing these variables for motor control system, known as mechanical sensors. When the position is measured the control is called sensed. However, various disadvantages may arise, as for example the increase of the drive cost and electromagnetic interference due to the power conductors that disturbs the transmission between sensor and control system. In many applications, these additional sensors not only increase the mounting and maintenance cost, but also reduce the reliability of the whole system, as they are prone to environmental disturbances.

Sensorless motor control is a cost-saving practical alternative to the sensed control scheme. Currently, most commercial motor drives have a sensorless option embedded in the control system. Using this option improves the motor system reliability, thus reducing maintenance. There are many sensorless control methods used in commercial products or presented in literature.

It is common to categorize the position estimation of permanent magnet synchronous machine in two main groups: back-electromotive force methods and saliency-based methods. The reason of the distinction is evident: the back-*EMF* depends on the rotor motion, while the saliency is a motor structure property. However, observer-based estimation is capable to use both back-*EMF* and saliency methods, making difficult to confine the methods to two different groups. In addition, new methods have been developed, e.g. the hypothetical position estimation. According to the technical literature, the rotor position and rotor speed estimation methods can be divided in five groups, as shown in Fig. 5.1.

The back-*EMF*-based method, as the most traditional, is still attractive for both salient and non-salient *PMSM* because it considers the interaction of permanent magnet with the stator windings directly. The back-*EMF* is position dependent; thus, it can be manipulated by different schemes to compute the rotor position. Two different schemes belong to this category, as shown in Fig. 5.1 [29].

The second method is based on the estimation of the stator flux linkage vector in terms of the position and speed. The flux linkage contributions provided by both the permanent magnets and winding currents are considered [30], making this method applicable to both salient and non-salient *PMSM*. Four different schemes based on this method can be derived, as shown in Fig. 5.1.

The third method is based on the machine saliency. The inductances of the salient machines depend on the rotor position, allowing their use to estimate the rotor position over the entire speed range. Three schemes can be derived by this method (Fig. 5.1).

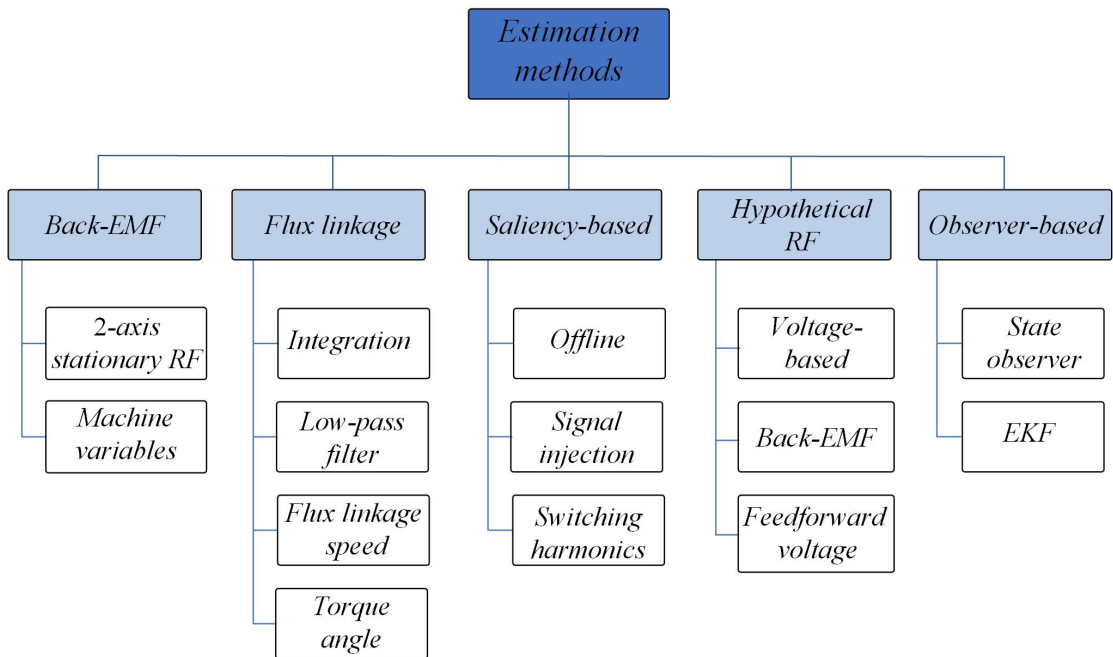


Figure 5.1: A classification of position and speed estimation methods (blue blocks) and schemes (white blocks).

The fourth method is based on the hypothetical rotor position. The machine model is considered in a reference frame oriented along a hypothetical rotor position. Using the measured motor signals, the error between the hypothetical and real rotor position is estimated. This method is applicable to both salient and non-salient *PMSM*. Three different schemes are available in literature [31], as shown in Fig. 5.1.

The last method for rotor position estimation is based on the use of closed-loop observers. Many schemes are available under this category. A simple observer-based rotor position scheme is reported in [32]. By using the state-space model of the *PMSM*, model-based estimator is designed. The estimator is subjected to parameter detuning and noise. Therefore, extended Kalman filter [33] is used as the basis of the most common observer-based scheme for rotor speed and position estimation over the entire speed range. In addition, it is applicable to both salient and non-salient *PMSM*.

The back-*EMF* method is preferred in applications where production cost is very important and low speed operation is not required. The back-*EMF* is induced if there is the relative motion between permanent magnets and the windings, making this method not applicable under zero and low speed conditions. Consequently, a starting method is required to accelerate the motor. Several methods for *PMSM* starting can be found in literature. Methods based on *V-f* control are presented

in [34] - [35]; methods based on high-frequency signal injection [36] - [37]. Finally,  $I$ - $Hz$  starting methods with transition to sensorless field-oriented control are proposed in [38]. In the latter mentioned methods, the current vector is controlled with a constant value together with the imposed a frequency profile.

In this thesis the back-electromotive force method is used to estimate the rotor position and speed. The idea was to get these informations using a *State Observer scheme*, but as it will be explained later, no current observer is implemented as the thesis goal is achieved using the third back-*EMF* harmonic estimator. However, according with the previous considerations, this method fails with the motor at standstill and at low speed. The consequence is the implementation of a hybrid sensorless control. This consists of an  $I$ - $Hz$  starting method for smooth and fast transition to sensorless field-oriented control. Using the *PLL*, the rotor position for the sensorless *FOC* scheme is computed. The specific distribution of back-*EMF* and proportional resonant controllers employed in  $(x, y)$  subplanes are code-saving solution for many possible scheme presented in Fig. 5.1.



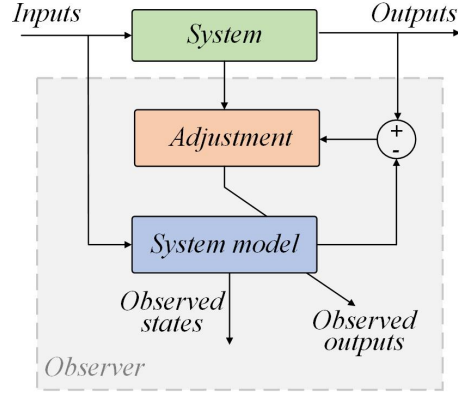


Figure 5.3: A schematic view of a closed-loop observer.

adaptive system, is composed by the *PMSM* model in *VSD* variables to estimate the stator currents. These are compared with their measurement values, generating a regulation errors. Finally, the adjustment component is composed by the controller/s. Usually, proportional integral controllers are used to modify observer operation and this block is also known as corrective regulator. The observer gains are defined by making the dynamics of the observer much faster than the frequency of the disturbance.

The model of surface *PMSM* is non-linear and the system is assumed to satisfy:

$$\begin{cases} \frac{d[x(t)]}{dt} = [A[x(t)]] + [B[u(t)]] \\ [y(t)] = [C[x(t)]] + [D[u(t)]] \end{cases} \quad (5.1)$$

where:

- $[x(t)]$  is the vector of plant's state,
- $[u(t)]$  are the input vector,
- $[y(t)]$  is the measured output vector of the system and
- $[A]$ ,  $[B]$ ,  $[C]$  and  $[D]$  are the matrices.

Note that the vectors of a state observer are commonly denoted by  $\hat{\cdot}$  to distinguish them from the variables of the equations satisfied by the physical system. For this reason, the Eq. (5.1) for estimated variables can be written as:

$$\begin{cases} \frac{d[\hat{x}(t)]}{dt} = [A[\hat{x}(t)]] + [B[u(t)]] \\ [\hat{y}(t)] = [C[\hat{x}(t)]] + [D[u(t)]] \end{cases} \quad (5.2)$$

If this system is observable then the output of the system,  $[y(t)]$ , can be used to steer the state of the state observer. The observer model of the physical system is

derived from the above equations. Additional terms are included to ensure that, on receiving successive measured values of the plant's inputs and outputs, the model's state converges to that of the plant. In particular, the output of the observer may be subtracted from the output of the plant and then multiplied by a matrix  $K_{obs}$ ; this is then added to the equations for the state of the observer to produce a so-called *Luenberger* observer, defined by the Eq. (5.3).

$$\frac{d[\hat{x}(t)]}{dt} = [A[\hat{x}(t)]] + [B[u(t)]] + K_{obs}([y(t)] - [\hat{y}(t)]) \quad (5.3)$$

In surface *PMSM* the plant's state, input and measured output vectors are:

$$[x(t)] = [i_{x3}(t), \quad i_{y3}(t), \quad e_{x3}(t), \quad e_{y3}(t)] \quad (5.4)$$

$$[y(t)] = [i_{x3}(t), \quad i_{y3}(t)] \quad (5.5)$$

$$[u(t)] = [v_{x3}(t), \quad v_{y3}(t)] \quad (5.6)$$

Using the machine stator voltage equation in the third subplane:

$$\underline{v}_{xy3} = \tilde{R}_s \cdot \underline{i}_{xy3} + \tilde{L}_{ls} \cdot \frac{d\underline{i}_{xy3}}{dt} + \underline{e}_{PM,xy3} \quad (5.7)$$

and assuming that derivative of disturbances is equal zero, the observer equations can be written as:

$$\left\{ \begin{array}{l} \frac{d\hat{i}_{x3}}{dt} = \frac{v_{x3}}{\tilde{L}_{ls}} - \frac{\tilde{R}_s}{\tilde{L}_{ls}} \cdot \hat{i}_{x3} - \frac{1}{\tilde{L}_{ls}} \cdot \hat{e}_{x3} + K_{obs} \cdot (i_{x3} - \hat{i}_{x3}) \\ \frac{d\hat{i}_{y3}}{dt} = \frac{v_{y3}}{\tilde{L}_{ls}} - \frac{\tilde{R}_s}{\tilde{L}_{ls}} \cdot \hat{i}_{y3} - \frac{1}{\tilde{L}_{ls}} \cdot \hat{e}_{y3} + K_{obs} \cdot (i_{y3} - \hat{i}_{y3}) \\ \frac{d\hat{e}_{x3}}{dt} = K_{obs} \cdot (i_{x3} - \hat{i}_{x3}) \\ \frac{d\hat{e}_{y3}}{dt} = K_{obs} \cdot (i_{y3} - \hat{i}_{y3}) \end{array} \right. \quad (5.8)$$

where:

- $K_{obs}$  is the observer gains. In case of the observer gain corresponds to *PI* regulator, the current observer shown in Fig. 5.4 is obtained,

- $[\hat{i}_{xy3}, \quad \hat{i}_{xy3}]^T$  are the measured and estimated current in third subplane and

- $[\hat{e}_{xy3}, \quad \hat{e}_{xy3}]^T$  are the measured and estimated back-*EMF* in third subplane.

Since in the third subplane a *PRES* is employed, the third harmonic of the current is eliminated. Therefore, the integral output in the system model (adaptive

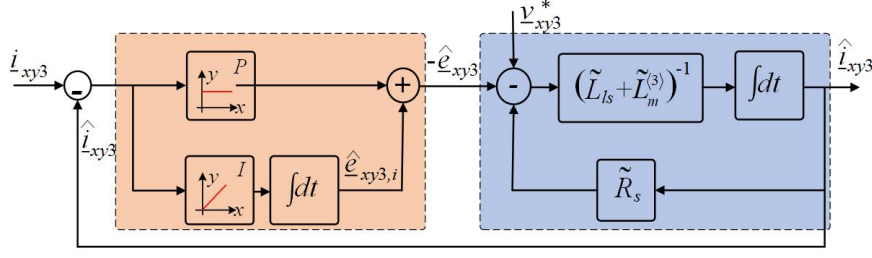


Figure 5.4: Observer current in third subplane.

system, blue block) is a constant value. In other words, the integral input is zero because the estimated back-EMF is equal to the voltage reference. This means that, in steady state the *PI* input error is constant (the measurement current is equal to zero) and just integral component is activated. The output of integral component in corrective regulator (pink block) is filtered by high-frequency disruption. As the reference voltage in the control is equal to the back-EMF, the corrective regulator is not employed in this work.

Following from stated, the electrical rotor position is obtained by the reconstruction of command phase voltages, corresponding to a value three times higher than *d*-axis position. The obtained angle is computed as:

$$3 \cdot \hat{\theta} = \arctan\left(\frac{\sin(3 \cdot \hat{\theta})}{\cos(3 \cdot \hat{\theta})}\right) = \arctan\left(-\frac{\hat{e}_{x3}}{\hat{e}_{y3}}\right) \quad (5.9)$$

About the trigonometric functions related to estimated angle:

$$\sin(3 \cdot \hat{\theta}) = \frac{\hat{e}_{x3}}{\sqrt{\hat{e}_{x3}^2 + \hat{e}_{y3}^2}} \quad (5.10)$$

$$\cos(3 \cdot \hat{\theta}) = \frac{-\hat{e}_{y3}}{\sqrt{\hat{e}_{x3}^2 + \hat{e}_{y3}^2}} \quad (5.11)$$

The use of the command voltages instead of the measured ones is a straightforward approach that improves the robustness of the system. However, it introduces an error due to the inverter nonlinear drops, which should be properly compensated, especially at low speed. In detail, the command phase voltages in vector space variables can be written as:

$$v_{xy3}^* \simeq e_{PM,xy3} + \Delta V_{xy3} \quad (5.12)$$

The inverter non linear drops in *VSD* variables are modelled as:

$$\Delta V_{xy3} = v_{dt,xy3} + v_{on,xy3} \quad (5.13)$$

where:

$$\underline{v}_{dt,xy3} = \frac{4}{9} \cdot V_{dc} \cdot \frac{t_{dt}}{T_{sw}} \cdot \text{sgn}(\underline{i}_{xy3}) \quad (5.14)$$

$$\underline{v}_{on,xy3} = V_{th} \cdot \text{sgn}(\underline{i}_{xy3}) + R_{ON} \cdot \underline{i}_{xy3} \quad (5.15)$$

where:

- $\underline{v}_{dt,xy3}$  is the voltage error given by inverter dead time,
- $\underline{v}_{on,xy3}$  is the voltage error given by ON-state voltage drop of the power switches,
- $V_{th}$  is threshold voltage,
- $V_{dc}$  is the dc-link voltage,
- $R_{on}$  is ON-state resistance of the model for the insulated-gate bipolar transistor (*IGBT*)/diode,
- $\underline{i}_{xy3}$  is the current in third subplane,
- $t_{dt}$  is the *IGBT* turn-on dead time and
- $T_{sw}$  is the *PWM* switching period.

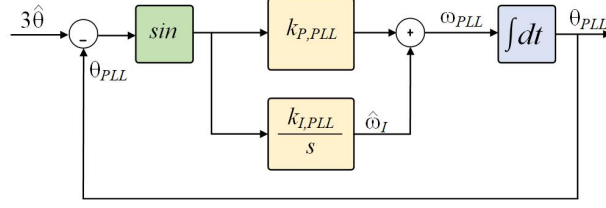
In this work, the inverter compensation in third subplane is not employed because the inverter nonlinear drops depend on the current  $\underline{i}_{xy3}$ , which is controlled to zero using *PRES* controller.

The arc-tangent algorithm, presented in Eq. (5.9), is difficult to implement in digital controllers because the reference phase voltages are characterised by disturbances. For this reason, the rotor position and speed information are computed by the means of *PLL* and angle demodulation block or harmonic *PLL*.

### 5.2.1 Position Estimation using Phase-Locked Loop

The phase-locked loop [40] is a computational method that avoids derivative operation. The input of it is the mechanical angle, which can be estimated or measured, as shown in Fig. 5.5. The alternative to *PLL* is derivative method.

The derivative operation produces many disturbances and the consequence is the low-pass filter implementation, which introduces a delay. The delay is incompatible with high driver dynamic. For this reason, the speed is estimated with *PLL*. This generates an output signal whose phase is related to the one of the input signal. The *PLL* is composed by a proportional-integrator controller, whose input is the sine function of the error (green block in Fig. 5.5), which is a continuous function. Instead, the discontinuous functions, such as the normalised angle, may introduce unjustified control errors. The output of the *PI* regulator corresponds to a speed variable. Therefore, a further integration (blue blok in Fig. 5.5) is performed to get the feedback angle. Note that the feedback is based on the estimated value, indeed on measurement value. On the basis of *PLL* theory [41], the block diagram of rotor position estimation can be drawn, as shown in Fig. 5.5. The speed should be observed at the output of *PI* controller (pink blocks). Since the integral component


 Figure 5.5: Block diagram of rotor position and speed estimations based on  $PLL$ .

is already filtered, this value is usually employed as feedback of the speed loop regulation. Note that, the  $PLL$  input and output are related to  $(3 \cdot \theta)$  because they are obtained on the basis of third back- $EMF$  harmonic.

The  $PLL$  input error, with assumption that it is small enough, can be approximated as follows:

$$\epsilon_{\theta} = \sin(3\hat{\theta} - \theta_{PLL}) \simeq \sin(3\hat{\theta}) \cdot \cos(\theta_{PLL}) - \cos(3\hat{\theta}) \cdot \sin(\theta_{PLL}) \quad (5.16)$$

The modified PLL schematic is shown in Fig. 5.6, where *Angle Demodulation* (grey block) is shown. In Fig.5.7 the corresponding zoom of this block is shown. Following from stated, the  $PLL$  output angle  $\theta_{PLL}$  is denormalized to obtain a continuous function and so divided by three to obtain the electrical rotor position.

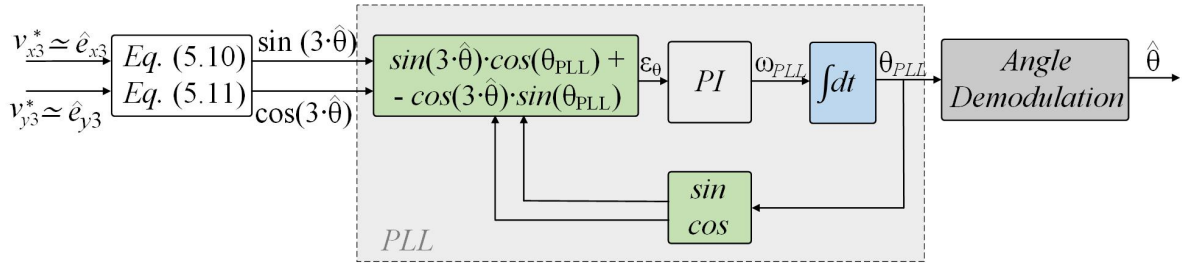
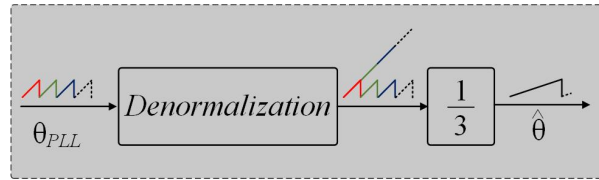

 Figure 5.6: Block diagram of  $PLL$  using trigonometric functions.


Figure 5.7: Block diagram of angle demodulation.

According to Fig. 5.5, the design of the  $PI$  gains is based on the open-loop transfer function, which is written as:

$$H_{PLL,OL}(s) = \left( k_{P,PLL} + \frac{k_{I,PLL}}{s} \right) \cdot \frac{1}{s} \quad (5.17)$$

In Fig. 5.8 the asymptotic Bode magnitude plot of the open-loop transfer function  $PLL$  is shown. By performing the computation of both magnitude and phase belonging to the open-loop transfer function, the following results are obtained:

$$\begin{cases} |H_{PLL,OL}(\omega)| = \frac{k_{I,PLL}}{\omega^2} \cdot \sqrt{1 + \left( \frac{\omega \cdot k_{P,PLL}}{k_{I,PLL}} \right)^2} \\ \angle H_{PLL,OL}(\omega) = \arctan\left(\frac{\omega \cdot k_{P,PLL}}{k_{I,PLL}}\right) - \frac{\pi}{2} - \frac{\pi}{2} \end{cases} \quad (5.18)$$

By computing Eq. (5.18) at the crossover frequency, corresponding to unitary magnitude (0 dB) of the open-loop transfer function, the following equation system is obtained:

$$\begin{cases} \frac{k_{I,PLL}}{\omega_{cr,PLL}^2} \cdot \sqrt{1 + \left( \frac{\omega_{cr,PLL} \cdot k_{P,PLL}}{k_{I,PLL}} \right)^2} = 1 \\ \phi_{pm,PLL} = \left( \arctan\left(\frac{\omega_{cr,PLL} \cdot k_{P,PLL}}{k_{I,PLL}}\right) - \pi \right) + \pi \end{cases} \quad (5.19)$$

where  $\phi_{pm,PLL}$  is the  $PLL$  phase-margin. This parameter influences the  $PLL$  dynamics and depends on the input signal accuracy. If the input angle is not accurately discretized, the  $PLL$  phase-margin must take higher values, but this means

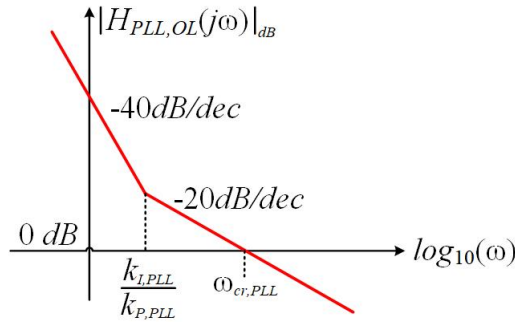


Figure 5.8: Asymptotic Bode plot of the  $PLL$  open-loop transfer function magnitude.

slow dynamics. Once the phase-margin is imposed, it is possible to write as follows:

$$\omega_{cr,PLL} \cdot \frac{k_{P,PLL}}{k_{I,PLL}} = \tan(\Phi_{pm,PLL}) \quad (5.20)$$

By replacing the Eq. (5.20) in Eq. (5.19), the  $PI$  gains are computed as:

$$\begin{cases} k_{P,PLL} = \frac{\omega_{cr,PLL}^2 \cdot \tan(\Phi_{pm,PLL})}{\sqrt{1 + \tan^2(\Phi_{pm,PLL})}} \\ k_{I,PLL} = \frac{\omega_{cr,PLL}^2}{\sqrt{1 + \tan^2(\Phi_{pm,PLL})}} \end{cases} \quad (5.21)$$

Note that the degree of freedom are both crossover frequency and phase-margin. The design of  $PI$  gains is performed on the basis of selected crossover frequency and phase-margin and Eq. (5.20) must be verified. The crossover frequency is positioned near the bandwidth of the  $PLL$ . The bandwidth is approximately equal to  $PLL$  proportional parameter. To ensure control loop stability, the following equations must be verified:

$$\frac{k_{I,PLL}}{k_{P,PLL}} < \frac{k_{P,PLL}}{4} \iff \Phi_{pm,PLL} > \frac{\pi}{4} \quad (5.22)$$

Finally, the design of  $PI$  gains is:

$$\begin{cases} k_{P,PLL} = \frac{\omega_{cr,PLL}^2 \cdot \tan(\Phi_{pm,PLL})}{\sqrt{1 + \tan^2(\Phi_{pm,PLL})}} \\ k_{I,PLL} = \frac{\omega_{cr,PLL}^2}{\sqrt{1 + \tan^2(\Phi_{pm,PLL})}} \\ \Phi_{pm,PLL} > \frac{\pi}{4} \end{cases} \quad (5.23)$$

The  $PLL$  setting parameters are presented in Table 5.1. These values allow sufficient margin of error and robustness.

Table 5.1: Phase-Locked Loop parameters.

<b>PLL tuning</b>	
Parameter	Value [Units]
$\Phi_{pm,PLL}$	60 [deg]
$\omega_{cr,PLL}$	188.5 [rad/s]
$k_{P,PLL}$	163.3[1/s]
$k_{I,PLL}$	17765 [1/s <sup>2</sup> ]

The effectiveness of the employed *PLL* and corresponding angle demodulation is shown in Figs. 5.9 - 5.14. The simulation are performed in *Simulink* environment under *FOC* without load torque. The real machine data are considered and the parameters are consistent with the ones defined in previous chapters.

In Fig. 5.9 the speed sequence is shown. Initially, the speed reference is zero. At 0.1 s the speed reference is increased up to 1500 *rpm* with ramp function. The ramp function is used to design the *PI* gains and to evaluate the effectiveness of the *PLL*. The entire sequence takes 3.5 s. In this figure, when a ramp speed is applied the fast response of the machine in terms of mechanical speed is shown. Therefore, focusing the attention on *PLL* output, note that it follows the measured value demonstrating the effectiveness of the employed *PLL*. This consideration is verified when the motor is accelerated. In other words, the employed *PLL* is sufficiently accurate when the estimated back-*EMF* are accurately evaluated. On the other side, the *PLL* output does not follow the measured value at low speed. If the speed estimation is obtained as output of *PLL* integral, without considering the *PLL* proportional contribution, an already filtered value is obtained. The time trend of *No Filtered* speed is obtained as sum of *PLL* proportional and integral contributes. This consideration highlight one of *PLL* advantages than derivative method, as shown in Fig. 5.10.

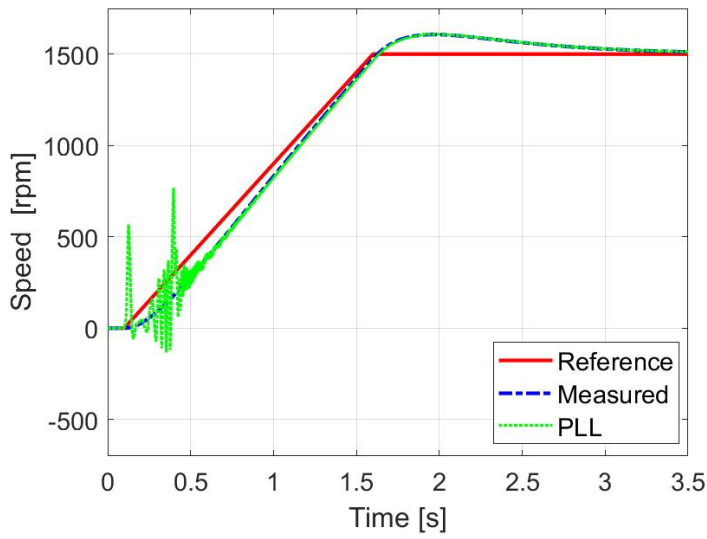


Figure 5.9: *PLL* effectiveness: speed response.

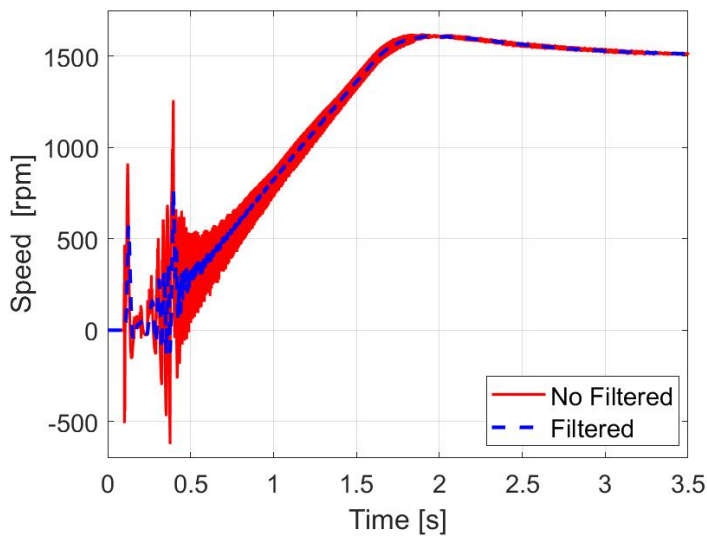


Figure 5.10: *PLL* effectiveness: speed filtered and no filtered responses.

In Figs. 5.11 and 5.12 a zoom areas of the trigonometric functions at low and high speed, respectively, are shown. The computed functions, calculated using the measured values, are compared with the ones estimated and *PLL* output. However, the employed *PLL* is sufficiently accurate when the back-*EMF* can be accurately estimated. The effectiveness of *PLL* fails with the motor at standstill and for low speed because its input is not accurate. Conversely, as shown in Fig. 5.12, at high speed estimated trigonometric functions follow the computed values.

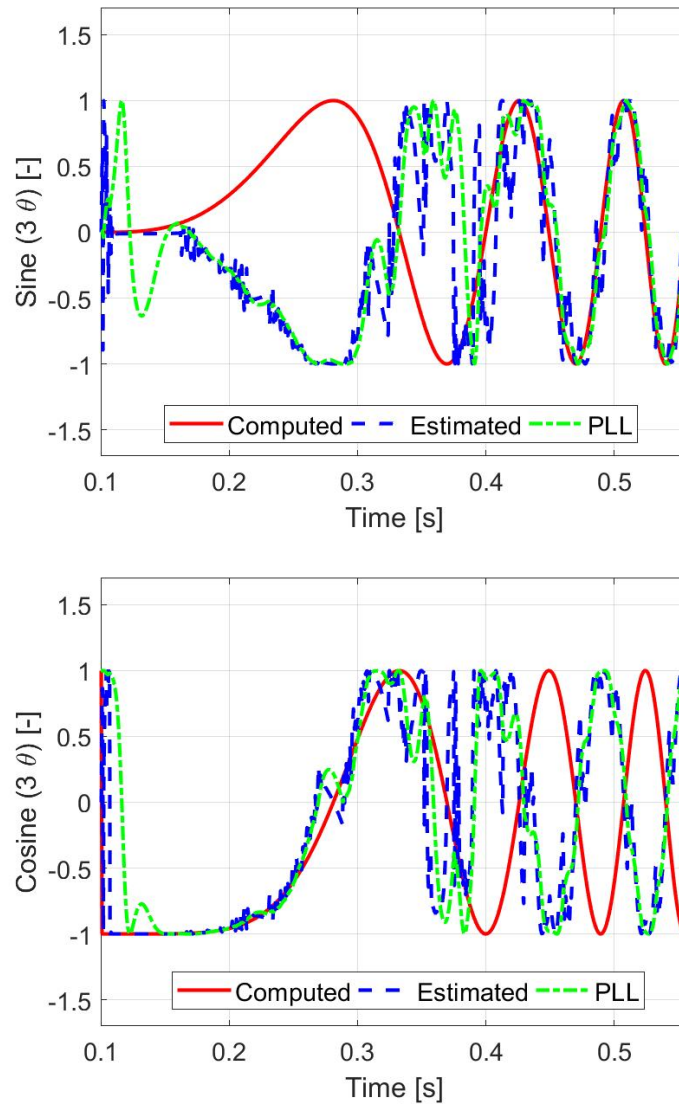


Figure 5.11: *PLL* effectiveness: trigonometric functions at low speed. From top to bottom: sine; cosine.

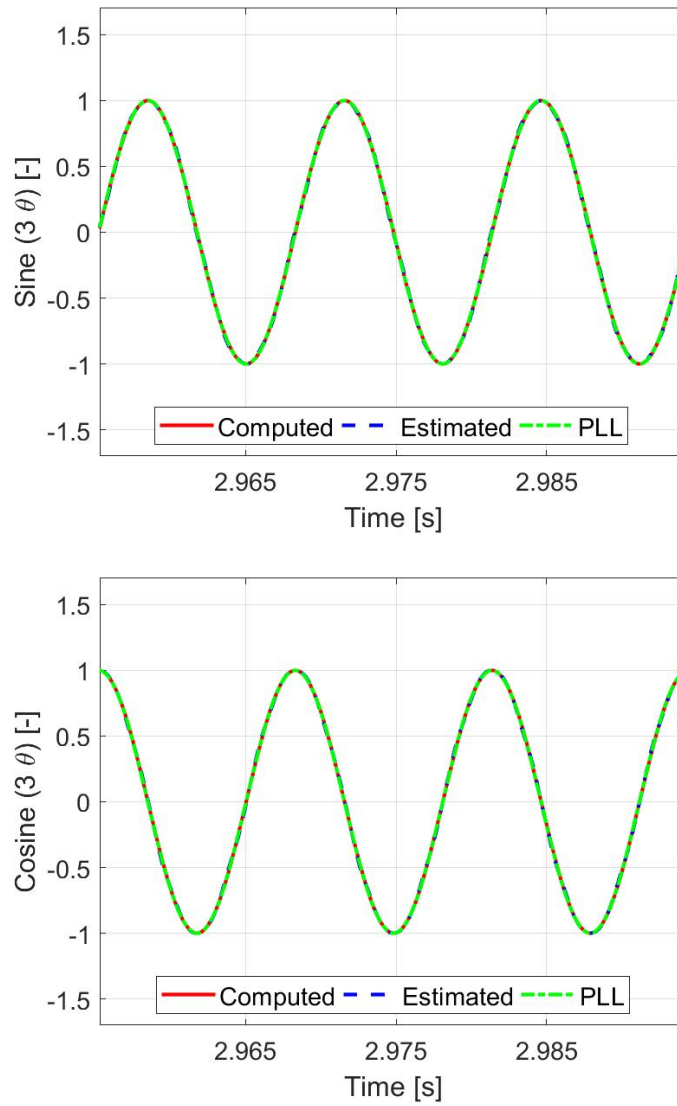


Figure 5.12: *PLL* effectiveness: trigonometric functions at high speed. From top to bottom: sine; cosine.

In Figs. 5.13 and 5.14 zoom areas of measured, demodulated angle and *PLL* output at low and high speed, respectively, are shown. The time trends of *PLL* output is three times faster than the measured value, as it is clearly visible in the mentioned figures (top), related to *PLL* input. In bottom of Figs. 5.13 and 5.14 the demodulated angle at low and high speed are shown. The demodulated angle follows the measured value at medium-high speed. This confirms the good performance of *PLL* and employed demodulation method at medium-high speed.

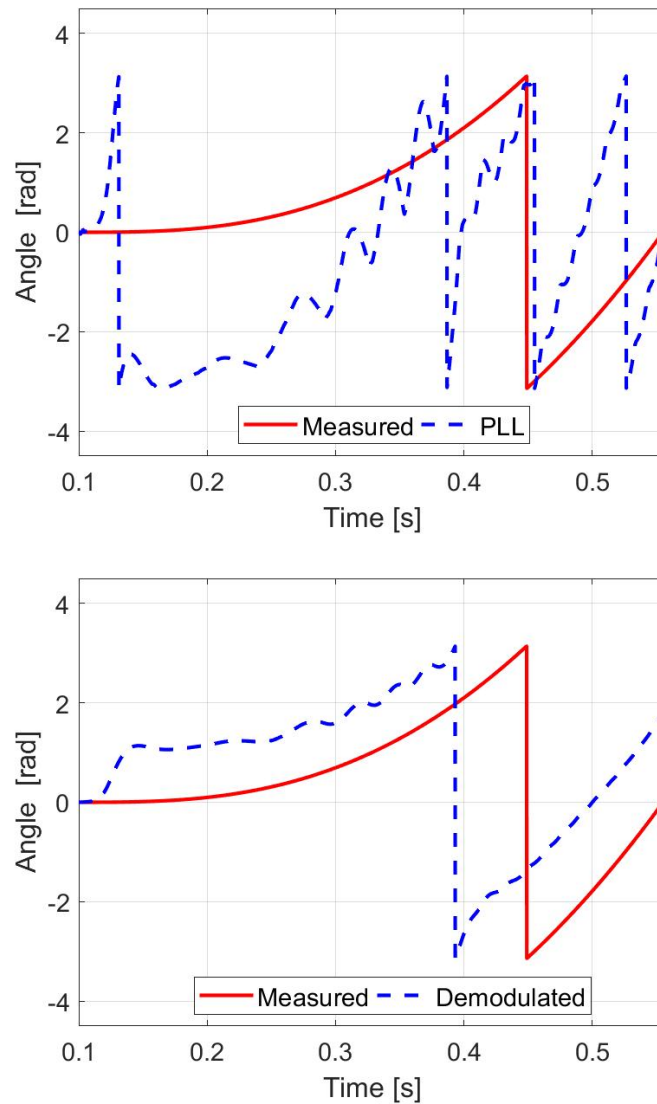


Figure 5.13: *PLL* effectiveness: rotor position at low speed. From top to bottom: *PLL* output; demodulation output.

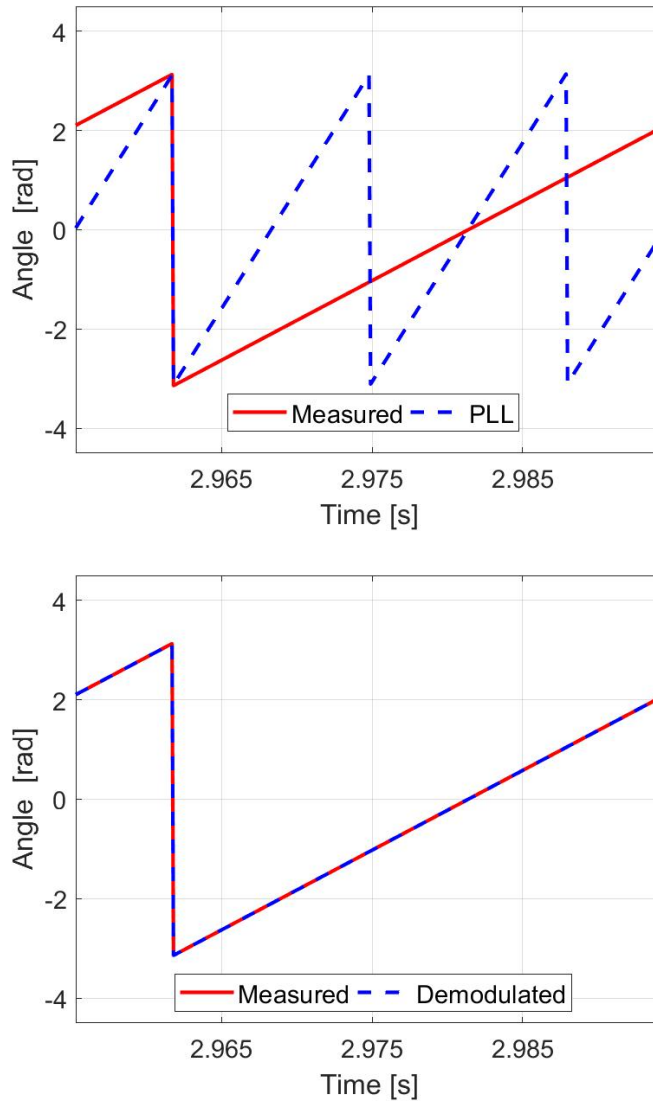


Figure 5.14: *PLL* effectiveness: rotor position at high speed. From top to bottom: *PLL* output; demodulation output.

### 5.2.2 Position Estimation using Harmonic Phase-Locked Loop

To avoid the block diagram of the angle demodulation, shown in Fig. 5.7, the harmonic phase-locked loop can be employed. The output of harmonic *PLL* corresponds to the estimated rotor position due to the gain  $h$  added in feedback, as shown in Fig. 5.15. Concerning the design of the proportional and integral gains, by using the same approach described in previous section, it possible to conclude that a new values are computed as:

$$\begin{cases} k_{P,PLLh} = \frac{k_{P,PLL}}{h} \\ k_{I,PLLh} = \frac{k_{I,PLL}}{h} \end{cases} \quad (5.24)$$

Regardless the harmonic angle, the presented block diagram is able to obtain the estimated rotor position. This means that the rotor position can be estimated for each harmonic order in straightforward way. It is just necessary to set harmonic *PLL* inputs properly.

The effectiveness of harmonic *PLL* is shown in Figs. 5.16 and 5.17. By using the estimated back-*EMF* in  $(x,y)$ 2 subplane, the trigonometric functions in input to harmonic *PLL* are obtained. This input is related to the fifth and thirteenth back-*EMF* harmonic. Consider just *PRES* output to eliminate the fifth harmonic, in Fig. 5.16 a zoom areas of the trigonometric functions are clearly faster than the measured rotor position due to the harmonic *PLL* inputs related to the mentioned harmonic.

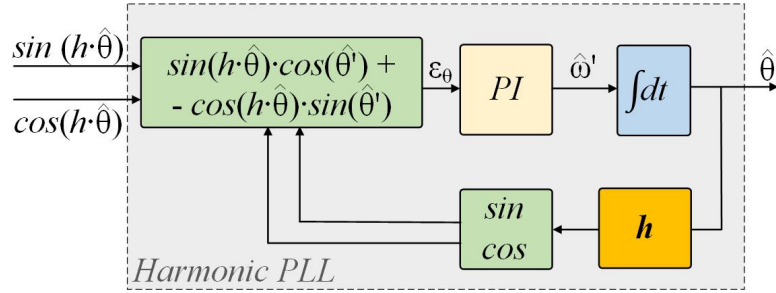


Figure 5.15: Block diagram of harmonic *PLL*.

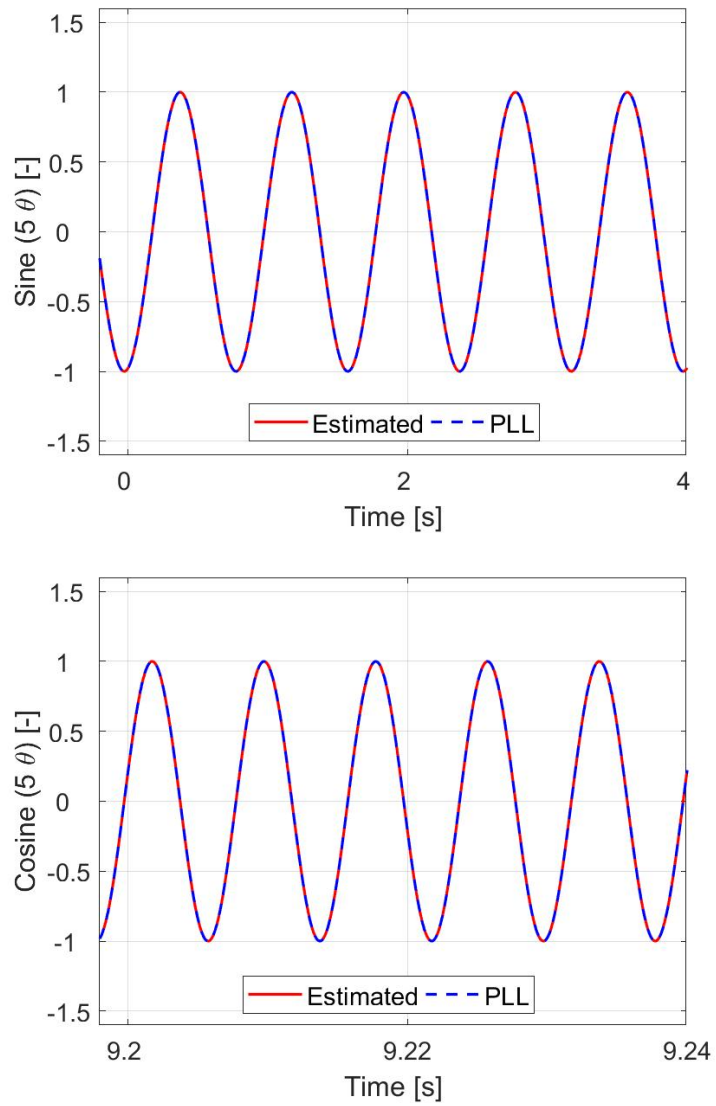


Figure 5.16: Harmonic *PLL* effectiveness: trigonometric functions at high speed. From top to bottom: sine; cosine.

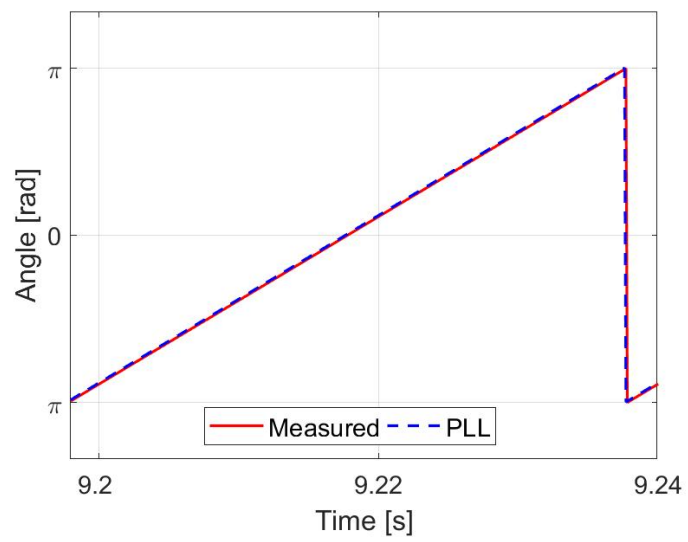


Figure 5.17: Harmonic *PLL* effectiveness: estimated rotor position.

### 5.3 An $I$ -Hz Starting Method

The sensorless control based on back- $EMF$  estimation method fails with the motor at standstill and at low speed. The well-known disadvantage is the lack of information at low speed and standstill, which requires the use of specific starting procedures and usually restricts the application to medium-high speed operations. At low speed the back- $EMF$  amplitude is not sufficiently high. Therefore it can not be used to estimate the rotor position and speed informations, as confirmed in Figs. 5.9 - 5.14. For this reason, a starting method is necessary to accelerate the motor to a target speed that allows the back- $EMF$  to be estimated accurately.

In this thesis, an  $I$ -Hz starting method for smooth and fast transition to sensorless field-oriented control is implemented. This control have a good performance and robustness and it is highly recommended for  $PM$  machines. Compared to the  $V/f$  starting method, it prevents the  $PM$  demagnetization because the stator currents are controlled. In  $I$ -Hz control the current is controlled in arbitrary reference frame: the current vector is controlled with a constant value and a frequency profile is imposed. It is important to note that the arbitrary reference frame is different from the rotor one. To explain the idea, consider Fig. 5.18. The rotor reference frame ( $d, q$ ) (physical  $RF$ ) is used in the field-oriented control: the speed of reference frame is equal to rotor electrical speed and the angle between this reference frame and stationary reference frame ( $\alpha, \beta$ ) is equal to the rotor electrical position. Unlike, the arbitrary reference frame ( $d^*, q^*$ ) is not in phase with rotor reference frame and it is rotating at arbitrary speed  $\omega^*$ .

In  $I$ -Hz control the speed is not controlled in closed-loop, as shown in Fig. 5.19. The angular reference frame of rotating magnetic field is imposed with smooth ramp

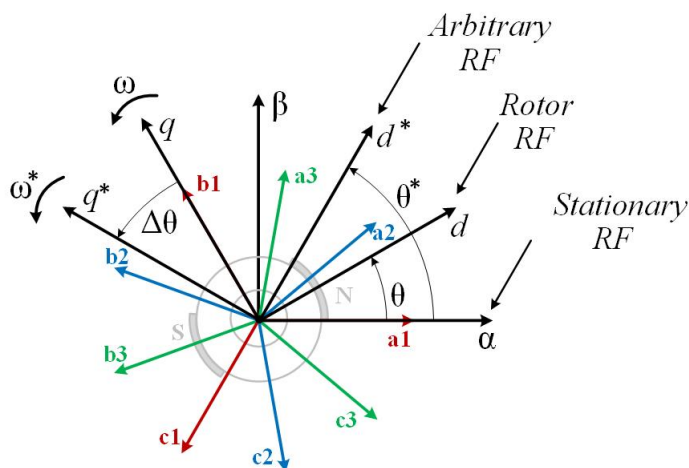
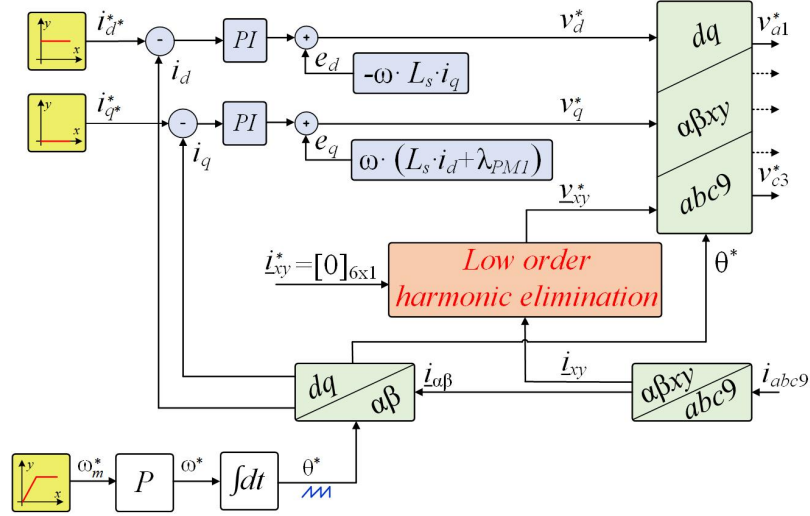


Figure 5.18: Relationship among stationary, rotor and arbitrary  $RF$ s.


 Figure 5.19: Block diagram of  $I$ -Hz starting method.

to a desired speed (yellow block). The desired speed is the value to which the back- $EMF$  can be evaluated accurately. In Section 5.2.1 it is also possible to see how at speed exceeding 300  $rpm$  the rotor position and speed estimations are acceptable. This value represents the desired speed which will be achieved under  $I$ -Hz control.

With reference to Fig. 5.19, the current is controlled in closed-loop with two proportional-integral controllers (blue blocks), presented in Chapter 6.25, Section 3.2 and Subsection 3.3. The result is a rotating vector with imposed frequency. The  $PI$  regulators are employed to control the current in  $(d^*, q^*)$  reference frame. The current references are used to produce a rotating vector which amplitude depends on rated motor current, as shown in Eq. (5.25) where  $I_{s,RMS}$  stands for the rated stator current:

$$\begin{cases} i_{d^*}^* = \sqrt{2} \cdot I_{s,RMS} = I_{s,pk} \\ i_{q^*}^* = 0 \end{cases} \quad (5.25)$$

Furthermore, the vector proportional-integral or proportional resonant regulators are employed to eliminate the low-order harmonics in  $(x, y)$  subplanes, as described in Chapter 6.26, Section 4.3.

The performance of nine-phase surface  $PMSM$  with non-sinusoidal back- $EMF$  under  $I$ -Hz control has been evaluated in *Matlab/Simulink* environment. The parameters of machine model used in simulation are given in Chapter 6.25, Section 6.22, Table 3.1 and in Chapter 6.26, Section 4.2.1, Table 4.1. A friction contribution is included in machine model to consider the dissipation in real system. All mechanical and electrical parameters used in simulation have been experimentally evaluated, as explain in Chapter 6.32. The inputs in *Simulink* model are the mechanical speed reference, the stator current in arbitrary reference frame and the load torque.

The testing sequence of the real machine is presented:

- Initially, the stator current is zero. At 0.05 s the step current change from 0 up to 1.5 A (Fig. 5.22). The amplitude of current references is set in accordance with Eq. (5.25).
- Initially, the speed is zero. At 0.2 s the speed ramp is applied and it is saturated to 300 rpm and for speed exceeding this value the sensorless FOC will be started.
- The simulation is performed without additional load torque and the entire sequence takes 2 s.

In Fig. 5.20 when a ramp speed is applied the response of electrical machine in terms of mechanical speed is shown. The measured speed is characterised by oscillations. The reason of the these is evident: the speed is not controlled in closed-loop and just the reference speed in open-loop is present under  $I$ -Hz control. Furthermore, the PLL output (integral component) does not follow the measured value at low speed. The simulation ends with damped oscillations. At 300 rpm, when these oscillations are enough damped, the rotor reference frame is synchronous to arbitrary one. This does not mean that the two reference frame are in phase.

In Fig. 5.21 the electromagnetic torque is shown: the produced torque is not null. The torque depends on the control algorithm for speed transients and friction contribution when the machine is spinning. The double contributions in friction

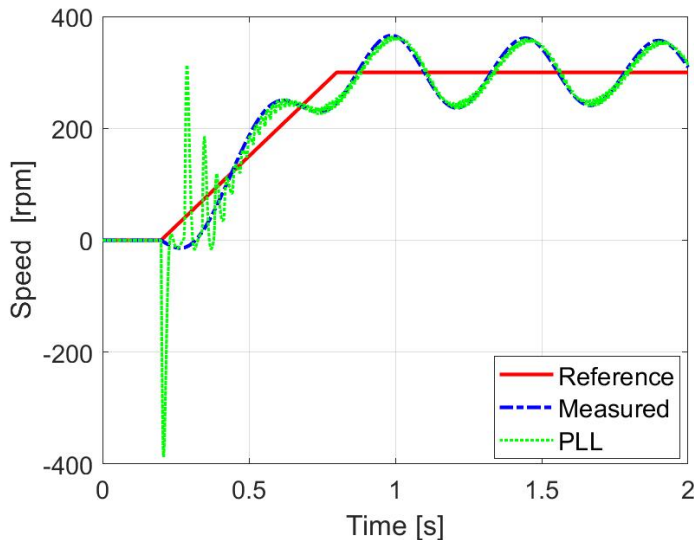
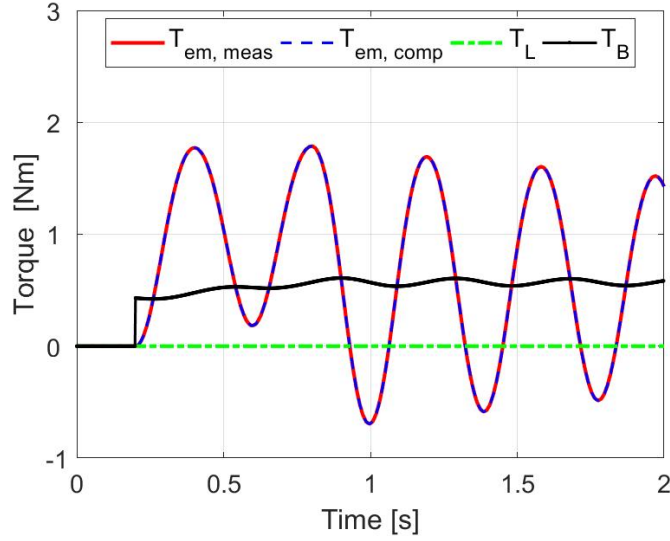


Figure 5.20: Open-loop  $I$ -Hz: speed response.

Figure 5.21: Open-loop  $I$ -Hz: torque response.

torque is evident: a static torque, which depends on the speed sign (offset), and a linear torque, which depends on the rotor speed, presents the oscillations related to the speed. The computed electromagnetic torque is obtained by the product between the  $q$ -axis current in synchronous reference frame and the constant coefficient  $k_1$ , given in Chapter 6.25.

In Figs. 5.22 and 5.23 the stator currents are shown in arbitrary  $(d^*, q^*)$  and rotor  $(d, q)$  reference frames. Thanks to the proportional-integral regulators the currents converge to the reference signals during the  $I$ -Hz control. Comparison of Fig. 5.21 and Fig. 5.23 shows that quadrature axis current  $i_q$  has the same waveform of electromagnetic torque, as well known by the theory presented in Chapter 6.24. Note that the current in  $(d, q)$  rotor reference frame are evaluated on the basis of the estimated rotor position as shown below, despite the  $PLL$  is not accurate.

In Figs. 5.25 and 5.24 the zoom areas of angle are shown. In the top of mentioned figures the obtained angle with  $PLL$  at low speed and at 300 rpm, respectively, are shown. In bottom of these is shown the angle under the same speed conditions, but the angle is demodulated: by applying some mathematical manipulations on the  $PLL$  angle, the rotor position of the machine is obtained. The  $PLL$  output and, consequently, the demodulated angle is not accurate at low speed, making this plots not relevant. This is just the confirmation that at medium speed the  $PLL$  output follows the measured rotor position. However, the shift between the arbitrary reference frame, which rotates at reference speed, and rotor reference frame, which rotates at estimated speed, can be noted in these figures. The angle between rotor reference frame and arbitrary reference frame is not constant during the simulation:

the two reference frames initially are not synchronous and not in phase, unlike when the speed oscillations are damped the reference frames are synchronous.

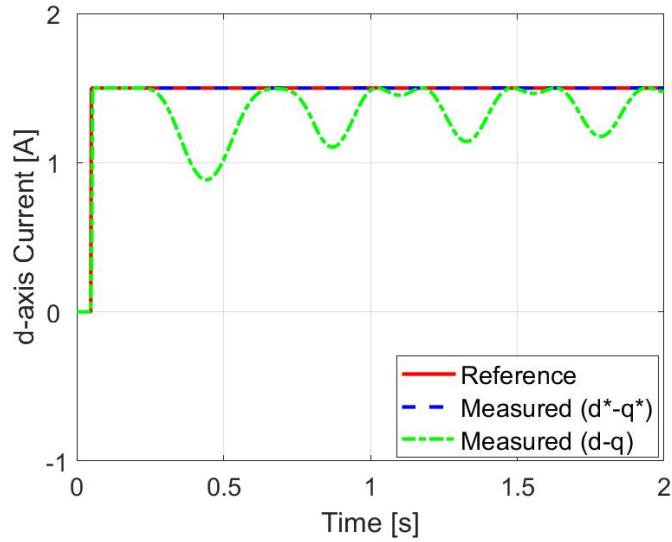


Figure 5.22: Measured current along  $d$ -axis in estimated rotor and arbitrary  $RF$ s.

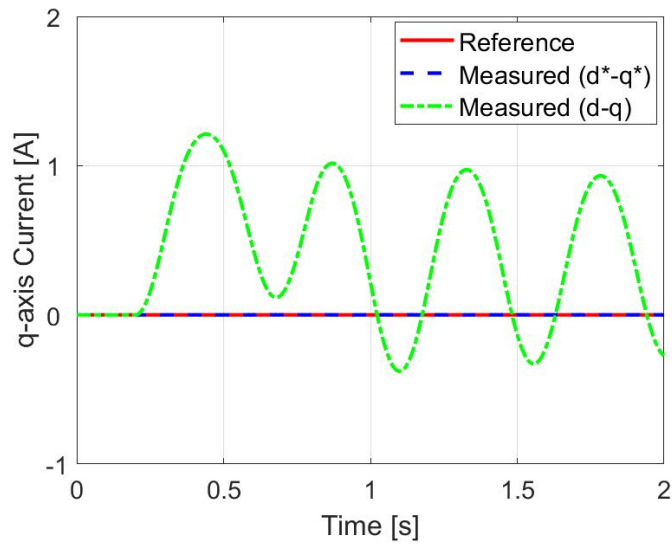


Figure 5.23: Measured current along  $q$ -axis in estimated rotor and arbitrary  $RF$ s.

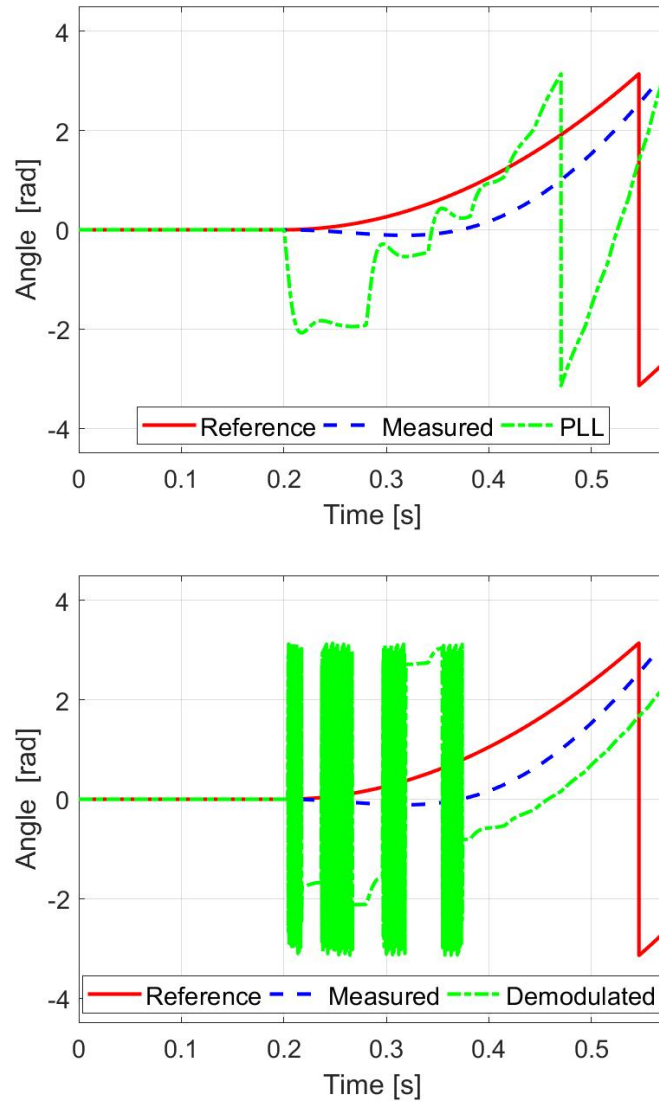


Figure 5.24: Reference, measured and estimated angle in  $I$ -Hz control at low speed. From top to bottom:  $PLL$  output; demodulated.

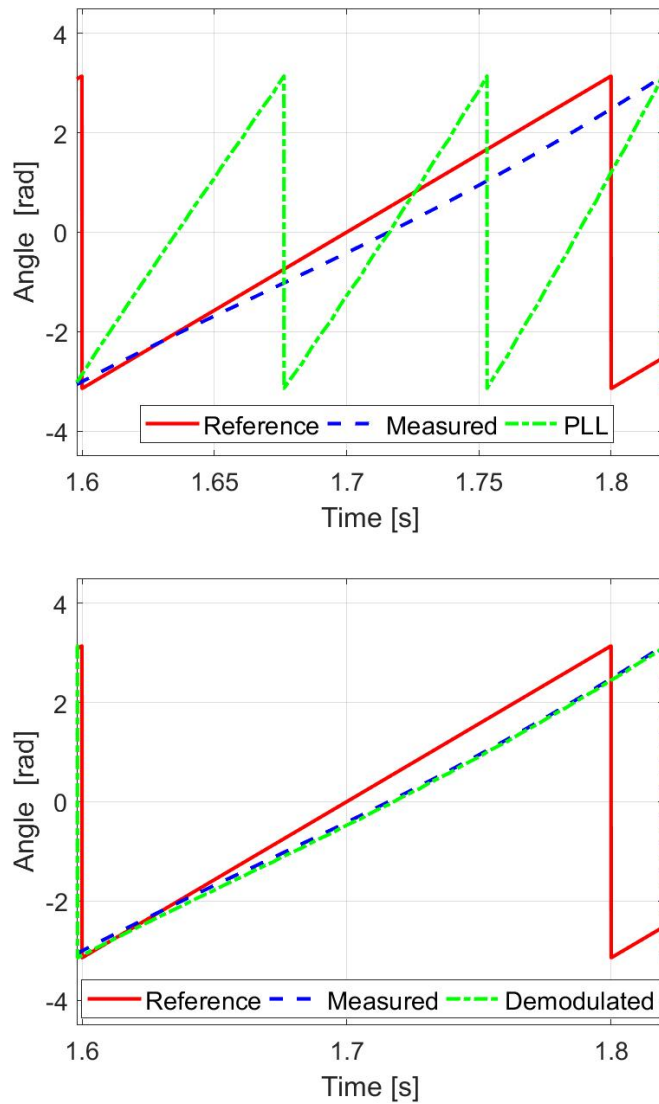


Figure 5.25: Reference, measured and estimated angle in  $I$ -Hz control at high speed. From top to bottom:  $PLL$  output; demodulated.

To conclude, during  $I$ -Hz starting method the estimated speed and angle are not accurately evaluated: the estimated speed is not used in control algorithm, but the  $PLL$  is operating. The input angle to rotational transformation during starting method is the reference angle obtained from speed reference integration. The estimated angle is used in sensorless  $FOC$  after the switch from  $I$ -Hz control to sensorless  $FOC$ , as shown in following sections.

## 5.4 Smooth and Fast Transition to Sensorless FOC

A concern about back-*EMF* method is the transition between open-loop frequency control at low speed and sensorless control at medium-high speed. Several methods can be found in the literature: in [42] a first-order lag compensator is employed to ensure a transition to FOC; in [43] a transient control is employed with electromagnetic torque approximately constant; in [38] the reduction of quadrature reference current in ramp to minimize the orientation error during the transition is employed; in [44] a frequency-dependent gain is used to provide a smooth transition and the convergence depends on the compensator design.

In this thesis, the *I-Hz* starting method for smooth and fast transition to sensorless FOC is proposed. By initializing the sensorless FOC references to measured values evaluated in estimated reference frame, the transition between open-loop frequency and sensorless control is performed. In other words, supposing that the rotor position is correctly estimated during the starting method and in particular when the speed reaches the desired value (300 rpm), the measured stator currents can be evaluated in both arbitrary and estimated reference frames. The measured stator currents are evaluated in estimated rotor reference frame because these values represent the initializing of reference currents in sensorless FOC. At switch instant the reference current values in rotor reference frame are set equal to measured current components evaluated in arbitrary reference frame. After that, the reference currents in sensorless FOC reach the desired references according to a current ramp. As already noted, in surface PMSM the reference current under FOC along *d*-axis is equal to zero and the reference current along *q*-axis is related to speed loop output, as shown in Chapter 6.25, Section 3.2.

The switch takes some conditions, as shown in Fig. 5.26:

- The estimated electrical speed reaches the desired value under *I-Hz* control.

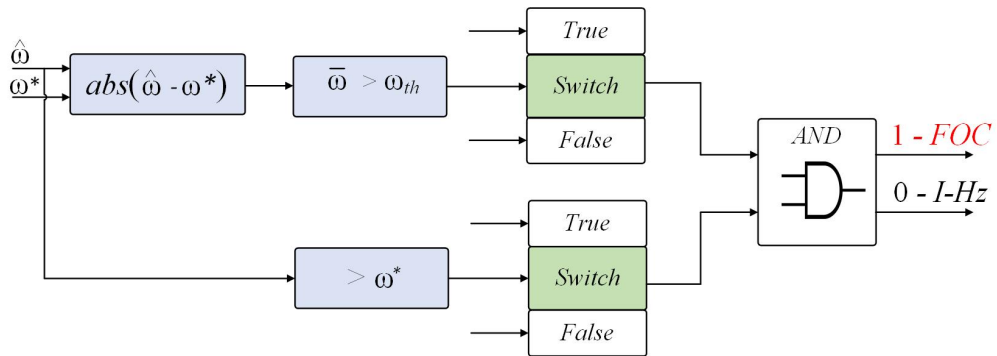


Figure 5.26: Switch conditions from *I-Hz* control to sensorless FOC.

- The oscillations between the estimated speed and its reference value are sufficiently damped. This condition is verified when the mean  $\bar{\omega}$  is higher than an imposed threshold  $\omega_{th}$ . The mean is computed on the absolute value of the difference between the estimated electrical speed and its reference value.

The performance of the transition has been evaluated in *Matlab/Simulink* environment. The electrical parameters of surface *PMSM* are consistent with the ones defined in previous chapter. In addition, the control scheme has been fully discretized using both Euler and Tustin integration method. However, to use the *PLL* output in speed loop regulation, it has been necessary to introduce a low-pass filter for estimated speed.

The simulation results presented below will include the switch instant and the transition stage. The time transition is the necessary interval so that the reference currents and speed reach the desired values under sensorless *FOC*. The switch and transition are detailed in Fig. 5.27 - 5.30.

In Figs. 5.27 and 5.28 it is possible to note that at switch instant initial conditions and target values under *FOC* along *d*-axis and *q*-axis are different. The consequence is evident: the time necessary to achieve the desired reference values in sensorless *FOC*, called *Transition (Trans.)*, is not the same. This interval depends on the slope ramp of the current and its measured value at switch instant. The current ramp must ensure a smooth transition between *I-Hz* and sensorless control. Finally, in Fig. 5.30 the transition interval is the time necessary to achieve the reference value (300 rpm) under sensorless *FOC*.

In top of Figs. 5.27 and 5.28 the reference and measured response of the current along *d*-axis and *q*-axis, respectively, are shown. The measured currents are evaluated in both reference frame, as mentioned above. In Figs. 5.27 (bottom) and 5.28 (bottom) the *PI* initializations of current loop regulations under sensorless *FOC* are highlighted. At switch instant the reference currents take instantly the measured values evaluated in estimated rotor reference frame (*d, q*). After that, in accordance with current ramp, the target value along *d*-axis ( $i_d^* = 0$ ) is reached. Conversely, the reference current along *q*-axis under second control depend on reference torque, which represents the speed control output, as shown in Eq. (5.26). All symbols are consistent with the ones defined in previous chapters.

$$i_q^* = T_{em}^* \cdot \tilde{k}_1, \quad \tilde{k}_1 = \frac{2}{9} \cdot \frac{1}{P \cdot \tilde{\lambda}_{PM}} \quad (5.26)$$

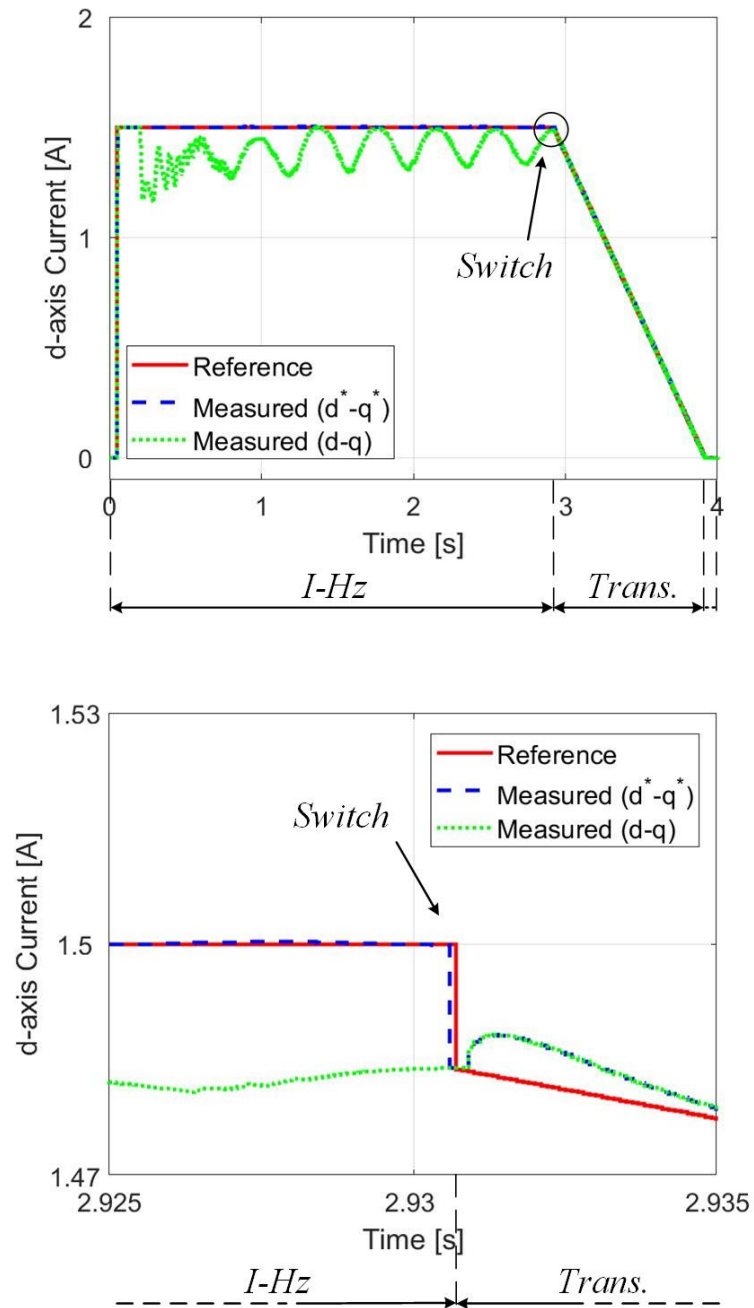


Figure 5.27: Measured current along estimated  $d$ -axis in transition to sensorless FOC. From top to bottom: the time trend; corresponding zoom.

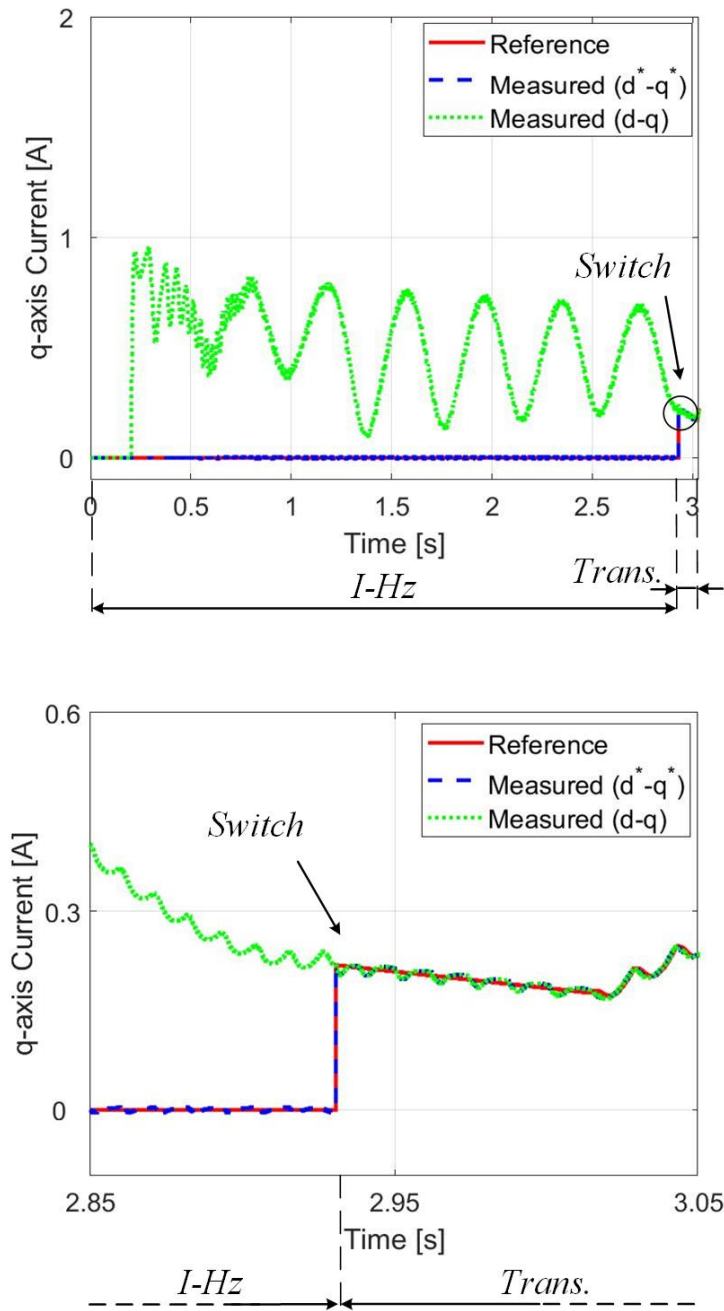


Figure 5.28: Measured current along estimated  $q$ -axis in transition to sensorless FOC. From top to bottom: the time trend; corresponding zoom.

In Fig. 5.29 the phase currents in  $a1$ ,  $a2$  and  $a3$  windings, which are shifted for  $2\alpha/9$ , are shown. It is possible to note the effectiveness of the vector proportional integral or proportional resonant controllers employed in  $(x,y)$  subplanes to eliminate the other harmonics contributions. The current waveforms are perfectly sinusoidal and under  $I$ -Hz control their amplitude is equal to the reference current along  $d^*$ -axis (i.e.  $1.5\text{ A}$ ), while after the switch instant the amplitude of the phase currents depend on the speed loop output.

In Fig. 5.30 the reference, measured speed response and  $PLL$  output are shown. Note that the  $PLL$  output follows the actual value at speed exceeding  $200\text{ rpm}$ , thus demonstrating the effectiveness of the  $PLL$  for medium-high speed. In particular, the small temporary speed drop (about  $100\text{ rpm}$ ) due to the switch operation can be also seen.

To conclude, the employed switch strategy allows at avoiding undesired transients during the transition, as confirmed in Figs. 5.27 - 5.30.

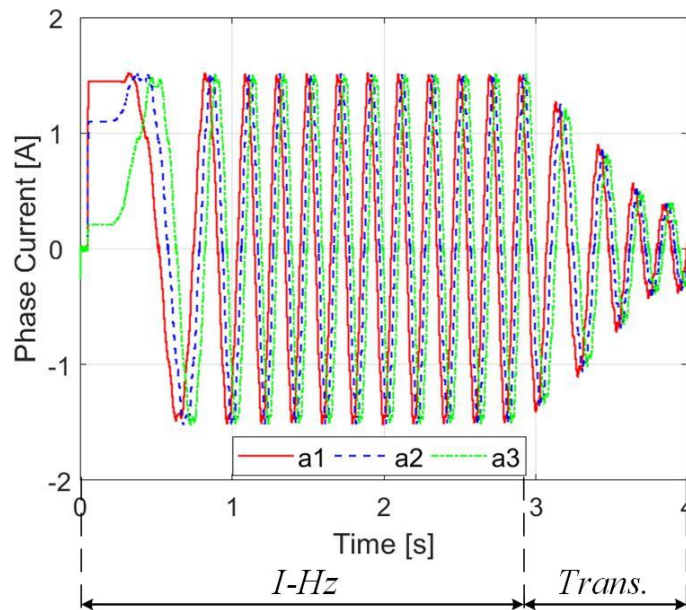


Figure 5.29: Transition to sensorless FOC: phase currents.

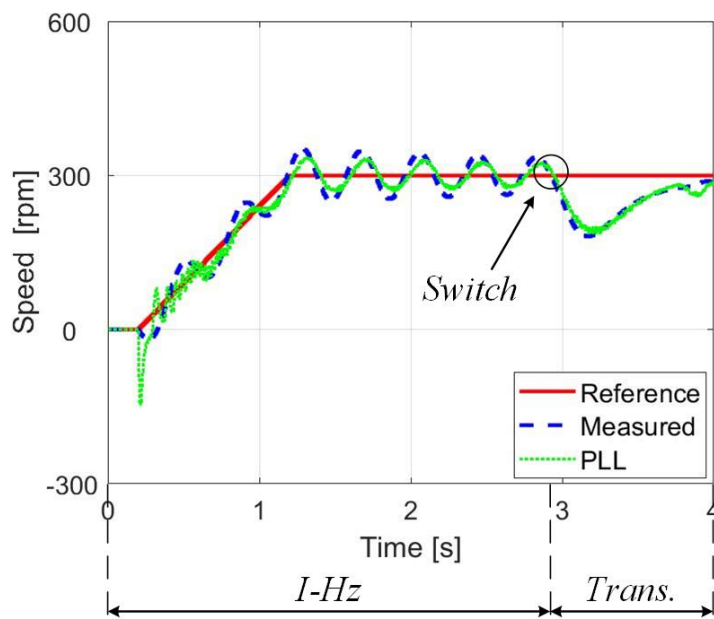


Figure 5.30: Transition to sensorless *FOC*: speed response.



up to 300 *rpm* with ramp function. The speed is not controlled in closed-loop under *I-Hz* control and all switches are connected to terminal 1. At switch instant all switches are connected to terminal 2: the speed is controlled in closed-loop because the speed loop is activated. At time exceeding the automatically switch and the transition interval, the speed is increased. Therefore, when the system is operated in sensorless field-oriented control the ramp command is employed: at 4.5 *s* the speed value varies from 300 *rpm* to 1500 *rpm*.

- Initially, the rotational transformation input is the reference angle under *I-Hz* control, obtained as result of speed reference integral. The open-loop frequency control is field at switch instant. In the second control the *PLL* output represents rotational transformation input.
- Initially, the stator current is zero. At 0.05 *s* its value is increased up to 1.5 *A* (yellow block in Fig. 5.31). The current components in  $(d^*, q^*)$  reference frame are controlled with *PI* regulators. At switch instant all switches are connected to terminal 2 and the new references (orange blocks) are shown in Fig. 5.31. The reference currents change in accordance to the current ramp and the desired quantities under sensorless *FOC* are achieved: the references along *d*-axis and *q*-axis depend on the principle control and reference electromagnetic torque in surface *PMSM*, respectively.
- The simulation is performed without load torque. The friction and inertia contributions are added to consider the dissipation in real system, obtained according to the *Test rig Characterization*, presented in Chapter 6.32, Section 6.2.4.

In Fig. 5.32 (top), when a ramp speed is applied under *I-Hz* control, at low speed the *PLL* output is not aligned with measured value. For this reason, this quantity is not an input of the speed loop, but the speed is imposed in open-loop, as shown in Section 5.3. At about 3 *s*, when the switch conditions are verified, the speed loop regulation is activated and in transition interval the small temporary speed drop is shown. Therefore, in sensorless *FOC* the *PLL* output follows measured value precisely. The measured and estimated value in sensorless *FOC* do not follow perfectly the reference for speed transients.

In Fig. 5.32 (bottom) the electromagnetic torque is shown. In the first control the reference electromagnetic torque is zero because the speed loop is not activated. It should be noted once again that the reference electromagnetic torque is speed loop output. The other way around, its measured value is characterised by oscillations due to the speed open-loop, as confirmed by speed oscillations. The electromagnetic torque, when the motor is spinning, is related to the load torque, friction contribution and inertia in speed transients.

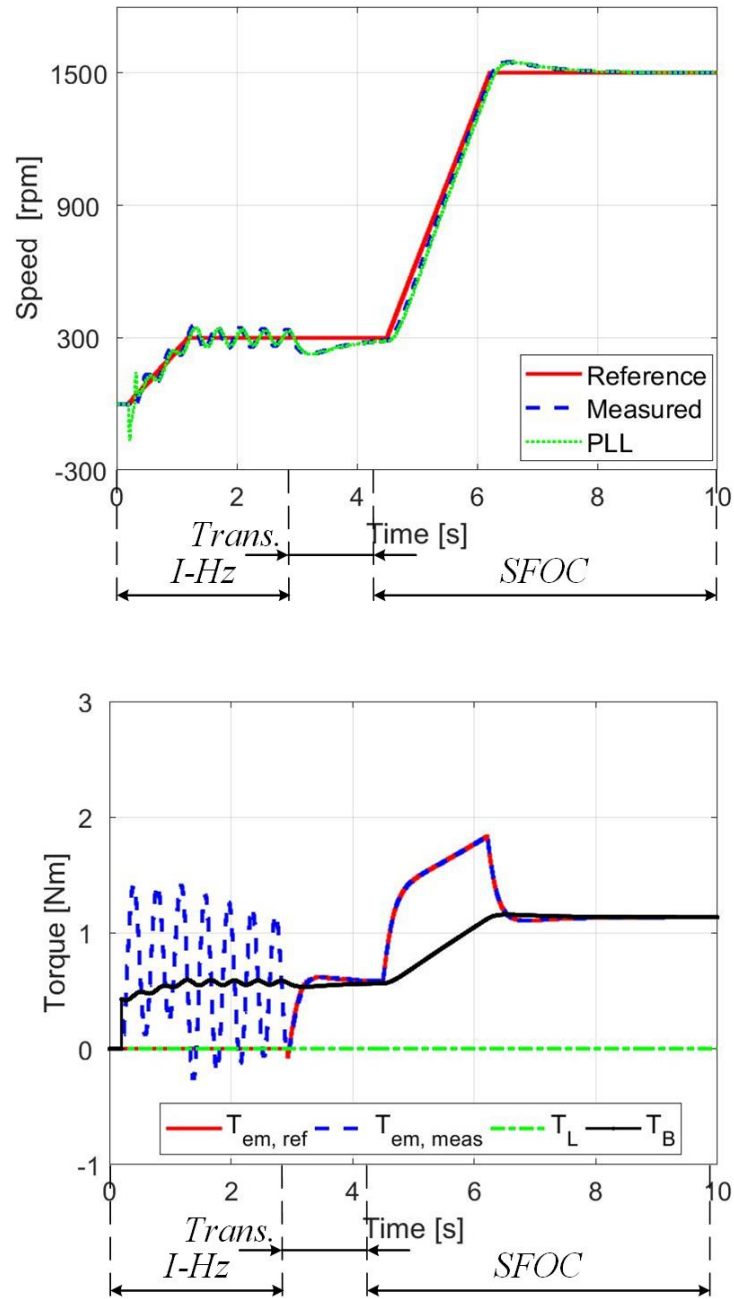


Figure 5.32: Hybrid control under no-load conditions. From top to bottom: speed response; torque response.

In Fig. 5.33 (top) the angle error in hybrid control is shown. The error is computed as difference between the measured angle and its estimated value. It shall be possible to observe that the angle error under  $I$ -Hz control is about  $7 - 8^\circ$ , which becomes about  $1.5^\circ$  under sensorless control at medium-high speed. This value is in line with the typical error in sensorless control.

In Fig. 5.33 (bottom) the zoom area of the rotor position is shown during the transition interval. The  $PLL$  output is three times faster than measured rotor position related to the  $PLL$  input. Using the demodulation block diagram (Fig. 5.7), demodulated angle follows the measured signals, demonstrating the effectiveness of  $PLL$  and the demodulation algorithm.

As mentioned above, the  $PLL$  input is the estimated back-EMF in third subplane, which corresponds to the reference command voltage, using the relation  $\underline{v}_{xy3}^* \simeq \hat{\underline{e}}_{xy3}$  (Section 5.2). The vectors amplitude  $\hat{\underline{e}}_{xy3}$  and  $\underline{e}_{xy3}$  are shown in top of Fig. 5.34. The amplitude of the computed vector in third subplane  $\underline{e}_{xy3}$  is obtained on the basis of the measured rotor speed and position, using the model shown in Chapter 6.26, Section 4.2.2. The other way around, the  $PLL$  input  $\hat{\underline{e}}_{xy3}$  represents the amplitude of the command control vector in third subplane. It is noted that the time trend of the amplitude is proportional to the machine speed (Fig. 5.32 (top)). The reason is evident: the back-EMF force depends on the rotor motion, as mentioned above.

In Fig. 5.34 (bottom) the phase error is computed as difference between the phase of both vectors  $\hat{\underline{e}}_{xy3}$  and  $\underline{e}_{xy3}$ . It is noted that except for the starting operation, in which the phase angle error is not relevant, after the switch instant (about 3 s) the phase error is acceptable being lower than 5 electrical degrees (typical acceptable threshold in sensorless control).

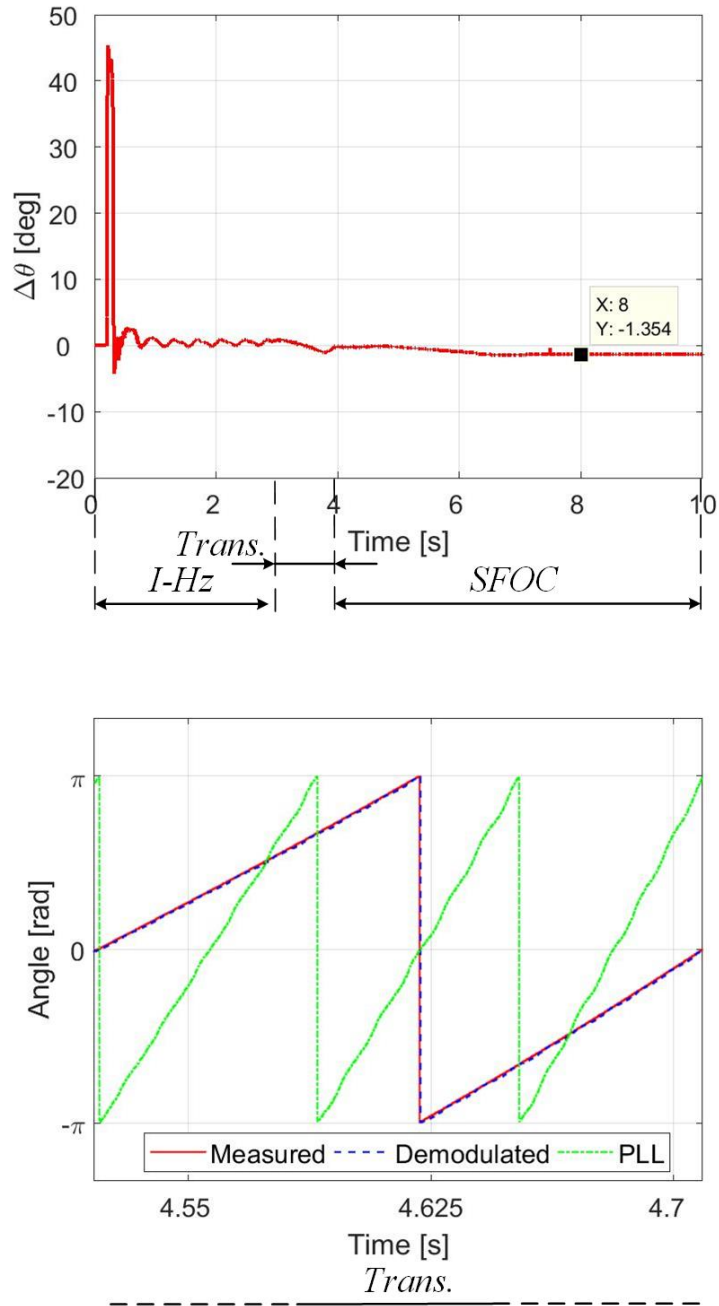


Figure 5.33: Hybrid control under no-load conditions. From top to bottom: angle error; zoom area of the angle.

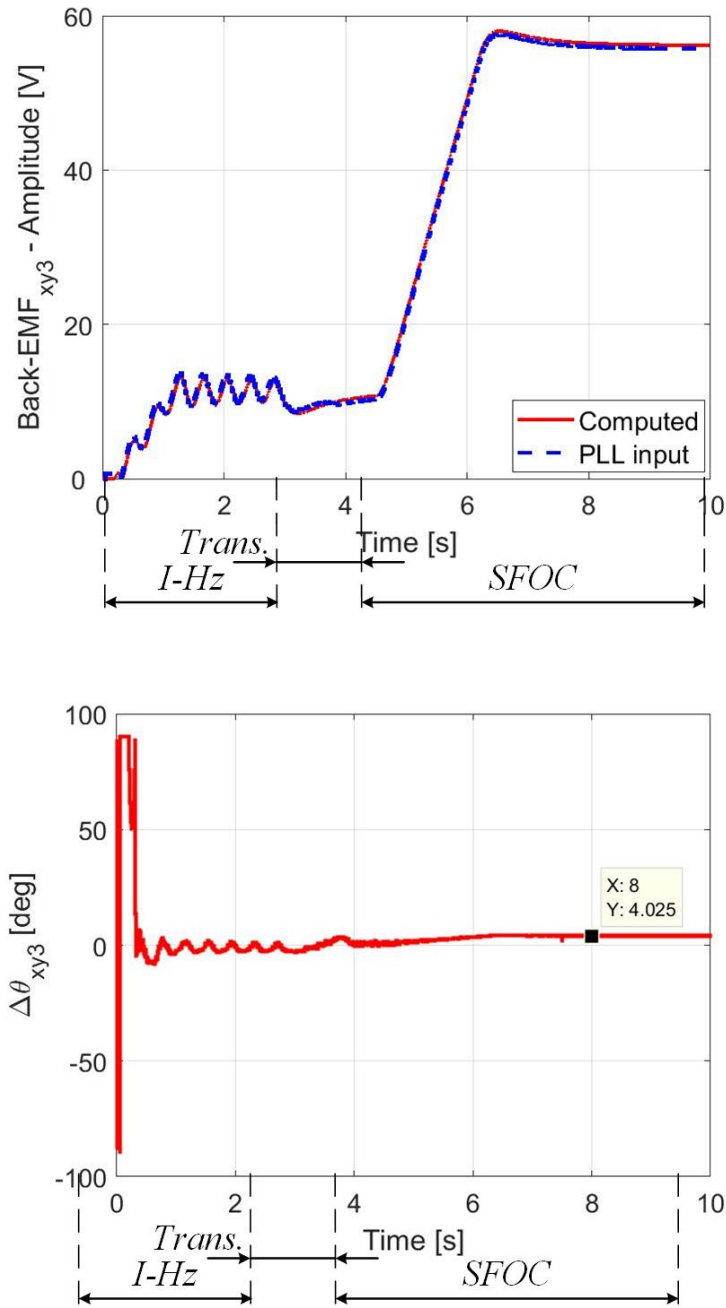


Figure 5.34: Hybrid control under no-load conditions. From top to bottom: vector  $\underline{e}_{xy3}$  magnitude; phase error.

In Fig. 5.35 the flux and torque producing currents are shown. During the  $I$ -Hz control the waveforms are the time trends of the measured currents evaluated in estimated rotor reference frame  $(d, q)$ . As well-know, in sensorless  $FOC$  the flux producing  $i_d$  is equal to zero, while the torque producing  $i_q$  follows the electromagnetic torque. The latter consideration is confirmed by comparison between Fig. 5.32 (bottom) and Fig. 5.35 (bottom).

Finally, to demonstrate the effectiveness of the  $VPI$  during the hybrid control at any speed and control type, in Fig. 5.36, the phase current in phase variable domain are also shown. The sinusoidal waveform of the phase current is highlighted in Fig. 5.36 (bottom). With reference to Fig. 5.37 (bottom), it is noted how the phase voltage references are characterized by strong distortion. Indeed, these must compensate the harmonic distribution of the back- $EMF$  and the phase voltage error introduced by the voltage supply inverter.

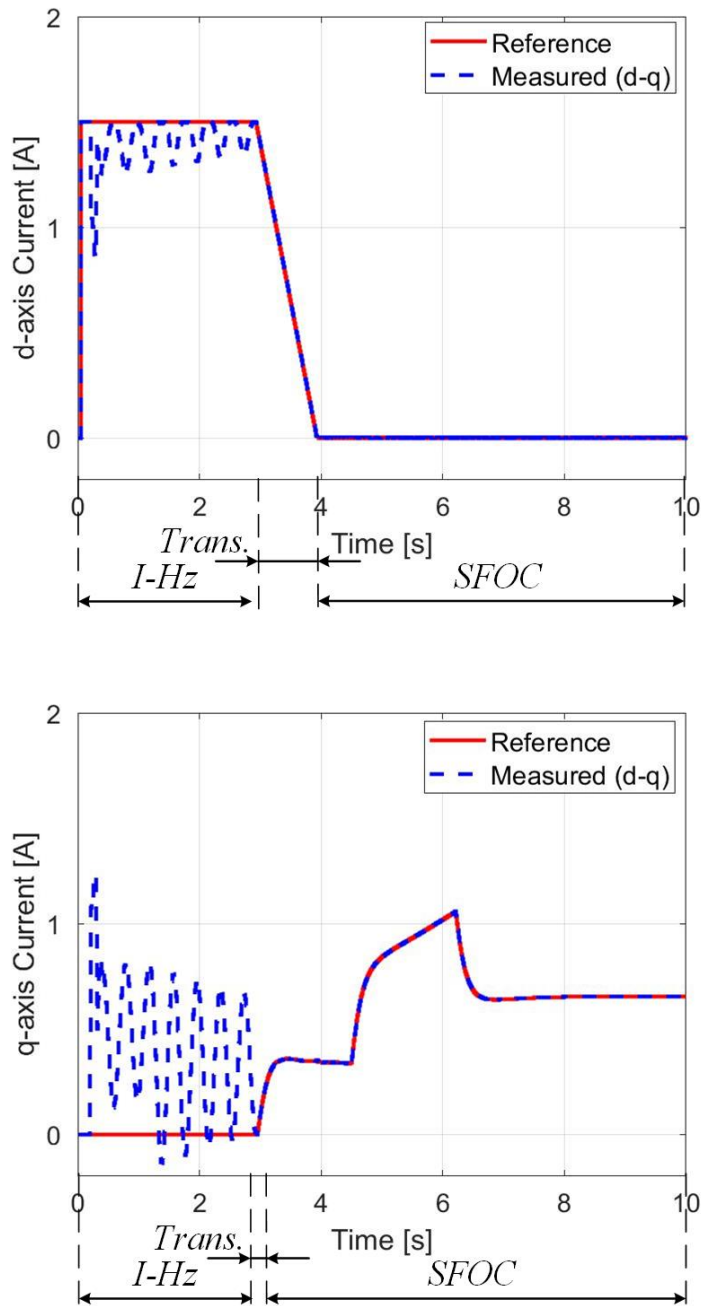


Figure 5.35: Measured currents in estimated rotor  $RF$ . From top to bottom:  $d$ -axis;  $q$ -axis.

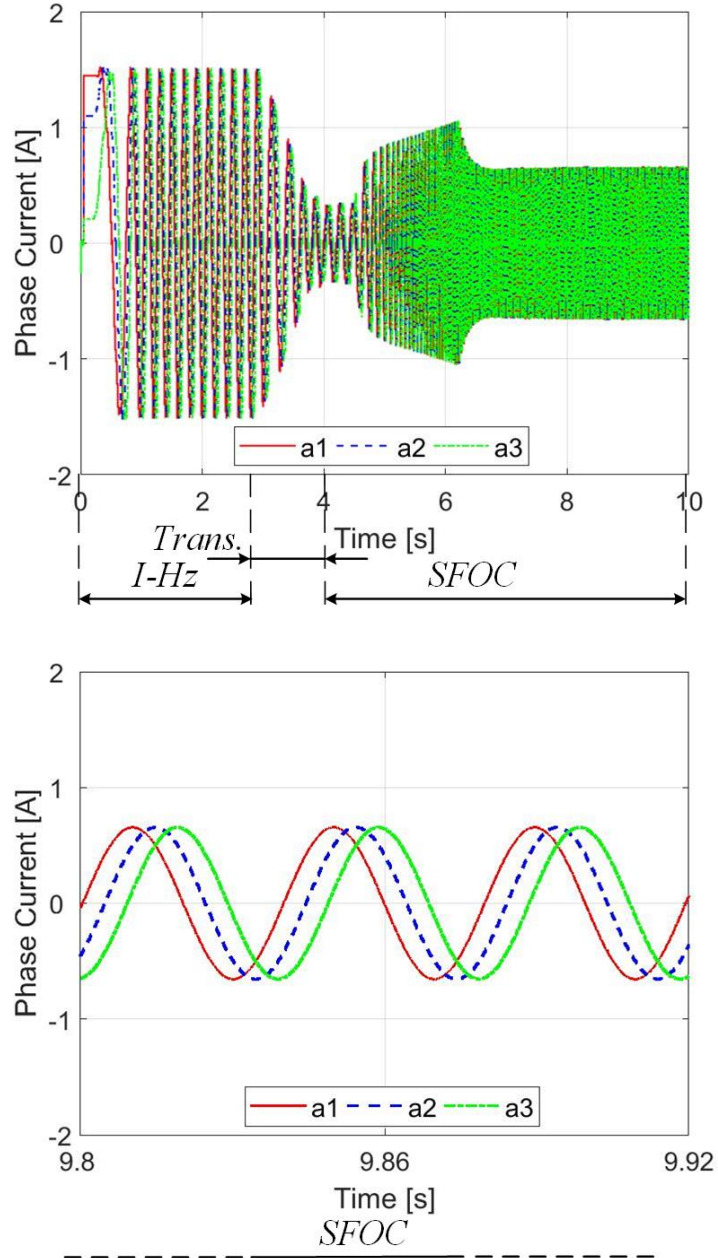


Figure 5.36: Hybrid control under no-load conditions. From top to bottom: phase current responses; corresponding zoom area.

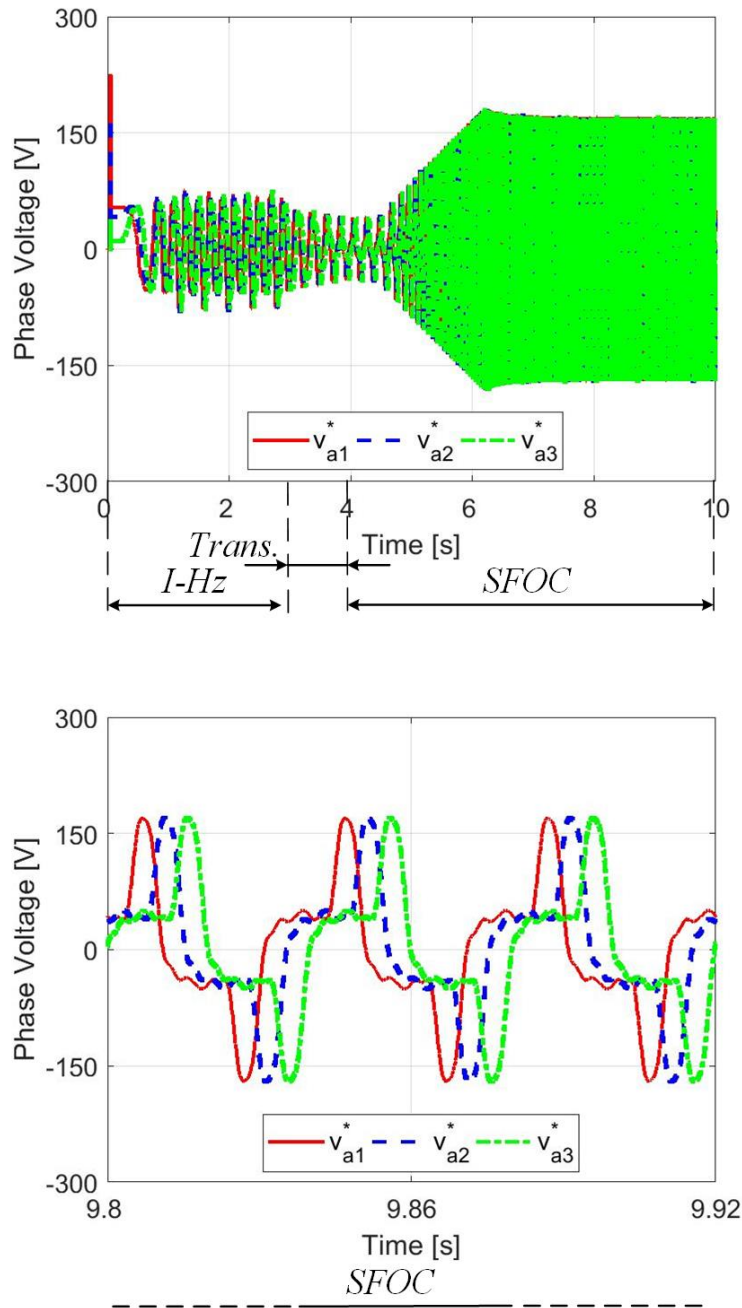


Figure 5.37: Hybrid control under no-load conditions. From top to bottom: phase voltage references; corresponding zoom area.

In addition to already explained simulation another test with load torque is performed. The load torque can be set, as shown in testing sequence in Fig. 5.38 (bottom). All the others inputs are consistent with the ones defined in previous simulation. In this test at 7.5 s a step load torque (about nominal torque) is added, corresponding to the temporary speed drop (about 150 rpm). It can be noted how the speed control is perfectly able to recover the speed drop according with the design of the *PI* speed loop regulation gains.

To conclude, the implemented hybrid control of the machine in *Matlab/Simulink* environment achieves desired dynamic response. This means that the rotor speed and position are correctly estimated with employed *PLL* for medium-high speed. Indeed, the estimated quantities are perfectly aligned with the measured quantities, therefore the sensorless control works properly at medium-high speed. At speed exceeding 300 rpm the control, completely sensorless, is characterised by satisfactory dynamic. As can be seen from the figures, the fast response and absence of overshoot confirms the effectiveness of employed control.

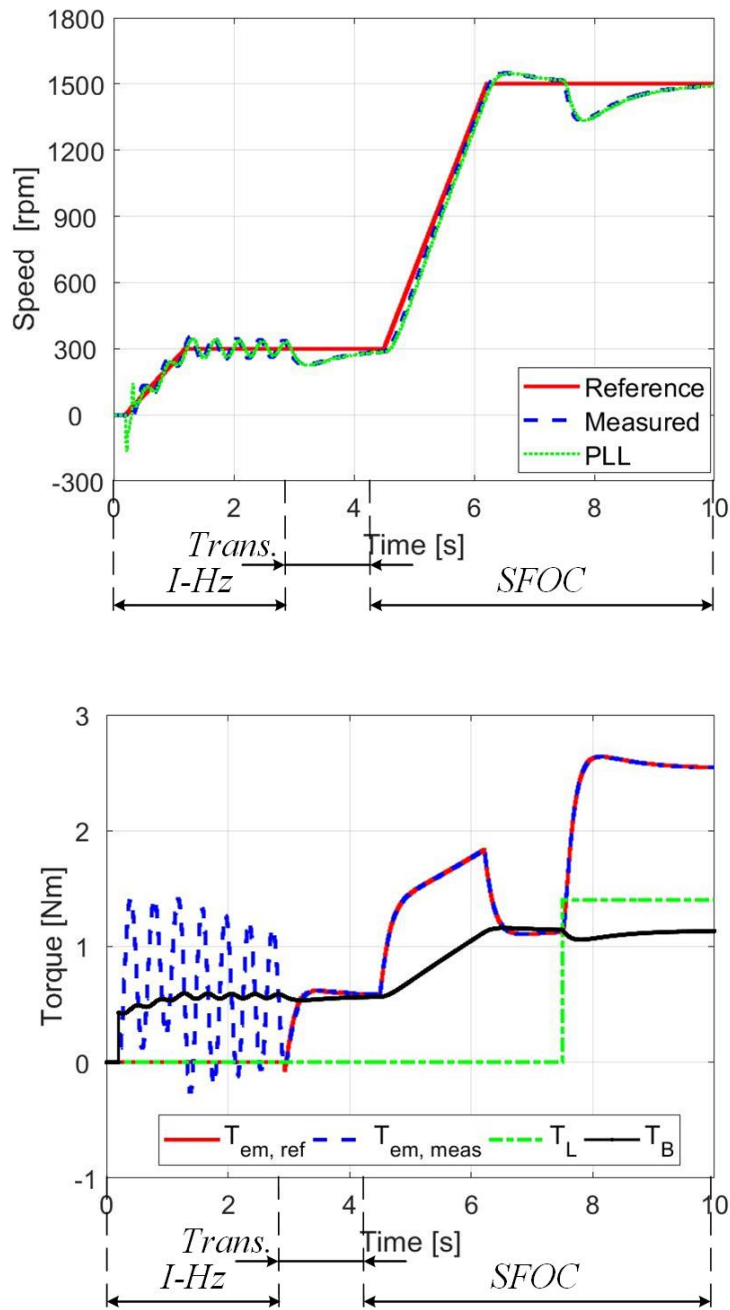


Figure 5.38: Hybrid control under load conditions. From top to bottom: speed response; torque response.

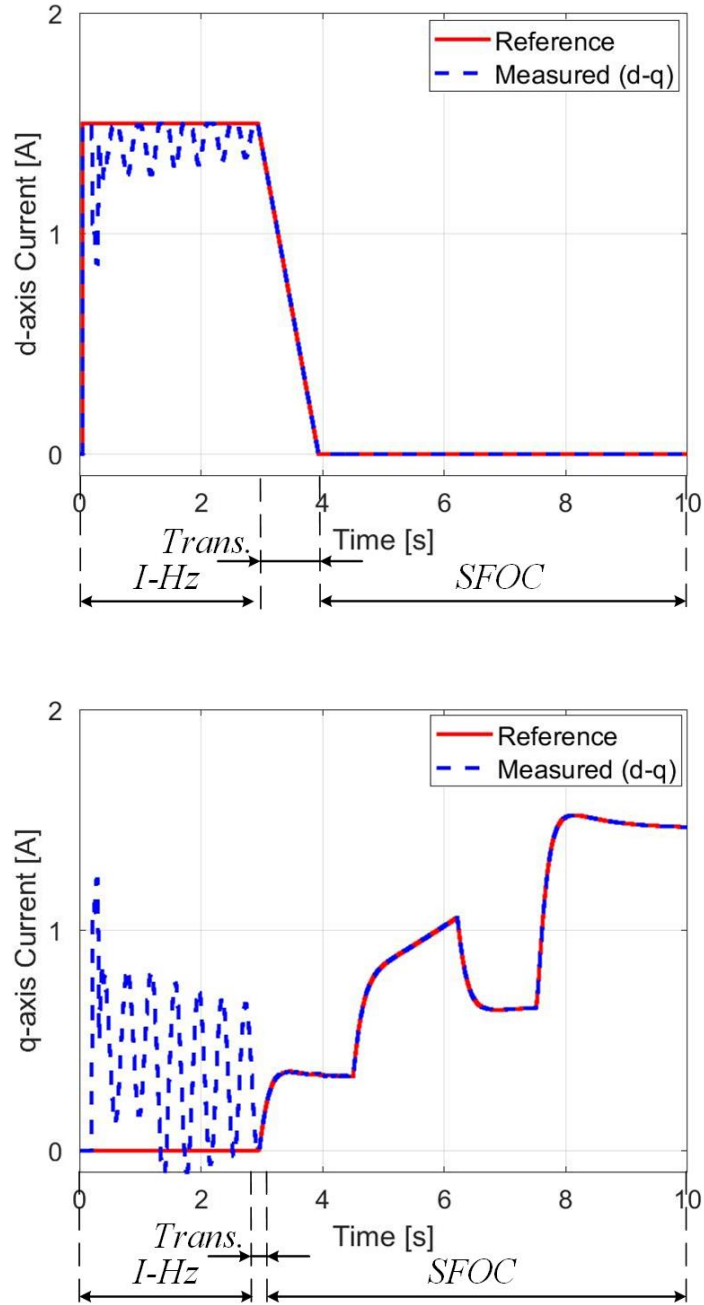


Figure 5.39: Measured currents in estimated rotor RF. From top to bottom:  $d$ -axis;  $q$ -axis.



# Chapter 6

## Experimental Validation

In this chapter the experimental characterization of the machine, test rig parameters and the experimental validation of the hybrid control scheme for symmetrical nine-phase surface *PMSM* with non-sinusoidal back-*EMF* is dealt.

Chapter is organised as follows:

- In Section 6.1 the main elements of the test rig are presented.
- In Section 6.2 the tests to obtain the mechanical and electrical data of the machine are shown.
- In Section 6.3 the experimental validation of the hybrid control scheme is dealt.

## 6.1 Test rig

The hybrid control is validated on real nine-phase surface *PMSM* with highly non-sinusoidal back-*EMF*. The experimental validation is obtained using a test rig composed of the following elements:

- Nine-phase surface *PMSM*.
- Two voltage supply inverter.
- Digital controller.

To validate the hybrid control, the rotor shaft of the machine under test has been coupled to a permanent magnet dc machine acting as mechanical active load, as shown in Figs. 6.1 and 6.2. The mechanical and electrical data of the machine correspond to the ones provided in Chapter 6.25, Section 6.22, Table. 3.1 obtained with the tests presented below.

Namely, the machine is supplied by two 2-level six-phase *VSI* in the same manner as shown in Fig. 6.1. *VSI*s are supplied by single voltage dc link created by *Sorensen SGI 600/25*, which provides a supply equal to 450 V. The power converter consists of two custom-made inverters, based on Infineon *FS50R12KE3 IGBT* modules fed by the power source. The inverters have hardware-implemented dead time equal to 6  $\mu$ s. The dc power source, which consists of a programmable voltage source, and *VSI*s are shown in Fig. 6.3 and 6.4, respectively.

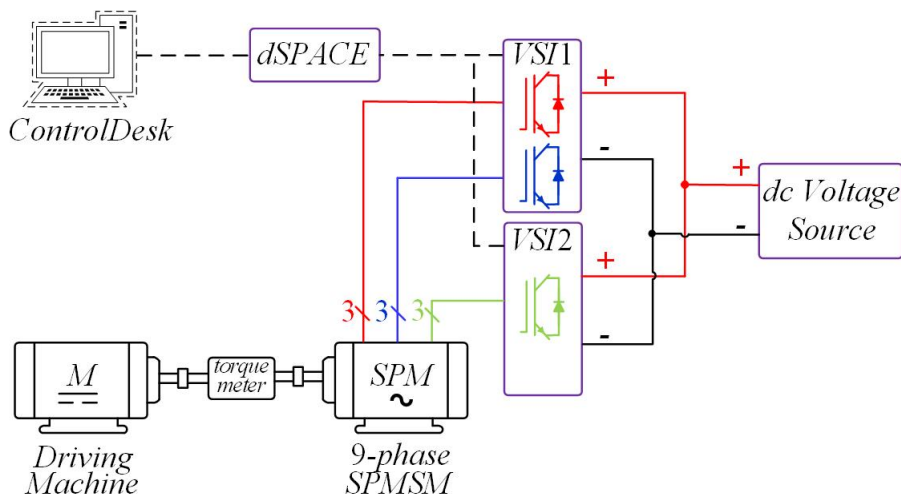


Figure 6.1: Block diagram of experimental setup.

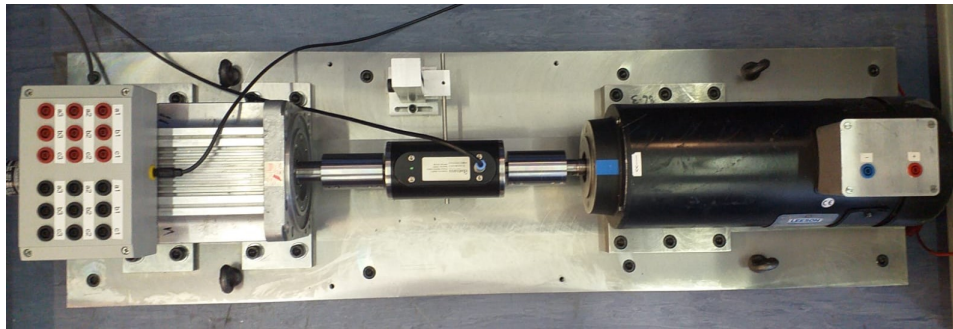


Figure 6.2: The machine under test (left) and the driving machine (right).



Figure 6.3: dc voltage source *Sorensen SGI 600/25*.

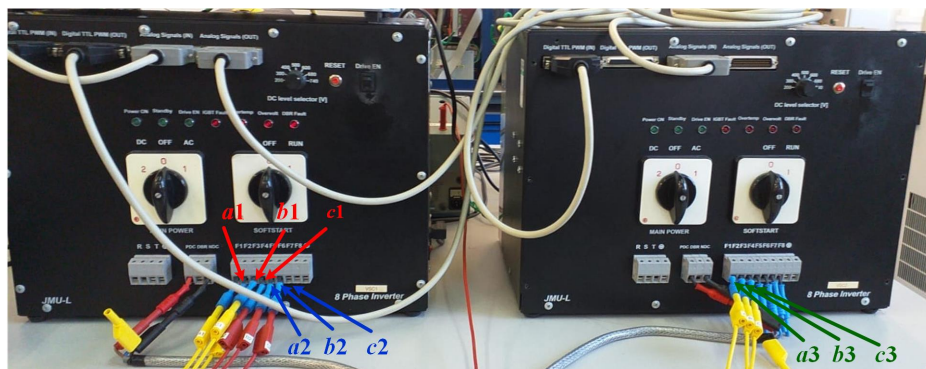


Figure 6.4: Modular power converter.

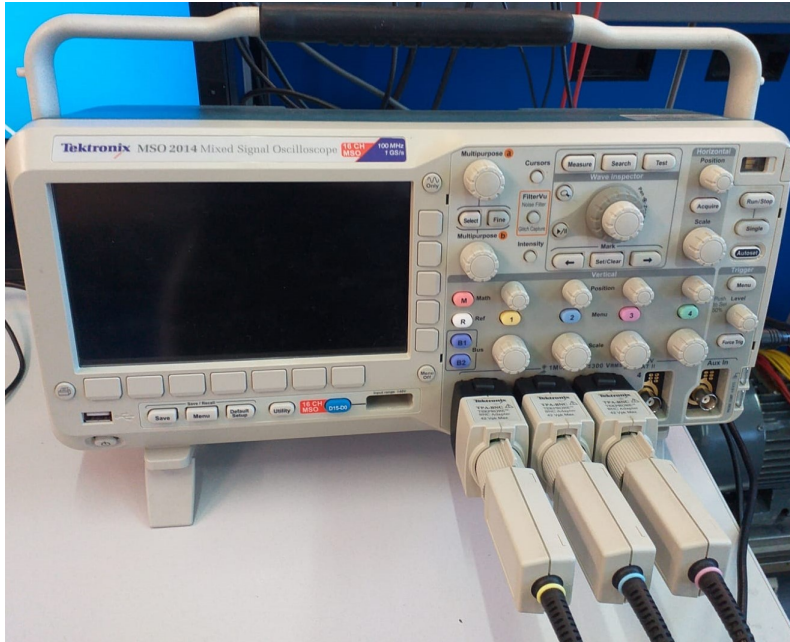


Figure 6.5: *Tektronix* oscilloscope.

Control and measurement are performed by a *dSPACE* rapid prototyping system, while additional measurements are available through *Tektronix* oscilloscopes *MISO2014* (Fig. 6.5) and isolated current and high voltage differential voltage probes. *dSPACE* consists of main processor board *DS1006* and multiple peripheral boards:

- *DS5101*, digital waveform output board, used for gating signal generation.
- *DS2004*, analogue to digital converter board, used for current/voltage measurements.
- *DS3002*, encoder board, used for capturing encoder pulses and finding position and speed.
- *DS101*, digital to analogue converter board, used to provide synchronisation with oscilloscopes.

All experiments conducted in the thesis are initially tested by simulation in *Simulink* environment. Since *dSPACE* workflow is capable of using *Simulink* files by means of *Simulink Coder*, initial *Simulink* file is adapted by removing blocks that simulate hardware physically available in the laboratory and adding *dSPACE* specific blocks to create an interface to the *dSPACE* peripheral boards. This enables

execution of the developed control on *dSPACE* processor board *DS1006*, while all user inputs are provided by graphic user interphase developed in *Control Desk*. The machine model, *VSI* model, and *PWM* modulator are removed. Generated interrupt triggers, the timer task and whole control code is executed. Furthermore, interrupt is synchronised with *PWM* signals so that control code is executed exactly at the beginning and in the middle of the switching period . By doing so, *dSPACE* sampling/execution frequency ( $10\text{ kHz}$ ) is double the switching frequency ( $5\text{ kHz}$ ).

Last but not least, graphic user interface to the *dSPACE* platform is created by *Control Desk*. This software allows for real time access to the control variables. An example of the developed graphic user interface is shown in the Fig.6.6. All basic drive controls can be seen, such as: turn the drive on/off, set a speed reference, set a inverter nonlinear compensation, set a slope ramp.

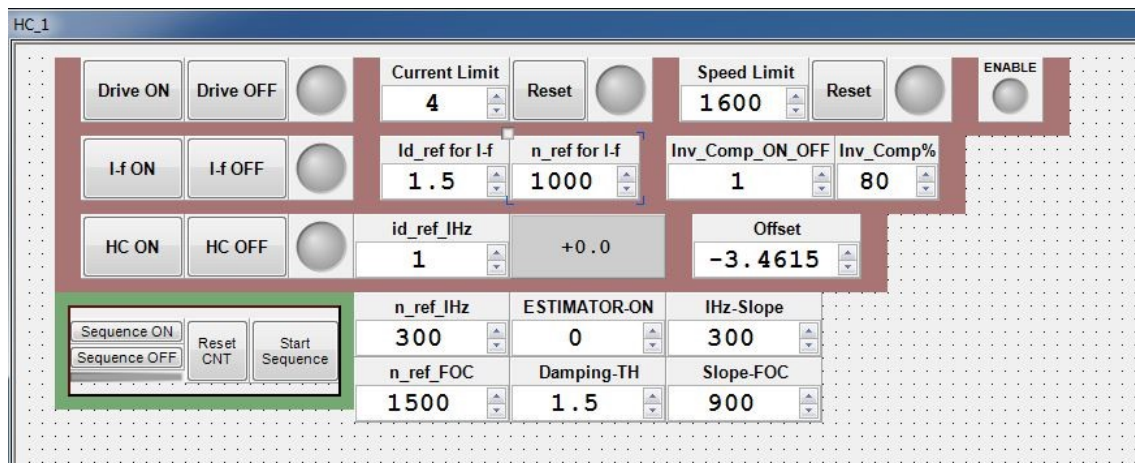


Figure 6.6: Example of the graphic user interface developed in *Control Desk*.

## 6.2 Characterization of the Machine Parameters

The accurate simulation and control of *PMSM* requires accurate knowledge of the electrical machine parameters. The machine parameters are obtained with several experimental tests. The tests carried out are as follows:

- Zero-Sequence Test,
- Single Phase Test,
- Short Circuit Test and Design approach and
- Test rig characterization.

The parameters measurement for multiphase *PMSM* is performed by means of mentioned offline tests.

Finally, it is recalled that the back-*EMF* is presented in Chapter 6.25 on the basis of the recorded data, obtained in no-load condition and open-winding configuration.

### 6.2.1 Zero-Sequence Test

The aim of zero-sequence test is to obtain the leakage inductance value, useful in machine modelling and in machine control. In this test, the machine rotor is locked while the single set  $i$  ( $i = 1, 2, 3$ ) is supplied with an alternate voltage source: *Spitzenberger Spies* PAS2500 linear power amplifier. The voltage and currents measurements are performed by *Tektronix* oscilloscopes.

In zero-sequence equivalent circuit the following considerations shall in particular be taken into account. Consider that the total flux is due to the permanent magnet flux and the stator currents in the windings, it can be modelled as:

$$\begin{aligned} [\lambda_{abc9}] &= [[L_{ss}] \cdot [i_{abc9}] + \lambda_{PM,abc9}] = \\ &= [L_{ls}] \cdot [i_{abc9}] + [M_{ss}] \cdot [i_{abc9}] + [\lambda_{PM,abc9}] \end{aligned} \quad (6.1)$$

where all symbols are consistent with the ones defined in previous chapters.

The single set  $i$  is supplied and the consequence is evident: the mutual inductance contribution present in Eq. (6.1) is related to the windings belonging to the same supplied set  $i$  and the time derivative permanent magnet contribution is zero because it is related to the rotor motion. Consider the first set (set 1:  $a1, b1, c1$ ), the mentioned equation can be written now as:

$$[\lambda_{a1b1c1}] = [L_{ls}] \cdot [i_{a1b1c1}] + [M_{ss,a1b1c1}] \cdot [i_{a1b1c1}] + [\lambda_{PM,a1b1c1}] \quad (6.2)$$

Delivering the matrix form in Eq. (6.2), the following equation system is obtained:

$$(6.3) \quad \left\{ \begin{array}{l} \lambda_{a1} = L_{ls} \cdot i_{a1} + M_I \cdot (i_{a1} \cdot \cos(\theta_{a1} - \theta_{a1}) + i_{b1} \cdot \cos(\theta_{a1} - \theta_{b1}) + \\ \quad + i_{c1} \cdot \cos(\theta_{a1} - \theta_{c1})) + \lambda_{PM1} \cdot \cos(1 \cdot (\theta - 0 \cdot \alpha) + \theta_{sh1}) + \dots + \\ \quad + \lambda_{PM13} \cdot \cos(13 \cdot (\theta - 0 \cdot \alpha) + \theta_{sh13}) \\ \lambda_{b1} = L_{ls} \cdot i_{b1} + M_I \cdot (i_{a1} \cdot \cos(\theta_{b1} - \theta_{a1}) + i_{b1} \cdot \cos(\theta_{b1} - \theta_{b1}) + \\ \quad + i_{c1} \cdot \cos(\theta_{b1} - \theta_{c1})) + \lambda_{PM1} \cdot \cos(1 \cdot (\theta - 3 \cdot \alpha) + \theta_{sh1}) + \dots + \\ \quad + \lambda_{PM13} \cdot \cos(13 \cdot (\theta - 3 \cdot \alpha) + \theta_{sh13}) \\ \lambda_{c1} = L_{ls} \cdot i_{c1} + M_I \cdot (i_{a1} \cdot \cos(\theta_{c1} - \theta_{a1}) + i_{b1} \cdot \cos(\theta_{c1} - \theta_{b1}) + \\ \quad + i_{c1} \cdot \cos(\theta_{c1} - \theta_{c1})) + \lambda_{PM1} \cdot \cos(1 \cdot (\theta - 6 \cdot \alpha) + \theta_{sh1}) + \dots + \\ \quad + \lambda_{PM13} \cdot \cos(13 \cdot (\theta - 6 \cdot \alpha) + \theta_{sh13}) \end{array} \right.$$

By introducing the Clarke transformation related to three phases, which is written as:

$$[C]_{3 \times 3} = \frac{2}{3} \cdot \begin{bmatrix} 1 & -\frac{1}{2} & -\frac{1}{2} \\ 0 & \frac{\sqrt{3}}{2} & -\frac{\sqrt{3}}{2} \\ \frac{1}{2} & \frac{1}{2} & \frac{1}{2} \end{bmatrix} \quad (6.4)$$

To compute the zero-sequence component, the presented matrix is applied to the flux in phase variable domain as follows:

$$[\lambda_{\alpha\beta 0}] = [C]_{3 \times 3} \cdot [\lambda_{a1b1c1}] \quad (6.5)$$

With simple mathematical manipulations, it is possible to note that the zero-sequence component does not depend on the mutual inductance contributions. Following from stated, consider the zero-sequence component (subscript 0) in first set (subscript 1), the following equation is obtained:

$$\lambda_{01} = \frac{L_{ls}}{3} \cdot (i_{a1} + i_{b1} + i_{c1}) + \lambda_{PM3} \cdot \cos(3 \cdot \theta + \theta_{sh3}) + \lambda_{PM9} \cdot \cos(9 \cdot \theta + \theta_{sh9}) \quad (6.6)$$

By introducing the electrical equation for zero-sequence component, by replacing the magnetic equation and consider the locked rotor, the following equation is

obtained:

$$\begin{aligned} v_{01} &= R_s \cdot i_{01} + \frac{d\lambda_{01}}{dt} = \\ &= R_s \cdot i_{01} + L_{ls} \cdot \frac{di_{01}}{dt} \end{aligned} \tag{6.7}$$

In steady-state operations, the final zero-sequence equation in stationary arbitrary reference frame is:

$$\bar{V}_{01} = R_s \cdot \bar{I}_{01} + j\omega \cdot L_{ls} \cdot \bar{I}_{01} \tag{6.8}$$

where the overline symbols stand for phasor.

The Eq. (6.8) confirms the alternate voltage supply and on the basis of the mentioned equation, the equivalent circuit under zero-sequence test is given in Fig. 6.7.

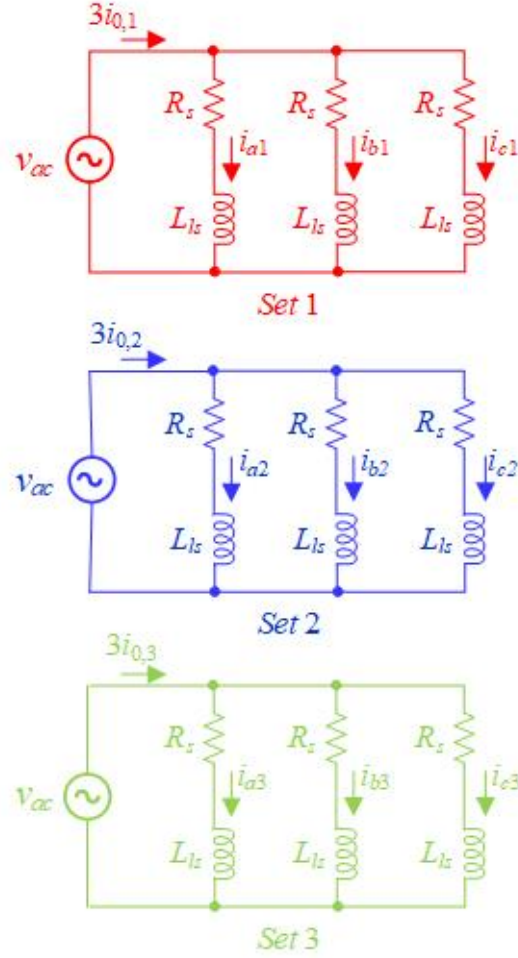


Figure 6.7: Equivalent circuit of the zero-sequence test.

Consider this equivalent circuit, the zero-sequence voltages and zero-sequence currents for a generic set  $i$  are as follows:

$$\begin{cases} v_{0i}(t) = \frac{v_{ai}(t) + v_{bi}(t) + v_{ci}(t)}{3} = v_{ac}(t), & i = 1, 2, 3 \\ i_{s0,i}(t) = \frac{i_{ai}(t) + i_{bi}(t) + i_{ci}(t)}{3}, & i = 1, 2, 3 \end{cases} \quad (6.9)$$

On the basis of the measured signals, it is considered the single electrical period  $T_{ac}$ . According with the sample frequency of the oscilloscope  $F_{os}$ , this time window corresponds to  $N$  digital consecutive samples computed as follow:

$$N = T_{ac} \cdot F_{os} \quad (6.10)$$

Defined digital samples and measured signals, the voltage root mean square  $V_{RMS}$  and current root mean square  $I_{RMS}$  are computed as:

$$V_{0,RMS} = \sqrt{\frac{1}{N} \cdot \sum_{k=1}^N v_0^2(k)} \quad (6.11)$$

$$I_{0i,RMS} = \sqrt{\frac{1}{N} \cdot \sum_{k=1}^N i_{0i}^2(k)}, \quad i = 1, 2, 3 \quad (6.12)$$

where  $k$  stands for a generic sample.

In addition, the active power in one electrical period is computed as:

$$P_{0i} = \frac{1}{N} \cdot \sum_{k=1}^N (v_0(k) \cdot i_{0i}(k)), \quad i = 1, 2, 3 \quad (6.13)$$

Therefore, in equivalent circuit of every set  $i$ , the apparent power and reactive power are computed as:

$$S_{0i} = V_{0,RMS} \cdot I_{0i,RMS}, \quad i = 1, 2, 3 \quad (6.14)$$

$$Q_{0i} = \sqrt{S_{0i}^2 - P_{0i}^2}, \quad i = 1, 2, 3 \quad (6.15)$$

Consider the reactive power, the leakage inductance is computed as:

$$L_{ls,0i} = \frac{Q_{0i}}{I_{0i,RMS}^2} \cdot \frac{1}{2 \cdot \pi \cdot f}, \quad i = 1, 2, 3 \quad (6.16)$$

where  $f$  is the supply frequency corresponding to the reciprocal of the single electrical period  $T_{ac}$ .

According with machine modelling, all individual phase windings are identical than each other. For this reason, unique value of the leakage inductance is considered, which is computed as the average value between all sets:

$$L_{ls} = \frac{L_{ls,01} + L_{ls,02} + L_{ls,03}}{3} \quad (6.17)$$

The zero-sequence test has been carried out at three different frequencies, as shown in Table 6.1.

Table 6.1: Zero-sequence test: leakage inductance.

Leakage inductance values [mH]			
f [Hz]	$L_{ls,01}$	$L_{ls,02}$	$L_{ls,03}$
25	87.1	88.5	87.6
50	85.5	84.8	82.9
100	83.5	82.4	80.3
$\bar{L}_{ls,0i}$	85.4	85.3	83.67
$L_{ls}$	84.7		

### 6.2.2 Single Phase Test

The aim of single phase test is to obtain the isotropic inductance  $M_I$ , useful in machine modelling. In this test, the rotor is locked while the single phase  $n$  ( $n=a1, a2, \dots, c3$ ) is supplied with an alternate voltage source: *Spitzenberger Spies* PAS2500 linear power amplifier. The voltage and current measurements are performed with the *Tektronix* oscilloscopes.

In single phase test the electrical equation taken into account is:

$$\begin{aligned} v_n &= R_s \cdot i_n + L_{ls} \cdot \frac{di_n}{dt} + M_I \cdot \cos(\theta_n - \theta_n) \cdot \frac{di_n}{dt} = \\ &= R_s \cdot i_n + L_{ls} \cdot \frac{di_n}{dt} + M_I \cdot \frac{di_n}{dt} \end{aligned} \quad (6.18)$$

In steady-state operations., the electrical equation in phase variable domain for a generic winding is:

$$\bar{V}_n = R_s \cdot \bar{I}_n + j\omega L_{ls} \cdot \bar{I}_n + j\omega M_I \cdot \bar{I}_n \quad (6.19)$$

The Eq. (6.19) confirms the alternate voltage supply and on the basis of this equation, the equivalent circuit for single phase test is given in Fig. 6.8.

On the basis of the digital consecutive samples  $N$ , the voltage and current root mean square  $V_{RMS}$  and  $I_{RMS}$ , defined in Section 6.2.1, the active power, apparent power and reactive power are computed as:

$$P_{sf,n} = \frac{1}{N} \cdot \sum_{k=1}^N (v_{sf,n}(k) \cdot i_{sf,n}(k)), \quad n = a1, b1, \dots, c3 \quad (6.20)$$

$$S_{sf,n} = V_{sf,n,RMS} \cdot I_{sf,n,RMS}, \quad n = a1, b1, \dots, c3 \quad (6.21)$$

$$Q_{sf,n} = \sqrt{S_{sf,n}^2 - P_{sf,n}^2}, \quad n = a1, b1, \dots, c3 \quad (6.22)$$

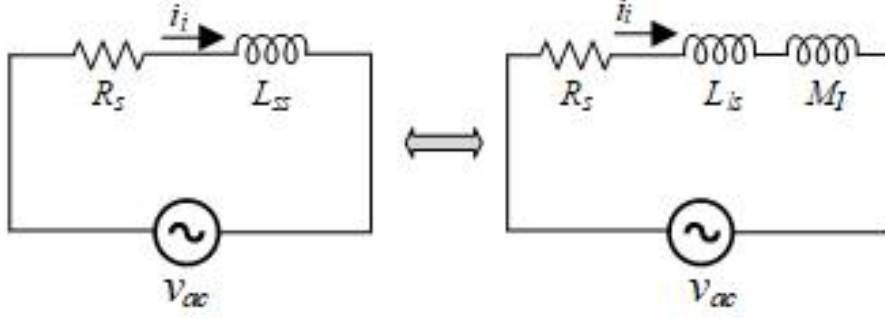


Figure 6.8: Equivalent circuit of the single phase test.

The impedance of a generic stator phase under test  $n$  is computed as:

$$Z_{s,n} = \frac{S_{sf,n}}{I_{sf,n,RMS}^2} \quad (6.23)$$

and the power factor is:

$$\cos(\phi_{s,n}) = \frac{P_{sf,n}}{S_{sf,n}} \Rightarrow (\phi_{s,n}) = \arccos(\phi_{s,n}) \quad (6.24)$$

On the basis of the power factor, the stator resistance and reactance are computed as:

$$R_{s,n} = Z_{s,n} \cdot \cos(\phi_{s,n}) \quad (6.25)$$

$$X_{s,n} = Z_{s,n} \cdot \sin(\phi_{s,n}) L_{ss,n} \quad (6.26)$$

About the inductance:

$$L_{ss,n} = \frac{X_{s,n}}{2 \cdot \pi \cdot f} \quad (6.27)$$

It is nevertheless well-known the leakage inductance value by the zero-sequence test, the isotropic contribution is computed as:

$$\begin{aligned} M_{I,n} &= L_{ss,n} - L_{ls,n} = \\ &= L_{ss,n} - L_{ls} \end{aligned} \quad (6.28)$$

According with machine modelling, an unique value of isotropic inductance is considered, which is computed as the average value between all phases at three different frequencies.

The synchronous inductance in rotor reference frame is computed as follow:

$$L_s = L_{ls} + \frac{9}{2} \cdot M_I, \quad L_s = L_{s,d} = L_{s,q} \quad (6.29)$$

Table 6.2: Single phase test: isotropic inductance.

Isotropic inductance values [mH]									
f [Hz]	$M_{I,a1}$	$M_{I,a2}$	$M_{I,a3}$	$M_{I,b1}$	$M_{I,b2}$	$M_{I,b3}$	$M_{I,c1}$	$M_{I,c2}$	$M_{I,c3}$
25	81.9	94.3	75.3	74.5	78.2	91.0	85.0	67.0	72.9
50	78.4	90.4	70.6	74.2	72.9	86.9	81.2	65.0	68.7
100	72.6	84.9	65.5	69.3	68.5	81.3	75.9	60.4	63.7
$\overline{M}_{I,i}$	77.6	89.8	70.5	72.7	73.2	86.4	80.7	64.1	68.4
$M_I$	75.9								

### 6.2.3 Short Circuit Test and Design approach

The aim of this test is to obtain the magnetizing inductance related to  $h^{th}$  harmonic ( $h = 1, \dots, 13, h \neq 2i, i \in \mathbb{N}$ ) in stator short-winding configuration. The rotor position is measured by encoder, the speed is obtained through *PLL* use (to avoid derivative method) and the currents are measured.

According with the model in *VSD* variables, presented in Chapter 6.26, Section 4.2.2, in subplanes the electrical equation taken into account are:

$$\begin{cases} v_{\alpha\beta} = R_s \cdot \dot{i}_{\alpha\beta} + L_{ls} \cdot \frac{d\dot{i}_{\alpha\beta}}{dt} + L_m^{(1)} \cdot \frac{d\dot{i}_{\alpha\beta}}{dt} + \frac{d\lambda_{PM1}}{dt} \\ \underline{v}_{xyi} = R_s \cdot \dot{i}_{xyi} + L_{ls} \cdot \frac{d\dot{i}_{xyi}}{dt} + L_{eq}^{(h)} \cdot \frac{d\dot{i}_{xyi}}{dt} + \frac{d\lambda_{PMh}}{dt}, \quad i = 1, 2, 3 \end{cases} \quad (6.30)$$

When the subplanes is containing more than one harmonics, the distorting power related to the harmonics must taken into account. For this reason, the single harmonic approach is preferred than the power approach for each subplane.

On the basis of the rotor speed (*PLL* output) and permanent magnet flux ( $\lambda_{PMh}$ ), the back-*EMF* in phase variable domain are reconstructed as:

$$\begin{aligned} [e_{PM,abc9}] = & -\omega \cdot \left( 1 \cdot \lambda_{PM1} \cdot \sin(1 \cdot (\theta - [\theta_n]) + \theta_{sh1}) + \right. \\ & + 3 \cdot \lambda_{PM3} \cdot \sin(3 \cdot (\theta - [\theta_n]) + \theta_{sh3}) + \\ & + 5 \cdot \lambda_{PM5} \cdot \sin(5 \cdot (\theta - [\theta_n]) + \theta_{sh5}) + \dots \\ & \left. \dots + 13 \cdot \lambda_{PM13} \cdot \sin(13 \cdot (\theta - [\theta_n]) + \theta_{sh13}) \right) \end{aligned} \quad (6.31)$$

where all symbols are consistent with the ones defined in previous chapters. Using the *VSD* transformation, the back-*EMF* are expressed in *VSD* variables. In Figs. 6.9 - 6.12, the time trends of the reconstructed back-*EMF* in *VSD* variables and measured current during the test are shown. The short circuit test is performed at 10 *Hz* electrical frequency.

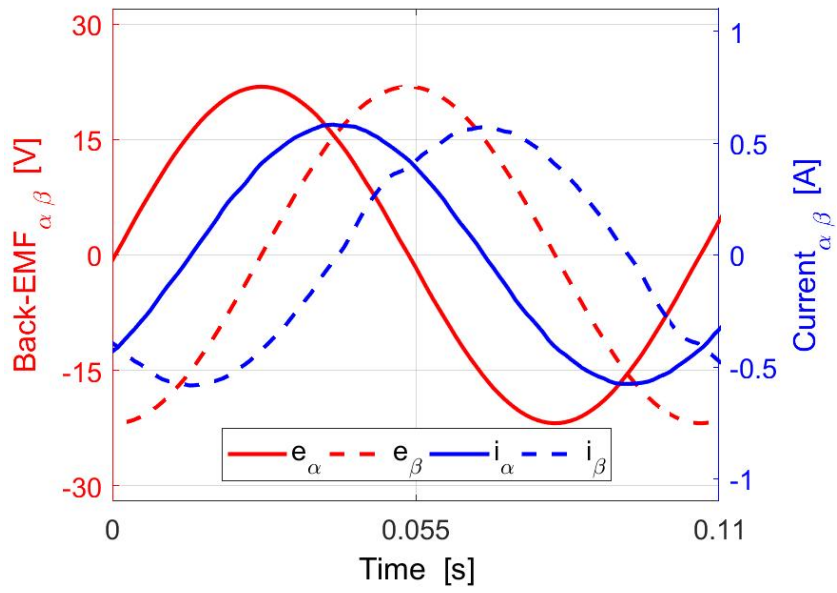
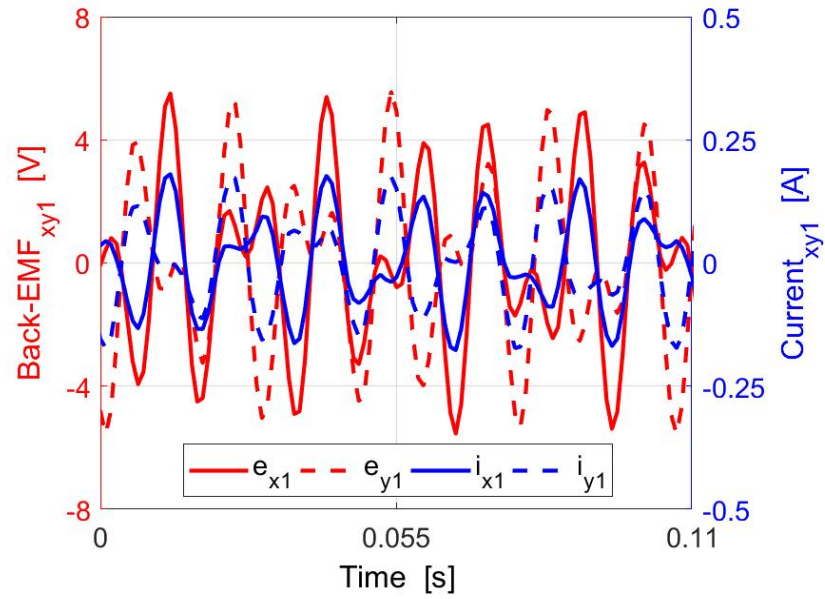
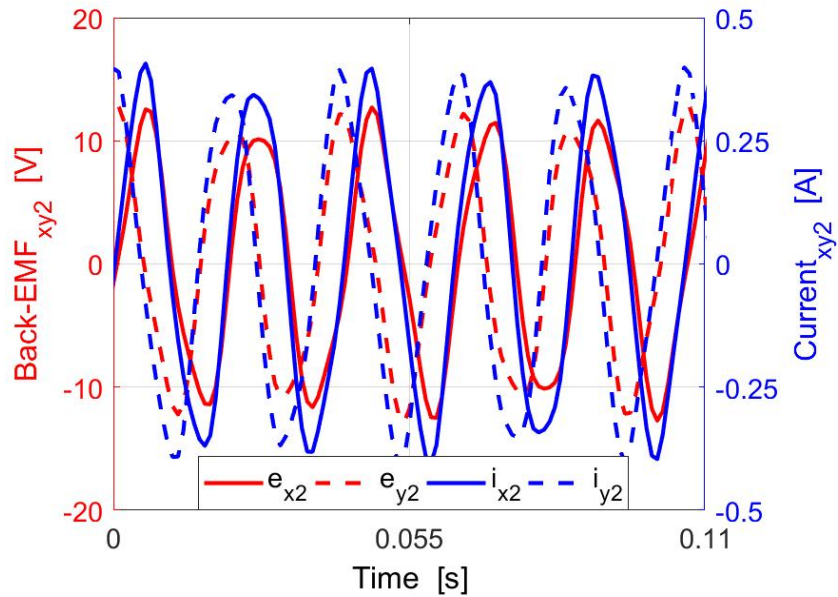


Figure 6.9: Short circuit test: back-*EMF* and current in  $(\alpha, \beta)$  subplane.

Figure 6.10: Short circuit test: back- $EMF$  and current in  $(x,y)1$  subplane.Figure 6.11: Short circuit test: back- $EMF$  and current in  $(x,y)2$  subplane.

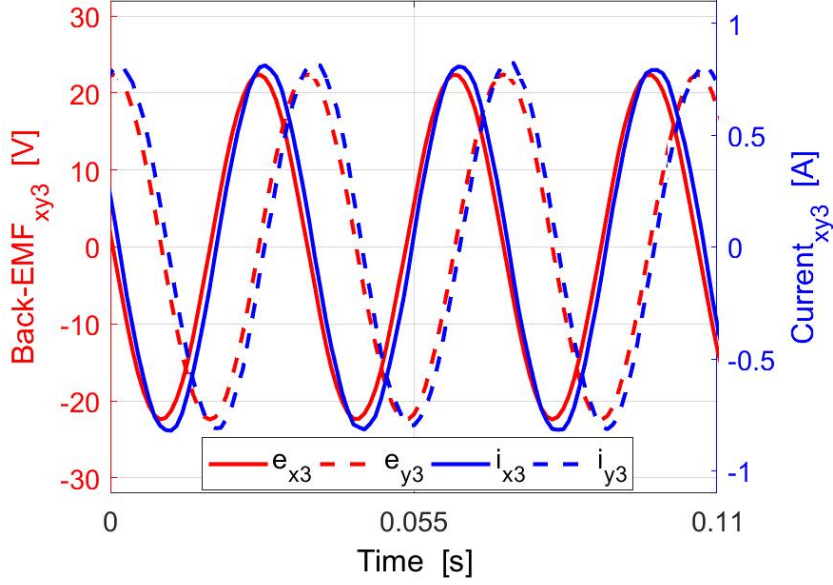


Figure 6.12: Short circuit test: back- $EMF$  and current in  $(x,y)3$  subplane.

The  $FFT$  analysis performed on time trends presented above leads to the results, shown in Table 6.3. It is noted how the set low frequency did not allow the computation of the magnetizing harmonic inductances, except for the fundamental one. On the basis of the short circuit test the obtained value is:

$$L_{ls} + L_m^{(1)} = 459mH \Rightarrow L_m^{(1)} = 375mH \quad (6.32)$$

This value is almost equal to the  $dq$  stator inductance ( $L_{s,d} = L_{s,q} = L_s$ ). Following from stated, it is possible to note how the set frequency in this test has been low. This means that the employed test is correct, but in this part is preferable a design approach. Concerning the computation of the magnetizing inductance related to the others subplanes, the design approach is used. The design data are shown in Table 6.4.

According with the data in table, the distribution factor  $k_d$  is computed as ratio between result effective back-*EMF* and sum of effective back-*EMF*s of individual coils [45]. If  $\alpha$  is the angle between the slots, the distribution factor related to the  $h$  harmonic is computed as:

$$k_d^{(h)} = \frac{\sin\left(h \cdot q \cdot \frac{\alpha}{2}\right)}{q \cdot \sin\left(h \cdot \frac{\alpha}{2}\right)} \quad (6.33)$$

The magnetizing inductance  $h^{th}$  is computed as:

$$L_m^{(h)} = \frac{9}{2} \cdot \left( \frac{Z_f}{\pi \cdot 2 \cdot p} \cdot \frac{k_d^{(h)}}{h} \right)^2 \cdot \frac{1}{\mathfrak{R}_{ag}} \quad (6.34)$$

where  $Re_{ag}$  is the equivalent airgap reluctance, defined as:

$$\mathfrak{R}_{ag} = \frac{k_{ch} \cdot l_{ac}}{\mu_0 \cdot \pi \cdot \frac{D_{ag}}{2} \cdot l_{ac}} \quad (6.35)$$

where  $k_{ch}$  is the Carter coefficient related to the  $h$  harmonic (assumed equal to 1). The computed values are shown in Table 6.5. These inductances are used in the machine model, defined in Chapter 6.26 and subsequent.

## 6.2.4 Test rig characterization

The aim of this test is to obtain the inertia value and static, linear and parabolic friction torque related to the test rig. The test rig parameters allow an accurate tuning of the speed control regulator. The rotor position is measured by the encoder. Machine has shaft-mounted *Omron* E6B2-CWZ1X rotary incremental encoder for

Table 6.3: *FFT* analysis: back-*EMF* and current in *VSD* variables.

<b>FFT analysis</b>			
$h^{th}$	Back- <i>EMF</i> amplitude [V]	Current amplitude [A]	Power factor [-]
1	21.84	0.58	0.697
3	22.42	0.817	0.983
5	11.49	0.375	0.982
7	2.916	0.108	1
11	2.673	0.074	0.982
13	1.409	0.036	0.951

Table 6.4: Main data of nine-phase *PMSM* machine.

<b>Design Data</b>	
Parameter	Value [Units]
Phase number	9 [-]
Rotor type	Shortened <i>PM</i> [-]
Winding configuration	Symmetrical [-]
Pole number $p$	2 [-]
Slot/pole/phase number $q$	2 [-]
Winding type	Distributed
Winding layout	Full-pitched [-]
Airgap thickness $l_{ag}$	8.4 [mm]
Diameter airgap $D_{ag}$	75 [mm]
Active length $l_{ac}$	55[mm]
Conductor/slot number	220 [-]
Conductor/phase number $Z_f$	880 [-]

Table 6.5: Magnetizing inductance related to  $h$  harmonic.

<b>Harmonic magnetizing inductance</b>	
Harmonic	Value [mH]
3	35.7
5	11.3
7	4.7
9	2.1
11	0.9
13	0.4

position measurement. Encoder resolution is 1024 pulses per revolution and it is connected to *dSPACE* DS3002 encoder board. The measured angle represents a *PLL* input to obtain the speed profile, avoiding the derivative method.

The mentioned test is organised essentially as follows: the reference electromagnetic torque is imposed in open-loop (the speed loop regulation is not activated). The speed limit is set to 1300 *rpm*, which is achieved without control in acceleration mode. When this limit is reached, the machine is no longer supplied and it is left in free natural deceleration. The combination of the mechanical parameters used to construct the speed in acceleration mode and deceleration mode, allows to characterize the test rig.

Using an iterative methodology the acceleration and deceleration profiles are constructed (Eulero-time integration), thus obtaining the inertia and friction contributions (static, linear and parabolic torque).

In acceleration mode the mechanical speed is constructed on the basis of the motor acceleration computed as:

$$a_{a,n} = \frac{T_{a,n}}{J_{eq,n}} \quad (6.36)$$

where  $J_{eq,n}$  is the equivalent inertia set to the step  $n$  and the torque  $T_{a,n}$  is computed as:

$$\begin{aligned} T_{a,n} &= T_{em}^* - (T_{B0,n} + T_{B1,n} + T_{B2,n}) = \\ &= T_{em}^* - (T_{B0,n} + k_{B1,n} \cdot \omega_m + k_{B2,n} \cdot \omega_m^2) \end{aligned} \quad (6.37)$$

where  $T_{B0,n}$ ,  $k_{B1,n}$  and  $k_{B2,n}$  are the static torque, linear and parabolic coefficients, respectively, set to the step  $n$ .

Therefore, the same approach is used to interpolate the speed in deceleration mode. In deceleration mode, the deceleration at the step  $n$  is computed as:

$$a_{d,n} = -\frac{T_{d,n}}{J_{eq,n}} \quad (6.38)$$

where the torque  $T_{d,n}$ , which is opposed to machine braking, is computed as:

$$T_{d,n} = (T_{B0,n} + k_{B1,n} \cdot \omega_{m,n} + k_{B2,n} \cdot \omega_{m,n}^2) \quad (6.39)$$

This iterative procedure is concluded when the interpolated speed matches up pretty well with the *PLL* output in acceleration and deceleration mode. The interpolated speed and *PLL* output in acceleration and deceleration mode are shown in top e bottom of Fig. 6.13, respectively. The obtained mechanical parameters are shown in Table 6.6.

Table 6.6: Test rig characterization: mechanical parameters.

<b>Mechanical parameters</b>	
Parameter	Value [Units]
$J_{eq}$	$9.4 \cdot 10^{-3} [kgm^2]$
$T_{B0}$	$450 \cdot 10^{-3} [Nm]$
$k_{B1}$	$4.3 \cdot 10^{-3} [Nm/(rad/s)]$
$k_{B2}$	$0.0 \text{ Nm}/(\text{rad}/\text{s}^2)$

It is necessary to highlight how the test rig characterization allows at obtaining just approximative values of both inertia and friction coefficients. Indeed, the results in Fig. 6.13 are extremely sensitive to parameters detuning. Therefore, the results in Table 6.6 are used in simulation validation. In experimental validation, the inertia

parameter present in table is used to set the starting values of the speed  $PI$  gains. As it will be shown later, the experimental time trends of torque and current along  $q$ -axis are qualitative the same to the ones in simulation. The only difference regards the absolute values of these variables, corresponding to the detuning of both inertia and friction coefficients. Nevertheless, because the scope of this thesis is to propose a harmonic model and sensorless control scheme for multiphase machine, the accurate parameters evaluation of the used test rig is not a aim primary. Indeed, the proposed control solution can be validated in any test rig, thus requiring a specific test rig characterization.

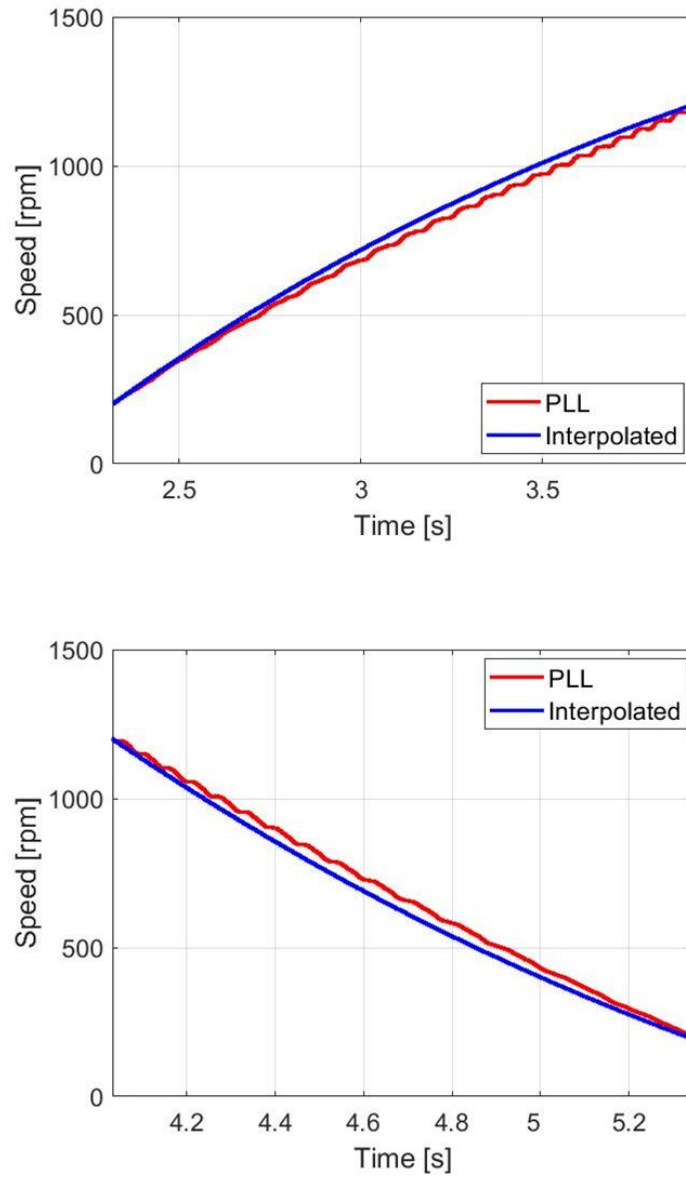


Figure 6.13: Test rig characterization: iterative methodology. From top to bottom: acceleration; deceleration.

### 6.3 Experimental results

Developed hybrid control has been experimentally validated for nine-phase surface *PMSM* with non-sinusoidal back-*EMF*. In Fig. 6.14, the overview of the digital control implemented in laboratory is shown. In mentioned figure four main elements are highlighted:

- *dSPACE PWM Board Interrupt* - dwell times are calculated and provided by use of *DS5101DWO* block from the *dSPACE* specific *Real-Time Interface (RTI)* (grey block) library. *DS5101* board uses custom written code to create gating signals based on calculated dwell time. Triangular carrier is assumed. Since *DWO* board uses high precision counter, it is used to generate an interrupt. *DWO* board interrupt is enabled and acknowledged by *System Start and System Outputs* (white) blocks from the *Simulink Coder library*, respectively. Generated interrupt triggers the timer task and whole control code is executed. Furthermore, interrupt is synchronised with *PWM* signals so that control code is executed exactly at the beginning and in the middle of the switching period.
- *INPUT CONTROL PARAMETERS* - receives the measured stator currents (they are measured to employ the machine control) and rotor position (not used in the control, but it is measured in order to be compared with its estimated signal). Finally, the reference speed and *dc* power source are set (blue blocks).
- *CONTROL ALGORITHM* - contains two different control: *I-Hz* control (magenta block), where it is necessary to set the reference speed and the current along  $d^*$ -axis in arbitrary reference frame, and the *Hybrid control* (magenta block), where the current along  $d^*$ -axis in arbitrary reference frame, the target speed to achieve under *I-Hz* control and, finally, the reference speed in *SFOC* are set. The phase voltage references are the outputs of both controls.
- *PWM, LOGIC and PROTECTION* - acquires the phase voltage references in order to obtain the duty-cycle of the voltage supply inverter, using the sinusoidal *PWM* modulation (*SPWM*). This is performed by the *PWM Generator* (pink block). In addition, the inverter hardware protection system is implemented in *Protection* block.

In Fig. 6.15 the main blocks inside *Hybrid Control* are shown. Within each block, the *Matlab* function is present, marked by specific inputs and outputs according to the theory. The mentioned inputs, which depend on the employed control, are set through *Control Desk* mask, shown in Fig. (6.6). All variables are connected to it and the variable waveforms are visible through plots.

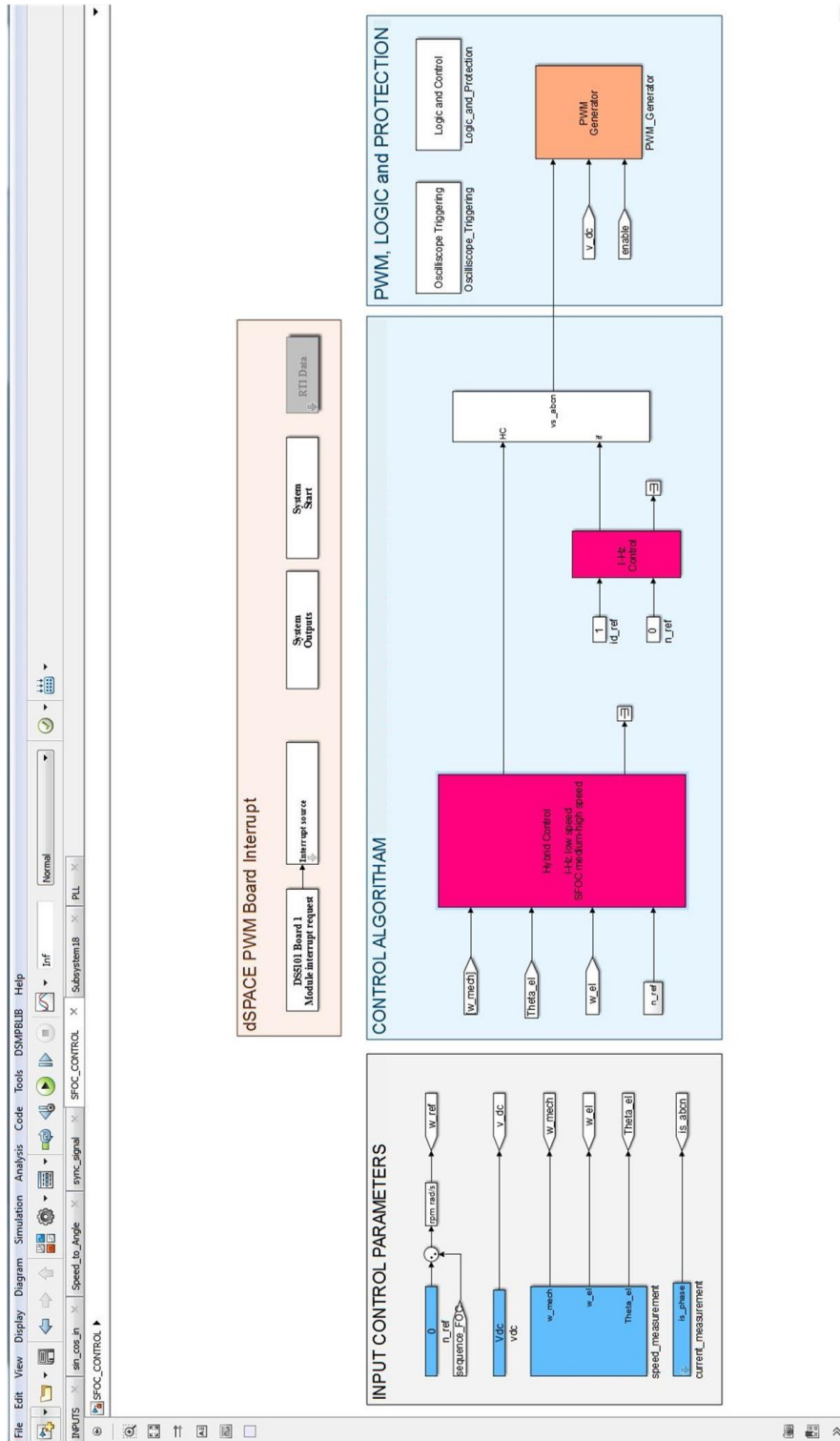


Figure 6.14: The digital control implemented in laboratory.

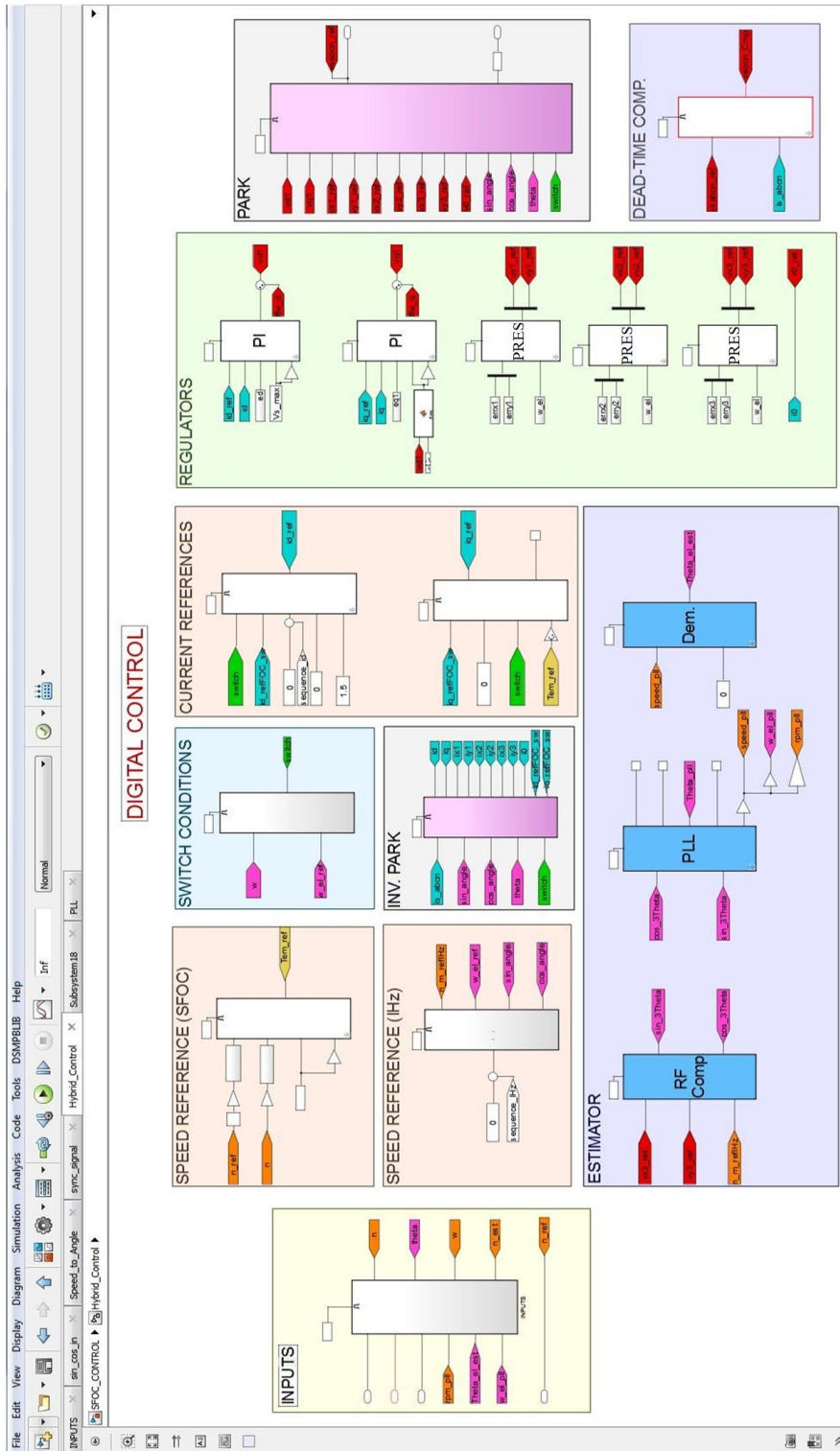


Figure 6.15: Hybrid control for experimental validation.

With reference to the theory, presented in Chapter 6.25, in Table 6.7 the *PI* of speed, current loop regulations and *PRES* gains are shown. The table is concluded with the *PLL* gains used in experimental setup.

The experimental time trends for hybrid control under no-load and load conditions are provided. The experimental result are related to the motoring operation and the speed is limited at  $\pm 1500$  *rpm* due to the mechanical limitations of the driving machine (Fig. 6.2). The machine under test is speed controlled while the dc *PM* machine is not controlled. The drive is tested with the settings shown in Eq. (6.40).

Table 6.7: Values of the control parameters.

<b>Control gains</b>	
Parameter	Value [Units]
Drive Control - Speed <i>PI</i> controllers	
Proportional gain $k_{P,\omega}$	0.06 [Nm/(rad/s)]
Integral gain $k_{I,\omega}$	0.075 [Nm/rad]
Machine Control - Current <i>PI</i> controller	
Proportional gain $k_{P,i}$	535 [V/A]
Integral gain $k_{I,i}$	170000 [V/(As)]
Machine Control - Proportional Resonant Controllers	
Proportional gain $k_{P,PRES}$	126 [V/A]
Integral gain $k_{I,PRES}$	46500[V/(As)]
Phase-Locked Loop	
Proportional gain $k_{P,PLL}$	163 [1/s]
Integral gain $k_{I,PLL}$	17765 [1/s <sup>2</sup> ]

$$\left\{ \begin{array}{l} f_s w = 5kHz \\ f_s = 10kHz \\ v_{dc-link} = 450V \\ \omega_m^* \in \begin{cases} [0, 300]rpm & I - Hz \\ (300, 1500]rpm & SFOC \end{cases} \\ i_d^* \in \begin{cases} 1.5A & I - Hz \quad (d, q)^* \\ 0A & SFOC \quad (d, q) \end{cases} \\ i_q^* \in \begin{cases} 0A & I - Hz \quad (d, q)^* \\ (T_{em}^* \cdot k_1)A & SFOC \quad (d, q) \end{cases} \\ T_L = 0Nm \end{array} \right. \quad (6.40)$$

Setting the conditions shown in Eq. (6.40), the test is performed by imposing the machine's rated torque in sensorless control. The experimental results for the sensorless control under no-load conditions are shown in Figs. 6.16 - 6.26.

As a result, a smooth and fast transition between open-loop frequency and sensorless *FOC* based on third back-*EMF* harmonic is verified and it is characterized by speed drop (about 100 *rpm*), as explained before in simulation results. Note that the speed oscillations are damped quickly and, consequently, the switch is rapidly happened. The references initializations of the current controllers under sensorless field-oriented control, using the measured values during the first control referred in the estimated rotor reference frame, are clearly visible in zoom areas of the Figs. 6.17 (bottom) and 6.18 (bottom). Subsequently, in sensorless control the direct axis current converges to zero in order to control the rotor magnetizing flux while the quadrature axis current corresponds to the motor torque. The target values of direct and quadrature currents are obtained following a ramps, which are resulted compatible with dynamic system. This confirms the correctness of the speed and current *PI* controllers. When the speed is increased up to 1500 *rpm*, the reference electromagnetic torque reaches the nominal value. Finally, in steady-state this value decrease, according to the friction torque. Note that during the transition interval the current loop along *q*-axis is characterized by the oscillations related to speed loop output settling. According with the simulation results, the *PLL* input is in agreement with the computed back-*EMF* vector in third subplane  $\underline{e}_{xy3}$ , based on measured angle and speed. The phase error between the computed back-*EMF* and the *PLL* input vectors is close to zero in sensorless control, as shown in Fig. 6.19 (bottom). In detail, in mentioned figure the error is close to 5°. These differences in terms of vector amplitude and phase are related to the error between the measured and estimated rotor position and speed. However, in experimental is confirmed that the error in estimated angle than its measured value is conformed to typical error in sensorless control three-phase drives. The single electrical period is shown in bottom of Fig. 6.20, where it is possible to note how the demodulated angle follows its measured value pretty well. A zoom area in transition interval is performed in bottom of the Fig. 6.20.

Finally, to demonstrate the *PRES* effectiveness, the phase currents and voltages are shown. In bottom of the Fig. 6.21 the inverter nonlinear errors are visible, having an effect on phase voltages (Fig. 6.22), where all back-*EMF* harmonic contributions are relevant.

In conclusion, good agreement in simulation and experimental results is recorded.

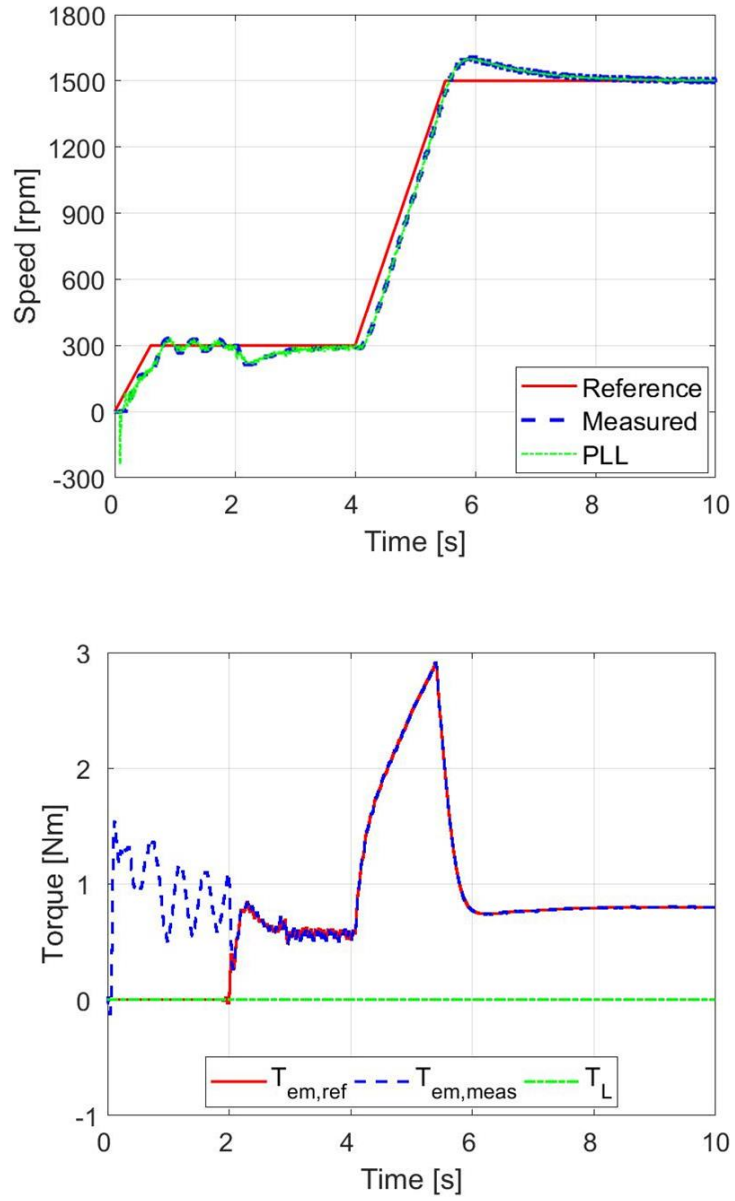


Figure 6.16: No-load conditions in experimental validation. From top to bottom: speed response; torque response.

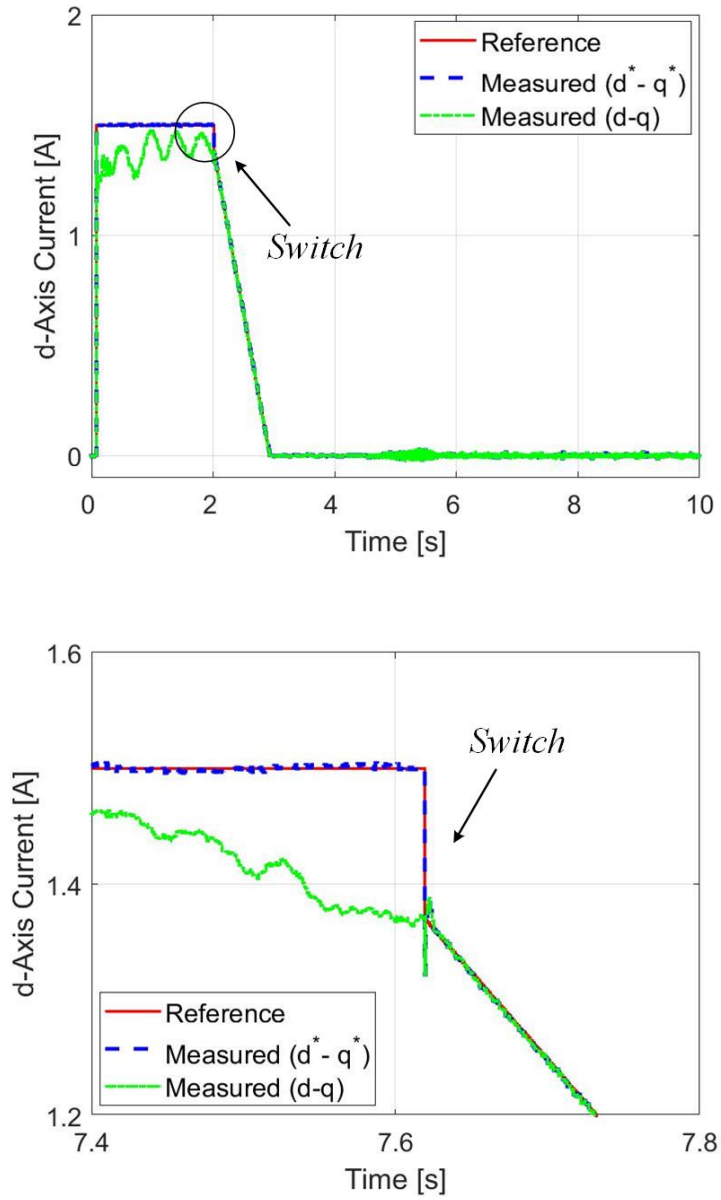


Figure 6.17: Measured current along estimated and arbitrary  $d$ -axes. From top to bottom: the time trend; corresponding zoom.

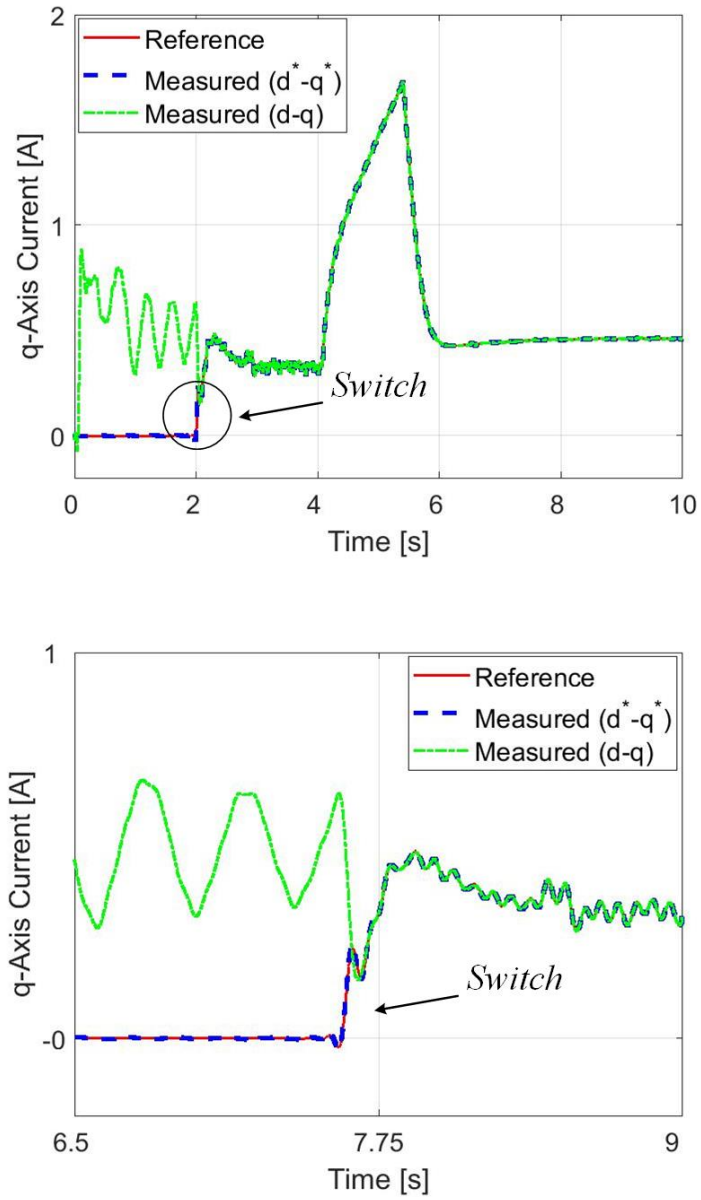


Figure 6.18: Measured current along estimated and arbitrary  $q$ -axes. From top to bottom: the time trend; corresponding zoom.

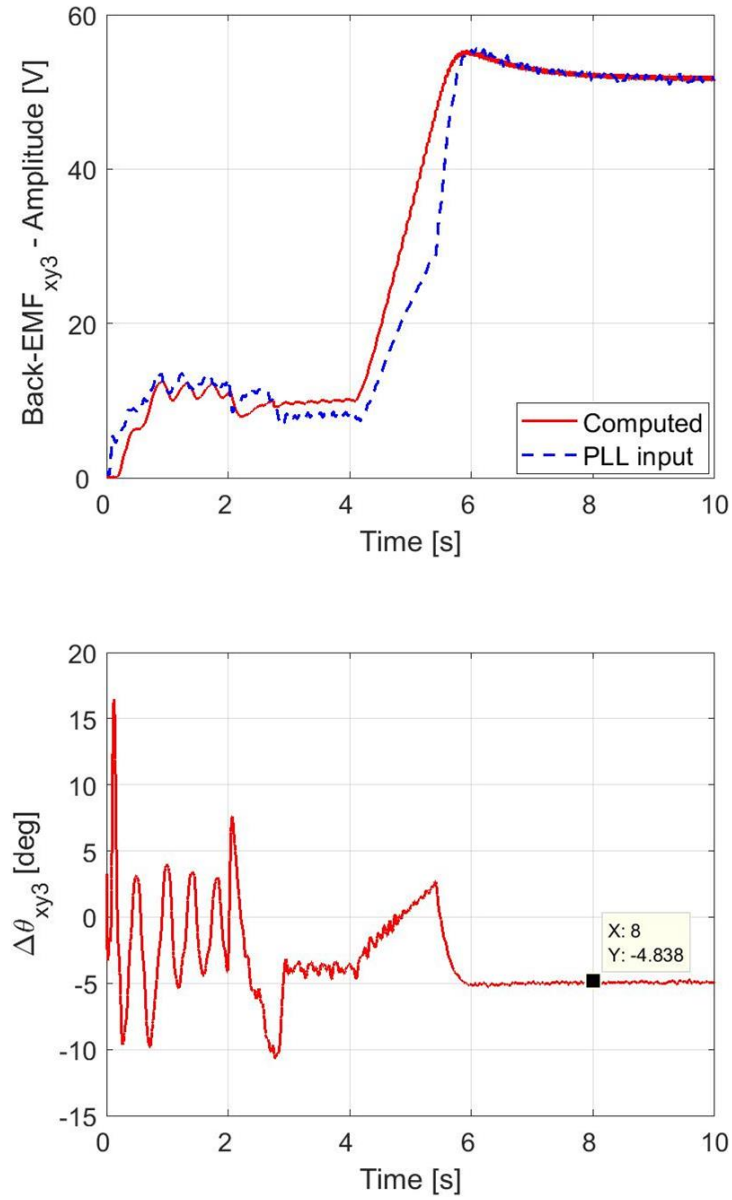


Figure 6.19: No-load conditions in experimental validation. From top to bottom: vector  $\underline{e}_{xy3}$  magnitude; phase error.

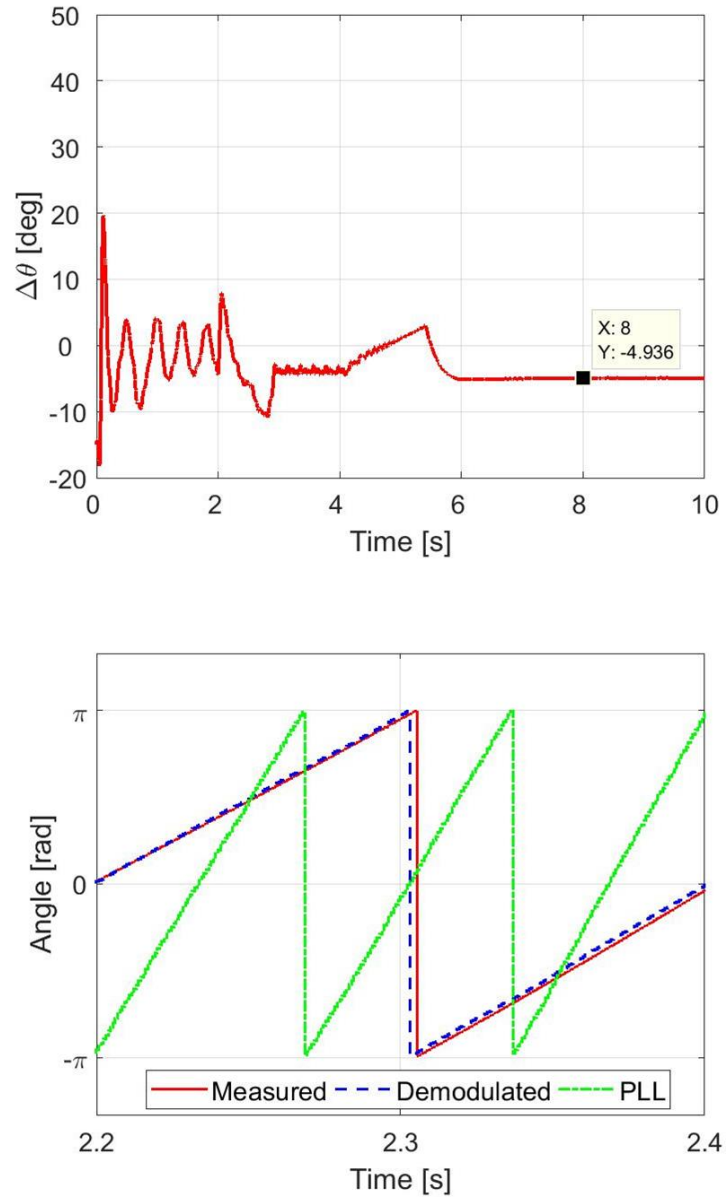


Figure 6.20: No-load conditions in experimental validation. From top to bottom: angle error; zoom area of the angle.

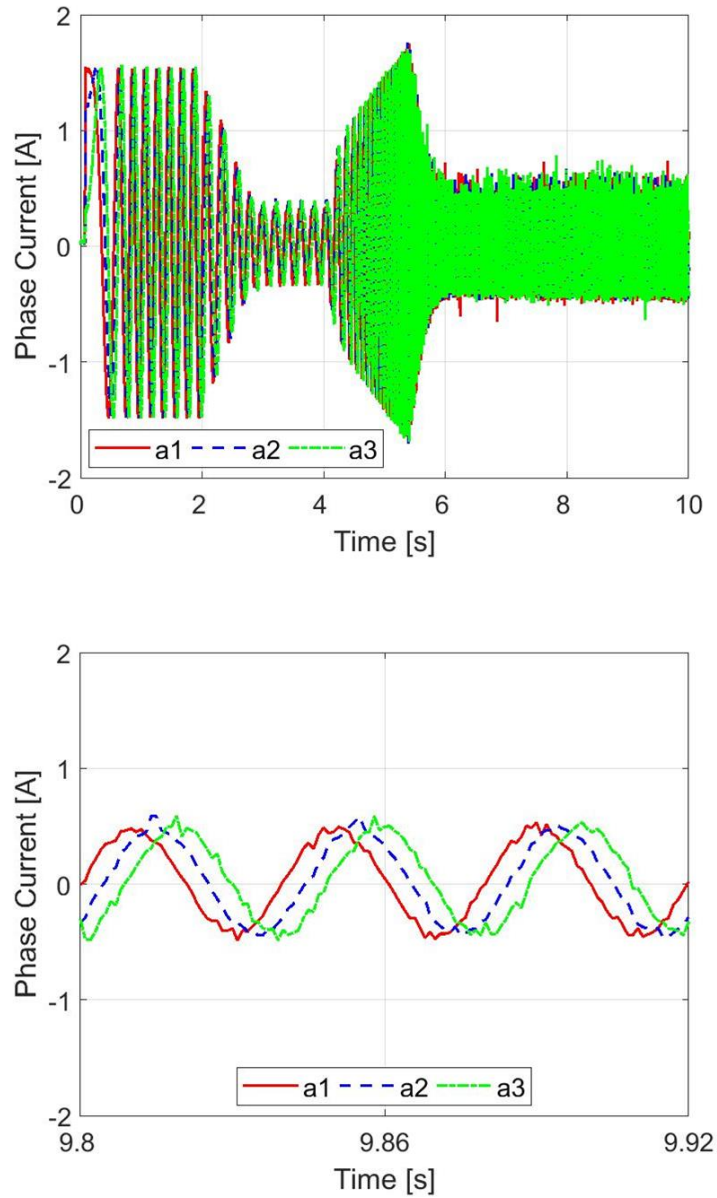


Figure 6.21: No-load conditions in experimental validation. From top to bottom: phase current responses; corresponding zoom area.

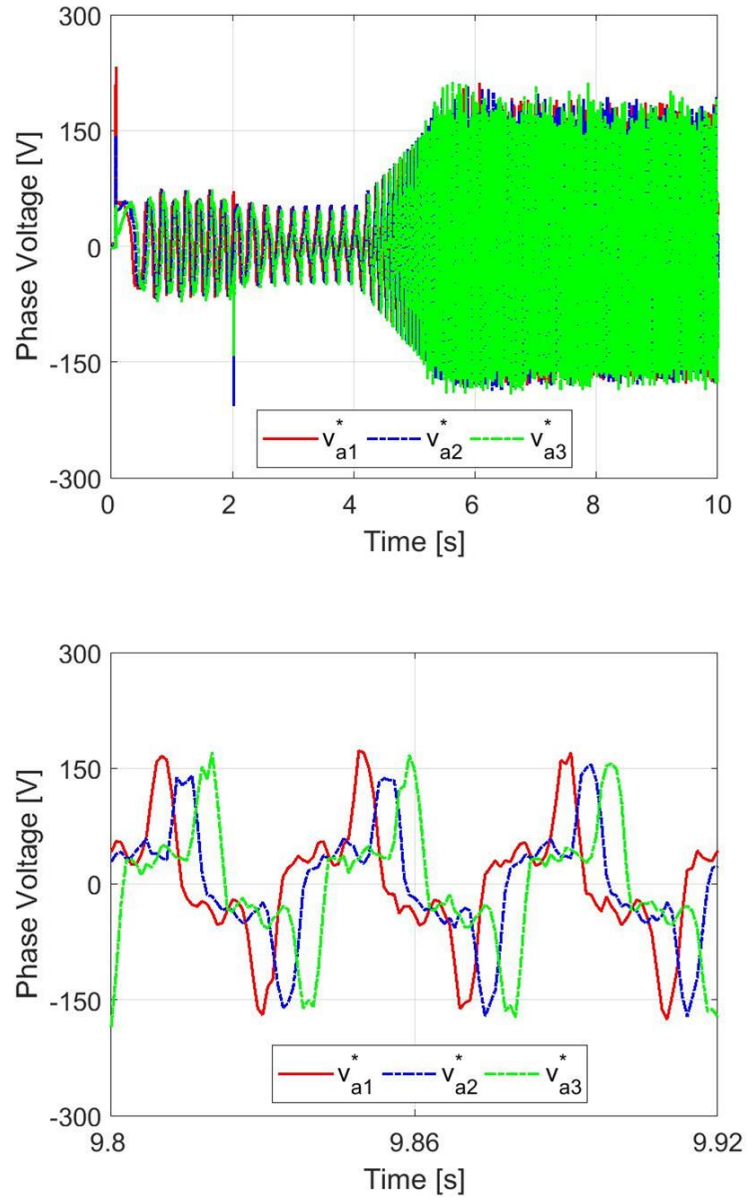


Figure 6.22: No-load conditions in experimental validation. From top to bottom: phase voltage references; corresponding zoom area.

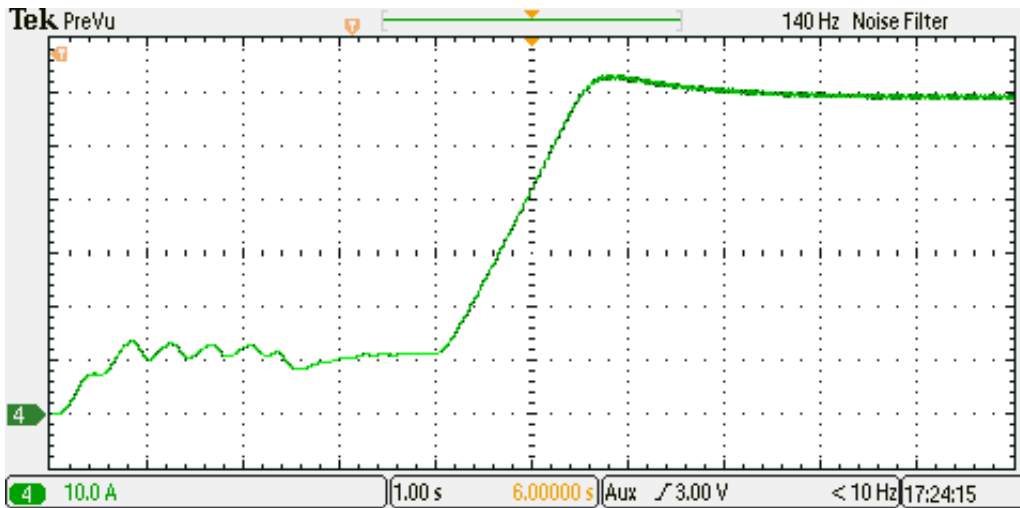


Figure 6.23: No-load conditions: speed response. 250 rpm/div.

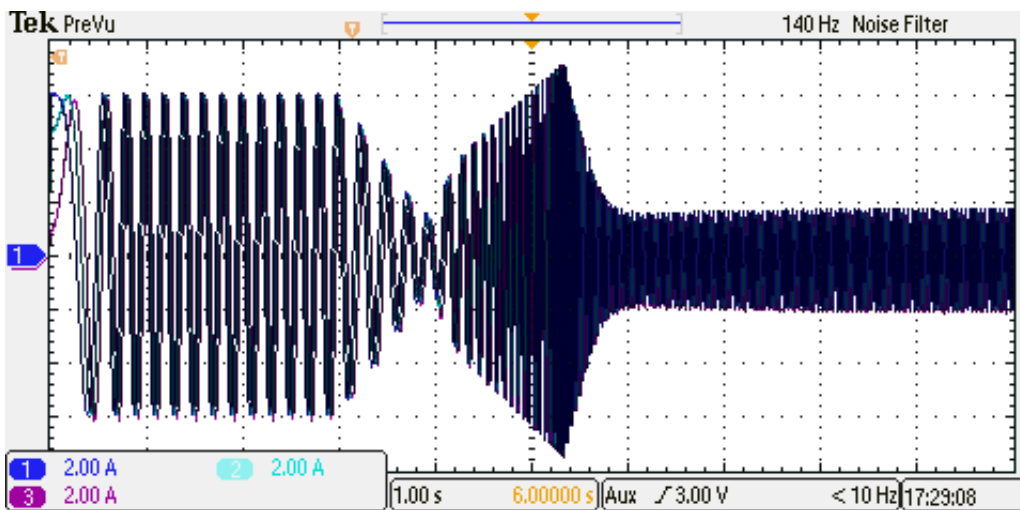


Figure 6.24: No-load conditions: currents response. 2 A/div.

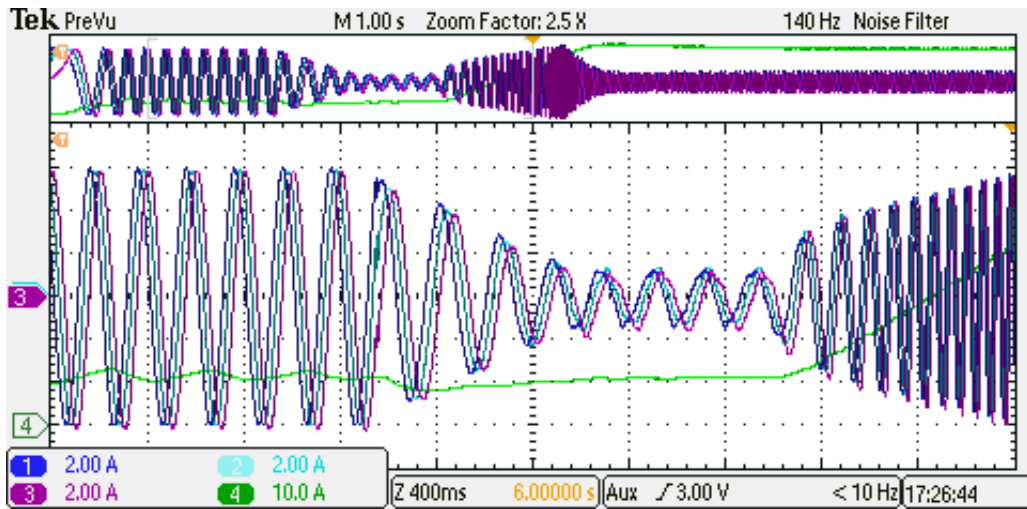


Figure 6.25: No-load conditions: currents and speed response during the transition. CH.1 - CH.3: 2 A/div; CH.4: 250 rpm/div.

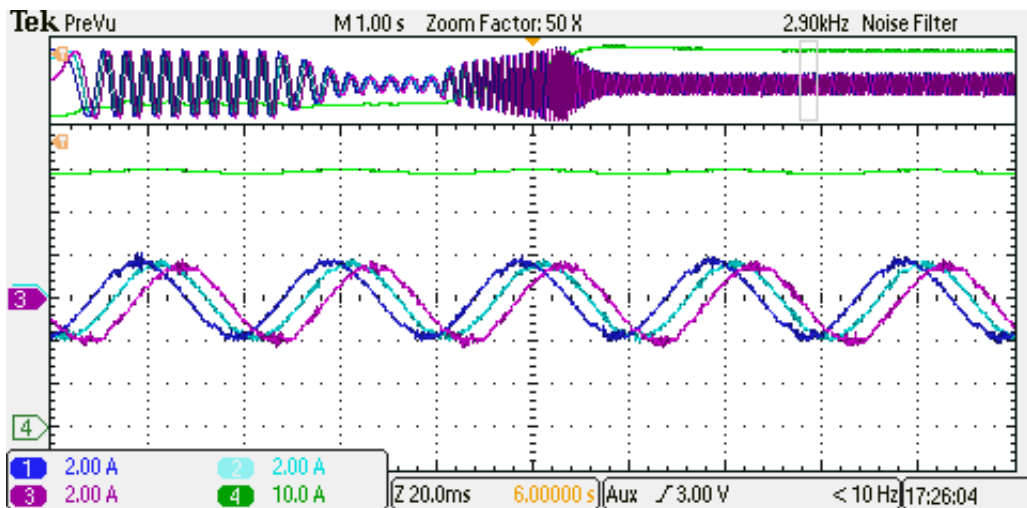


Figure 6.26: No-load conditions: currents and speed responses in steady-state at 1500 rpm. CH.1 - CH.3: 2 A/div; CH.4: 250 rpm/div.

To validate the hybrid control the load torque is set. The *PM dc* machine is used as mechanical load and it is additionally connected to resistor bank. The value of load torque is about  $1.4 \text{ Nm}$ . Setting the conditions shown in Eq. (6.40), except for the load torque, the test is performed. The experimental results for hybrid control under load condition are shown in Figs. 6.27 - 6.33.

At the instant when the load torque is added (about  $7.5 \text{ s}$ ) the speed drop is shown (about  $100 \text{ rpm}$ ). The electromagnetic torque follows the load torque, the friction torque and the inertia contributions when the machine is not operated in steady-state. It is noted how both speed and electromagnetic torque are perfectly controlled after the switch instant.

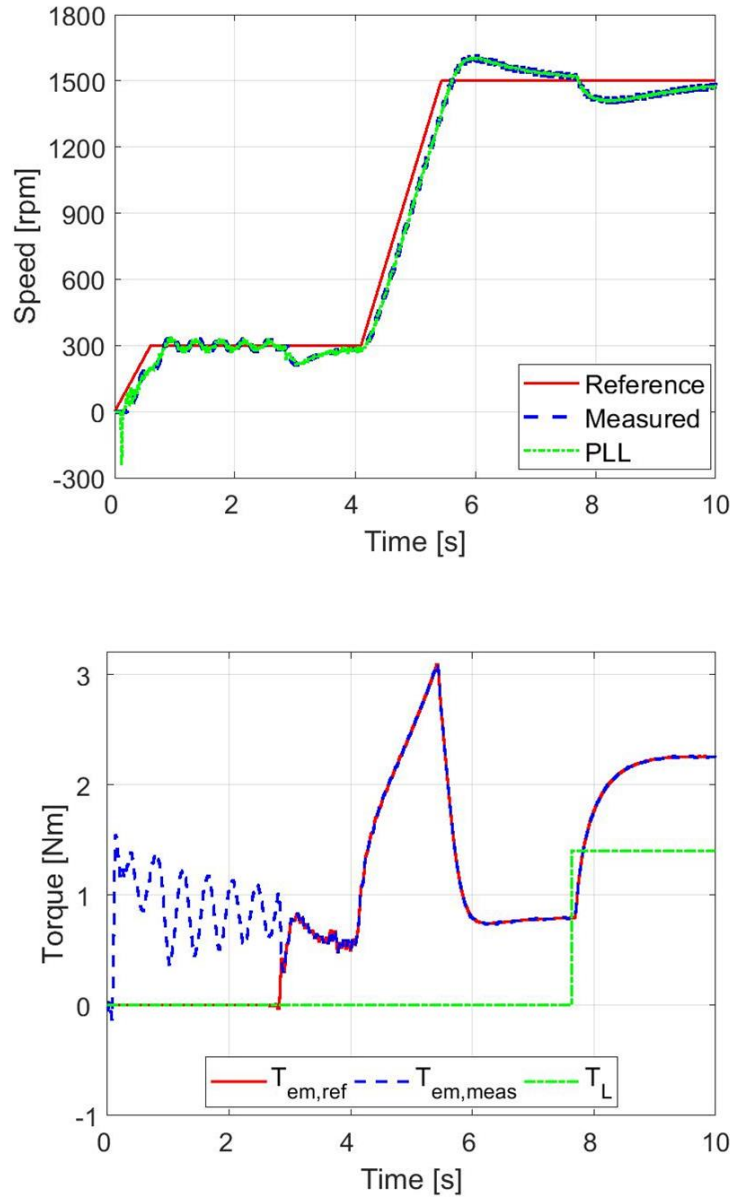


Figure 6.27: Load conditions in experimental validation. From top to bottom: speed response; torque response.

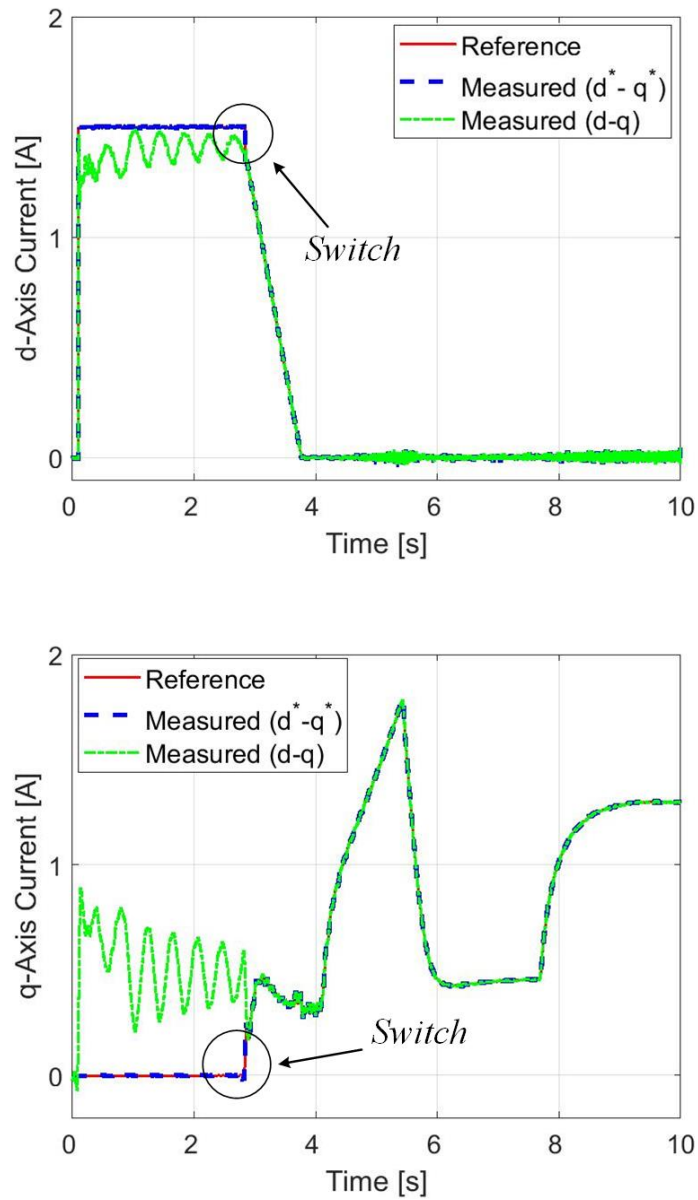


Figure 6.28: Measured currents along estimated and arbitrary RFs. From bottom to top:  $d$ -axes;  $q$ -axes.

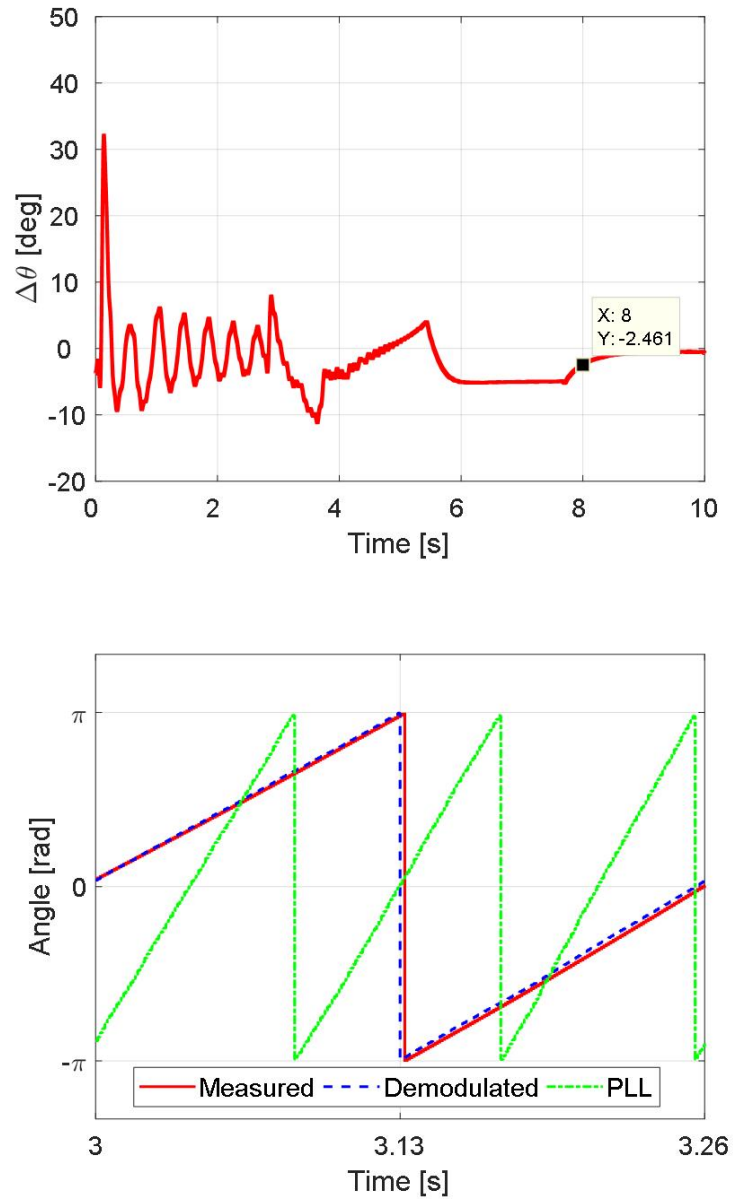


Figure 6.29: Load conditions in experimental validation. From top to bottom: angle error; zoom area of the angle.

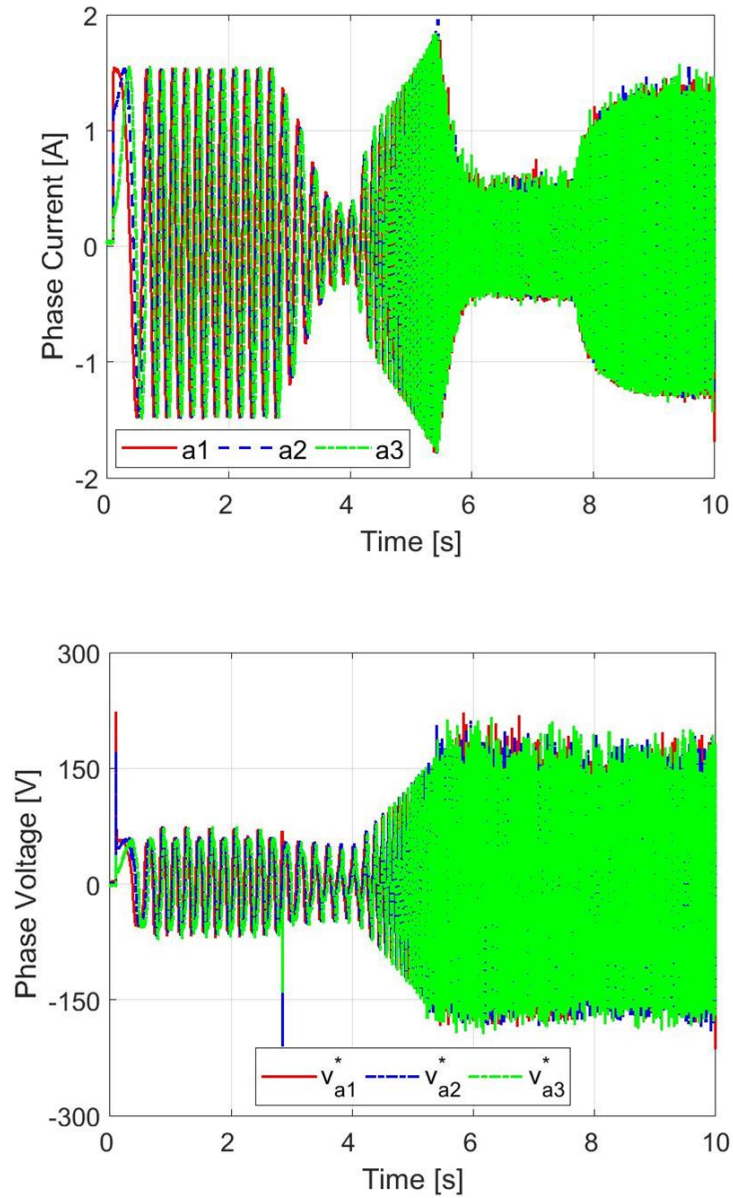


Figure 6.30: Load conditions in experimental validation. From top to bottom: phase currents; phase voltage references.

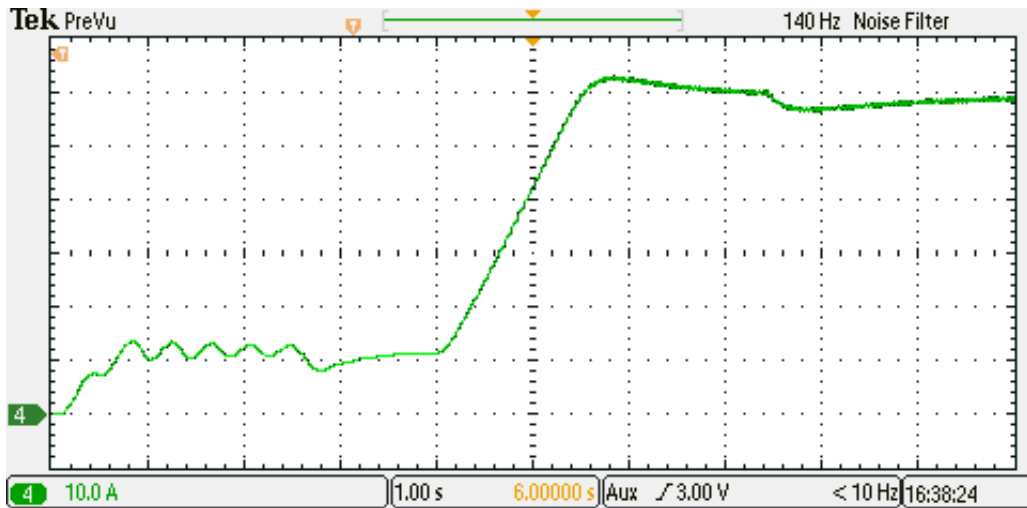


Figure 6.31: Load conditions: speed response. 250 rpm/div.

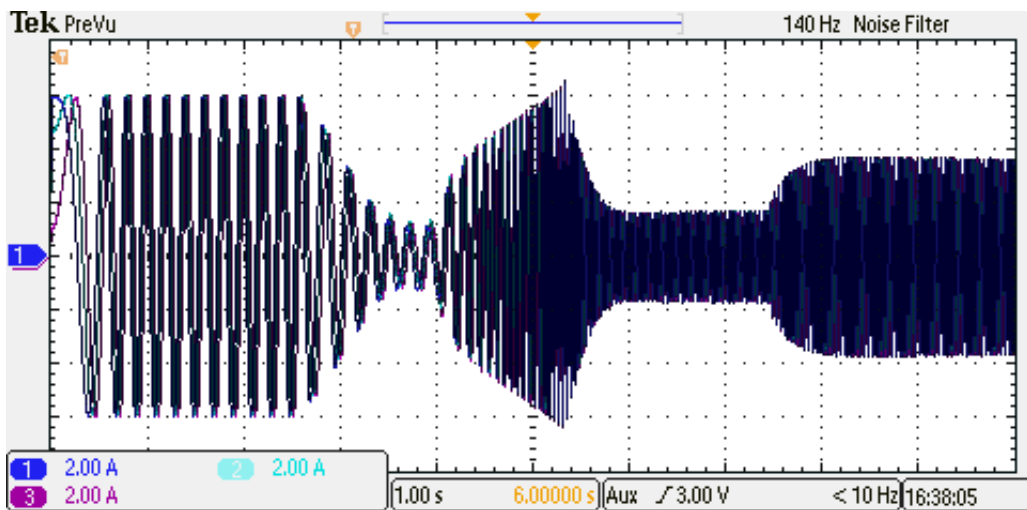


Figure 6.32: Load conditions: currents response. 2 A/div.

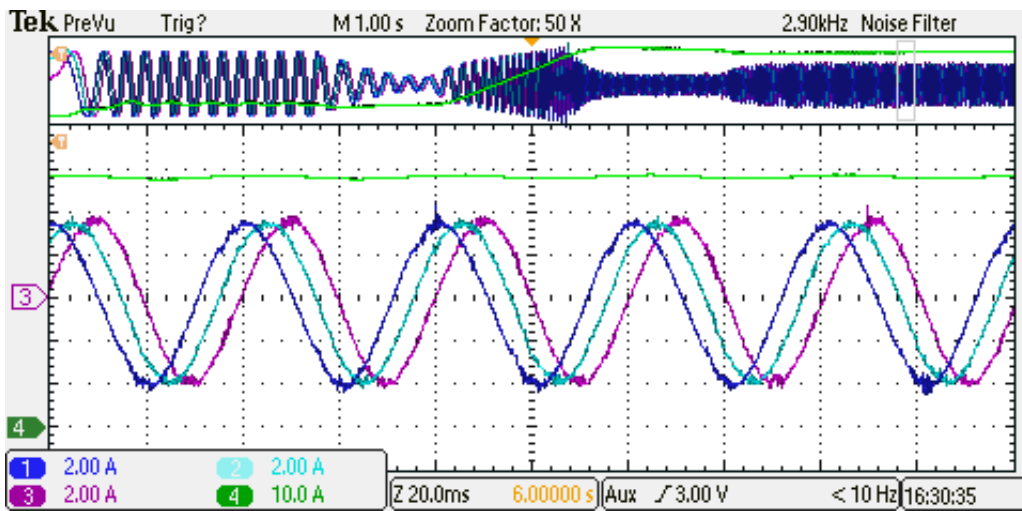


Figure 6.33: Load conditions: currents and speed responses in steady-state at 1500 rpm. CH.1 - CH.3: 2 A/div; CH.4: 250 rpm/div.

# Chapter 7

## Conclusion

### 7.1 Conclusions

The thesis explored sensorless field-oriented control of nine-phase surface permanent magnet synchronous machine with a symmetrical winding configuration. Reduced magnet span on rotor causes production of highly non-sinusoidal back-electromotive force in the stator windings. Fourier analysis of the back-*EMF* reveals a high magnitude low-order harmonic spectrum, with third-harmonic magnitude almost equal to the fundamental. Harmonics with such magnitude has been used to estimate the rotor position.

In this work *I-Hz* starting method for smooth and fast transition from open-loop frequency to sensorless *FOC* based on back-*EMF* method has been implemented. The estimation of the back-*EMF* was not necessary nor achievable as in observers. Considering the harmonic machine model in *VSD* variables, in third subplane the third harmonic of the stator current is mapped. The harmonic currents, induced by back-*EMF* and winding distribution, have been eliminated using the resonant controllers to reduce losses. Following from the harmonic model, after reconstruction of references phase voltages, rotor position was easily estimated. The use of the command voltages instead of the measured ones is a straightforward approach that improves the reliability and robustness of the system. Furthermore, the inverter errors compensation has not been implemented due to the resonant controller employed in third subplane (i.e. inverter losses are almost zero). To avoid time derivative of the angle, the rotor position and speed information have been determined using a phase-locked loop, for which inputs are the trigonometric functions computed from the reference phase voltage at the previous sample time instant in output of the control.

The *I-Hz* control is a simple starting method, which has been used to accelerate the machine in the experimental setup. The stator currents under the first control

have been controlled in the arbitrary reference frame and the angular frequency has been imposed in open-loop. The rotor follows the imposed frequency of the rotating magnetic field from standstill to a desired speed. The target speed which must be achieved under the first control scheme has been defined as the limit beyond which the error of estimated rotor position/speed is acceptable. This starting method allows the back-*EMF* signal to be sensed properly upon appropriate motor acceleration to obtain the accurate input phase-locked loop. When the speed under *I-Hz* control reaches the base target speed, after a settling interval to reduce the speed oscillations caused by the open-loop control, the estimated variables are acceptable, and can be forwarded to the sensorless *FOC* control algorithm. Therefore, when this time interval elapses, the estimated rotor position/speed has been used in the control algorithm. Switching between open-loop frequency control and sensorless control has been made smooth and regular in this way, thus avoiding undesired transient behaviour in terms of currents. The transition strategy has been performed as explained next: during *I-Hz* control, the stator currents, although not used, have been evaluated in the estimated rotor reference frame. This procedure allows to initialize the references of the current controllers under sensorless field-oriented control using the measured values during the first control, referenced to the estimated rotor reference frame. Subsequently in the second step the rotor speed has been controlled in closed-loop on the basis of estimated variables. In sensorless *FOC* the direct axis current converges to zero (to control the rotor magnetizing flux) and the quadrature axis current corresponds to the motor torque. The target values of direct and quadrature currents have been obtained following the compatible ramps with dynamic system.

As it has been shown, the main advantage of the new proposed method has been related to the reduced computation time and algorithm complexity. Derived hybrid control schematic and corresponding simulation results have been shown in the thesis. Note that, the hybrid control has been based on harmonic model, which is analysed in detail. On the basis of the back-*EMF* and *PM* harmonic distribution, both harmonic model in *VSD* model and in phase variable domain of the prototype machine have been computed. To obtain the magnetizing inductance related to  $h^{th}$  harmonic, these model in stator *Short Circuit Test and design approach* configuration has been validated, useful for a good knowledge of the machine modelling. The other machine parameters have been obtained with several experimental tests i.e. zero-sequence, single phase, and test rig characterization to tune carefully the speed and current control regulators and to know the complete mathematical model. With *Zero-Sequence Test* the leakage inductance value has been carried out. The aim of *Single Phase Test* is to obtain the isotropic inductance. Finally, the aim of *Test Rig Characterization* is to obtain the inertia value and static, linear and parabolic torque related to the test rig friction.

The thesis work has been concluded with the the experimental validation of the hybrid control using prototype machine in speed control mode. The rotor shaft has been coupled to *dc* machine acting as a mechanical load. The power converter consists of two custom-made inverters fed by a single dc power source. The digital controller is the *dSpace DS1006* development board. The mechanical rotor position has been measured with an encoder in order to compare the measured value with its estimate. The experimental results have been obtained under sensorless control. Good agreement between simulation and experimental results has been achieved.

## 7.2 Future Work

The work presented in this thesis has contributed to harmonic machine model and sensorless control of multiphase surface *PMSM*. Theoretical concepts about the harmonic model have been used to develop the hybrid control, with subsequent simulation and experimental verification on a real nine-phase machine prototype with non-sinusoidal back-*EMF*. On the basis of presented theory, work conducted here can be further continued as follows:

- The rotor position may be obtained on the basis of the fifth harmonic based on the harmonic phase-locked loop. While the third harmonic current injection may be used to obtain torque improvement on the basis of the optimal injection ratio.
- The sensed control with harmonic currents injections for each harmonic order to obtain the full torque improvement may be implemented.

# Bibliography

- [1] S. Rubino, R. Bojoi, A. Cavagnino and S. Vaschetto, 'Asymmetrical twelve-phase induction starter/generator for more electric engine in aircraft', in 2016 *IEEE Energy Conversion Congress and Exposition (ECCE)*, Milwaukee, WI, 2016, pp. 1-8.
- [2] I. Zoric, M. Jones and E. Levi, 'Arbitrary Power Sharing Among Three-Phase Winding Sets of Multiphase Machines', in *IEEE Transactions on Industrial Electronics*, vol. 65, no. 2, pp. 1128-1139, Feb. 2018.
- [3] Levi, E., (2008), 'Multiphase electric machines for variable-speed applications', *IEEE Transactions on Industrial Electronics*, vol. 55, no. 5, pp. 1893-1909.
- [4] G. Pellegrino, T. M. Jahns, N. Bianchi, W. L. Soong, and F. Cupertino, *The Rediscovery of Synchronous Reluctance and Ferrite Permanent Magnet Motors: Tutorial Course Notes*. Springer International Publishing, 2016.
- [5] C. White and H. H. Woodson. *Electromechanical Energy Conversion*, John Wiley and Sons: New York, 1959.
- [6] R.H. Park, 'Two-reaction theory of synchronous machines—I', *AIEE Transactions*, 48, 716–731, July 1929.
- [7] Zhao, Y., Lipo, T. A., (1995), 'Space vector PWM control of dual three-phase induction machine using vector space decomposition', *IEEE Trans. on Industry Applications* vol. 31, no. 5, pp. 1100-1109.
- [8] R. I. Bojoi, G. Griva, V. Bostan, M. Guerriero, F. Farina and F. Profumo, "Current control strategy for power conditioners using sinusoidal signal integrators in synchronous reference frame," in *IEEE Transactions on Power Electronics*, vol. 20, no. 6, pp. 1402-1412, Nov. 2005.
- [9] Lasca, C., Asiminoaei, L., Boldea, I., Blaabjerg, F., (2007), 'High performance current controller for selective harmonic compensation in active power filters', *IEEE Trans. on Power Electronics*, vol. 22, no. 5, pp. 1826-1835.
- [10] Lasca, C., Asiminoaei, L., Boldea, I., Blaabjerg, F., (2009), 'Frequency response analysis of current controllers for selective harmonic compensation in active power filters', *IEEE Trans. on Industrial Electronics*, vol. 56, no. 2, pp. 337-347.
- [11] Yepes, A. G., (2011), ei, L., Boldea, I., Blaabjerg, F., (2009), 'Digital resonant

- current controllers for voltage source converters', University of Vigo, PhD Thesis, Vigo, Spain.
- [12] E. Levi, 'Multiphase electric machines for variable-speed applications', *IEEE Transactions on Industrial Electronics*, 55(5), 1893–1909, 2008.
- [13] S. Rubino, R. Bojoi, S. A. Odhano and P. Zanchetta, 'Model predictive direct flux vector control of multi three-phase induction motor drives', *2017 IEEE Energy Conversion Congress and Exposition (ECCE)*, Cincinnati, OH, 2017, pp. 3633-3640.
- [14] Klingshirn, E.A.: 'High phase order induction motors—Part I—Description and theoretical considerations', *IEEE Transaction Power Appar. System*, 1983, 102, (1), pp. 47– 53
- [15] Toliyat, H.A., Waikar, S.P., and Lipo, T.A.: 'Analysis and simulation of five-phase synchronous reluctance machines including third harmonic of airgap mmf', *IEEE Transaction Industial Applications*, 1998, 34, (2),pp. 332–339
- [16] R. H. Nelson and P. C. Krause, 'Induction Machine Analysis for Arbitrary Displacement Between Multiple Winding Sets', in *IEEE Transactions on Power Apparatus and Systems*, vol. PAS-93, no. 3, pp. 841-848, May 1974.
- [17] Yifan Zhao and T. A. Lipo, 'Space vector PWM control of dual three-phase induction machine using vector space decomposition', in *IEEE Transactions on Industry Applications*, vol. 31, no. 5, pp. 1100-1109, Sept.-Oct. 1995.
- [18] E. Clarke, *Circuit Analysis of A-C Power*, Vols. 1 and 2, John Wiley Sons, New York, 1941 (Vol. 1) and 1950 (Vol. 2).
- [19] I. Zoric, M. Jones and E. Levi, 'Vector space decomposition algorithm for asymmetrical multiphase machines', *2017 International Symposium on Power Electronics (Ie)*, Novi Sad, 2017, pp. 1-6.
- [20] S. Rubino, R. Bojoi, S. A. Odhano and P. Zanchetta, 'Model Predictive Direct Flux Vector Control of Multi-three-Phase Induction Motor Drives', in *IEEE Transactions on Industry Applications*, vol. 54, no. 5, pp. 4394-4404, Sept.-Oct. 2018.
- [21] P. Krause, O. Wasynczuk, S. D. Sudhoff, and S. Pekarek, *Analysis of Electric Machinery and Drive Systems*. John Wiley Sons, 2013.
- [22] J. Holtz. *Sensorless Control of Induction Machines- With or Without Signal Injection* *IEEE Transactions on Industrial Electronics*, Vol. 53, pp. 7-30, Feb. 2006.
- [23] P. P. Acarnley and J. F. Watson. 'A Review of Position Sensorless Operation of Brushless Permanent-Magnet Machines' *IEEE Transactions on Industrial Electronics*, Vol. 53, pp. 352-362, April 2006.
- [24] E. Levi, 'Magnetic variables control' in *Encyclopaedia of Electrical and Electronics Engineering*, Vol. 12, J.G.Webster(ed.), John Wiley Sons, New York, 1999, pp. 242–260.
- [25] P. Vas, *Vector Control of AC Machines*, Clarendon Press, Oxford, U.K., 1990.

- [26] M. Slunjski, M. Jones and E. Levi, 'Analysis of a Symmetrical Nine-phase Machine with Highly Non-Sinusoidal Back-Electromotive Force', *IECON 2018 - 44th Annual Conference of the IEEE Industrial Electronics Society*, Washington, DC, 2018, pp. 6229-6234.
- [27] Joohn-Sheok Kim, Seung-Ki Sul, 'High performance PMSM drives without rotational position sensors using reduced order observer', *Conference Rec. of the Thirtieth IAS Annual Meeting, IAS '95*, vol.1, pp. 75-82, 1995.
- [28] M. Pulvirenti, D. Da Rù, N. Bianchi, G. Scarcella and G. Scelba, 'Secondary saliencies decoupling technique for self-sensing integrated multi-drives', *2016 IEEE Symposium on Sensorless Control for Electrical Drives (SLED)*, Nadi, 2016, pp. 1-6.
- [29] A. Antonioli, M. Antoniol, S. Calligaro and R. Petrella, 'An A low cost sensorless drive for hybrid stepper motors based on back-EMF observer and d-axis current injection for industrial labelling machines', *2014 IEEE Applied Power Electronics Conference and Exposition - APEC 2014*, Fort Worth, TX, 2014, pp. 2492-2499.
- [30] T. Wang, W. Ding, Y. Hu, S. Yang and S. Li, 'Sensorless control of switched reluctance motor drive using an improved simplified flux linkage model method', *2018 IEEE Applied Power Electronics Conference and Exposition (APEC)*, San Antonio, TX, 2018, pp. 2992-2998.
- [31] H. Tanaka and M. Hasegawa, 'Improvements of speed adaptation response for IPMSM position sensorless vector control with parallel feedforward compensator', *Proceedings of the 2011 14th European Conference on Power Electronics and Applications*, Birmingham, 2011, pp. 1-10.
- [32] J. S. Park, S. H. Lee, C. Moon and Y. A. Kwon, 'State observer with stator resistance and back-EMF constant estimation for sensorless PMSM', *TENCON 2010 - 2010 IEEE Region 10 Conference*, Fukuoka, 2010, pp. 31-36.
- [33] M. Bendjedja, Y. Ait-Amirat, B. Walther, A. Berthon, 'Position Control of Sensorless Stepper Motor', *IEEE Transactions on Power Electronics* 27, no. 2, pp. 578-587, Feb. 2012.
- [34] R. Wu and G. R. Slemon, 'A permanent magnet motor drive without a shaft sensor', *IEEE Transactions on Industry Applications*, vol. 27, no. 5, pp. 1005-1011, 1991.
- [35] K.-W. Lee, D.-K. Kim, B.-T. Kim, and B.-I. Kwon, 'A novel starting method of the surface permanent-magnet bldc motors without position sensor for reciprocating compressor', *IEEE Transactions on Industry Applications*, vol. 44, no. 1, pp. 85-92, 2008.
- [36] G. H. Jang, J. H. Park, and J. H. Chang, 'Position detection and start-up algorithm of a rotor in a sensorless bldc motor utilising inductance variation', *IEEE Proceedings of Electric Power Applications*, vol. 149, no. 2, pp. 137-142, 2002.

- [37] F. Briz and M. W. Degner, 'Review of position estimation methods for ipmsm drives without a position sensor part ii: Adaptive methods', in *Proceedings of ICEM 2010*, pp. 1–6, 2010.
- [38] Z. Wang, K. Lu, and F. Blaabjerg, 'A simple startup strategy based on current regulation for back-emf-based sensorless control of pmsm', *IEEE Transactions on Power Electronics*, vol. 27, no. 8, pp. 3817–3825, 2012.
- [39] P. Vas, *Sensorless Vector and Direct Torque Control*. Oxford University Press, 1998.
- [40] V. Kaura and V. Blasko, 'Operation of a phase locked loop system under distorted utility conditions', *IEEE Transaction Industrial Applications*, vol. 33, no. 1, pp. 58–63, Jan. 1997.
- [41] A. Varatharajan, P. Pescetto and G. Pellegrino, 'Injectionless Sensorless Control of Synchronous Reluctance Machine for Zero to Low Speeds Region', *018 IEEE 9th International Symposium on Sensorless Control for Electrical Drives (SLED)*, Helsinki, 2018, pp. 72-77.
- [42] M. Fatu, R. Teodorescu, I. Boldea, G. Andreescu, and F. Blaabjerg, 'I-f starting method with smooth transition to emf based motion-sensorless vector control of pm synchronous motor/generator', in *Proceeding of PESC 2008*, pp. 1481–1487, 2008.
- [43] C. L. Baratieri and H. Pinheiro, 'I-F starting method for smooth and fast transition to sensorless control of BLDC motors', *2013 Brazilian Power Electronics Conference*, Gramado, 2013, pp. 836-843.
- [44] A. Stirban, I. Boldea, and G. Andreescu, 'Motion sensorless control of bldc-pm motor with offline fem information-assisted position and speed observer', *Industry Applications, IEEE Transactions on*, vol. 48, no. 6, pp. 1950–1958, 2012.
- [45] J. Pyrhonen, T. Jokinen, and V. Hrabovcova, *Design of Rotating Electrical Machines*. John Wiley Sons, 2013.